Molecular Dynamics Investigation of Hydrogen Embrittlement in Steel

Ángel Alberto Izquierdo Sánchez

A Thesis Submitted for the Degree of Doctor of Philosophy

School of Engineering

July, 2022

Declaration

This thesis records work carried out in the School of Engineering at Newcastle University between January 2018 and September 2022 and is original except where acknowledged by reference to work of others. Several sections of this work have already been published (or are in press) in different journals, and these papers are summarised below.

1. Izquierdo-Sánchez, Á., Oila, A. and Charles, A., 2020. Atomistic simulation of tensile tests on iron and ferrite. Materialia, 13, p.100822.

No portion of this work is being, nor has been, submitted for a degree, diploma or any other qualification at any other university.

Acknowledgements

I want to thank God for the opportunity to fulfil my dreams. To my sponsor, CONACyT, for providing me with the resources to carry out my doctoral studies. To my supervisors, Dr. Oila and Dr. Charles, for their valuable guidance and hours of discussion. To my partner, for her patience and unconditional support. Finally, a special thank to my family, for always supporting me and believing in me.

Abstract

Hydrogen embrittlement, the detrimental effect of hydrogen on the mechanical properties (strength, ductility, toughness, etc.) of metals and alloys, has been an important engineering challenge. Despite the great effort devoted to this subject in the past, the mechanisms by which hydrogen embrittles most metallic materials remain unclear. In this work, molecular dynamics (MD) studies have been carried out in order to investigate hydrogen embrittlement in steel.

Tensile test simulations of pure iron and ferrite have initially been performed. Noticeable differences in the strength and the deformation behaviour of pure iron and the solid solution were found. These differences become sufficiently large at strain rates below $10^9\,\mathrm{s}^{-1}$ in the $[1\,1\,1]$ and $[1\,\overline{1}\,0]$ directions, confirming the strengthening role of carbon atoms.

MD simulations using a periodic array of dislocations were performed to investigate the effects of hydrogen on the dislocation mobility in the presence and absence of a C interstitial under applied shear stress. Due to the high tensile stresses, hydrogen diffuses to and accumulates at the tensile side of the dislocation core, forming a Cottrell cloud. Hydrogen solutes decrease dislocation mobility by several orders of magnitude. The presence of hydrogen in a dislocation pinned by a carbon interstitial increases the stress needed to unpin the dislocation. These results suggest that hydrogen is unlikely to facilitate dislocation glide or to aid dislocations overcoming C interstitials.

The effect of hydrogen on the fracture process was also studied. Crack propagation was studied on the $(1\,1\,1)[1\,1\,\overline{2}]$, the $(1\,1\,1)[1\,\overline{1}\,0]$ and the $(1\,0\,0)[0\,1\,0]$ orientations. The results show a range of mechanisms leading to inferior fracture toughness as the hydrogen concentration is increased. For the chosen simulation conditions, the operation of these mechanisms depends mostly on the crystal orientation and the hydrogen concentration. On the $(1\,1\,1)[1\,1\,\overline{2}]$ orientation at low hydrogen concentrations, fracture resembles that of the Adsorption Induced Dislocation Emission (AIDE) mechanism while at higher concentrations the nucleation of dislocations is prevented and fracture occurs via a cleavage-like mechanism. This trend was also repeated on the $(1\,1\,1)[1\,\overline{1}\,0]$ orientation. Furthermore, at higher concentrations, increased plasticity caused by intense dislocation activity leading to nano-void formation was also seen on this orientation. These features are consistent

with the Hydrogen Enhanced Localised Plasticity (HELP) model. On the (1 0 0)[0 1 0] orientation, hydrogen reduces the lattice cohesion and fracture occurred at lower values of stress intensity, which is in agreement with the Hydrogen Enhanced Decohesion (HEDE) model.

Based on these simulations, it has been concluded that there exists a spectrum of operational hydrogen embrittlement mechanisms in the nanoscale fracture process of Fe. The dominance of HEDE, HELP, AIDE or other failure mechanism depends on the crack-tip conditions, such as the local hydrogen concentration, crack orientation and crack velocity.

Nomenclature

α_{p} = coefficient of thermal expansion

$\bar{\rho}_i$ = local electron gas density at position of atom i

Δa = crack extension

$\dot{\varepsilon}$ = strain rate

ϵ = energy at equilibrium distance for Lennard-Jones potentials

γ_{us} = unstable stacking fault energy

$\langle A \rangle_{\mathrm{ensemble}}$ = ensemble average of property A

$\langle A \rangle_{\mathrm{Time}}$ = time average of property A

$\mathbf{a}_{\mathrm{pre}}$ = predicted acceleration for Predictor-Corrector algorithm

$\mathbf{a}_i$ = acceleration of atom i

$\mathbf{F}_i$ = force acting on atom i

$\mathbf{r}_{\mathrm{cor}}$ = corrected position for Predictor-Corrector algorithm

$\mathbf{r}_{\mathrm{pre}}$ = predicted position for Predictor-Corrector algorithm

$\mathbf{r}_i$ = position of atom i

$\mathbf{u}$ = displacement

$\mathbf{v}_{\mathrm{cor}}$ = corrected velocity for Predictor-Corrector algorithm

$\mathbf{v}_{\mathrm{pre}}$ = predicted velocity for Predictor-Corrector algorithm

$\mathbf{v}_i$ = velocity of atom i

ν = Poisson's ratio

ϕ_{ij} = pair potential (chapter 3)

σ = distance at which energy is zero for Lennard-Jones potentials (chapter 3)

σ_{max} = maximun tensile stress

σ_{yield} = yield strength

σ_{ij} = stress component ij

τ_{ij} = shear stress component ij

θ = angle with crack plane

B = drag coefficient

b = Burgers vector magnitude

b_{ij} = bond order parameter for Tersoff potentials

C_0 = far-field H solutes concentration

D = diffusion coefficient

E_i = energy of bond i

f_c = cut-off function for bond-order potentials

F_i = embedding function for EAM potentials

G = shear modulus

$g(r)$ = radial distribution function

G_{Ie} = energy release rate for dislocation emission

H = total energy of the system

K = kinetic energy of the system (for chapter 3)

K = stress intensity factor (for chapter 6)

K_{I} = stress intensity factor for mode I loading

k_B = Boltzmann constant

L_i = size of simulation box on the i direction

m = strain rate sensitivity

m_i = mass of atom i

N = number of particles in the system

P = pressure of the system

r = distance from with crack tip

r = interatomic distance (chapter 3)

r_0 = cut-off radius

r_{mobile} = radius of mobile region for K-controlled simulations

r_{pz} = radius of plastic zone around the crack-tip

T = temperature of the system

t = time

U = potential energy of the system

u_i = displacement component i

V = volume of the system

v = dislocation glide velocity

V_A = function describing attractive interaction for Bond-order potentials

V_R = function describing repulsive interaction for Bond-order potentials

V_{ij} = energy of bond between atom i and j

MSD = mean-square displacement

Contents

List of Figures

List of Tables

Chapter 1

Introduction

Steel is the structural material most widely used globally. Its abundance, relatively low cost and ability to greatly change its mechanical properties by alloying and processing make it suitable for the vast majority of engineering tasks. Steels are widely used in a number of industries such as the construction and transport industries. The energy sector is also no exception to applications of this alloy.

Hydrocarbons are presently the main source of energy as they account for more than half of energy production worldwide [1]. Pipelines are the most efficient and safest mean of hydrocarbon transport. However, like any other engineering assets, pipelines are exposed to a variety of hazards that compromise their integrity. Only surpassed by third-party interference, environmental damage is one of the main causes of pipeline failure, which is usually manifested in the form of stress corrosion cracking and hydrogen damage. While the former is considerably more common than the latter, newer pipelines, made out of higher-grade steel, are highly susceptible to some form of hydrogen damage, such as hydrogen embrittlement (HE). While it is true that the change to energy sources with smaller impact on the environment than hydrocarbons is necessary, this change will take time. From the possible future sources of clean energy, hydrogen is one of the most prominent. This technology is likely to repurpose part of the gas infrastructure such as pipelines and storage facilities. This will unavoidably expose these assets to high pressures of hydrogen gas, conditions that are known to result in hydrogen embrittlement.

The deleterious effect of hydrogen on steel was first reported more than a century ago [2]. Now it is well-known that steel, among other alloys and pure metals, has its mechanical properties significantly affected when exposed to a hydrogen environment. Hydrogen concentrations as low as 10^{-3} at.% are reported to have significant impact on toughness and strength. However, hydrogen embrittlement remains far from being completely understood. Several theories have been proposed in order to rationalise HE, each of them with their own supporting and contradictory evidence. Hydrogen Enhanced Decohesion (HEDE) [3, 4], Hydrogen Enhanced Localised Plasticity (HELP) [5–7] and Adsorption

Induced Dislocation Emission (AIDE) [8, 9] are some examples of HE models relevant to steel. Nevertheless, at the time of this work, a model that can satisfactorily establish quantitative conditions at which HE will take place is not available.

Part of the reason why HE is difficult to investigate is the high mobility and low solubility of hydrogen atoms, making direct observation and detection almost impossible. Modern steels are very complex engineering materials and contain a great number of microstructural defects such as point defects, dislocations and grain boundaries. The macroscopic effects of hydrogen on steel are the consequence of the strong interactions of hydrogen atoms with these defects. Therefore, knowledge of events occurring at the atomic level will benefit our understanding of the HE process.

With the continuous increase in computational capabilities, atomistic simulations have proven valuable for our current understanding of modern materials. Ab-initio calculations are highly accurate and are usually employed to calculate formation and interaction energies at the ground state. This data can be used to fit interatomic potentials that can be employed in larger scale simulations such as Molecular Dynamics (MD), Molecular Statistics (MS) and Monte Carlo (MC) simulations. MD simulations can be used to predict the time evolution of the system, and have been widely use to study topics in fracture mechanics and plasticity.

In the field of hydrogen embrittlement, MD simulations offer the opportunity to study mechanistic aspects that otherwise could not be studied. For instance, hydrogen is known to modify the behaviour of dislocations, which drive the main mechanism for plastic deformation. While direct observations of dislocations are readily available, the distribution of hydrogen atoms around these defects cannot be determined experimentally. Similarly, continuum dislocation theory stops being valid at the core region, where hydrogen atoms are more likely to migrate, and quantum mechanics treatments remain too computationally expensive to accommodate the large number of atoms needed to recreate realistic models of dislocations. However, the limitations described above are not present in MD simulations, making them a viable option to study hydrogen-dislocation interactions. Therefore, when tailored correctly, they can be used to test specific concepts of proposed HE models.

MD simulations have important limitations that need to be recognised, namely, reduced time and length scales when compared with experiments, and dependence on the accuracy of interatomic potentials obtained from experimental or *first-principles* data. However, over the past few decades, more powerful computers and more efficient algorithms have been developed, suggesting that these limitations will become less significant. Embedded-Atom Method (EAM) interatomic potentials [10] allow fast computations with relatively good levels of accuracy in metals. Simulations of systems comprising several millions of atoms are in reach of most high performance computing services. Time scales close to the order of magnitude of microseconds can be achieved for systems containing hundreds

of thousands of atoms. Furthermore, new types of interatomic potentials such as the Reactive Force Field (ReaxFF) potentials [11] have shown good accuracy when describing complex systems, such as the Fe-C-H system [12]. These advances suggest that atomistic simulations will continue to play a role in understanding hydrogen related phenomena.

In this thesis, a study of hydrogen embrittlement using molecular dynamics simulations is presented. The effect of hydrogen in ferrite is studied using widely used EAM interatomic potentials [13, 14]. A newer reactive force field potential [12] have also been considered as it offers the opportunity to study hydrogen behaviour under scenarios that have not been studied with MD simulations, namely, dislocation glide through C interstitials in the presence of H solutes. Finally, the effect of hydrogen in fracture of pure Fe is also studied using K-controlled simulations. These simulations attempt to evaluate the viability of relevant HE models as mechanisms for fracture of an atomically sharp crack.

1.1 Aims and Objectives

The aim of this work is to elucidate the mechanisms of hydrogen embrittlement that operate in steel by performing molecular dynamics simulations.

- To study the impact of C on the mechanical properties of ferrite by performing tensile test simulations.
- To investigate the effect of hydrogen on edge dislocation mobility using a periodic array of dislocations (PAD) model for dislocation glide.
- To investigate the fracture behaviour of Fe as a function of the concentration of hydrogen solutes using K-controlled fracture simulations.

1.2 Structure of thesis

This thesis is structured as follows. Chapter 1 discusses the importance and some of the challenges of researching hydrogen embrittlement. Aims and objectives of this work are also stated in this chapter. Chapter 2 provides a background to hydrogen embrittlement and discusses some of the challenges of studying HE and highlighting the importance of understanding it. The hydrogen embrittlement process, from the uptake of hydrogen into the metal to the induction of embrittlement is also discussed. A summary of the main proposed HE mechanisms with their own relevant evidence and limitations is also included. In chapter 3, the foundations of Molecular Dynamics simulation are presented. The typical process of performing MD simulations is also discussed. A brief discussion on different interatomic potentials with special focus on EAM and ReaxFF potentials is included, as the simulations presented on this thesis made use of them. A summary of relevant HE studies performed with MD simulations is also provided. In chapter 4, a comparison between mechanical properties of pure iron and ferrite, the solid solution of

C in body-centred cubic Fe, predicted by molecular dynamics using a widely-used EAM potential are presented. This is done in order to estimate the effect of C atoms, which are commonly neglected in atomistic simulations of ferrite. Chapter 5 examines one of the manifestations of HE, the effect on dislocation mobility, which is one of the main concepts proposed in the Hydrogen-Enhanced Localised Plasticity model. The mobility of an edge dislocation in pure iron and in the presence of C interstitials is estimated. Comparison is made between the mobility in the presence and absence of hydrogen solutes. Chapter 6 studies the effect of hydrogen in the nanoscale fracture process of pure Fe, using K-controlled fracture, a simulation technique in which the stress intensity factor K is the only loading variable. Brittle fracture and ductile failure at different H concentrations were studied in order to identify the fracture mechanism and relate it to HE mechanisms proposed in the literature. Conclusions will be presented in chapter 7, together with suggestions on future research relevant to this topic.

Chapter 2

The Hydrogen Embrittlement Challenge

Hydrogen embrittlement (HE) is the detrimental effect of hydrogen on the mechanical properties of metals and alloys. In low carbon steels, the presence of atomic hydrogen in concentrations as low as 10 ppm [15], significantly reduces strength, ductility and toughness. This reduction on the ability of the material to bear load can lead to unpredictable catastrophic failure and limits the structural applicability of the affected materials.

Hydrogen embrittlement has been a technical challenge for over a century, as the adverse effects of hydrogen on steel was first recognised by Johnson in 1875 [2]. Despite the great effort devoted, the issue is still unresolved for most materials. While the embrittlement process is understood in materials in which hydride formation is possible (e.g. V, Zr Ti and their alloys [7, 16, 17]), the mechanisms by which hydrogen embrittles steel and other non hydride-forming materials has not been satisfactorily explained.

Hydrogen embrittlement is difficult to study for a number of reasons. One of them is the fact that modern steels are complex materials. The microstructure, which controls mechanical properties, is usually finely tuned during the steel making process, and contains a wide variety of defects. Hydrogen interacts with all these defects in different ways, as shown in figure 2.1. Depending on these interactions, hydrogen embrittlement can be increased or reduced. For instance, microstructural defects can function as irreversible traps and prevent atomic H diffusion to regions ahead of the crack-tip, where embrittlement occurs, which might limit hydrogen embrittlement. Conversely, reversible traps can increase the amount of hydrogen uptake during H charging, which can then become free and diffuse to the crack-tip, resulting in increased hydrogen damage. Because of the different interactions with microstructural defects, there is significant spread when assessing hydrogen embrittlement, which gives rise to a large number of controversial findings. Furthermore, direct observations of the role of hydrogen on the nanoscale deformation process in bulk material is not possible, and even in experiments using thin TEM samples, the H

distribution in the affected area is unknown.

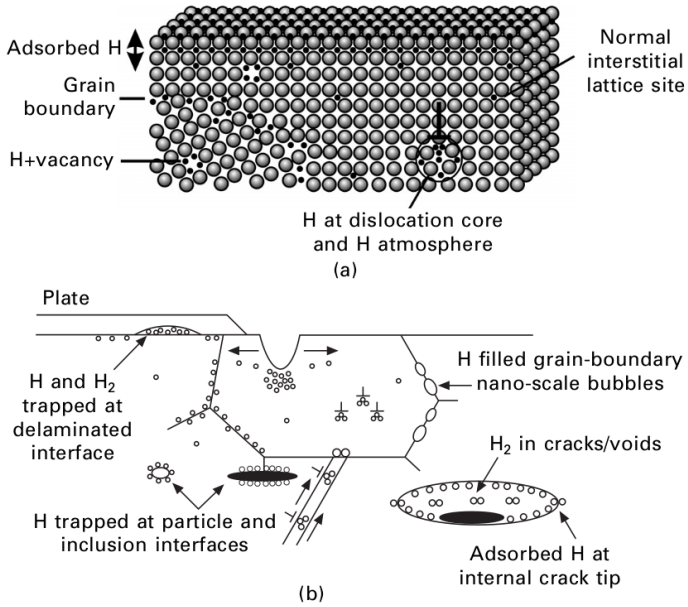

Figure 2.1. Schematic representation of hydrogen interactions with microstructural defects at the a) atomic scale and b) microscopic scale [18].

The inability of experimental techniques to resolve the atomic scale make atomistic simulations an attractive alternative to study hydrogen embrittlement. Density functional theory calculations have already offered valuable findings regarding the binding energies of H around different defects [19–23], and molecular dynamics simulations have also contributed to study the effects of hydrogen in nanoscale deformation phenomena and to test concepts proposed by relevant HE mechanisms [24]. As greater computational resources become available to researchers, the H-related phenomena that will be possible to study using atomistic simulations will continue to increase.

The aim of this chapter is to provide a background regarding hydrogen embrittlement, the conditions under which it becomes severe and the proposed mechanisms with the most relevance to steels. Comprehensive reviews on these topics can be found in the literature [18, 24–26]. This chapter is organised as follows: Sections 2.1 and 2.2 discuss the impact of HE, and the main factors influencing the conditions under which it becomes significant, respectively. Section 2.3 describes the HE process, and relevant HE mechanisms are discussed in section 2.4. Finally, a brief overview relevant Molecular Dynamics studies of HE is provided in section 3.8.

2.1 Impact of hydrogen embrittlement

A wide variety of metallic materials are susceptible to hydrogen embrittlement. Some examples of these materials are low carbon steels [27], high Mn steels [28], Al alloys [29], and high strength Ni alloys [30], among many others. Furthermore, with the aim to reduce material costs, the demand for high strength materials continues to increase. In

steels, higher strength is usually achieved with more complex microstructures containing phases such as martensite and bainite. However, higher strength generally leads to higher susceptibility to hydrogen, which poses a problem for more recent structures made with higher strength alloys.

Because of the large number of alloys affected, HE is a risk for many industrial applications. The oil and gas, automotive and nuclear industries are some examples of sectors in which HE is relevant. In the oil and gas industry, HE affects pipelines and other pressure vessels, which are well-known for being susceptible to hydrogen damage, especially when operating in sour service conditions (in presence of H_2S or H_2SO_4) or under corrosive environments. In the automotive sector, HE affects high strength steels employed to manufacture automotive components. High strength steels are often used as they offer an inexpensive way to reduce weight. In the nuclear sector, gaseous hydrogen additions to the water coolant used to improve corrosion control, can lead to a reduction of the fracture toughness of Ni-based alloys [31]. These examples are just some of the many risks HE represents for modern society.

Aside from its impact in current industrial applications, HE is expected to continue to be problematic in future applications. The pursuit of reducing CO_2 emissions has led to the search for cleaner energy technologies. Some of these technologies are based on hydrogen as an energy carrier. For instance, fuel cell vehicles (FCV) are one of the candidates to replace internal combustion engine cars in the future. FCV generate electricity from hydrogen, which has to be somehow stored in the vehicle. Hydrogen storage is a non-trivial issue, and one of the possible ways to do it is as compressed hydrogen gas. While state-of-the-art hydrogen tanks are not made with metallic materials [32], some of the components (e.g. valves, fittings, etc.) would still be. Furthermore, the success of FCV and other hydrogen based technologies, would undoubtedly result in an increase of hydrogen demand, which would require further hydrogen storage and distribution facilities. Existing gas storage facilities and pipeline networks could be repurposed to hydrogen, which would signify an important reduction of resources and waste. However, for this to be possible, a better understanding of the hydrogen embrittlement process is needed.

2.2 Factors affecting hydrogen embrittlement

There is a large number of factors that can lead to hydrogen embrittlement. These factors can be divided into three main categories, as shown in figure 2.2. The first main category is related to the material itself. An important factor in this category is the microstructure. Hydrogen interacts with microstructural defects, and depending on the nature of such interactions, hydrogen embrittlement can be increased or decreased. For instance, the presence of metalloid impurities and second phase particles usually leads to more severe hydrogen damage, while the presence of some strong H traps might mitigate it [18]. Microstructures containing hard phases such as martensite are highly affected by HE, as

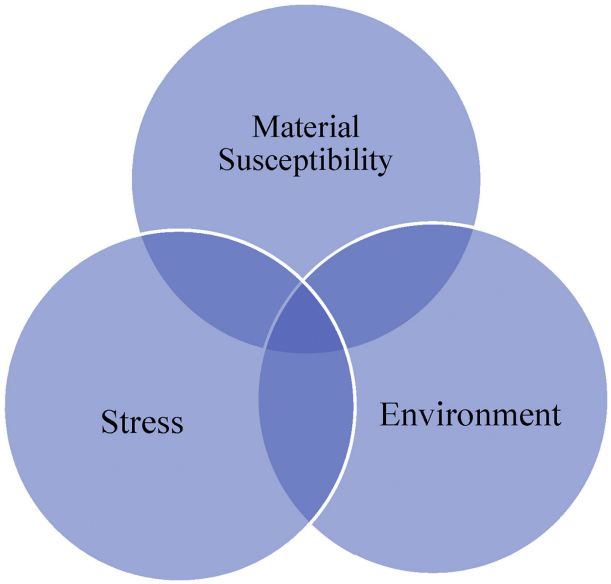

Figure 2.2. Factors affecting hydrogen embrittlement [15]. A combination of a susceptible material, a H-rich environment and high stress is required for HE.

hydrogen can accumulate at lath interfaces [33]. Hydrogen can also accumulate along prior austenite grain boundaries and produce intergranular failure [25]. Another material related factor for HE susceptibility, which is tightly related to the microstructure, is strength. Susceptibility generally increases with tensile strength. For instance, hydrogen susceptibility in the form of loss of ductility due to hydrogen charging was found to increase with strength in pipeline steel [34] and in steel fasteners [35].

The second category of factors affecting hydrogen embrittlement is the environment to which the material is exposed. The magnitude and the mode of the hydrogen damage depends on a number of factors. The degree of HE normally increases with the exposure to hydrogen, but there could be a saturation value after which little increase in embrittlement would take place [18]. The exposure could be in the form of H_2 gas pressure or current density during cathodic charging. The charging procedure is important because these techniques can induce some damage to the sample that affects the hydrogen uptake. For instance, polished specimens have been reported to adsorb more hydrogen than ground specimens during cathodic charging [36]. Another important environment related variable is the temperature. Hydrogen diffusion rates increase with temperature and tend to be several orders of magnitude greater in BCC metals than in FCC and HCP metals. The diffusion coefficient of H in pure Fe samples almost free from dislocations has been determined experimentally as $D\,[\mathrm{m^2/s}] = 5.8 \times 10^{-8} \exp\left(-4.5\,\left[\mathrm{kJ\,mol^{-1}}\right]/RT\right)$ [37], where R and T are gas constant and the temperature, respectively. These values are in agreement with diffusion coefficients reported in MD simulations [38]. For instance, at 300 K the diffusion coefficient has been reported as $9.55 \times 10^{-9}\,\mathrm{m^2/s}$ and $8.96 \times 10^{-9}\,\mathrm{m^2/s}$ from experiments and simulation, respectively. Even though H diffusion increases with temperature, HE susceptibility as a function of temperature seems to depend on several other factors, which often lead to a temperature window within which HE is more se-

vere. The temperature at which HE susceptibility is the highest has been reported close to room temperature and depends on factors such as microstructure, loading conditions and hydrogen exposure [39]. HE is often limited at temperatures outside this temperature window, probably due to limited H transport at lower temperatures and limited H trapping by defects at higher temperatures [40].

Finally, the third category is related to the load to which the material is subjected. As expected, the stress must be sufficiently high for HE to occur, which can come from applied or residual stresses. High stresses can also be achieved microscopically near defects (e.g. plastic zone ahead of cracks or at dislocation cores). Strain rates in tensile tests also affect the degree of embrittlement. The susceptibility of HE normally decreases as the strain rate is increased. For instance, the extent of HE in martensitic steel was found to decrease considerably when increasing the strain rate from $8.3 \times 10^{-6}\,\mathrm{s}^{-1}$ to $8.3 \times 10^{-3}\,\mathrm{s}^{-1}$ [41]. This difference was attributed to the insufficient time for hydrogen to accumulate along prior austenite grain boundaries, preventing intergranular failure.

2.3 The hydrogen embrittlement process

While the underlying mechanisms of HE are still under debate, the following steps of the embrittlement process must occur: 1) Hydrogen needs to be present within the material in enough quantities to induce embrittlement, which can come from either internal or external sources. 2) Hydrogen has to be transported to regions near microstructural defects (e.g. crack-tips and grain boundaries). 3) Hydrogen must somehow induce embrittlement by interacting with these defects[1].

Hydrogen leading to hydrogen embrittlement, that is, hydrogen supplied to the plastic zone ahead of the crack-tip, can come from different sources. Depending whether these sources are internal or external, hydrogen embrittlement can be classified into two categories, namely, *Internal Hydrogen Assisted Cracking* (IHAC) and *Hydrogen Environment Assisted Cracking* (HEAC)[2]. In IHAC, hydrogen enters the metal during the manufacturing process. Some of the manufacturing operations that can lead to hydrogen uptake are casting, welding, surface cleaning, electroplating and heat treatments. For instance, hydrogen adsorption can occur during casting and welding due to the high temperatures of these processes that provide enough energy to dissociate the water molecule, present in the environment as moisture. Other internal hydrogen sources can also arise during service due to cathodic protection via impressed current or sacrificial anodes. Hydrogen can also be produced as a by-product of the cathodic reaction during the corrosion process, and can be absorbed into the metal. In HEAC, hydrogen comes from external sources when combined with stress. External sources might come in the form of a pres-

[1] The possible mechanisms by which hydrogen induces embrittlement are discussed in section 2.4.

[2] IHEC and HEAC are also referred to as Internal Hydrogen Embrittlement (IHE) and Hydrogen-Environment Embrittlement (HEE), respectively.

surised hydrogen rich fluid in contact with a steel component, or as chemical reactions (e.g. combustion) of products containing hydrogen. When atomic hydrogen is produced at the crack surfaces near the crack-tip, it can be absorbed and diffuse to the plastic zone ahead of the crack-tip, resulting in hydrogen damage.

Once hydrogen enters the parent metal, either by internal or external sources, transport via diffusion to the plastic zone ahead of the crack-tip is required. Hydrogen diffusion in ferrite can readily happen, due to its body-centred cubic crystalline structure which allows for high diffusion coefficients (e.g. at 300 K $D \approx 10^{-8}\,\mathrm{m^2/s}$ [42]). The diffusion of hydrogen in steel can be enhanced or reduced by the presence of microstructural defects, as the ones shown in figure 2.1. Once sufficient hydrogen is present in the plastic zone ahead of the crack-tip, embrittlement occurs. The exact mechanisms by which this occurs are still unclear. Some of the proposed models relevant to steels are discussed next.

2.4 Relevant proposed mechanisms

A number of proposed mechanisms can be found in the literature, each of them with their own supporting evidence and limitations. The mechanisms included in this review are the Hydrogen-Enhanced Decohesion (HEDE), Hydrogen-Enhanced Localised Plasticity (HELP) and Adsorption-Induced Dislocation Emission (AIDE) mechanisms.

2.4.1 Hydrogen-Enhanced Decohesion (HEDE)

The Hydrogen-Enhanced Decohesion model [3, 4, 43], shown in figure 2.3, proposes that the presence of H atoms reduces the cohesive strength of the lattice, resulting in the separation of the atomic planes. This separation becomes permanent once it reaches a critical crack-tip-opening displacement, and takes place in sites where H atoms accumulate: at crack-tips, areas of high hydrostatic stress (e.g. ahead of crack-tips), at particle-matrix interfaces or grain boundaries. It has been suggested in the past that the weakening of the interatomic bonds was due to the transfer of the hydrogen 1s electron to the 3d shell of the iron [3], and was thought to shift the preference in failure mode from slip to cleavage. The HEDE model is usually evoked to explain planar cleavage-like fracture surfaces in which little plastic deformation is visible.

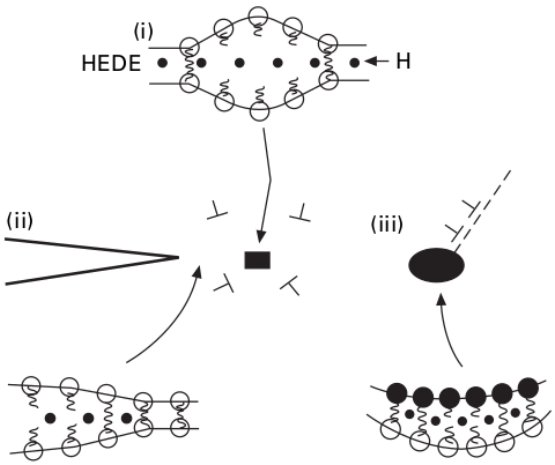

Figure 2.3. Schematic representation of the HEDE mechanism. Hydrogen weakens interatomic bonds and induces tensile separation of the atomic planes when present in sufficient quantities e.g. i) regions ahead of the crack-tips, ii) at crack-tips, and iii) at particle-matrix interfaces [18].

Direct experimental evidence of HEDE is difficult to obtain due to the lack of techniques capable of detecting deformation events at the atomic scale in bulk material. Therefore, the main sources of evidence for the HEDE mechanism come from atomistic simulations. These simulations have shown that H can induce weakening of the interatomic bonds and such weakening can lead to cleavage-like fracture when no slip plane is favourably oriented [44, 45]. The reduction of the cohesive strength of grain boundaries with increasing H exposure has also been reported from atomistic simulations [26]. Other atomistic studies have also shown decohesion of grain boundaries due to hydrogen and attribute it to the stronger binding of H atoms with free surfaces compared to that of grain boundaries [46]. Furthermore, it is known that when impurities segregate to grain boundaries in steels, integranular brittle fracture can occur [47]. When segregated to grain boundaries and other interfaces, hydrogen (or the interplay of H with other impurities) could similarly lead to embrittlement, although impurities can also arrest hydrogen transport along grain boundaries.

For decohesion to occur, hydrogen atoms need to be present in sufficient quantities to lower the cohesive strength of the material significantly. Whether or not achieving such high concentrations is possible is up for debate. While the solubility of H in a perfect crystal is low, it can be significantly higher where defects, functioning as trapping sites, are present. The local H concentration in regions containing such defects could be very high. For instance, computer simulations of iron have shown that elastic stress can reach values of 20 GPa in regions ahead of the crack-tip due to dislocation shielding effect [48] Such stresses might be high enough for hydrogen to accumulate in sufficient quantities to induce decohesion.

Brittle integranular fracture surfaces are normally attributed to the HEDE mechanism

[25, 49, 50]. However, it is uncertain if hydrogen is the sole reason for such embrittlement as other impurities, such as Mn, S, P and Si, are also often present at grain boundaries. It has also been proposed that the interplay between H and other embrittlement agents could lead to more severe reduction of the cohesive energy [51, 52]. Furthermore, it has been suggested that dimples, small enough to be seen using the SEM and TEM magnifications, can still be present in apparently featureless fractographs [25]. Therefore, although planar fracture surfaces can be an indication of the HEDE mechanism being operative, the presence of other mechanisms in which plasticity is involved cannot be ruled out.

2.4.2 Hydrogen-Enhaced Localised Plasticity (HELP)

The Hydrogen-Enhanced Localised Plasticity mechanism [5, 6, 53] proposes that hydrogen increases dislocation activity, leading to subcritical crack growth. A schematic diagram of the HELP mechanism is shown in figure 2.4. Solute hydrogen accumulates ahead of the crack-tip due to the high hydrostatic stresses found in that region. The presence of hydrogen in high enough quantities results in enhanced dislocation motion and higher dislocation densities, which leads to increased plastic deformation. The material is weakened because less stress is needed to produce crack growth compared with the H-free scenario. Crack growth takes place by a process of microvoid-coalescence which is why the HELP mechanism is usually cited to explain crack surfaces with visible plastic deformation.

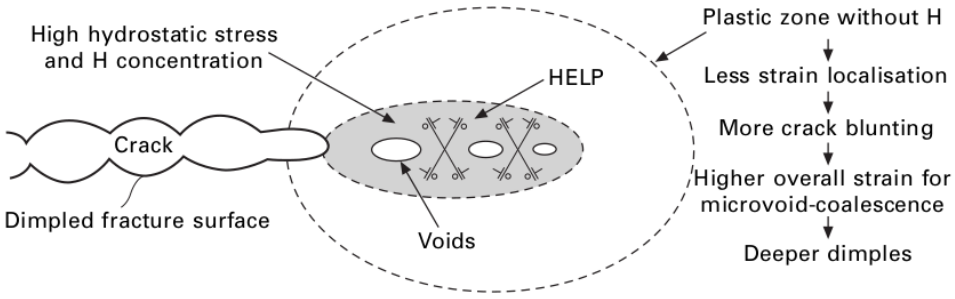

Figure 2.4. Schematic representation of the HELP mechanism. Solute H facilitates dislocation activity in regions ahead of the crack-tip, allowing for subcritical crack growth [18].

The central concept of HELP is that hydrogen can enhance dislocation activity. This could happen by increasing the mobility of dislocations, by easing dislocation nucleation or by reducing dislocation-dislocation interactions. Evidence supporting this hypothesis can be found in the literature in different forms: elasticity theory calculations showing shielding of dislocation interactions due to H [53]; *in-situ* transmission electron microscopy (TEM) observations of increased dislocation mobility and reduced separation distance between dislocation in pile-ups when exposed to H gas [7]; decrease of the flow stress and modification of the slip characteristics on H charged bulk specimens during tensile tests [54, 55], atomistic simulations showing a reduction of the core energy of dislocations when

H is present [56]; and nanoidentation experiments showing a reversible reduction of the pop-in load with H charging [57, 58].

Perhaps the main argument against the HELP model is that the loading conditions applied to the samples used for the TEM observations used to conceive it are different from those found when bulk material is deformed. The small thickness of the TEM samples (smaller than 200 nm) will lead to two-dimensional stress states and the high fugacity produced by H_2 dissociation in the electron beam could result in other surface effects [25]. All these artefacts could be responsible for the enhanced dislocation mobility, as opposed to the H-dislocation core interaction.

While HELP is commonly used to explain the H effects listed above, the mechanisms by which it does remain unclear. For instance, the TEM observations of enhanced dislocation mobility were attributed to a shielding effect that hydrogen produces on the repulsion of dislocations with other dislocations or other obstacles [6, 53]. Such shielding was attributed to the volumetric strain and change in constitutive moduli produced by interstitial H in Cottrell atmospheres [6, 59]. This claim, however, has been contradicted by atomistic simulations of Fe showing that H Cottrell atmospheres on edge dislocations reduce dislocation mobility and have no impact on the separation distance of dislocations in pile-ups [60]. Furthermore, *in-situ* TEM nanocompression tests in Al have shown reduced dislocation mobility due to dislocation pinning with vacancies, which are stabilised by the presence of H [61]. The contradictory evidence found in the literature might suggest that the presence of H in the lattice normally leads to hardening, and that softening occurs only under special circumstances. Finding the conditions under which the latter occurs has proven challenging.

2.4.3 Adsortion-Induced Dislocation Emission (AIDE)

The Adsorption-Induced Dislocation Emission model [8, 18, 62] proposes that hydrogen adsorbed on the crack-tip eases the nucleation of dislocations exactly from the crack-tip. The slip planes of nucleated dislocations are oriented favourably to produce crack advance. Figure 2.5 shows a schematic representation of this mechanism. For a H-free material, the emission (nucleation and subsequent movement away) of dislocations from the crack-tip requires the formation of both a dislocation core and a surface step, a process that requires the shearing of surface atoms. Such re-arrangement requires interatomic bonds to be broken and re-established, which in inert environments is difficult. Consequently, crack advance takes place by the egress of dislocations nucleated at other sites in the plastic zone. This egress would only lead to crack growth when it takes place exactly at the crack-tip, which is unlikely. Most commonly, dislocations will egress behind the crack-tip resulting in blunting, or contribute to the strain ahead of the crack-tip [62]. The AIDE mechanism proposes that hydrogen facilitates dislocation emission from the crack-tip, which takes place alternatively on opposite slip planes bisecting the crack front

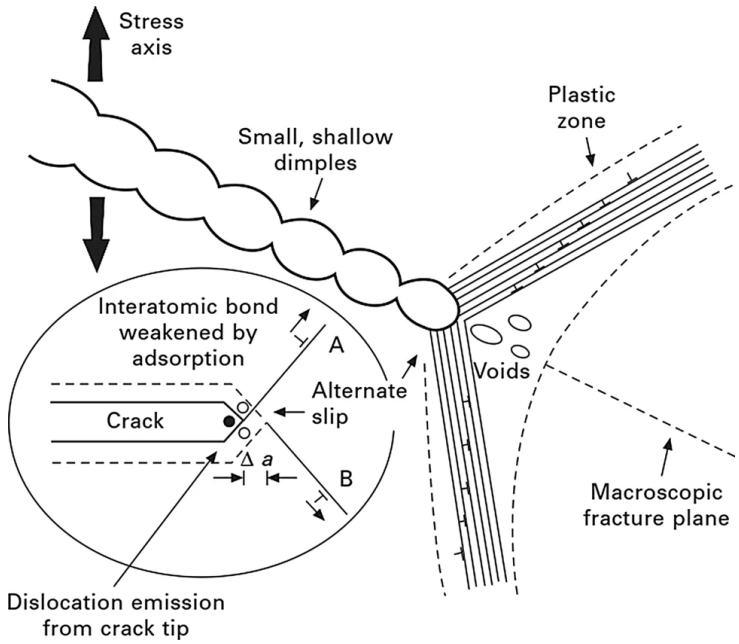

Figure 2.5. Schematic representation of the AIDE mechanism [18]. Dislocation nucleation from and movement away from the crack-tip is eased by hydrogen adsorbed on the crack surfaces. Dislocation slip planes are shifted and produce crack growth via microvoid-coalescence as opposed to blunting.

direction [62]. Furthermore, crack growth can be assisted by the formation of microvoids ahead of the crack-tip due to the high stresses needed for dislocation emission. The nucleation of voids at sites in the plastic zone such as slip-band intersections and second-phase particles [18] can help to re-sharpen the crack.

As mentioned before, a requirement of the HELP mechanism is the diffusion of solute hydrogen to areas of high hydrostatic stress ahead of the crack-tip. This process takes time and might not be possible in cases where H diffusion is slow and crack advance is fast. Under this circumstances, however, hydrogen embrittlement with ductile features has been reported [63, 64], which suggests that the embrittlement could be happening only on the surface.

The AIDE mechanism proposes that it is the hydrogen adsorbed on the crack surfaces that is responsible for facilitating the nucleation of dislocations from the crack-tip, which then leads to embrittlement due to slip planes being oriented favourably for crack growth to occur [8, 65]. The most direct evidence supporting this claim comes from fractographic observations of heavy dislocation activity and slip planes intersecting the crack path with the presence of small dimples.

The main hypothesis of AIDE is that hydrogen adsorbed on crack surfaces can facilitate the nucleation of dislocations from the crack-tip. For this process to occur, hydrogen needs to accumulate on the surface crack-tip in sufficient amounts, which has been shown to occur in different metals [66, 67]. Hydrogen molecules dissociate on metallic surfaces (e.g. Fe, Ni and Ti) when exposed to hydrogen gas and occupy specific sites on the

first surface layers due to a strong binding energy with these sites compared with bulk interstitial sites. Furthermore, an important piece of evidence supporting the idea that hydrogen embrittlement is related to adsorption of hydrogen on the crack surfaces is the similarity of HE fracture surfaces with those produced by liquid metal embrittlement [62]. In both cases, dimpled fracture surfaces can be observed. For liquid metal embrittlement, crack growth is rapid, so that only adsorption can take place (e.g. no diffusion to internal trapping sites) [8, 62], which suggests that adsorption plays an important role in HE. This evidence agrees with the fact that in scenarios where H diffusion is slow and crack advance is fast, H diffusion to the crack-tip should not take place, which is required by HELP. Nevertheless, localised plasticity on fracture surfaces have been reported under this conditions, which indicates that AIDE might be operative [8, 62].

The range of possible HE mechanisms reflects both the range of alloys and environments where HE is observed, and the difficulty in understanding the behaviour of this mobile element. Given the range of materials and conditions at which HE has been reported, it is possible that there is a spectrum of HE mechanisms, as opposed to a single one that explains a certain set of experimental observations. The large number of controversial findings might be an indications of the different mechanisms that can become operative under certain circumstances. The key to understanding HE embrittlement might lie on identifying the conditions under which each mechanism comes into play.

Chapter 3

Molecular Dynamics Simulation

The goal of a computer simulation is to describe a well-defined physical system to obtain relevant information about it. This is done by solving a mathematical model, and depending on its complexity, phenomena occurring at different time and length scales, ranging from the nanoscale to the macroscopic scale, can be studied. Some of the most popular computer simulation methods in materials science are the finite element method, the Monte Carlo method, molecular dynamics, and *ab-initio* methods. Each of them span different length scales, as shown in figure 3.1, and have their own advantages and disadvantages. Their choice usually depends on the type of system of interest as well as the desired level of accuracy and computational resource available. These simulation methods are briefly discussed next.

3.1 Overview of computer simulation methods

The finite element method (FEM) is a method in which the simulation domain is divided into small elements (finite elements) and local solutions of the differential equations describing the system are obtained numerically [68]. By combining individual solutions of the finite elements, a global solution can be obtained. This method is useful for solving engineering problems related to elasticity, fracture, heat transfer, etc. While FEM is widely used for design of engineering components, it might not be the most suitable method for investigating hydrogen embrittlement mechanisms. Length scales of FEM are in the macroscopic scale, reaching simulation domains as big as 10^2 m, making it difficult to study the interactions of hydrogen atoms with defects.

Monte Carlo (MC) methods are based on random sampling of probability distributions. In an atomic system, the potential energy can be associated to a Boltzmann distribution, in which states with lower potential energy have a higher probability of occurring. As Monte Carlo methods rely on random sampling, the accuracy of the final result depends significantly on the number of samples evaluated.

The goal of MC simulations of atomic systems is to calculate the thermodynamics of the system, which is done by direct evaluation of an ensemble average [69]. In the Metropolis algorithm, atoms are moved from their initial configuration depending on the energy change of the subsequent configuration. Lower energy configurations are accepted, while those resulting in higher configurations are accepted with a probability $\Delta E/k_BT$. This series of moves is repeated until equilibrium is achieved. The energy change associated with a MC move can be calculated via a number of methods, depending on the system. Interatomic potentials are commonly used, although *ab-initio* methods can also be employed. The latter are particularly accurate when describing bond breaking and formation. In an atomic system, the number of configurations that are likely to occur is very small compared to the total number of possible configurations. Monte Carlo methods use *importance sampling* to sample only those configurations that are likely to happen and ignore those that are not. MC methods have typical length scales between 10^{-8} and 10^{-6} m, which make them suitable for the study of microstructures. MC simulations might be preferred over Molecular Dynamics simulations when changing the number of particles is needed or when the problem studied is limited by high energy transition barriers e.g. interdiffusion in metals. However, since they are based on random sampling, they do not provide direct information regarding the dynamics of the system, although some MC based methods such as kinetic Monte Carlo can be used to simulate the time evolution of some processes by using as input a list of possible events and the rate at which they occur. These methods are appealing because they span timescales beyond those of Molecular Dynamics.

In molecular dynamics (MD), a system made of atoms, represented as solid particles as opposed to electrons and nuclei, is simulated. This simplification allows the system to be described by Newton's equations of motion involving relatively simple differential equations. Interatomic forces are described by interatomic potentials which are usually obtained from experimental or ab-initio data. Once atomic interactions and initial positions and velocities are defined, the time evolution of the system can be predicted. MD simulations allow to study systems in the nanoscale with typical time and length scales ranging from 10^{-10} to 10^{-6} seconds and metres. The accuracy and applicability of MD simulations greatly depend on the availability of suitable interatomic potentials, which is usually a decisive factor when choosing MD over other simulation methods. Furthermore, because electrons are disregarded in molecular dynamics, electromagnetic properties cannot be studied. MD is discussed in greater detailed in the next section.

In first principles or ab-initio methods, nuclei and electrons are considered, which requires the system to be described by quantum mechanics. These methods do not require external parameters or fitted interatomic potentials and can describe with good accuracy structural properties of materials. Furthermore, since nuclei and electrons are considered, electronic and magnetic properties can also be obtained. Ab-initio methods involve solving difficult partial differential equations which require great computational resource. For this reason,

first principles calculations typically involve less than a thousand atoms.

3.2 Molecular Dynamics

Molecular dynamics (MD) is a computer simulation method in which the time evolution of a system composed of a set of interacting particles (atoms or molecules) is predicted, allowing us to obtain properties of interest. In this method, rather than considering atoms as nuclei and electrons, they are treated as solid particles whose positions, velocities and accelerations can be described by Newtonian mechanics. Accelerations are obtained from instantaneous forces acting on each atom which are calculated from potential energy functions. These functions, however, must be fitted to experimental or ab-initio data. This simplification allows the system to be described by relatively simple differential equations, allowing for simulations of systems significantly larger than those in first-principles calculations. Figure 3.1 shows an overview of the most popular computer simulation methods in terms of time and length scale. Classical molecular dynamics stands between quantum mechanics and Monte Carlo methods. Molecular dynamics is the preferred simulation method for systems containing more than a thousand atoms, when a quantum treatment becomes computationally unfeasible, and can be used in simulations of several million atoms. This number highly depends on the system being studied and the computational resource available. MD simulations with systems consisting of billions of atoms have been reported [70, 71] and will become more common as computers become more powerful and MD software becomes more efficient.

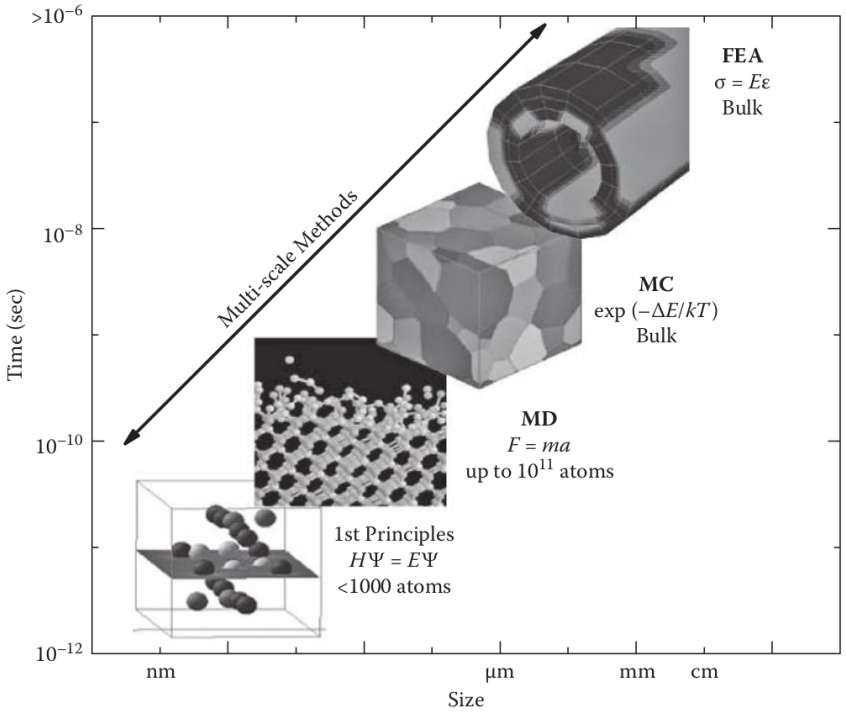

Figure 3.1. Time and length scale of computer simulation methods [72].

MD simulations have been widely used in the field of materials science in the past few

decades. One of the most useful applications of molecular dynamics is the study of the properties of defective solids. Defects such as vacancies, interstitials, dislocations, grain boundaries, interfaces and surfaces have been widely studied using MD simulations [73–79]. Certain mechanisms involved in the dynamics of these defects (e.g. the formation of Cottrell atmospheres [80] around dislocations) cannot be easily captured with experimental techniques, making molecular dynamics an attractive alternative. Failure of materials is another area of interest that can be investigated using molecular dynamics. For instance, in brittle materials, fast fracture can reach speeds in the order of $1{,}000\,\mathrm{m\,s^{-1}}$ or $1\,\mathrm{nm\,ps^{-1}}$ [81], which falls in the timescale of MD simulations. Molecular dynamics simulations are also useful when studying the behaviour of materials under extreme conditions (e.g. under high pressure, near absolute zero temperatures, high strain rates), that can be difficult to achieve experimentally. Computer simulations are sometimes the only alternative available when studying materials under these conditions. Properties obtained from MD simulations correspond to conditions which differ from those of experimental tests; thus, data obtained by MD simulations and experiments is not always comparable. Nevertheless, MD simulations can be useful to complement experimental observations as they provide insights on nanoscale processes that take place in the material and affect the macroscopic deformation process.

The basic idea behind molecular dynamics simulations is to extract thermodynamic and structural data from the system by predicting the motion of its atoms. A schematic representation of the molecular dynamics method is presented in figure 3.2. A typical simulation starts by setting up initial atomic positions and velocities, usually dictated by the crystalline structure and temperature. These initial positions and velocities are only set at the beginning of the simulation; for subsequent steps, they are completely dictated by the interatomic forces and boundary conditions. Forces acting on each atom, directly related to their accelerations, can be computed from the potential energy function which is provided in the form of interatomic potentials (section 3.6). Using the equations of motion (section 3.3) and numerical integration schemes (section 3.4) the positions of the atoms are updated by a small step. Thermodynamic properties of interest are computed from the collective behaviour of all atoms (section 3.7). If the desired number of steps has been reached, then the simulation finishes; otherwise, new forces are computed and the cycle starts again. These steps are discussed in greater detail in the next sections.

3.3 Molecular Dynamics Formulation

As mentioned above, atoms in molecular dynamics are represented as hard spheres which obey Newtonian mechanics. Each particle is characterised by their position $\mathbf{r}_i$ and velocity $\mathbf{v}_i$. The total energy of the system is the sum of the kinetic and potential energies

$$H = K + U \tag{3.1}$$

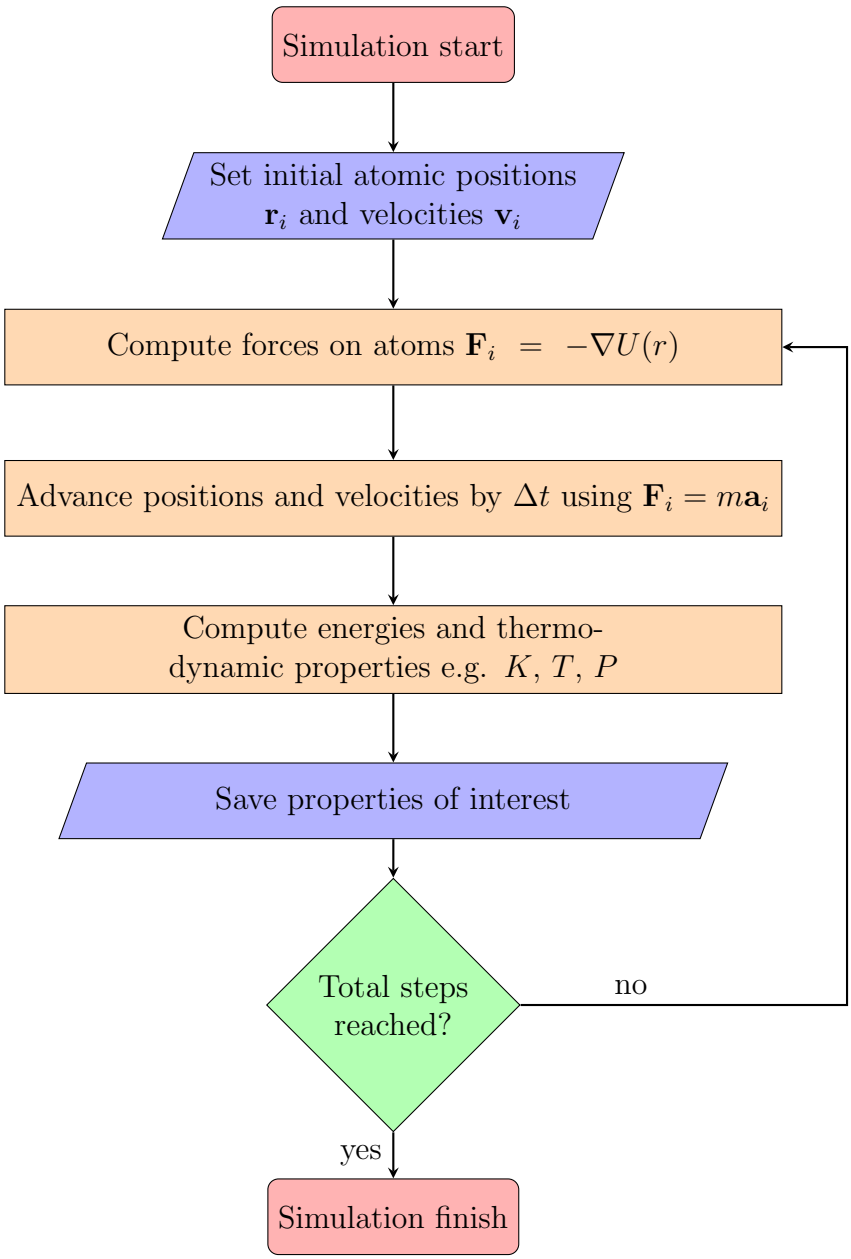

Figure 3.2. Main steps in molecular dynamics simulation.

where H is the total energy of the system (also referred to as the Hamiltonian), K is the kinetic energy and U is the potential energy. K is a function of all N particles

$$K = \frac{1}{2}\sum_{i=1}^{N} m_i \mathbf{v}_i^2 \tag{3.2}$$

where m_i and $\mathbf{v}_i$ are respectively the mass and velocity of the atom i, and U is the sum of the potential energy of every particle in the system, which depends on the position of itself and all other particles in the system[1], that is

[1]In equation (3.3), $U_i(r)$ is a function of all N atoms of the system. In practice this term is approxi-

$$U(r) = \sum_{i=1}^{N} U_i(r) \tag{3.3}$$

In classical mechanics, all particles follow Newton's second law $\mathbf{F}_i = m_i \mathbf{a}_i$, where $\mathbf{F}_i$, m_i and $\mathbf{a}_i$ are respectively the force, mass and acceleration for each particle in the system. For an isolated system, the equation of motion of the system is

$$m_i \frac{d^2 \mathbf{r}_i}{dt^2} = -\frac{dU(r)}{d\mathbf{r}_i} \tag{3.4}$$

Equation (3.4) represents a system of partial differential equations corresponding to an N-body problem for which no exact solution exists for $N > 2$. However, this equation can be solved numerically by discretising equations in time. Common integration schemes used to solve equation (3.4) are discussed in the next section.

3.4 Numerical integration of equations of motion

The potential energy function $U(r)$ in equation (3.4) is a function of the position of all atoms, N. Because the atomic position is defined by 3 coordinates, $U(r)$ depends upon $3N$ variables, making its analytical solution impossible for systems with $N > 2$. However, if the initial positions, velocities and accelerations are known, it is possible to integrate the equations of motion numerically by replacing differentials with finite differences. While there is a wide range of integration schemes available, most modern molecular dynamics codes only implement a few of them. Due to stability, performance and accuracy considerations, the most prominent schemes are based on Taylor series expansions [72]. For instance, the position at a later time $t + \Delta t$ can be approximated from the position at time t in a Taylor series expansion

$$\mathbf{r}_i(t + \Delta t) = \mathbf{r}_i(t) + \mathbf{v}(t)\Delta t + \frac{1}{2!}\mathbf{a}_i(t)\Delta t^2 + \frac{d^3 \mathbf{r}_i(t)}{3! dt^3}\Delta t^3 + ... \tag{3.5}$$

where Δt is a sufficiently small timestep. The accuracy of the Taylor expansion increases as more terms are included in the polynomial. However, this also introduces more demanding calculations, so that truncation of higher order terms is needed. Integration schemes implemented in MD codes, attempt to increase the efficiency while keeping the errors introduced by the algorithm low. The most widely used methods are discussed next.

mated using pair or manybody interatomic potentials, as discussed in section 3.6.

3.4.1 Verlet algorithm

The Verlet integration scheme [82], also known as the Verlet central differential scheme, is one of the most prominent in MD simulations. It is simple and inexpensive, while achieving high accuracy and stability [72]. The Verlet integration scheme is obtained from the forward and backwards Taylor expansion of the positions in time

$$\mathbf{r}_i(t+\Delta t) = \mathbf{r}_i(t) + \mathbf{v}_i(t)\Delta t + \frac{1}{2!}\mathbf{a}_i(t)\Delta t^2 + \frac{d^3\mathbf{r}_i(t)}{3!dt^3}\Delta t^3 + \mathcal{O}(\Delta t^4) \tag{3.6}$$

and

$$\mathbf{r}_i(t-\Delta t) = \mathbf{r}_i(t) - \mathbf{v}_i(t)\Delta t + \frac{1}{2!}\mathbf{a}_i(t)\Delta t^2 - \frac{d^3\mathbf{r}_i(t)}{3!dt^3}\Delta t^3 + \mathcal{O}(\Delta t^4) \tag{3.7}$$

where $\mathcal{O}(\Delta t^4)$ are fourth order terms. Adding equation (3.6) and (3.7), the basic form of the Verlet algorithm is obtained

$$\mathbf{r}_i(t+\Delta t) = 2\mathbf{r}_i(t) - \mathbf{r}_i(t-\Delta t) + \mathbf{a}_i(t)\Delta t^2 + \mathcal{O}(\Delta t^4) \tag{3.8}$$

The Verlet algoritm is a second order method as truncation takes place from third order terms; however, only 4th order truncation errors for the position remain, making it both efficient and accurate.

While the Verlet algorithm is overall a good and inexpensive integration scheme, there are a couple of inherent issues that should be noted. This algorithm requires the current positions $\mathbf{r}_i$ and the positions from the step before $\mathbf{r}(t-\Delta t)$, which are undefined at the beginning of the simulation. This problem can be circumvented by using a normal Taylor series expansion for the first step. A more significant issue is that, as can be seen from equation (3.8), the velocity is not explicitly calculated. While this is not an issue for the prediction of the time evolution of the system, velocities are needed to calculate the kinetic energy, equation (3.2), and thermodynamic quantities depending on it. Velocities can be calculated indirectly by subtracting equation (3.7) from (3.6)

$$\mathbf{v}_i(t) = \frac{\mathbf{r}_i(t+\Delta t) - \mathbf{r}_i(t-\Delta t)}{2\Delta t} \tag{3.9}$$

The resulting truncation error is $\mathcal{O}(\Delta t^2)$ as opposed to $\mathcal{O}(\Delta t^4)$ [72]. When accuracy in the velocity computation is needed, integration schemes in which velocities are explicitly calculated, such as Velocity Verlet, might be preferred.

3.4.2 Velocity Verlet algorithm

This algorithm is the most commonly implemented in most MD codes. In this method, positions, velocities and accelerations are calculated explicitly at any given time $t + \Delta t$. The Velocity Verlet scheme consists on the following steps [83]

1. Compute $\mathbf{r}_i$ at $t + \Delta t$

$$\mathbf{r}_i(t + \Delta t) = \mathbf{r}_i(t) + \mathbf{v}_i(t)\Delta t + \frac{1}{2!}\mathbf{a}_i(t)\Delta t^2 \tag{3.10}$$

2. Evaluate the acceleration at $t + \Delta t$

$$\mathbf{a}_i(t + \Delta t) = -\frac{1}{m_i}\frac{dU[\mathbf{r}(t + \Delta t)]}{dt} \tag{3.11}$$

3. Compute velocities at $t + \Delta t$

$$\mathbf{v}_i(t + \Delta t) = \mathbf{v}_i(t) + \frac{\mathbf{a}_i(t) + \mathbf{a}_i(\Delta t)}{2}\Delta t \tag{3.12}$$

With the positions, velocities and accelerations for the new step $t + \Delta t$ known, the algorithm can be repeated for subsequent steps. Equations (3.10) through (3.12) show that the Velocity Verlet scheme is self-starting and computes the velocities explicitly. Velocity Verlet is simple, efficient and generates the same trajectories as the original Verlet (in absence of roundoff errors), which explains its prominence in MD simulations.

3.4.3 Predictor-Corrector algorithm

The predictor-corrector algorithm [84] uses higher order terms in the Taylor series expansion of the position. It is widely used because of its high accuracy which is obtained from a correction step that uses the data from the previous step. This scheme consists of the following steps

1. *Predictor*: Positions, velocities and accelerations at time $t + \Delta t$ are predicted using Taylor series expansions

$$\mathbf{r}_{\text{pre}}(t + \Delta t) = \mathbf{r}_i(t) + \mathbf{v}_i(t)\Delta t + \frac{1}{2!}\mathbf{a}_i(t)\Delta t^2 + \frac{d^3\mathbf{r}_i(t)}{3!dt^3}\Delta t^3 + \mathcal{O}(\Delta t^4) \tag{3.13}$$

$$\mathbf{v}_{\text{pre}}(t + \Delta t) = \mathbf{v}_i(t) + \mathbf{a}_i(t)\Delta t + \frac{1}{2!}\frac{d^3\mathbf{r}_i(t)}{dt^3}\Delta t^2 + \mathcal{O}(\Delta t^3) \tag{3.14}$$

$$\mathbf{a}_{\text{pre}}(t + \Delta t) = \mathbf{a}_i(t) + \frac{d^3\mathbf{r}_i(t)}{dt^3}\Delta t + \frac{1}{2!}\frac{d^4\mathbf{r}_i(t)}{dt^4}\Delta t^2 + \mathcal{O}(\Delta t^3) \tag{3.15}$$

2. *Error evaluation*: Forces are computed at $t + \Delta t$ from the gradient of the potential energy at the predicted new positions. The resulting acceleration $\mathbf{a}_i(t + \Delta t)$ is compared with the acceleration predicted in the *predictor* stage $\mathbf{a}_{\text{pre}}(t + \Delta t)$. An error $\Delta\mathbf{a}_i(t + \Delta t)$ is calculated from the difference between these two accelerations

$$\Delta\mathbf{a}_i(t + \Delta t) = \mathbf{a}_i(t + \Delta t) - \mathbf{a}_{\text{pre}}(t + \Delta t) \tag{3.16}$$

3. *Corrector*: Assuming that the errors for the positions and the velocities are both small, they can be considered to be proportional to each other and the acceleration error. Corrected positions and velocity can be then calculated

$$\mathbf{r}_{\text{cor}}(t + \Delta t) = \mathbf{r}_{\text{pre}} + c_0\Delta\mathbf{a}_i(t + \Delta t) \tag{3.17}$$

$$\mathbf{v}_{\text{cor}}(t + \Delta t) = \mathbf{v}_{\text{pre}} + c_1\Delta\mathbf{a}_i(t + \Delta t) \tag{3.18}$$

The constants c_0 and c_1 range from 0 to 1, and depend on the number of terms included in the Taylor series expansion. While this integration scheme is highly accurate and stable, it is not time reversible because of the applied corrections [72]. Furthermore, this method requires more memory than the Velocity Verlet scheme, as more quantities need to be stored.

3.4.4 Timesteps in MD simulations

When using any of the integration schemes discussed above, it is critical to ensure that the timestep Δt is small enough to preserve the accuracy of the run. Small timesteps result in heavy computational burden, so it is important to select an optimal value that minimises errors and allows useful simulation sizes and times. The timestep should be small enough to capture the fastest motion of the system, typically in the form of atomic vibrations, whose periods are of the order of 10^{-12} s. The timesteps needed to integrate the equations of motion depend on the integration scheme. For instance, Verlet integration usually requires 50 timesteps per vibrational period [69], resulting in timesteps of 10^{-14} to 10^{-15} s. The selection of the timestep depends on a number of factors, such as the atomic species in the system, the temperature, the interatomic potential and the type of simulation performed. Light atoms, such as hydrogen, at high temperature normally require timesteps as small as 10^{-16} s, which poses a great challenge when studying hydrogen related phenomena. For instance, with a timestep of 10^{-16} s, a single nano second of simulation, would require 10^7 steps.

The inherently small timesteps of MD simulations is one of their main limitations. Accelerated molecular dynamics methods attempt to extend the timescales of MD simulations, while retaining full atomistic accuracy [85]. These methods rely on different techniques, such as adaptive timesteps [86] and temperature accelerated dynamics [87], to increase the accessible timescales. While these techniques are promising, currently they have limited application.

3.5 Thermodynamic Ensembles

In MD simulations there are different *ensembles*, that is, ways in which the motion of the atoms can be synchronised to produce a system with a set of thermodynamic properties. Various thermodynamic ensembles are presented in table 3.1. The integration of the equations of motion discussed in section 3.3 will result in the microcanonical ensemble, in which the number of particles N, the volume V and the total energy E are held constant. This ensemble represents an isolated system in which no mass or energy exchange occurs. Often, temperature and pressure control are desired, so that other ensembles such as the canonical and isobaric-isothermal ensemble are preferred. Thermostatting (temperature control) is achieved by using algorithms that modify the equations of motion to produce ensembles that mimic the effect of a heat bath, such as the Nosé-Hoover thermostat [88, 89] or the Berendsen [90]. Similarly, barostatting (pressure control), is achieved by adjusting simulation box dynamically, which is done using algorithms such as the Parrinello–Rahman [91]. In the grand canonical ensemble, the chemical potential is fixed. This ensemble is equivalent to having, in addition to a heat bath, a particle reservoir which the system can exchange particles with.

Ensemble name	Fixed Variables	Remarks
Microcanonical	N, V, E	Isolated system
Canonical	N, V, T	Heat bath
Isobaric-isothermal	N, P, T	Heat bath + pressure control
Grand canonical	μ, V, T	Heat bath + particle reservoir

Table 3.1. Thermodynamic ensembles.

3.6 Interatomic Potentials

In molecular dynamics, the information describing how atoms interact with each other (repulsion and attraction) is contained in the interatomic potential. Interatomic potentials give numerical or analytical expressions for the potential energy landscape of the system. This potential energy landscape is present in the equations of motion in the force term in equation (3.4). It is paramount that interatomic potentials are accurate for the system and problem that is being studied in order to extract meaningful results. To achieve this, several approaches in describing the potential energy have been used, each of them with

their own strong and weak points. In this section, some of the most prominent interatomic potential styles in describing solids will be reviewed.

The potential energy of the system is a function of all N atoms in the system, and can be approximated by a many-body expansion [69]

$$U(\mathbf{r}_1, \mathbf{r}_2, ..., \mathbf{r}_N) = \sum_{i=1}^{N} v_1(\mathbf{r}_i) + \frac{1}{2}\sum_{i=1}^{N}\sum_{j=1}^{N}{}' \phi_{ij}(\mathbf{r}_i, \mathbf{r}_j) + \frac{1}{6}\sum_{i=1}^{N}\sum_{j=1}^{N}\sum_{k=1}^{N}{}' v_3(\mathbf{r}_i, \mathbf{r}_j, \mathbf{r}_k) + ..., \tag{3.19}$$

where $'$ indicates the exclusion of the terms in which $i = j$ and $i = j = k$. The first term in equation (3.19) represents the contribution of external fields (e.g. a gravitational field) in the potential energy. The second term represents the interaction between pairs of atoms. $\phi_{ij}(\mathbf{r}_i, \mathbf{r}_j)$ is referred to as a *pair potential* as it is a function of the distance $|\mathbf{r}_i - \mathbf{r}_j|$ between two atoms. This term is usually the main contribution to the potential energy and for some materials (such as rare gas solids), pair potentials are sufficiently accurate to describe the potential energy landscape. An example of pair potentials is the Lennard-Jones potential [92], which is discussed in section 3.6.1. The third term in equation (3.19), describes the 3-body interactions $v_3(\mathbf{r}_i, \mathbf{r}_j, \mathbf{r}_k)$, that is, the interaction between triplets of atoms. Interactions involving more than two atoms are called *many-body* interactions. These interactions are often needed to describe more complex bonding such as the ones found in metals and covalent solids. Some of the most commonly used many-body potentials in solids, such as the EAM and Tersoff are discussed in section 3.6.2.

3.6.1 Pair potentials

In a pair potential, the potential energy is given by

$$U = \frac{1}{2}\sum_{i=1}^{N}\sum_{j=1}^{N}{}' \phi_{ij}(\mathbf{r}_i, \mathbf{r}_j) \tag{3.20}$$

The factor $\frac{1}{2}$ eliminates the double count of the bonds. The function $\phi_{ij}(\mathbf{r}_i, \mathbf{r}_j)$ can take different forms, but the simplest representation is by the Lennard-Jones potential [92]. This potential, shown schematically in figure 3.3, is defined as

$$\phi_{ij}(r) = 4\epsilon\left[\left(\frac{\sigma}{r}\right)^{12} - \left(\frac{\sigma}{r}\right)^{6}\right] \tag{3.21}$$

where r is the distance between the two atoms. The first and second term are repulsive and attractive contributions, respectively. Long-range interactions are attractive and

proportional to $1/r^6$. At long distances the attractive term dominates as short-range interactions decay with $1/r^{12}$. Conversely, the repulsive term dominates at short distances, when r is smaller than the equilibrium distance (at which $d\phi/dr = 0$). The Lennard-Jones potential is characterised by two parameters, σ and ϵ. The former is the distance at which the potential energy is zero $\phi(\sigma) = 0$, and the latter is referred to as the *well depth*, the energy at the equilibrium distance. While the Lennard-Jones potential describes atomic interactions in rare gas solids reasonably accurately, it is unsuitable for most solid materials. Other pair potentials (e.g. Morse [93], Born-Mayer [94], etc.) might be more accurate than the Lennard-Jones potential for some systems. However, in order to accurately represent materials such as metals and covalent crystals, the inclusion of many-body contributions in the potential energy is needed. Some prominent many-body potentials are discussed next.

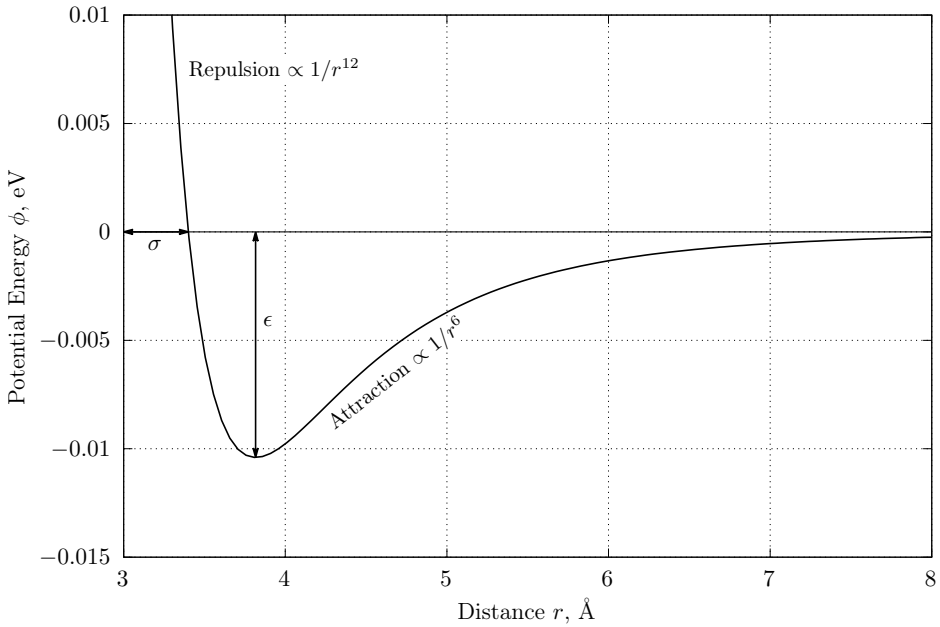

Figure 3.3. Example of a distance (r) versus potential energy (ϕ) curve for a Lennard-Jones potential. Fitted parameters for Ar [95]: $\sigma = 0.34\,\text{Å}$ and $\epsilon = 10.4\,\text{meV}$.

3.6.2 Many-body potentials

One great limitation of pair potentials is that they cannot account for complex situations in which the strength of the interactions is affected by the local environment (e.g. at surfaces or near defects). To accurately describe such scenarios, it is necessary to capture the dependence of the bond strength as a function of all nearby atoms. Many-body potentials attempt to achieve this in different ways such as taking into account the electronic gas density in metals or the directionality of bonds in covalent solids. Different approaches have been adopted depending on the material. Embedded-atom method potentials are a popular choice for metallic systems, whereas Tersoff and other bond order potentials are preferred when modelling covalent solids. The most widely used many-body potentials relevant to steels are discussed next.

Embedded-atom method potentials

When it comes to describing metals, one of the most used potentials is the Embedded-atom method potential [10, 96] (EAM). EAM potentials are more accurate than pair potentials because they take into account the effect of local environment on the potential energy. They do it by including a term describing the local electron density, a function that depends on neighbouring atoms. The general form of this potential is

$$U = \sum_i F_i \left[\sum_{j \neq i} f_{ij}(r_{ij}) \right] + \frac{1}{2} \sum_{i=1}^{N} \sum_{j=1}^{N}{}' \phi_{ij}(\mathbf{r}_i, \mathbf{r}_j) \tag{3.22}$$

where ϕ_{ij} is a pair potential, $f_{ij}(r_{ij})$ is an arbitrary function of the interatomic distance representing the electron density and F_i is a functional of a sum of functions f_{ij} depending on local positions. In the original formulation of the EAM potential [10], F_i, also referred to as the *embedding function*, represents the energy needed to embed the atom i in an uniform electron gas of density $\bar{\rho}_i$

$$U = \sum_i F_i(\bar{\rho}_i) + \frac{1}{2} \sum_{i=1}^{N} \sum_{j=1}^{N}{}' \phi_{ij}(\mathbf{r}_i, \mathbf{r}_j) \tag{3.23}$$

$\bar{\rho}_i$ was chosen to represent the local electronic density evaluated at the position of the atom i, which is defined as the sum of the electronic density contributions of neighbouring atoms, that is

$$\bar{\rho}_i = \sum_{j \neq i} \rho_j(r_{ij}) \tag{3.24}$$

The choice of the three functions F, $\bar{\rho}$ and ϕ in equation (3.23) depends on each model of the interatomic potential. For instance, if the embedding function F is chosen to be of the form $F(\bar{\rho}_i) = -A\sqrt{\bar{\rho}_i}$, the interatomic potential becomes the Finnis-Sinclair potential [97]. Embedded-atom method potentials are very useful in describing metals, as the embedding function is a good approximation of the metallic bond. Consequently, EAM potentials can reproduce elastic properties considerably more accurately than pair potentials, and are also good at describing defects in the crystal. EAM potentials, however, become more limited when describing multicomponent systems or angular bonds present in covalent solids. Modified embedded-atom method (MEAM) potentials [98] attempt to solve this issue by including angular dependence in the electronic density function ρ_j. MEAM potentials have been widely used to model multi-component alloys and covalent materials.

Due to its simplicity and relatively low computational cost, EAM potentials remain among the preferred choices when modelling transition metal systems. Fe is generally well de-

scribed by this type of potentials and its use extends to binary systems such as the Fe-C [99], Fe-H [13], Fe-Cr [100], among others. Ternary alloys systems, though also available, are usually challenging to reproduce with EAM potentials. Other approaches, such as bond-order potentials, might be preferred. Some of the bond-order potentials relevant to the Fe-C system are discussed next.

Bond-order potentials

Similarly to EAM potentials, bond-order potentials attempt to capture the dependence of the potential energy on the local environment of the atoms. However, instead of doing it via the electron density, bond-order potentials do it by considering the local coordination and bond angles [101]. The total potential energy of the system can be written as the sum of the energy of its atoms or as the sum of the energy of all the bonds [102, 103]:

$$U = \sum_i E_i = \frac{1}{2} \sum_{i \neq j} V_{ij} \tag{3.25}$$

where

$$V_{ij} = f_c(r_{ij}) \left[V_R(r_{ij}) + b_{ij} V_A(r_{ij}) \right] \tag{3.26}$$

In equation (3.26), f_c is a cut-off function and V_R and V_A are repulsive and attractive interactions, respectively. The strength of the bond is included in the bond-order parameter b_{ij} and its form is defined by the model, but usually includes the effect of nearest neighbours on the bond strength (the strength of a covalent bond reduces with the coordination since the valence electrons are shared between more bonds). The choice of b is rather arbitrary, for instance, in the original bond-order potential formulation by Abell [102], the atomic energy was given by

$$E_i = \frac{1}{2} \sum_{j=1}^{Z_I} \left[a e^{-\alpha r} - \frac{c}{Z^{1/2}} e^{-\gamma r} \right] \tag{3.27}$$

where $V_R = e^{\alpha r}$ and $V_A = -e^{-\gamma r}$. The bond order parameter is $b = c/Z^{1/2}$, where Z is the number of nearest-neighbour atoms. Higher values of Z indicate higher numbers of neighbours, representing higher coordination. In that case, the bond order b decreases and so do the attractive interactions.

A variation of bond-order potentials that has been successful in describing covalent solids with relative simplicity is the Tersoff potential [103]. In this potential, the bond order, aside from being a function of the coordination, is also a function of the angles of the

bonds with neighbouring atoms. In the Tersoff treatment of bond-order potentials, the bond order b_{ij} is given by

$$b_{ij} = b(\psi_{ij}) \tag{3.28}$$

where ψ is a function of the coordination and the angle between atoms. The analytical form of ψ can include as many terms as required and it is usually more complex than the approach proposed by Abell [102]. The increase in the complexity of the bond-order term allows Tersoff potentials to be applicable to a wide range of materials. While they were originally developed for Si and C, they are capable of describing several binary and ternary systems, including the Fe–C system. Tersoff potentials are an alternative to EAM potentials when simulating steels. They offer a more accurate description of cementite [104], Fe_3C than EAM and have even been used to study austenitic steels [105].

Another type of bond-order potential is the reactive (ReaxFF) potential. This type of potential attempts to describe the transition energies during chemical reactions without the need to rely on quantum treatments. The ReaxFF potential [106] is one of the most prominent approaches to reactive potentials. In the ReaxFF potentials bonded and non-bonded interactions are taken into account. For bonded interactions, the bond length is a function of the bond-order, so that transitions between single, double and triple bonded interactions can be accurately modelled. The general form of the energy in the ReaxFF potential is

$$U_{system} = U_{bond} + U_{over} + U_{under} + U_{val} + U_{pen} + U_{tor} + U_{conj} + U_{vdWaals} + U_{Coulomb} \tag{3.29}$$

The terms in the right-hand side of the equation are the covalent, over-coordination penalty, under-coordination stability, valence angle, angle penalty, torsion angle, conjugation energy, non-bonded van der Waals, and Coulomb energies, respectively. ReaxFF is a bond-order potential as the bonded interactions depend on the bond-order, a continuous function of the distance between atoms participating in bonds [107].

$$BO_{ij} = BO^{\pi}_{ij} + BO^{\sigma}_{ij} + BO^{\pi\pi}_{ij} \tag{3.30}$$

where BO^{π}_{ij}, BO^{σ}_{ij} and $BO^{\pi\pi}_{ij}$ are contributions from sigma, pi and double pi bonds, respectively. With this treatment all bonded interactions depend on the local bond state of the atom and can be removed when non-bonded interactions exist.

To equilibrate charges, ReaxFF potentials use the Charge Equilibration method QEq [108], a geometry dependant charge calculation scheme. QEq can calculate the effect of

polarization and appearance of partial charges in molecules as they change their shape.

Because ReaxFF potentials include in their definition of the potential energy all these different types of bonded and non-bonded contributions, with adequate parametrisation, they can be used in practically any system. The original ReaxFF force field was first used to study reactions in hydrocarbons [106], but its use has extended to other systems, such as metallic [109], metal hydrate [11] and carbide [110] systems. Furthermore, ReaxFF potentials for hydrogen embrittlement are starting to appear [12]. They can become important when investigating this phenomenon (e.g. hydrogen bubble formation, HE of cementite, etc.). However, the main limitation of this potential lies in the high computational cost required to compute so many different types of interaction. While the empirical approach of the ReaxFF potential is much faster than ab-initio methods, they tend to be significantly slower than EAM and Tersoff potentials, and use considerably more memory. For that reason, ReaxFF simulations involving millions of atoms with timescales of nanoseconds, though possible, are rare.

3.7 Property Calculation

One important aspect of MD simulations is the calculation of averaged macroscopic quantities, such as temperature and pressure, from instantaneous microscopic ones, such as atomic velocities. A macrostate may be defined by a given number of atoms N, a temperature T and a volume V. While these variables completely define the thermodynamic state of the system, there are multiple *microstates* (arrangements of positions and atomic velocities) corresponding to that thermodynamic state. Depending on their energy, some microstates are more probable than others, so that their weighted average results in the macrostate of the system. For macroscopic thermodynamic quantities to be calculated, it is necessary to compute their *ensemble average*, that is, to average them over multiple configurations. Averaging quantities in this way would require us to know all the possible microstates of the system, which is very difficult. Alternatively, quantities can be averaged over time. In this case, all is needed is to take a number of samples of the desired quantity and divide the total by the number of samples, assuming the number of samples is large enough to represent the system. In order to use the more convenient second approach, *Ergodicity* is assumed. The Ergodic hypothesis states that ensemble averages and time average of a property are equivalent [81], that is

$$\langle A \rangle_{\text{ensemble}} = \langle A \rangle_{\text{Time}} \tag{3.31}$$

where the $\langle A \rangle$ denote the average of the quantity A. The link between macroscopic and microscopic properties in MD simulations is possible thanks to this assumption.

Macroscopic properties, useful to extract meaningful conclusions from atomistic data, can be extracted from MD simulations. The way in which some relevant properties are computed is briefly presented next.

3.7.1 Temperature

Temperature is related to the kinetic energy of all atoms. As discussed above, properties whose value depend on the collective behaviour of all the atoms in the system, need to be averaged. Therefore, there is no instantaneous temperature, but rather an average temperature computed from the average kinetic energy of the system [69]. This temperature can be calculated as

$$\langle T \rangle = \frac{2}{3} \frac{\langle K \rangle}{N k_B} \tag{3.32}$$

where $\langle K \rangle$ is the average kinetic energy, N is the number of atoms and k_B is the Boltzmann constant.

3.7.2 Pressure

The average pressure of the system[2] is given by

$$\langle P \rangle = \frac{N k_B}{V} \langle T \rangle - \frac{1}{3V} \left\langle \sum_{i=1}^{N} \sum_{j>1}^{N} r_{ij} \frac{d\phi}{dr_{ij}} \right\rangle \tag{3.33}$$

where $\langle T \rangle$ is the temperature calculated as in equation (3.32), V is the volume occupied by the atoms, r_{ij} is the distance between the atoms i and j, and ϕ is the potential energy function. The first term in equation (3.33), represents the contribution of the particle collisions with the wall of the container. The second term represents the contribution of the interatomic forces.

3.7.3 Mean-square displacement

The mean-square displacement (MSD) is a measure of the distance that a group of atoms travels over some time interval. It can be calculated as

$$\text{MSD} = \frac{1}{N} \sum_{i=1}^{N} |\mathbf{r}_i(t) - \mathbf{r}_i(0)|^2 = \left\langle |\mathbf{r}_i(t) - \mathbf{r}_i(0)|^2 \right\rangle \tag{3.34}$$

[2]The pressure computed by equation (3.33) corresponds to that of a pair potential. Similar expressions for other types of interatomic potentials exist. In general, the pressure can be computed as $\langle P \rangle = \frac{N k_b}{V} \langle T \rangle - \frac{1}{3V} \left\langle \sum_{i=1}^{N} \mathbf{r}_i \cdot \nabla_i U \right\rangle$.

The mean-square displacement is useful for a number of reasons. For instance, sudden variations in the mean-square displacement are indicative of melting, phase transitions and plastic deformation. Furthermore, it is particularly useful when studying diffusion as the MSD is related to the diffusion coefficient by

$$D = \frac{1}{6}\frac{\langle|\mathbf{r}_i(t) - \mathbf{r}_i(0)|^2\rangle}{t} \tag{3.35}$$

For small systems, the MSD will fluctuate considerably due to the small number of atoms over which the MSD is averaged. For accurate diffusion coefficient calculations, the diffusing species must be present in large enough quantities.

3.7.4 Coefficient of thermal expansion

Since the coefficient of thermal expansion is a measure of the change in volume with temperature, at constant pressure, it can be calculated from the change in the simulation box as the temperature is changed. That is

$$\alpha_{\mathrm{p}} = \frac{1}{V}\left(\frac{\partial V}{\partial T}\right)_P \tag{3.36}$$

3.7.5 Radial distribution function

The radial distribution function (RDF) gives an indication of how particles are distributed around a certain atom compared to that of a random distribution. It measures the probability $g(r)$ of finding another particle at a distance r [72]. The radial distribution function is given by

$$g(r) = \frac{V}{N}\frac{\langle N(r, \Delta r)\rangle}{4\pi r^2 \Delta r} \tag{3.37}$$

where r is the radial distance, $\langle N(r, \Delta r)\rangle$ is the time average of the number of atoms in a shell volume of $4\pi r^2$ between r and Δr.

3.8 Molecular Dynamics Simulations of Hydrogen Embrittlement

Molecular dynamics simulation is a valuable resource to investigate hydrogen embrittlement. Early simulations were successfully used to investigate the adverse effects of hydrogen on the mechanical properties of metals, despite the limited computational capabilities available then. For instance, MD simulations using embedded-atom method potentials captured the effect of H on the cohesive strength of the Ni lattice, proving the viability of the HEDE mechanism [44, 45]. More recently, decohesion in different materials have been extensively studied using molecular dynamics simulations [76, 111].

MD simulations have been used to understand the behaviour of hydrogen around lattice defects such as point defects [38], dislocations [112] and grain boundaries [113]. They have also been used to study the effect of H on the tensile strength of materials [114, 115]. However, due to the inherent differences between simulations and experiments (e.g. time and length scale, perfect versus defective material, etc.), stress-strain data obtained via MD simulations are difficult to correlate to experimental data, so care must be taken when designing meaningful simulations.

When designed carefully, the intrinsic limitations of molecular dynamics can be circumvented and specific scenarios can be studied. Meaningful insights into hydrogen embrittlement can be gained if MD simulations are used to test concepts proposed by HE models (e.g. HEDE, HELP and AIDE). For instance, HELP related phenomena have been studied using molecular dynamics simulations, testing the behaviour of hydrogen around dislocations and its ability to increase dislocation mobility and density [60].

Aside from probing concepts proposed by HE models, MD simulations have also helped to support different HE mechanisms. An example of this is the ductile-to-brittle transition mechanism due to H proposed by Song and Curtin [14]. In this mechanism the role of H around the crack-tip is to impede the emission of dislocations from the crack-tip, leaving cleavage as the only stress relieving mechanism. Furthermore, mechanisms involved during other stages of the hydrogen embrittlement process have also been proposed from atomistic simulations. For instance, H transport to the plastic zone ahead of the crack-tip via dislocations dragging vacancy–hydrogen clusters have been proposed [116].

Finally, more recent approaches to modelling interatomic potentials, such as reactive and machine learning potentials [117], are promising candidates to increase the applicability of MD simulations. ReaxFF potentials offer a combination of the accuracy of quantum mechanical treatments and the performance of classical ones. ReaxFF potentials are versatile and can be adapted to study a variety of systems. Machine learning potentials offer an alternative to the exhaustive task of creating a model for interatomic forces. Interatomic potentials are usually fitted to computationally demanding DFT calculations, and are rarely available for multi-component systems. Machine learning interatomic po-

tentials attempt to accurately predict the energy landscape of the system via numerical interpolation of reference data [117]. The physics of the system might or might not be considered. The accuracy of machine learning potentials has increased considerably in the past years, and being a thriving research field, they are expected to improve.

Chapter 4

Atomistic Simulations of Tensile Test on Iron and Ferrite

Steels are widely used engineering materials and have been extensively researched. Their ability to drastically change their mechanical properties through alloying and processing makes them suitable for most engineering tasks. In the past decades, the field of computational materials science has advanced significantly, and has provided valuable insights of the deformation process of different materials. Plasticity, fracture, hydrogen embrittlement and solid solution strengthening are some of the topics that have been studied using atomistic simulations [24, 74, 118, 119]. Ferrite (the solid solution of carbon in body-centred cubic Fe), cementite (the iron carbide Fe_3C) and pearlite (the lamellar mixture of ferrite and cementite) are the microstructural constituents that can be found in annealed unalloyed steels. Classic molecular dynamics (MD) and density functional theory calculations (DFT) involving pearlite have been reported in the literature [78, 120, 121]. However, it seems that C solutes have been neglected from the ferrite lamellae, due to their relatively low concentration ($< 0.008\,\text{wt.}\%$).

It is known that interstitial atoms have a great influence on the mechanical properties of steels and other alloys. Due to their ability to pin dislocations and increase the resistance to slip, C interstitials have significant strengthening effects in Fe. MD simulations have been used to study the effect of interstitials on the dislocation glide in Fe [74], showing that C interstitials provide greater strengthening effects than other elements (e.g. Cu and Ni). While previous MD studies have reported the strengthening effects of C in Fe, their influence on the tensile behaviour has not been investigated.

There are several factors that affect the mechanical properties of single crystals, and the crystallographic direction is one of the most important. The strength of Fe whiskers has been investigated experimentally [122], and the [1 1 1] direction was found to be the strongest with a strength of 13.4 GPa. In that work, the maximum recorded stress was found to increase as the diameter of the whiskers was reduced.

The dependence of the strength on the crystal orientation and cross-sectional area has also been studied via MD simulations for α-Fe whiskers [123, 124]. The crystallographic directions with the highest strength were the [1 1 1] and [1 1 0] directions with 27.2 GPa and 22.7 GPa, respectively, both of them failing due to dislocation slip. For both experiments and simulations, the measured strength of the whiskers was sensitive to the dimensions of the sample.

The third significant factor that affects results of tensile tests is the strain rate, $\dot{\varepsilon}$. In MD simulations, due to the inherent timescale of the method, strain rates are several orders of magnitude greater than those in used in experimental testing. Furthermore, experimental strain rates cannot be directly compared to those in MD simulations because the former arise from the average dislocation velocity and control the contact time of dislocations with obstacles, whereas the latter describe the fluctuations in velocity of individual dislocations [125].

As reported in molecular dynamics and dislocation dynamics simulations, increasing the strain rate leads to a stress overshoot caused by delayed dislocation propagation [126–128].

In this work, MD simulations of tensile tests on BCC Fe and ferrite have been carried out in order to estimate the strengthening effects of C atoms. The influence of the strain rate in the C strengthening has also been investigated.

4.1 Simulation Methodology

4.1.1 Ferrite supercell

The solubility of C in α-Fe increases with temperature up to 727 °C, where the maximum solubility of 0.025 wt.% is reached. At room temperature, the commonly accepted values for C solubility in α-Fe is 0.008 wt.%. Due to the small concentration of C at room temperature, the lattice parameter of ferrite is usually taken equal to that of α-Fe.

The α-Fe unit cell shown in figure 4.1 with a lattice parameter $a = 0.2856$ nm [129] was used to build a ferrite unit cell. This unit cell was repeated to create a $21\times21\times21$ supercell, and C atoms were added in the 6*b* Wyckoff positions. The resulting ferrite unit cell, shown in figure 4.2, has a carbon content of 0.0069 wt.%, which is a good approximation to the room temperature value.

The ferrite unit cell shown in figure 4.2 was used to create a $5 \times 5 \times 5$ ferrite supercell (approximately $30 \times 30\times30$ nm) for simulations with three periodic boundary conditions (bulk configuration) and a $2 \times 2 \times 4$ supercell ($12 \times 12\times 24$ nm) for simulations with two non-periodic boundary conditions (nanowhisker configuration). In the former case, edge effects of surfaces are eliminated, allowing the study of bulk properties while in the latter case periodic boundary conditions were imposed only in the z direction, which is the

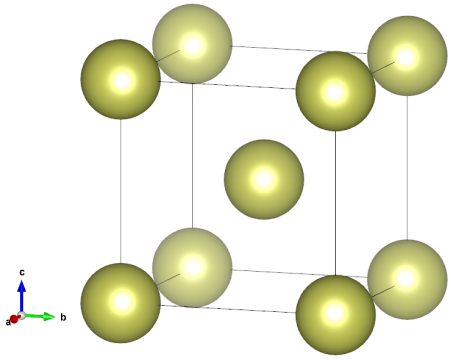

Figure 4.1. α-Fe unit cell: $a = 0.2856\,\text{nm}$, space group $\text{Im}\bar{3}\text{m}$ (229).

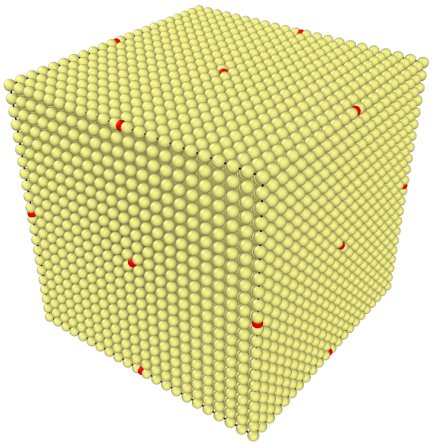

Figure 4.2. Ferrite unit cell: carbon atoms (red) occupy octahedral sites (Wyckoff 6*b*).

loading direction; in the other two directions the atoms were allowed to move freely. This type of boundary condition allows us to capture the interactions between dislocations and sample surfaces. The corresponding α-Fe supercells were made by removing the carbon atoms from the ferrite supercells.

4.1.2 Simulation setup

Molecular dynamics simulations have been performed using LAMMPS, the Large-scale Atomic/Molecular Massively Parallel Simulator [130] (http://lammps.sandia.gov). The interatomic potential used was the embedded-atom method (EAM) form developed by Hepburn and Ackland [99]. This potential describes the carbon and iron interactions for a wide range of systems containing defects and it has been used to study carbon interactions with dislocations and to calculate elastic constants of α-Fe [131, 132].

The equilibration was perfomed as follows. Initially, energy minimisation using the conjugate gradient method [133] was performed. The canonical ensemble (NVT) was used to bring the temperature of the system from 0.1 to 300 K in 100 ps. After heating, the temperature was maintained constant for 100 ps with the NVT ensemble. Finally, the isothermal-isobaric ensemble (NPT) was used to relax the supercell at 0 bar for 100 ps, for

the (bulk) configuration using three periodic boundary conditions. For the (nanowhisker) configuration using two non-periodic boundary conditions, only the P_{zz} component of pressure was set to 0 bar as periodic boundary conditions are imposed only in the z direction. The damping parameters for the thermostat and the barostat used were set to 100 and 1000 timesteps, respectively. For both equilibration and tensile test simulations, the integration of the equations of motion was done with the Velocity Verlet scheme using an integration timestep of 1 fs.

For the bulk configuration, the tensile test simulations were performed using the NPT ensemble. The non-loading axes were relaxed at 0 bar by adjusting the simulation cell dimensions in order to maintain the uniaxial stress state. For the nanowhisker setting, the NVT ensemble was used. The non-loading axes of the whisker are essentially surfaces, so the uniaxial stress state is also maintained.

The applied engineering strain rates for both types of boundary conditions were 10^{10}, 5×10^{9}, 10^{9}, 5×10^{8}, 10^{8} and $5 \times 10^{7}\,\mathrm{s}^{-1}$. Simulations were run for 30, 60, 300, 400, 3,000 and 4,000 ps respectively, to achieve the target strain. Nanowhiskers were also tested at $5 \times 10^{6}\,\mathrm{s}^{-1}$ and run for 40 ns. The stress was computed from the pressure tensor in the direction of the loading. Dislocations and twins were identified using the Dislocation Extraction Algorithm (DXA) and the Polyhedral Template Matching (PTM) [134, 135], respectively, as implemented in the Ovito code [136].

4.2 Results

4.2.1 Maximum stress and stress-strain curves

The maximum stresses calculated for the four crystallographic directions considered in this study at the applied strain rates are given in table 4.1, along with the Schmid factors for the bulk samples, and are shown in table 4.2 for the whiskers. Figure 4.3 shows the stress-strain curves obtained at $\dot{\varepsilon} = 10^{8}\,\mathrm{s}^{-1}$ for the bulk samples. It can be seen that the maximum stress in the [1 1 1] loading direction for ferrite was $\sigma_{\max}^{[1\,1\,1]} = 23.6\,\mathrm{GPa}$ while for α-Fe it was $\sigma_{\max}^{[1\,1\,1]} = 20\,\mathrm{GPa}$. The strength of ferrite was also higher than that of α-Fe when loading on the $[1\,\bar{1}\,0]$ direction, as $\sigma_{\max}^{[1\,\bar{1}\,0]} = 18.5\,\mathrm{GPa}$ and $\sigma_{\max}^{[1\,\bar{1}\,0]} = 15.9\,\mathrm{GPa}$ for ferrite and α-Fe, respectively.

The strengthening effect of C was less significant when loading along the $[1\,1\,\bar{2}]$ and [1 0 0] directions. The strength of ferrite was approximately 1 GPa higher than that of α-Fe when loading along the $[1\,1\,\bar{2}]$ direction, and no difference was observed along the [1 0 0] direction. In section 4.3.2, it will be shown that in the [1 1 1] and $[1\,\bar{1}\,0]$ directions deformation occurs by dislocation slip while in the $[1\,1\,\bar{2}]$ and [1 0 0] directions deformation is dominated by twinning. This suggests that the increase in $\sigma_{\max}$ is caused by the interaction of C atoms with dislocations.

		σ_{max} (GPa) on specified $[h\,k\,l]$			
	$\dot{\varepsilon}$ (s^{-1})	$[1\,1\,1]$	$[1\,\bar{1}\,0]$	$[1\,1\,\bar{2}]$	$[1\,0\,0]$
	1×10^{10}	25.3	21.3	14.7	9.4
	5×10^{9}	22.1	19.8	14.1	9.2
	1×10^{9}	21.8	16.7	13.8	9.0
α-Fe	5×10^{8}	21.1	15.2	14.4	9.2
	1×10^{8}	20.0	15.9	14.8	9.2
	5×10^{7}	20.3	15.8	15.0	9.2
	1×10^{10}	26.7	22.3	16.4	9.6
	5×10^{9}	23.4	21.6	16.2	9.4
	1×10^{9}	21.7	20.5	15.8	9.2
Ferrite	5×10^{8}	21.6	19.3	15.7	9.2
	1×10^{8}	23.6	18.5	15.6	9.2
	5×10^{7}	21.6	18.8	15.5	9.1
Schmid's factor		0.36	0.48	0.34	0.47

Table 4.1. Maximum stress and Schmid's factors for bulk samples.

		σ_{max} (GPa) on specified $[h\,k\,l]$			
	$\dot{\varepsilon}$ (s^{-1})	$[1\,1\,1]$	$[1\,\bar{1}\,0]$	$[1\,1\,\bar{2}]$	$[1\,0\,0]$
	1×10^{10}	20.5	18.7	14.6	9.4
	5×10^{9}	19.5	17.6	13.8	9.2
	1×10^{9}	17.6	15.8	13.2	9.1
α-Fe	5×10^{8}	17.3	15.4	13.0	9.0
	1×10^{8}	17.1	15.2	12.4	8.7
	5×10^{7}	16.9	14.6	12.0	8.5
	1×10^{7}	16.3	14.6	11.9	8.5
	1×10^{10}	21.1	18.2	14.3	9.5
	5×10^{9}	20.0	17.3	13.7	9.2
	1×10^{9}	18.1	15.8	13.0	9.1
Ferrite	5×10^{8}	17.4	-	13.8	8.8
	1×10^{8}	16.8	14.7	12.1	8.6
	5×10^{7}	16.4	14.6	12.0	8.4
	1×10^{7}	16.9	14.8	11.2	8.3

Table 4.2. Maximum stress for whiskers.

Stress-strain curves obtained for nanowhiskers at $\dot{\varepsilon} = 10^8\,s^{-1}$ are shown in figure 4.4. Similarly to the bulk configuration, the $[1\,1\,1]$ direction is the one with the highest strength, followed by the $[1\,\bar{1}\,0]$ direction, for both, α-Fe (figure 4.4a) and ferrite (figure 4.4b). However, only minor differences were seen between α-Fe and ferrite nanowhiskers, and the σ_{max} values were considerably lower relative to the bulk configuration.

4.2.2 Strain rate sensitivity

The stress-strain curves for the bulk configuration when loaded along the $[1\,1\,1]$ direction are presented in figure 4.5. As can be seen in this figure, except for $\dot{\varepsilon} = 5 \times 10^8\,s^{-1}$, σ_{max} is higher in ferrite than it is in α-Fe for all strain rates.

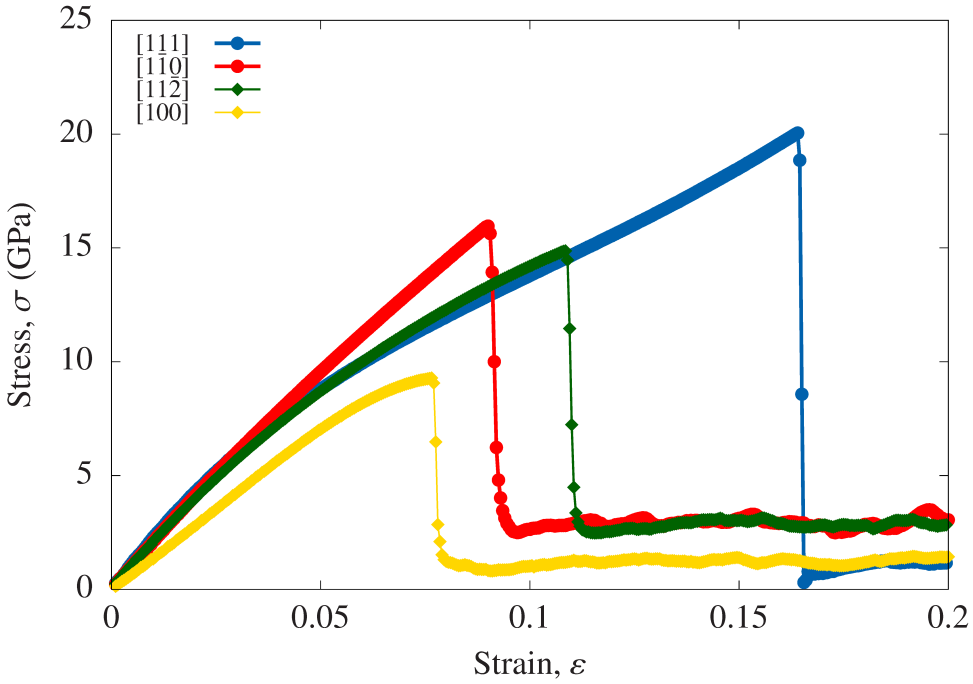

(a)

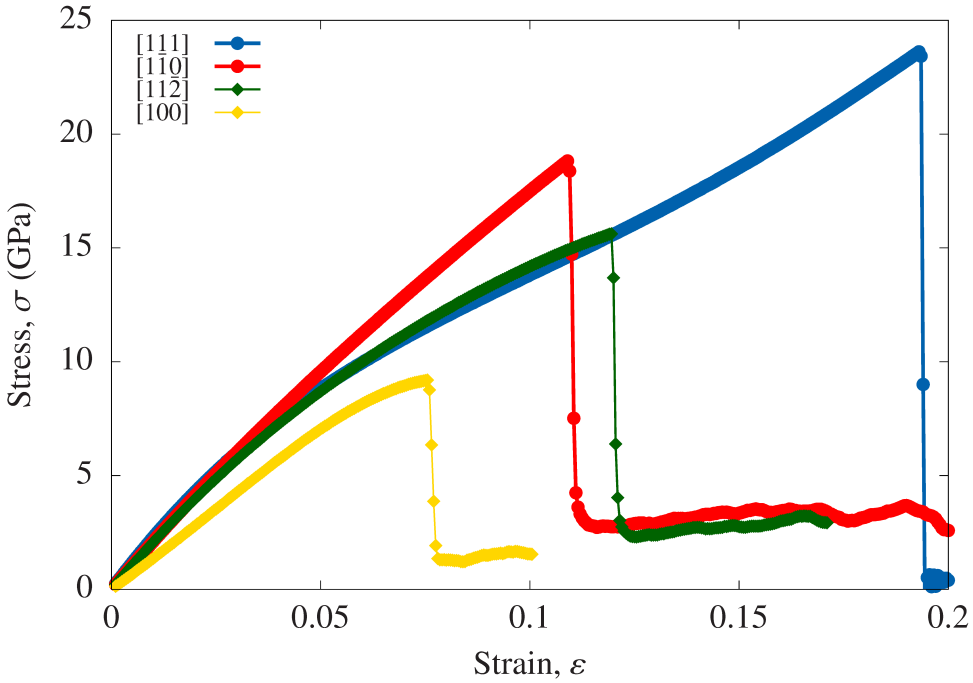

(b)

Figure 4.3. Stress-strain curves at $\dot{\varepsilon} = 10^8\,\mathrm{s}^{-1}$ for bulk samples: (a) α-Fe; (b) ferrite. $\sigma_{\max}$ for ferrite is higher when loaded in the $[1\,1\,1]$, $[1\,\bar{1}\,0]$ and $[1\,1\,\bar{2}]$ directions.

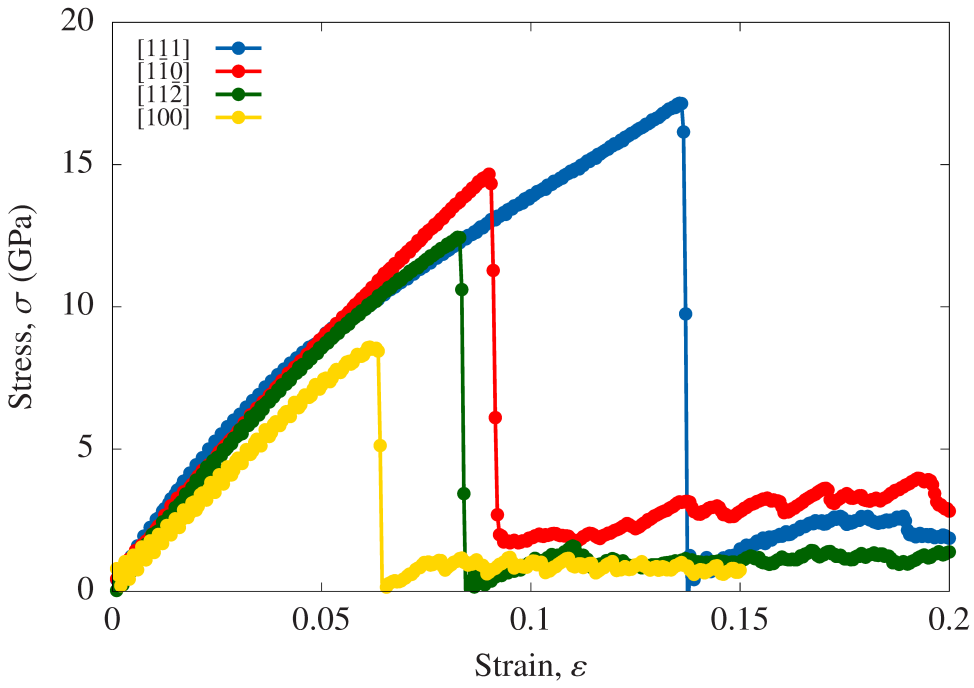

(a)

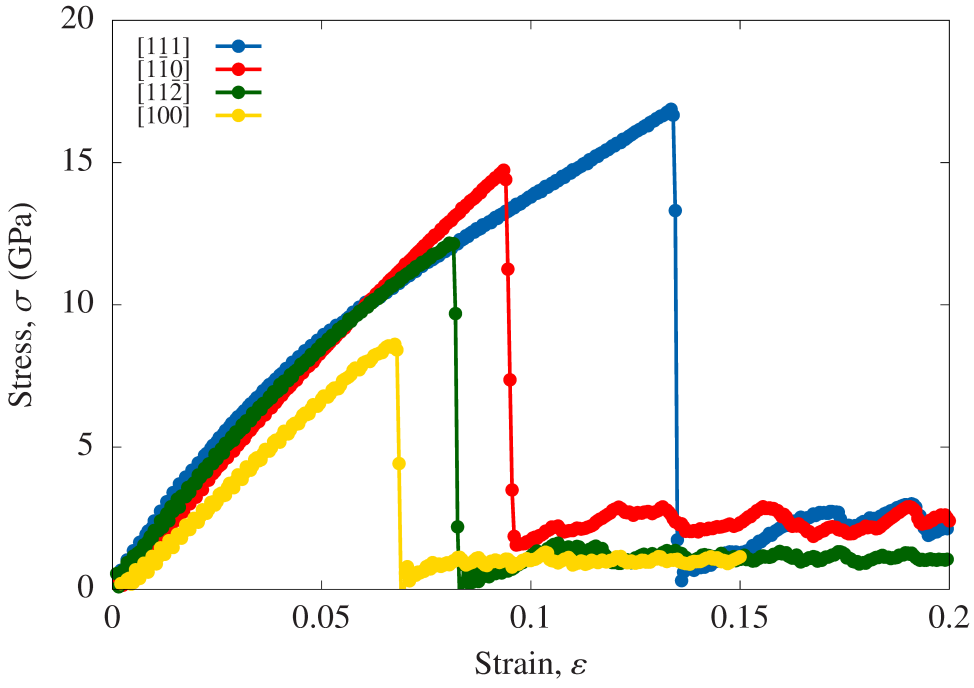

(b)

Figure 4.4. Stress-strain curves at $\dot{\varepsilon} = 10^8\,\mathrm{s}^{-1}$ for nanowhiskers: (a) α-Fe; (b) ferrite. No significant difference in $\sigma_{\max}$.

In order to understand how the strain rate affects strength, $\sigma_{\max}$ was plotted versus $\dot{\varepsilon}$ for the four loading directions and fitted to a power-law expression using the least squares method. Figure 4.6 shows the curves obtained for the bulk samples. Two distinct regions, characterised by different slopes can be observed for the [1 1 1] and [1 $\bar{1}$ 0] loading directions. At high strain rates, $\dot{\varepsilon}^{[1\,1\,1]} > 5 \times 10^9$ and $\dot{\varepsilon}^{[1\,\bar{1}\,0]} > 5 \times 10^8$ for α-Fe (figure 4.6a) and $\dot{\varepsilon}^{[1\,1\,1]} > 10^9$ and $\dot{\varepsilon}^{[1\,\bar{1}\,0]} > 8 \times 10^8$ for ferrite (figure 4.6b) the maximum stress decreases sharply as $\dot{\varepsilon}$ is decreased while for strain rates below than these values the influence of the strain rate becomes negligible and maximum stress remains almost constant. The strength in the [1 1 $\bar{2}$] and [1 0 0] direction is practically insensitive to strain rate.

For the nanowhiskers, $\sigma_{\max}$ decreases continuously as $\dot{\varepsilon}$ is reduced, as can be seen in figure 4.7, and a power law relationship exists between the maximum stress and the strain rate:

$$\sigma_{\max} = C\dot{\varepsilon}^m \tag{4.1}$$

where $\sigma_{\max}$ is the maximum stress, C is a constant, $\dot{\varepsilon}$ is the strain rate, and m is the strain rate sensitivity.

Table 4.3 lists the calculated values for strain rate sensitivity, m, and the constant C for each loading direction considered in this work. It can be seen that the strain rate sensitivity ranges between 0.015 and 0.039 for different directions. These values are comparable with experimental values for low carbon steels, which are reported between 0.01 and 0.015 [137].

The two distinct regions observed in the $\sigma_{\max}$ versus $\dot{\varepsilon}$ plots for the bulk configuration were not seen for the nanowhiskers. Furthermore, there was no noticeable difference between the strength of ferrite and α-Fe. These two facts suggest that the high surface-to-volume ratio of the nanowhiskers obscures the effect of the carbon atoms, due to constraint in the square-section whiskers.

		Direction			
		[1 1 1]	[1 $\bar{1}$ 0]	[1 1 $\bar{2}$]	[1 0 0]
C (GPa)	α-Fe	9.80	7.36	7.43	6.66
	Ferrite	9.04	8.59	6.78	6.34
m	α-Fe	0.0304	0.0389	0.0283	0.0152
	Ferrite	0.0350	0.0313	0.0319	0.0168

Table 4.3. Calculated strain rate sensitivity for α-Fe and ferrite for different directions.

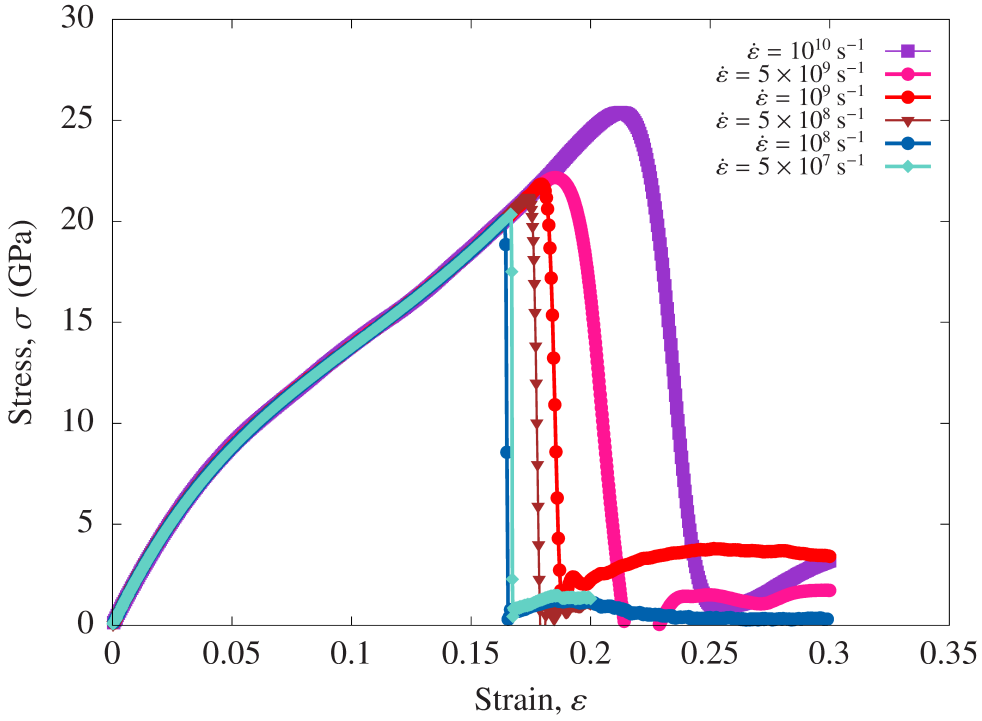

(a)

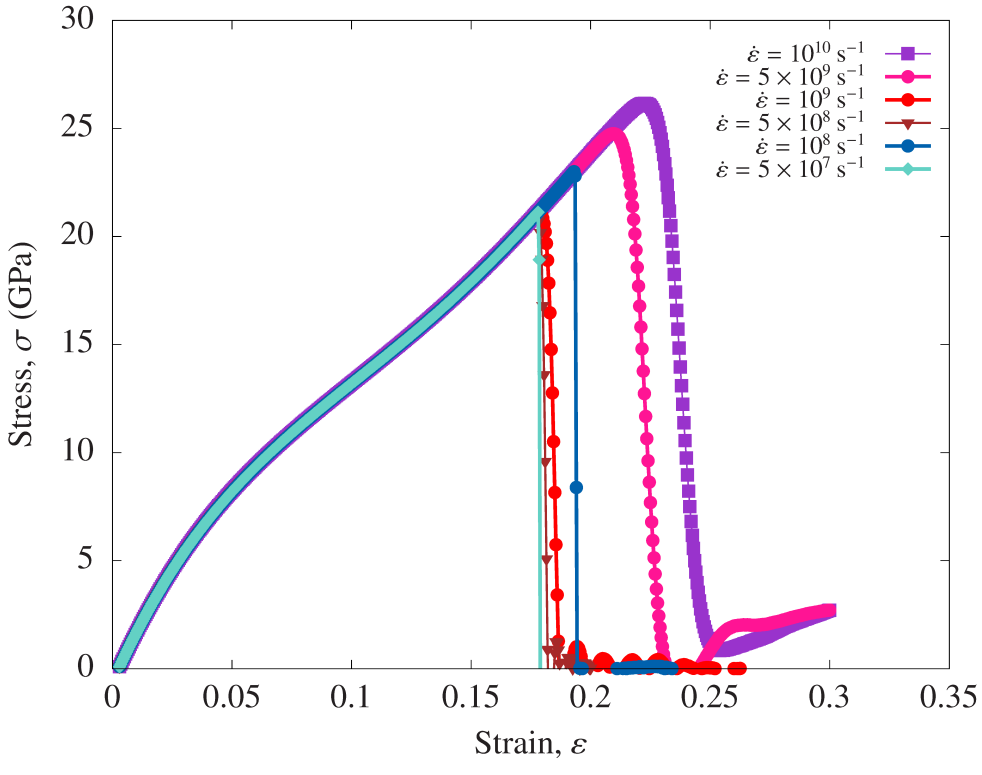

(b)

Figure 4.5. Stress-strain curves for bulk samples in the [1 1 1] direction: (a) α-Fe and (b) ferrite.

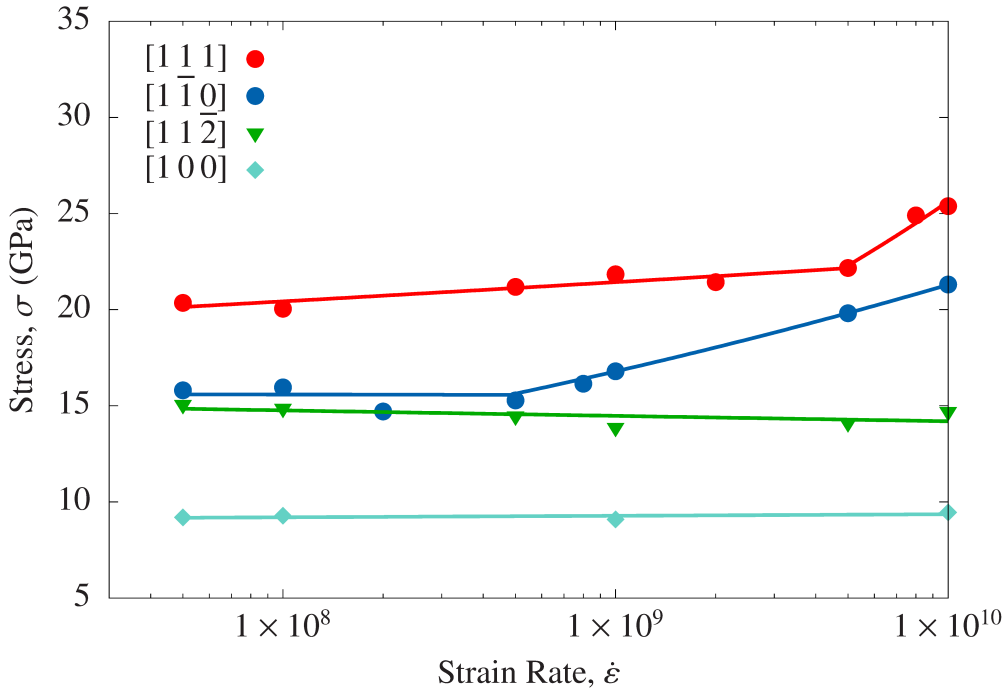

(a)

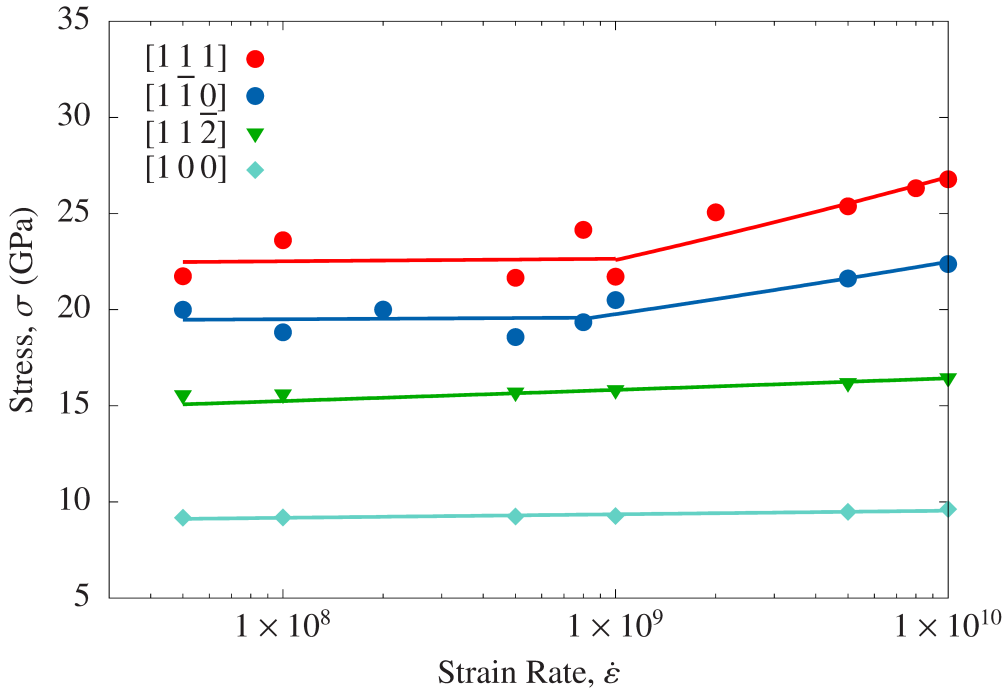

(b)

Figure 4.6. Maximum stress versus strain rate for different directions using periodic boundary conditions (bulk): (a) α-Fe and (b) ferrite. Two stages can be identified in the $[1\,1\,1]$ and $[1\,\bar{1}\,0]$ directions. At lower strain rates, $\sigma_{\max}$ is strain rate-insensitive while at higher values of strain rate, $\sigma_{\max}$ increases with $\dot{\varepsilon}$.

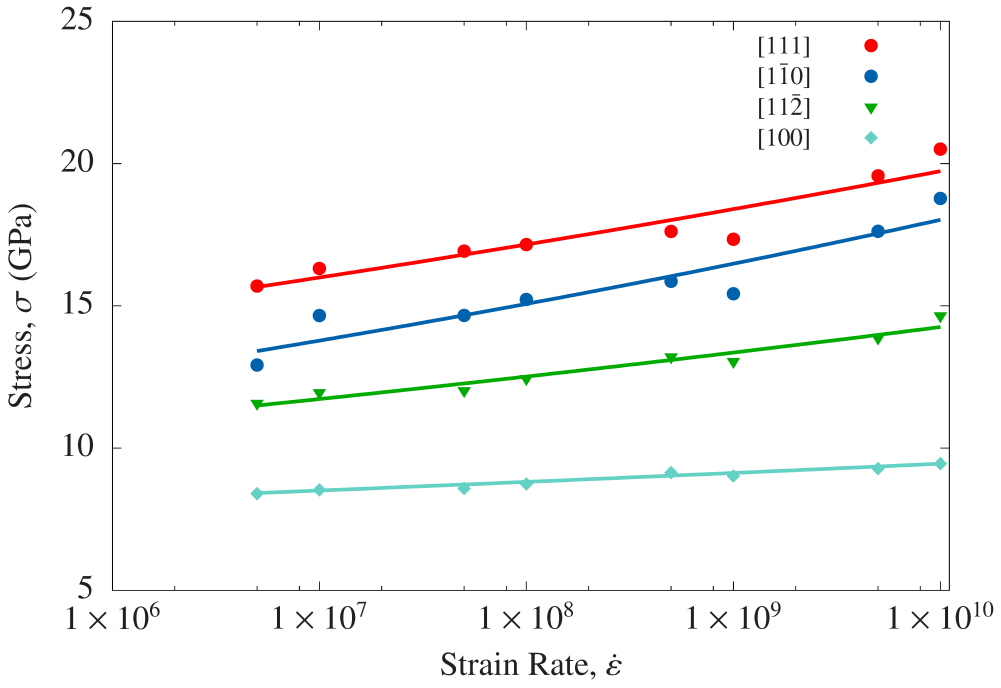

(a)

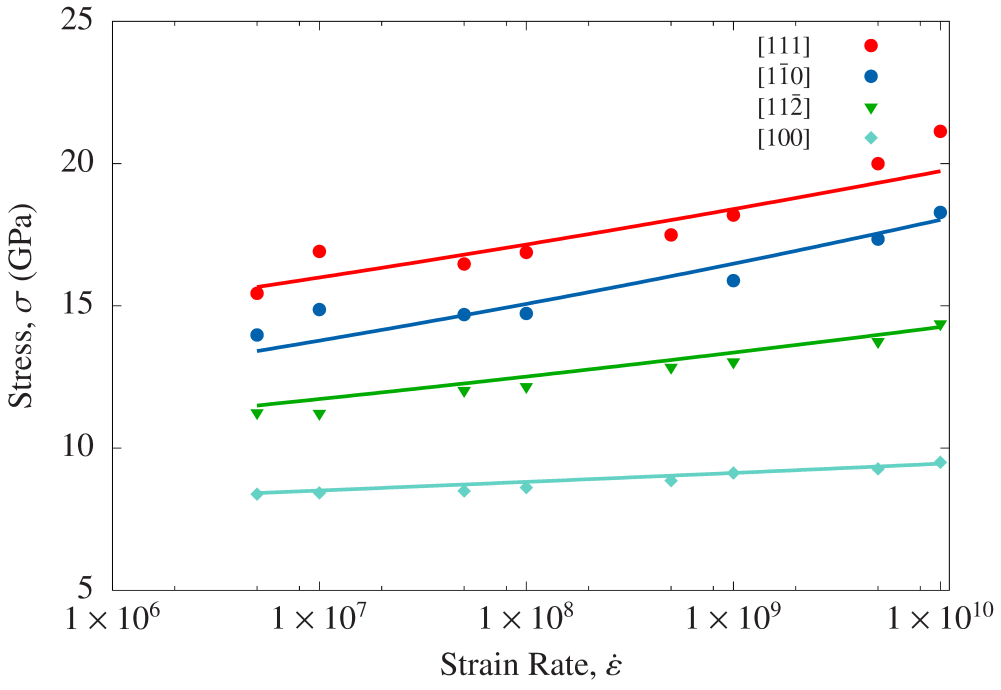

(b)

Figure 4.7. Maximum stress versus strain rate for different directions using non-periodic boundary conditions (nanowhisker): (a) α-Fe and (b) ferrite. $\sigma_{\max}$ is related to $\dot{\varepsilon}$ by the power law $\sigma_{\max} = C\dot{\varepsilon}^m$.

4.2.3 Deformation Mechanisms

Deformation by twinning

Snapshots of the deformation process of α-Fe nanowhiskers in the $[1\,1\,\bar{2}]$ direction, at strain rates $\dot{\varepsilon} = 10^{10}\,\mathrm{s}^{-1}$, $\dot{\varepsilon} = 10^{9}\,\mathrm{s}^{-1}$ and $\dot{\varepsilon} = 10^{8}\,\mathrm{s}^{-1}$ are shown in figure 4.8, 4.9 and 4.10, respectively. Surface atoms on the first $(1\,1\,1)$ plane, parallel to the page, were removed from the visualisation. From figures 4.8 to 4.10, it can be seen that at the yield point, the number of twins present in the crystal changes with the strain rate. At $\dot{\varepsilon} = 10^{10}\,\mathrm{s}^{-1}$ (figure 4.8a), several twins nucleate at the edges of the nanowhisker since they act as stress concentrators. These twins grow due to the propagation of $\frac{1}{2}[1\,1\,1]$ dislocations on $\{1\,1\,0\}$ planes, and they intercept other growing twins, as depicted in figure 4.8b. The clash of these growing twins leads to the formation of twinned regions, whose boundaries merge to accomodate the increasing strain, as shown in figure 4.8c.

At a strain rate of $10^{9}\,\mathrm{s}^{-1}$, the number of twins is lower. Figure 4.9a shows a twin nucleated on a $\{1\,1\,0\}$ plane at an angle of 45° with the loading axis. Then, it propagated through the whisker and reached the opposite surface while intercepting the advance of another growing twin, as shown in figure 4.9b. Similar processes occur in different regions of the nanowhisker. On further loading twin boundaries expand to account for the strain increase, as depicted in figure 4.9c. Once the whisker cannot accommodate the increasing strain, nano-voids and dislocations nucleate inside the nanowhisker at twin boundaries.

Figure 4.10 shows the deformation of a α-Fe nanowhisker at $\dot{\varepsilon} = 10^{8}\,\mathrm{s}^{-1}$. Only two twin boundaries can be seen suggesting that only a pair of twins nucleated. These twins propagate on $\{1\,1\,0\}$ planes, reaching the opposite surface of the whisker to grow into two full twins, as shown in figure 4.10a and figure 4.10b and they become the boundaries of the twinned region, as shown in figure 4.10c. Plastic deformation takes place due to the advance of these boundaries. On further strain increase, microvoids nucleate at twin boundaries and almost no dislocation activity is observed. This deformation behaviour is similar to the one described by Sainath et al. [123].

From Figs. 4.8, 4.9 and 4.10, it can be seen that the main effect of decreasing the strain rate on the deformation behaviour is the decrease in the number of twins which results in a lower strain at yield. The strain at yield is 0.124, 0.1015 and 0.093 for simulations at 10^{10}, 10^{9} and $10^{8}\,\mathrm{s}^{-1}$, respectively. Experimental observations of twins in iron single crytals is commonly observed at low temperatures and directions close to the $[1\,0\,0]$, with increasing twinning at higher strain rates [138].

Deformation by dislocation slip

Snapshots of the deformation process of α-Fe nanowhiskers in the $[1\,1\,1]$ direction at $\dot{\varepsilon} = 10^{10}\,\mathrm{s}^{-1}$ strain rate are presented in figure 4.11. It can be seen that plastic deformation begins with the nucleation of $\frac{1}{2}[1\,1\,1]$ dislocations at the edges of the nanowhisker, as shown

in figure 4.11a. The glide of these dislocations is accompanied by large localised distortions caused by the nucleation of several dislocation loops, as shown in figure 4.11b. As the strain increases, dislocations on main slip planes propagate through the nanowhisker, reaching the opposite surface, as can be seen in figure 4.11c. Due to the short run time of the simulations and the low mobility of screw dislocations compared with edge dislocations, the screw dislocations do not have enough time to slip and reach the surfaces. This results in a high dislocation density in the bulk of the nanowhisker.

Snapshots of the deformation process of a α-Fe nanowhisker at $\dot{\varepsilon} = 5\times10^{8}\,\mathrm{s}^{-1}$ are presented in Fig. 4.12. Plastic deformation begins with the nucleation of $\frac{1}{2}[111]$ dislocations at an edge of the nanowhisker, followed by propagation through the nanowhisker. The glide of these dislocations causes significant plastic deformation which results in the formation of a crack, as it can be seen in figure 4.12a. Dislocations nucleate from the crack-tip and slip to the surfaces of the nanowhisker resulting in steps, which can be seen in figure 4.12b. The crack growth continues with futher strain causing an in-plane slip of the two parts of the nanowhisker at approximately 45° from the loading axis, as depicted in figure 4.12c. This deformation is consistent with the one reported by Sainath & Choudhary [139].

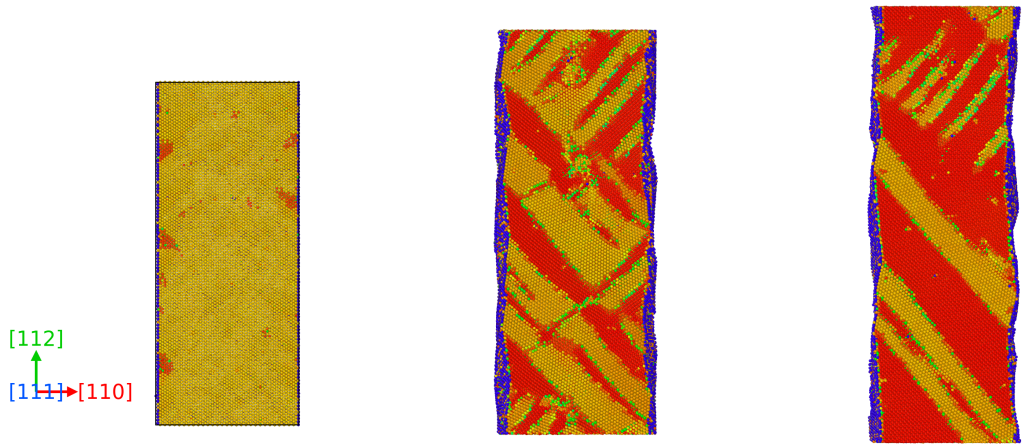

(a) $\varepsilon = 0.11$ (b) $\varepsilon = 0.15$ (c) $\varepsilon = 0.2$

Figure 4.8. Deformation of a α-Fe nanowhisker loaded in the $[1\,1\,\bar{2}]$ direction at $\dot{\varepsilon} = 10^{10}\,\mathrm{s}^{-1}$: (a) Several twins nucleate at the edges of the nanowhisker; (b) As they grow, they intercept other twins and reach the opposite edge of the nanowhisker; (c) Twin boundaries merge to accomodate the increasing strain, resulting in larger twinned regions. Colouring based on local lattice orientation. Yellow atoms: original orientation. Green atoms: medium rotation. Red atoms: large rotation. Blue atoms: surface atoms.

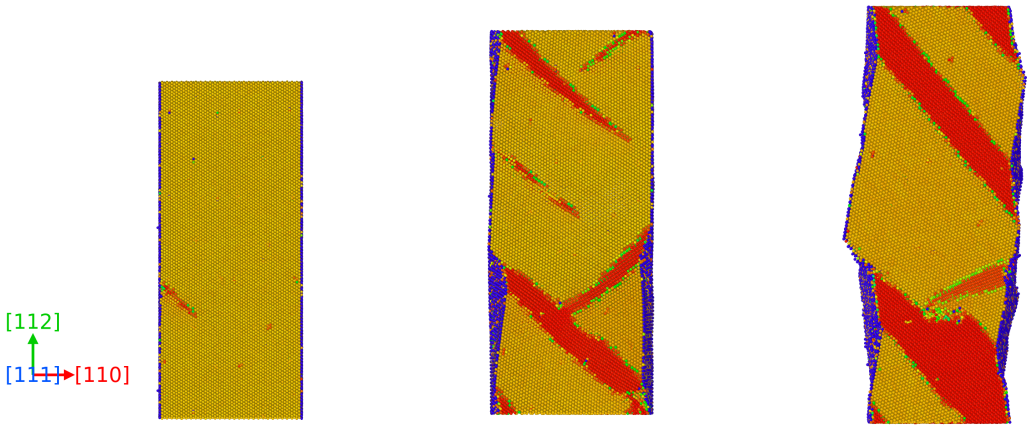

(a) $\varepsilon = 0.08$ (b) $\varepsilon = 0.09$ (c) $\varepsilon = 0.15$

Figure 4.9. Deformation of a α-Fe nanowhisker loaded in the $[1\,1\,\bar{2}]$ direction at $\dot{\varepsilon} = 10^9\,\mathrm{s}^{-1}$: (a) Twins nucleate at the edges of the nanowhisker; (b) They propagate until they reach the opposite surface or other growing twins; (c) Twin boundaries move and expand twinned regions, as the load increases. Colouring based on local lattice orientation. Yellow atoms: original orientation. Green atoms: medium rotation. Red atoms: large rotation. Blue atoms: surface atoms.

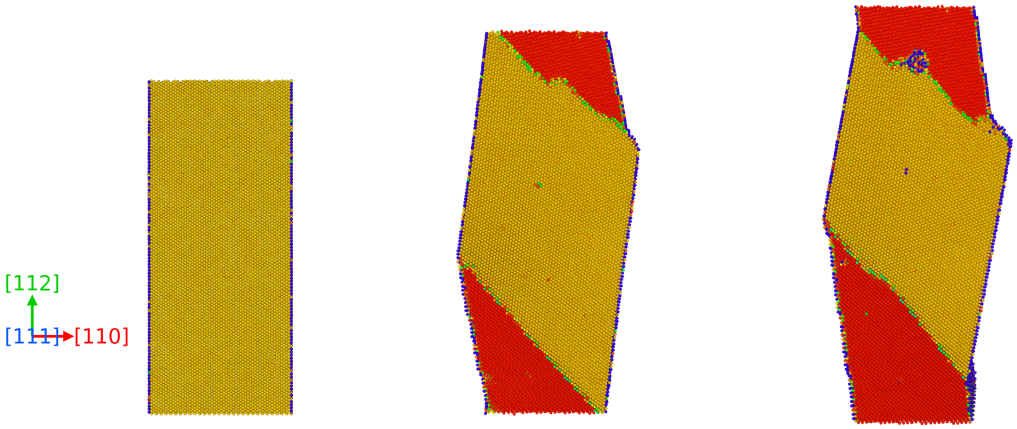

(a) $\varepsilon = 0.08$ (b) $\varepsilon = 0.09$ (c) $\varepsilon = 0.15$

Figure 4.10. Deformation of a α-Fe nanowhisker loaded in the $[11\bar{2}]$ direction $\dot{\varepsilon} = 10^8\,\mathrm{s}^{-1}$: (a) A pair of twins nucleate at the edges of the nanowhisker; (b) They grow through the nanowhisker, reaching the opposite surface to become the twin boundaries; (c) As the strain increases, the twin boundaries advance to extend the twinned regions. Nanovoids nucleate at twin boundaries with almost no dislocation activity. Colouring based on local lattice orientation. Yellow atoms: original orientation. Green atoms: medium rotation. Red atoms: large rotation. Blue atoms: surface atoms.

A further decrease in the strain rate does not show an important change in the deformation mechanism of the whiskers. As shown in figure 4.12d, a similar 45° slip failure was observed when loading at $\dot{\varepsilon} = 5 \times 10^6\,\mathrm{s}^{-1}$. However, when compared with the deformation at

$\dot{\varepsilon} = 5\times10^{8}\,\mathrm{s}^{-1}$ (figure 4.11), more slip-steps can be seen at the surface, indicating that more dislocations managed to leave the bulk of the whisker. After yield, the dislocation density was approximately ten times higher in the nanowhisker loaded at $\dot{\varepsilon} = 5\times10^{8}\,\mathrm{s}^{-1}$ compared with that at $\dot{\varepsilon} = 5\times10^{6}\,\mathrm{s}^{-1}$. This suggests that at higher strain rates, dislocations, especially of screw character, do not have enough time to move and reach surfaces. A higher number of dislocations results in a higher tensile stregth. For these two whiskers, there was a difference of more than 2 GPa in favour of the one loaded at $\dot{\varepsilon} = 5\times10^{8}\,\mathrm{s}^{-1}$.

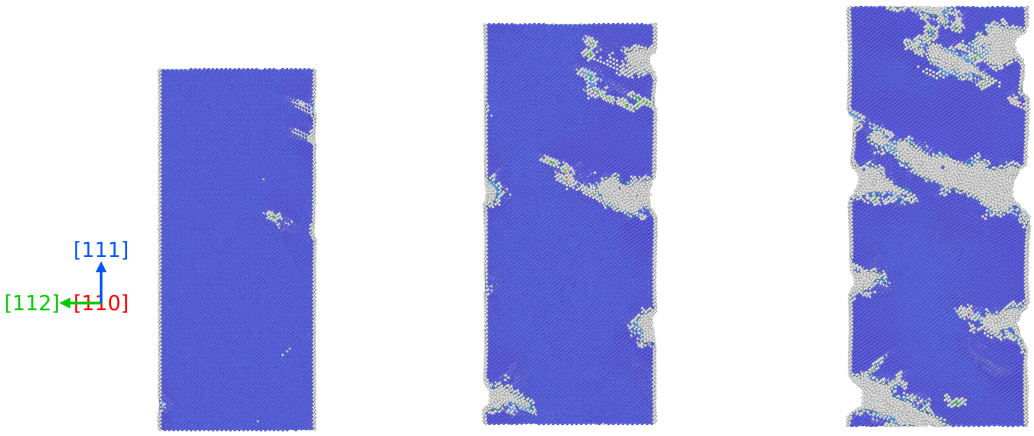

(a) $\varepsilon = 0.17$ (b) $\varepsilon = 0.175$ (c) $\varepsilon = 0.2$

Figure 4.11. Deformation of a α-Fe nanowhisker loaded in the [1 1 1] direction at $\dot{\varepsilon} = 10^{10}\,\mathrm{s}^{-1}$: (a) Several $\frac{1}{2}[111]$ dislocations nucleate at the edges of the nanowhisker; (b) and (c) Dislocations on main slip planes propagate through the nanowhisker and reach the opposite surface. Highly deformed areas are shown in grey.

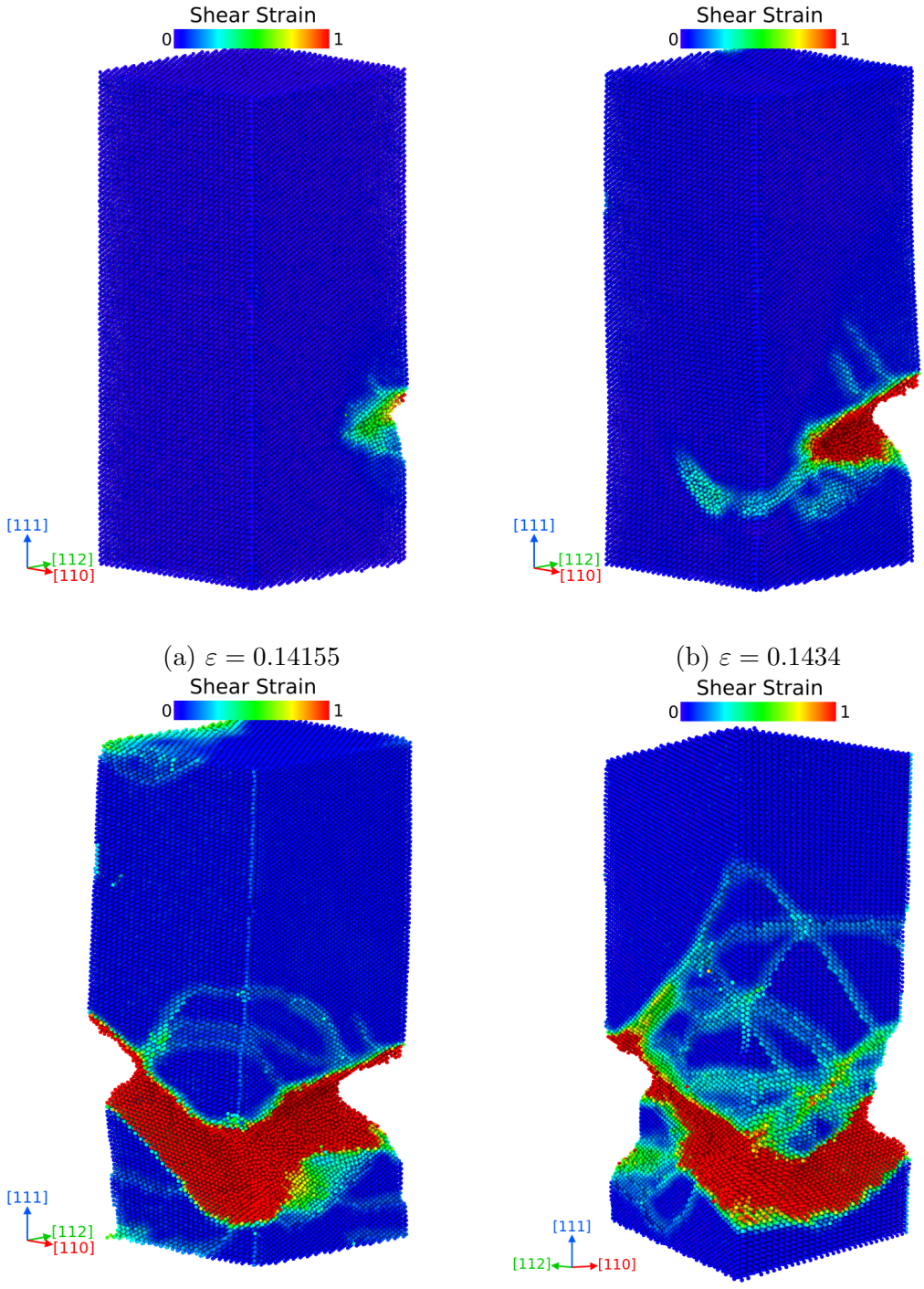

(a) $\varepsilon = 0.14155$ (b) $\varepsilon = 0.1434$

(c) $\varepsilon = 0.15$ (d) $\varepsilon = 0.15$, $\dot{\varepsilon} = 5 \times 10^6\,\mathrm{s}^{-1}$

Figure 4.12. Deformation of a α-Fe nanowhisker loaded in the [1 1 1] direction at $\dot{\varepsilon} = 5 \times 10^8\,\mathrm{s}^{-1}$: (a) Intense dislocation nucleation resulting in the formation of a crack; (b) Dislocation emission from the crack-tip and formation of surface steps; (c) In-plane slip at 45° from the loading axis; (d) Deformation at $\dot{\varepsilon} = 5 \times 10^6\,\mathrm{s}^{-1}$, showing significantly more slip steps than in (d). Atomic strains larger than 1 are shown in red.

4.3 Discussion

4.3.1 Orientation dependence of strength

The yield strength of a BCC single crystal is closely related to the stress required to nucleate $\frac{1}{2}\langle 1\,1\,1\rangle$ full dislocations responsible for slip deformation, or the $\frac{1}{6}\langle 1\,1\,1\rangle$ partial dislocations responsible for twinning. As discussed by Li et al. [140], the slip and twinning mechanisms compete at yield. Plastic deformation commences with the formation of a one-layer stacking fault through the nucleation of a $\frac{1}{6}\langle 1\,1\,1\rangle$ partial dislocation. Whether slip or twinning dominate is determined on the following step: if the subsequent step is the nucleation of another $\frac{1}{6}\langle 1\,1\,1\rangle$ partial dislocation, a twin will form. Further nucleation of partial dislocations of this type will extend the boundary of twinned crystal. On the other hand, if the nucleation of the initial $\frac{1}{6}\langle 1\,1\,1\rangle$ partial dislocation is followed by the nucleation of a $\frac{1}{3}\langle 1\,1\,1\rangle$ dislocation, a full $\frac{1}{2}\langle 1\,1\,1\rangle$ dislocation will form.

Twinning is crystallographically favoured when the crystal is loaded on the $[1\,1\,\overline{2}]$ and $[1\,0\,0]$ directions. Consequently, yield occurs at lower stress because the nucleation of a $\frac{1}{6}\langle 1\,1\,1\rangle$ partial dislocation requires lower energy than the nucleation of a full $\frac{1}{2}\langle 1\,1\,1\rangle$ dislocation [141]. On the other hand, slip is more favourably oriented when the loading axis lies along the $[1\,1\,1]$ and $[1\,\overline{1}\,0]$ directions, and high stress is needed for the nucleation of full $\frac{1}{2}\langle 1\,1\,1\rangle$ dislocations. Furthermore, the Schmid's factors for the $\langle 1\,1\,1\rangle\{1\,1\,2\}$ slip system when loaded on the $[1\,1\,1]$ and $[1\,\overline{1}\,0]$ direction are 0.36 and 0.48, respectively. The lower Schmid's factor when loading on the $[1\,1\,1]$ direction suggests that higher stresses are needed to initiate slip than when loading on the $[1\,\overline{1}\,0]$ direction.

4.3.2 Effects of C interstitials on strength

There is a noticeable difference between the strength of ferrite and that of α-Fe, shown in figure 4.6. This difference was attributed to the presence of carbon interstitials in the ferrite supercell. Moreover, the fact that the superior strength of ferrite was mainly seen when loading along orientations that fail due to dislocation slip, the $[1\,1\,1]$ and the $[1\,\overline{1}\,0]$ orientations, is another indication that the interaction of C interstitials with dislocations is responsible for such strengthening.

Molecular dynamics simulations of dislocation glide have shown that C atoms can significantly increase the critical shear stress needed to produce glide and decrease glide velocity [74]. However, C interstitials need to be a close proximity to the glide plane for dislocation pinning to be significant (closer than 0.2 nm). Therefore, the strengthening effect of C atoms depends on the encounters they have with dislocations. The supercells used in this work were approximately 14 times larger than those used by Schmauder & Kohler [74], in order to maximise the possibility of dislocations sliding on planes with C atoms. Since the magnitude of the strengthening effect depends on the position of both carbon atoms and slip planes, a large number of randomly distributed atoms is needed to

account for the variability of the Fe–C system. In figure 4.6b, data scatter at lower values of $\dot{\varepsilon}$ for ferrite loaded on the [1 1 1] and [1 $\overline{1}$ 0] can be observed, evidencing the random nature of the C atoms and dislocation core encounters.

4.3.3 Strain rate effects

As seen in the stress-strain curves presented in figure 4.5, the strength of the supercells increases with the strain rate. This occurs because at high strain rates, dislocations cannot move through the crystal and the large number of dislocations that nucleated at the yield point become trapped in the supercell. This increased dislocation density results in the observed stress overshoot. Transmission electron microscopy observations of samples deformed at high strain rates reported in the literature [142], confirm that the slip mechanism can operate at high strain rates, and that high dislocation densities are responsible for the increased strength. In this work, simulations performed at higher strain rates showed increased dislocation densities when compared with those at lower strain rates. This is consistent with the work reported by Wang et al. [142].

The two regimes describing the dependence of $\sigma_{\max}$ on $\dot{\varepsilon}$, observed when loading on the [1 1 1] and [1 $\overline{1}$ 0] directions using the periodic boundary conditions (bulk) can be explained as the transition between thermally assisted (at low strain rates) and athermal yielding. At low strain rates, the energy required by dislocations to overcome energy barriers and obstacles, such as C interstitials, is provided by the applied stress and by thermal vibrations [143]. The probability of thermal activation at higher strain rates decreases and with limited thermal assistance, dislocations require higher shear stresses to overcome obstacles, resulting in higher values of $\sigma_{\max}$.

4.4 Conclusions

Molecular dynamics simulations of tensile tests were carried out in pure Fe and ferrite in order to investigate the effect of C atoms on the strength and active deformation mechanisms. For the configuration using periodic boundary conditions in all three directions (bulk configuration), the strength of ferrite was found to be up to 20 % higher than that of pure Fe for certain crystallographic directions, i.e. the [1 1 1] and [1 $\overline{1}$ 0]. When loaded on these directions, yielding occurred via dislocation slip. When loaded on the [1 1 $\overline{2}$] and [1 0 0] directions, the deformation occurred via twinning, and C atoms did not produce any noticeable strengthening effect. For the configuration with non-periodic boundary conditions along non-loading axes (nanowhisker configuration), no noticeable difference between the tensile behaviour of pure Fe and ferrite was observed, suggesting that surface effects dominate the deformation.

The influence of strain rate on the deformation of iron and ferrite was investigated by running simulations with the following strain rates 10^{10}, 5×10^{9}, 10^{9}, 5×10^{8}, 10^{8} and

$5 \times 10^7\,\mathrm{s}^{-1}$. The values calculated for strain rate sensitivity, $m = 0.015$ to 0.039 are comparable with experimental values, $m = 0.01$ to 0.015 obtained for low carbon steels [137].

Two regimes describing the dependance of $\sigma_{\max}$ on the $\dot{\varepsilon}$, were observed for the $[1\,1\,1]$ and $[1\,\overline{1}\,0]$ directions when using periodic boundary conditions. This behaviour is associated with the deformation by dislocation slip, and the two regimes correspond to athermal ($\dot{\varepsilon} > 10^9\,\mathrm{s}^{-1}$) and thermally assisted yield ($\dot{\varepsilon} < 10^9\,\mathrm{s}^{-1}$).

Chapter 5

Hydrogen Effects on Dislocation Mobility

The hydrogen enhanced localised plasticity theory [5, 6, 53] is usually quoted to explain softening (e.g. reduction of the flow stress) observed in metals when exposed to a hydrogen environment. HELP theory has been used to explain TEM observations of enhanced dislocation mobility [7] and localised slip [144]. Reduction of the yield strength in tensile tests [54, 145] and pop-in load in nano-indentation [58] experiments are also examples of phenomena that have been attributed to HELP. While these observations suggest that the presence of hydrogen in metals leads to softening, at least locally, the mechanism by which it occurs has not been satisfactorily explained.

Three main possible mechanisms through which dissolved hydrogen atoms could induce softening have been proposed:

1. H increases dislocation mobility [54, 146], resulting in lower flow stress;
2. H reduces dislocation-dislocation interactions [147, 148], increasing planar slip and pile-ups;
3. H modifies dislocation-obstacle interactions, reducing the ability of obstacles to pin dislocations [149].

Mechanisms 2 and 3 have been investigated through continuum modelling [6, 150], concluding that while dislocation pile-ups are unlikely to be the cause of softening, reduced obstacle pinning of dislocations may be possible. Mechanism 1 is not suitable for continuum analysis due to the non-linear nature of dislocation cores, making atomistic simulations a more appealing approach.

In some metals, atomistic simulations involving H are challenging due to the high migration barrier of hydrogen that requires simulation timescales to be in the order of magnitude of microseconds (which is currently beyond the current capabilities of most supercomputers). In iron, however, hydrogen diffusion is fast, requiring timescales in the nanoseconds.

The effect of H on dislocation mobility in iron has been studied using MD simulations. Song and Curtin [60], used a well-known Fe-H embedded atom method interatomic potential [13, 14] to study hydrogen effects on dislocation mobility. They found out that mechanism 1 is not operative in Fe and instead, hydrogen decreases dislocation mobility due to solute drag. They also concluded that hydrogen has little effect on the separation distance of edge dislocation in pile-ups, thus suggesting that hydrogen induces softening through mechanism 3, by modifying dislocation-obstacle interactions.

While dislocation-obstacle interactions can also be studied using MD simulations, the type of obstacle is greatly limited by the interatomic potential used. Attractive scenarios would be dislocations interacting with interstitials and precipitates, as they are important strengthening mechanisms. Unfortunately, the lack of availability of accurate ternary interatomic potentials (metal–H–obstacle) poses a major limitation to study this scenario with MD simulations. In an attempt to circumvent this issue, Tehranchi et al. [151], studied the effects of hydrogen on dislocation mobility using vacancies as 'surrogates' of solutes in Ni. It was shown that hydrogen atoms reduce the misfit volume, decreasing the stress needed for the dislocation to glide through a field of other vacancies. However, in the same work, DFT calculations demonstrated that H atoms do not bind with C solutes in Ni, resulting in larger misfit volumes which would lead to hardening. Nonetheless, this work suggests that softening due to hydrogen in metals is possible, depending on the hydrogen-obstacle interactions.

Great research effort has been devoted to the development of accurate ternary interatomic potentials. One of the approaches that have shown interesting progress is the reactive force field (ReaxFF) interatomic potential developed by van Duin, Goddard and co-workers [12, 106, 107, 152]. This type of potential intends to bridge the gap between quantum mechanical and classical molecular dynamics methods, offering quantum mechanics accuracy to large-scale simulations. ReaxFF is a reactive bond order potential that takes into account covalent and electrostatic interactions. Early work on the ReaxFF potential was aimed to study the oxidation of hydrocarbons [106], and was later extended to study Fischer–Tropsch catalysis [110]. This ternary Fe-C-H potential was adapted by Islam et al. to study hydrogen embrittlement [12]. The potential can describe hydrogen, vacancy, ferrite, and cementite interactions accurately, and has been chosen to study dislocation-H-solute interactions, the aim of this chapter.

5.1 Simulation methodology

Molecular dynamics simulations were used to test HELP concepts such as enhanced dislocation mobility and reduced dislocation-obstacle interactions. An edge dislocation was recreated following the periodic array of dislocations (PAD) simulation technique discussed in detail by Osetsky and Bacon [75]. The main advantage of this simulation technique over other approaches, such as the conventional model (CM) [153, 154], and

the Green's function boundary conditions (GFBC) [155, 156], approaches in which the dislocation is created by displacing the atoms according to the elasticity theory, is that periodic boundary conditions are applied not only in the line direction but also to the glide direction. Having periodic boundary conditions along both the glide and dislocation line directions has two major benefits: The first one is that the dislocation can glide an infinite distance because once it reaches the edge of the supercell, it will be reinserted on the opposite side. This is useful to dislocation dynamics since there is no limit on the distance the dislocation can glide before reaching the end of the simulation cell. The second benefit is that the direction along the dislocation line does not need to be large, as it has been demonstrated that results are insensitive to the size of the supercell in that direction [75]. This allows the focus of computational resources on increasing the size of the other two dimensions, to achieve realistic values of dislocation density, and timescales of the simulations. The PAD approach can be used to study dislocation motion under different conditions (temperature, applied stress, applied strain) and dislocation interactions with defects. Simulations using this methodology have been widely used to study dislocations in different materials such as Fe [157–159], Ni [160, 161], Al [160, 162] and Cu [163]. Furthermore, the MD studies of H effects on dislocation mobility described in the previous section also made use of the PAD approach. The accuracy of the PAD approach has been widely studied. Guidelines on how to perform reliable modelling while avoiding simulation artefacts, such as artificial image forces, can be found in the literature [75, 164]. These guidelines has been followed in this study.

5.1.1 Periodic array of dislocation supercell creation

The PAD supercell was created by merging two Fe single crystals, one of which had an extra lattice plane along the glide direction, and by minimising the potential energy of the resulting supercell. The half-crystals were oriented to produce a dislocation representative of those found in body-centred cubic Fe. BCC iron has multiple slip systems from which the $\frac{1}{2}\langle 1\,1\,1\rangle\{1\,1\,0\}$ was chosen for this study since it is the one most commonly found in MD simulations in the literature, facilitating direct comparison of results. The glide direction, slip plane normal direction and the dislocation line direction are the orthogonal $[1\,1\,1]$, $[1\,\overline{1}\,0]$ and $[1\,1\,\overline{2}]$ directions. The initial supercell containing the two half-crystals is shown in figure 5.1a. The lower and upper crystal consisted of n and $n+1$ lattice planes along the glide direction[1], the $[1\,1\,1]$, respectively. Because one of the half-crystals is slightly larger, having an extra lattice plane, there is significant atomic mismatch between the two joint half-crystals. This can be seen by computing the potential energy per atom of the supercell, which is shown in figure 5.2a. It can be seen that merging two half-crystals results in a configuration in which atoms along the boundary have high potential energy. The atomic mismatch along the boundary plane between two half-crystals is energetically expensive, so the minimisation of the potential energy produces a much more favourable

[1]The number of lattice planes along the glide direction, n, was chosen in section 5.1.2.

configuration in which most of the strain is localised in an edge dislocation. After the minimisation only those atoms along the dislocation line have high potential energy, as can be seen in figure 5.2b.

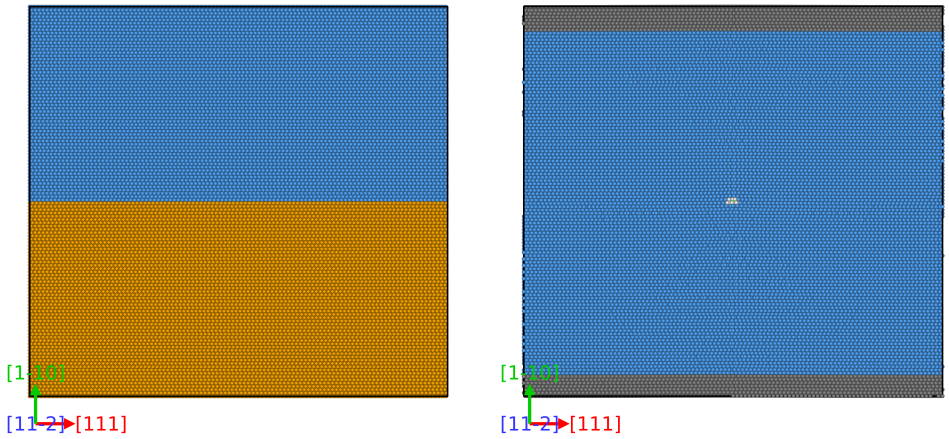

(a) Initial configuration (b) Final configuration

Figure 5.1. Creation of PAD supercell: a) Initial configuration consisted of two merged Fe single crystals (blue and orange). The upper crystal is larger than the lower one as it has an extra (1 1 1) plane. b) Final configuration of the PAD supercell containing a single $\frac{1}{2}[1\,1\,1]$ edge dislocation, whose line is perpendicular to the plane of the page. Blue, white and grey atoms represent atoms in bcc coordination, atoms at the dislocation core and traction atoms, respectively.

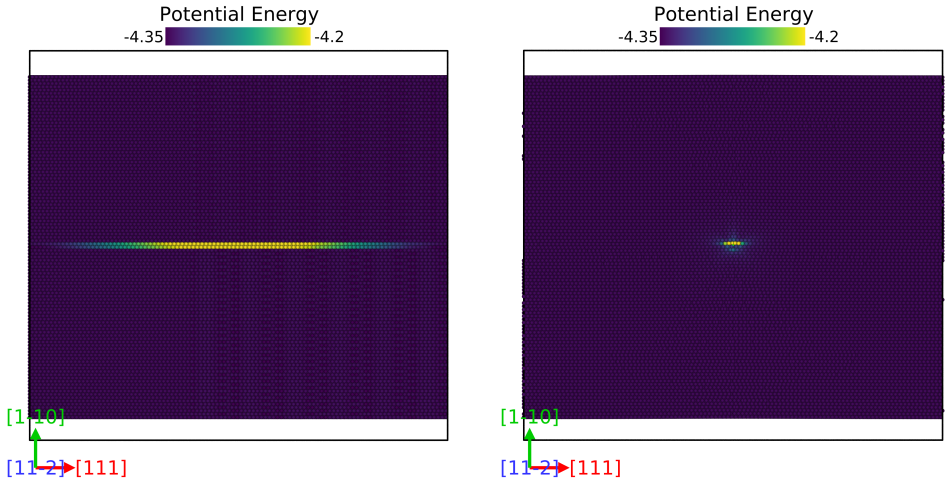

(a) Unrelaxed (b) Relaxed

Figure 5.2. Potential energy in eV/atom of PAD supercell before and after energy minimisation. a) Unrelaxed configuration: lattice mismatch along the boundary between two joint half-crystals results in high potential energy. b) Relaxed configuration: after minimisation of the potential energy, a $\frac{1}{2}[1\,1\,1]$ edge dislocation is created. Atoms with high potential energy can only be found along the dislocation line.

5.1.2 Size of the simulation box

In order to minimise size effects while keeping the computational cost of the simulation manageable, the size of the supercell was optimised. This was done by minimising the potential energy of supercells of different sizes and comparing the predicted stress field with the isotropic elasticity solution. As mentioned in section 5, the ReaxFF interatomic potential developed by Islam et al. [12] was used as it will allow study of the interactions between H with C interstitials in bcc Fe. The widely accepted EAM potential for Fe-H interactions developed by Ramasubramaniam et al. [13, 14] was also used as a comparison. After the minimisation, the shear stress σ_{xy} was computed and compared with the isotropic elasticity prediction [165] of the shear stress field around an edge dislocation, given by

$$\sigma_{xy} = Dx\frac{(x^2 - y^2)}{(x^2 + y^2)^2} \tag{5.1}$$

where x and y are the position coordinates and D is defined as

$$D = \frac{Gb}{2\pi\,(1 - \nu)} \tag{5.2}$$

G, b and ν in equation (5.2), are the shear modulus, the magnitude of the Burgers vector and the Poisson's ratio, respectively.

Due to the periodicity of the PAD supercell, a bowing dislocation is affected by image stresses arising from dislocations in neighbouring periodic supercells. Image forces act against the curvature of the dislocation, increasing the real stress needed to unpin a dislocation [164]. Therefore, in order to study H effects on dislocation pinning phenomena, it is important to minimise these image stresses. For a given dislocation line length Lz, artificial image stresses acting on the dislocation are a function of the cross-section aspect ratio $\bar{L} = L_x/L_y$, with optimal values close to 0.8 [164]. While $\bar{L}$ for simulations tested here is close to 1, difference in image stresses for values of $\bar{L}$ between 0.7 to 1.1 is rather small. Therefore, the aspect ratio used in this study is considered adequate. The direction along the dislocation line was made small, consisting of two lattice repeats along the $[1\,1\,\overline{2}]$ direction, or 1.4 nm. As discussed in [164], image stresses are quadratic in the dislocation line direction, thus PAD supercells along dislocation lines will suffer from increased image stresses when bow-out occurs.

With all these considerations taken into account, five simulation supercells of different sizes, shown in table 5.1, were tested. They range from $21 \times 12 \times 2$ to $159 \times 96 \times 2$ lattice repeats on the glide $[1\,1\,1]$, glide plane normal $[1\,\overline{1}\,0]$ and dislocation line $[1\,1\,\overline{2}]$ directions, respectively.

Figures 5.3 and 5.4 show the σ_{xy} stress field for the S2 and the S4 supercells (consisting

Supercell	**Unit cells** $n \times m \times l$	**Dimensions,** nm			**atoms,**$\times 10^3$	σ_{diff}, GPa
		$[1\,1\,1]$	$[1\,\bar{1}\,0]$	$[1\,1\,\bar{2}]$		
S1	$21 \times 12 \times 2$	5.1	4.6	1.4	2.9	1.71
S2	$41 \times 24 \times 2$	10	10	1.4	11.7	0.89
S3	$83 \times 48 \times 2$	20.1	19.2	1.4	47.5	0.43
S4	$105 \times 60 \times 2$	25.6	24	1.4	75.2	0.34
S5	$159 \times 96 \times 2$	39.1	38.5	1.4	182.6	0.23

Table 5.1. PAD simulation size optimization.

of $41 \times 24 \times 2$ and $105 \times 60 \times 2$ lattice repeats along the $[1\,1\,1]$, $[1\,\bar{1}\,0]$ and $[1\,1\,\bar{2}]$ directions, respectively) computed by the ReaxFF potential and by equation (5.1). The range of the colour map has been set at ± 6 GPa, so that atoms under stresses exceeding that range will be displayed in dark blue and yellow, for positive and negative shear stresses, respectively. While the prediction of the stress field might seem similar in all cases, some important remarks can be made: Close to the dislocation core, σ_{xy} computed by ReaxFF is very similar for both S2 and S4 supercells, with largest stresses being close to ± 5.5 GPa. In this region, the magnitude of the stresses predicted by the isotropic elasticity theory are overestimated, due to the $1/r$ dependence of the solution. Faraway from the dislocation core, the isotropic elasticity theory is accurate and the $1/r$ dependence translates into the long range of the stress field around the dislocation. However, this is not the case in the PAD model due to the periodicity of the supercell. As can be seen from figures 5.3 and 5.4, shear stresses to the right and left of the dislocation are positive and negative, respectively. This means that at the edge of the supercell σ_{xy} will be zero because of the interaction of the dislocation with its periodic image. In other words, the positive shear stress to the right of the dislocations will interact with the negative shear stress of its periodic image to the right, cancelling each other out at half the distance between them. This can be better illustrated by computing σ_{xy} versus x with $y = 0$, as shown in figure 5.5. For the isotropic elasticity prediction (black solid line), σ_{xy} decays very slowly for $|x| > 10$ nm, levelling off at approximately 0.3 GPa. For the atomistic solutions, σ_{xy} become zero at the edge of the supercell, so that smaller supercells show significant deviations from the isotropic elasticity prediction. Let us define σ_{diff} as the difference between σ_{xy} computed by the simulations at the edge of each supercell and that computed by the theoretical solution at the same position. High values of σ_{diff} indicate large deviations of σ_{xy} between the atomistic simulations and the isotropic elasticity solution. Table 5.1 shows σ_{diff} for all the supercells. It can be seen that σ_{diff} decreases as the size of the supercell is increased: For the smallest supercell (S1), σ_{diff} is 1.71 GPa, while for the largest (S5), it is only 0.23 GPa. It is clear that σ_{diff} decreases with increasing the size of the supercell. Figure 5.5 suggests that using supercells with L_x dimensions smaller than 15 nm (7.5 nm on each side of the dislocation) is not adequate as the stress field around the dislocation is shielded due to the elastic interaction with its periodic images.

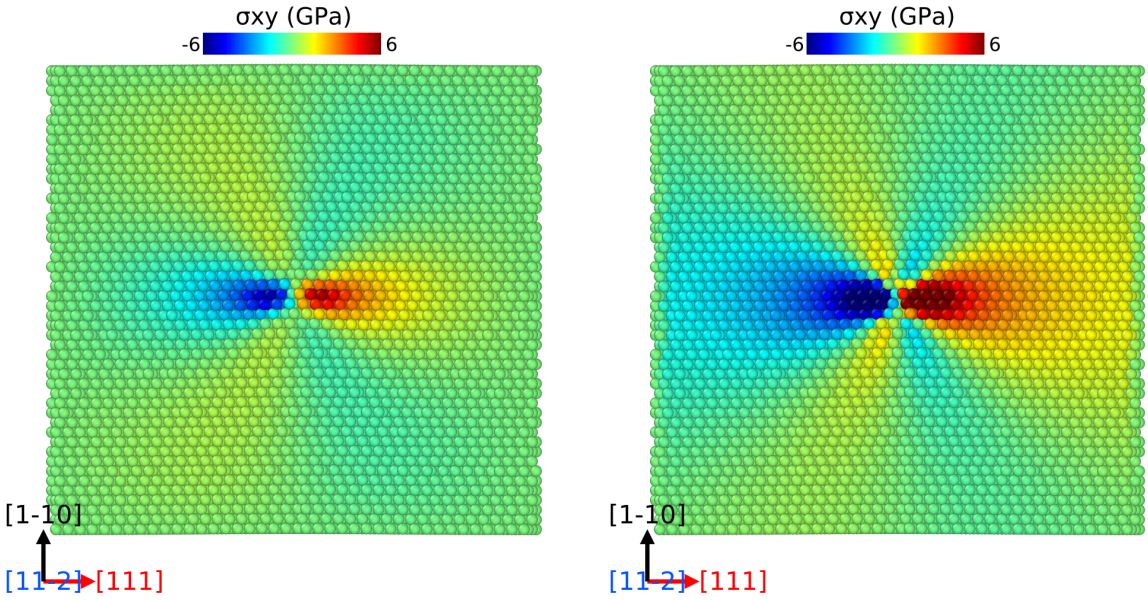

(a) ReaxFF (b) Isotropic elasticity

Figure 5.3. σ_{xy} stress field around the dislocation for the S2 supercell (see table 5.1) using a) ReaxFF potential and b) isotropic elasticity solution. For the ReaxFF prediction, atoms at the edges of the supercell have zero stress, deviating from the isotropic elasticity prediction.

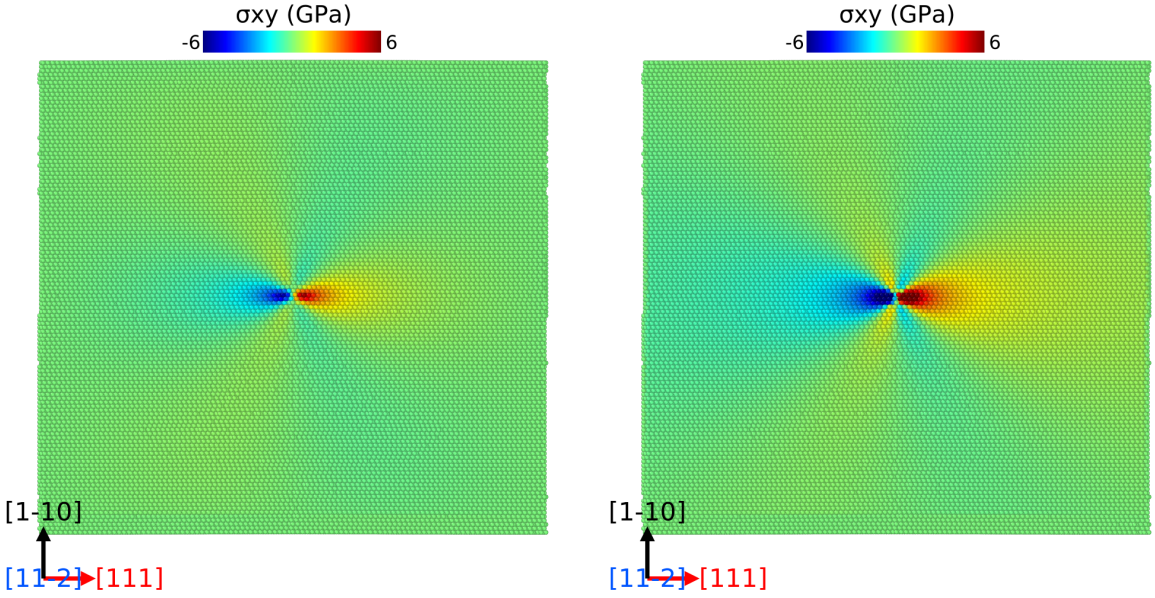

(a) ReaxFF (b) Isotropic elasticity

Figure 5.4. σ_{xy} stress field around the dislocation for the S4 supercell (see table 5.1) using a) ReaxFF potential and b) isotropic elasticity solution. For the ReaxFF prediction, atoms at the edges of the supercell have zero stress, inconsistent with the isotropic elasticity prediction. However, due to larger size of the supercell, the difference between both predictions is minor.

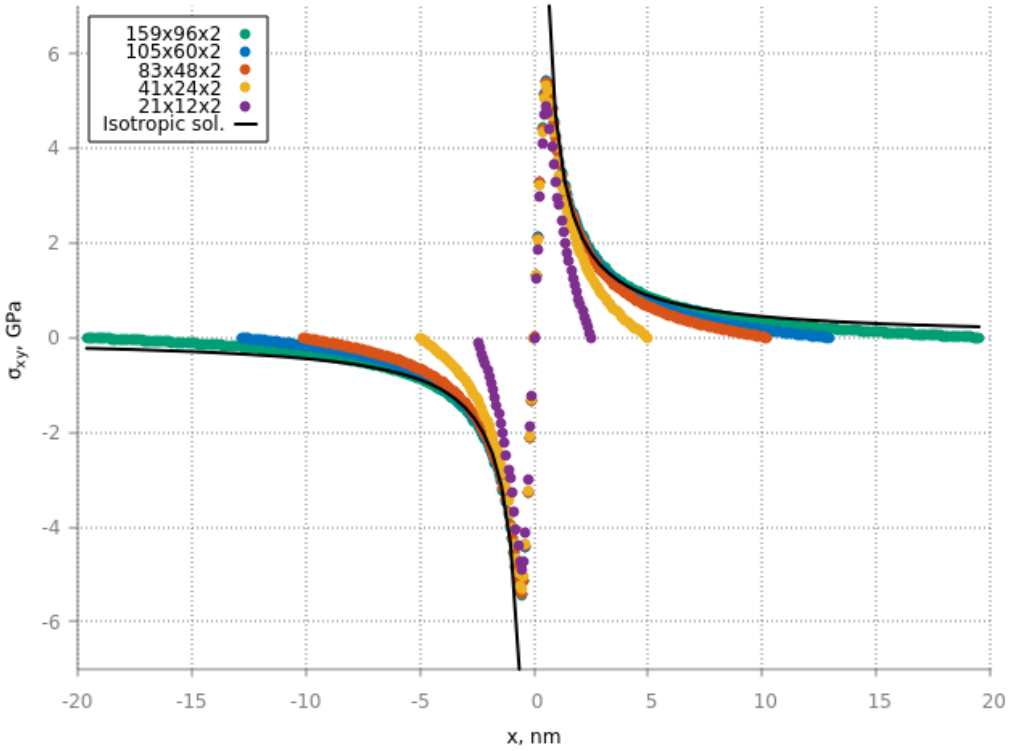

Figure 5.5. Dependence of σ_{xy} with position x along the [1 1 1] axis. The isotropic elasticity solution shows a weak decay of σ_{xy} for $\mid x \mid > 10\,\text{nm}$. For the atomistic prediction, σ_{xy} becomes zero at the edge of the supercell due to the periodicity of the supercells.

The S5 supercell shows good agreement with the isotropic elasticity solution, and would be the ideal choice should the computational resource allow it. However, the high computational cost of the ReaxFF potential used to describe interatomic forces, makes the choice of the largest supercell impractical. Furthermore, as the size of the simulation cell is increased, H diffusion requires longer times, which means that using larger size translates not only into longer times per integration step, but also into higher number of steps needed for the simulation. For those reasons, the S4 supercell, consisting of approximately 75,000 atoms was chosen for this study, as it reduces the computational requirements considerably while still keeping a good degree of accuracy. A similar behaviour was found also for the EAM prediction.

Both potentials seem to reproduce adequately basic properties of BCC Fe. A comparison of various physical properties of interest predicted by both potentials can be found in Appedix A. EAM potential predicts more accurately elastic properties. When comparing the description of the interactions of hydrogen solutes with defects, both force fields perform similarly. Depending on the property, energies are slight over or underestimated.

5.1.3 Simulation details

Once the atomic configuration and size of the supercell have been decided, testing conditions must be defined. In order to investigate the effects of H on dislocation mobility, the glide velocity of the dislocation in the presence and absence of H will be compared. Four different scenarios were tested:

1. dislocation glide in Fe,
2. dislocation glide in Fe pinned by a C atom
3. dislocation glide in Fe in the presence of H
4. dislocation glide in Fe pinned by a C atom in the presence of H.

For simulations involving hydrogen, concentrations tested ranged between 0.033 and 0.33 at.%. The PAD technique allows the dislocation glide to be driven by applying either shear stress or strain. To do that, two slabs consisting of the 8 topmost and bottommost atomic layers were used as traction, depicted as grey atoms in figure 5.1b. Lower traction atoms were fixed during the simulation while shear stress was applied to upper traction atoms.

Simulations were performed as follows. Equilibrium was achieved by relaxing the minimised supercell, so that it already contains a dislocation, using the NVT ensemble for 50 ps for the hydrogen-free supercells and until a stable configuration was achieved, as discussed in section 5.2.3, for supercells containing hydrogen. The time needed to achieve equilibrium in the supercells containing hydrogen depended upon the hydrogen concentration. This will be discussed in more detail in section 5.2.3. The temperature chosen for the simulations was 500 K in order to enhance H diffusion and reduce simulation time. The ReaxFF potential developed by Islam et. al [12] was used to describe the atomic interactions. Furthermore, embedded-atom method potentials were also used as a comparison. The EAM potential for Fe–C developed by Hepburn and Ackland [99] was used in the Fe and Fe–C simulations (scenarios 1 and 2, respectively). For Fe–H simulations (scenario 3) the EAM potential developed by Ramasubramaniam et al. [13, 14] was used. The integration step applied was 1 fs for pure Fe supercells and 0.4 fs for the rest of the supercells. After equilibrium was reached, shear stress or strain were applied to the upper traction atoms and the NVE ensemble was used to integrate the equations of motion. Simulations were run for at least 2 ns or until steady-state was achieved, e.g. dislocation gliding at constant velocity. The dislocation position was recorded over time by averaging the positions of the atoms at the core which were identified using the polyhedral template matching (PTM) [135] modifier implemented in Ovito visualization tool [136].

5.2 Results

5.2.1 Glide in pure Fe

Under applied shear stress σ_{xy}, the dislocations in pure Fe glide at a constant velocity. This can be illustrated by tracking the position of the core over time for a given applied stress. Figure 5.6 shows this for both the EAM and ReaxFF potentials under 100 MPa shear stress at 500 K. Aside from minor fluctuations, the position increases linearly and steadily over time for both potentials, suggesting that a quasi-equilibrium state has been reached. The slope of a line fitted to those plots represents the average velocity of the dislocation under that applied load and temperature. From figure 5.6, it can be seen that the predicted glide velocity of the dislocation is 371 m s^{-1} and 827 m s^{-1} for EAM and ReaxFF, respectively. The average glide velocity predicted by the latter is more than double that of the former. This behaviour is consistent over a wide range of applied shear stresses as illustrated in figure 5.7, which shows the dislocation position over time for applied shear stresses ranging from 20 to 800 MPa at 500 K.

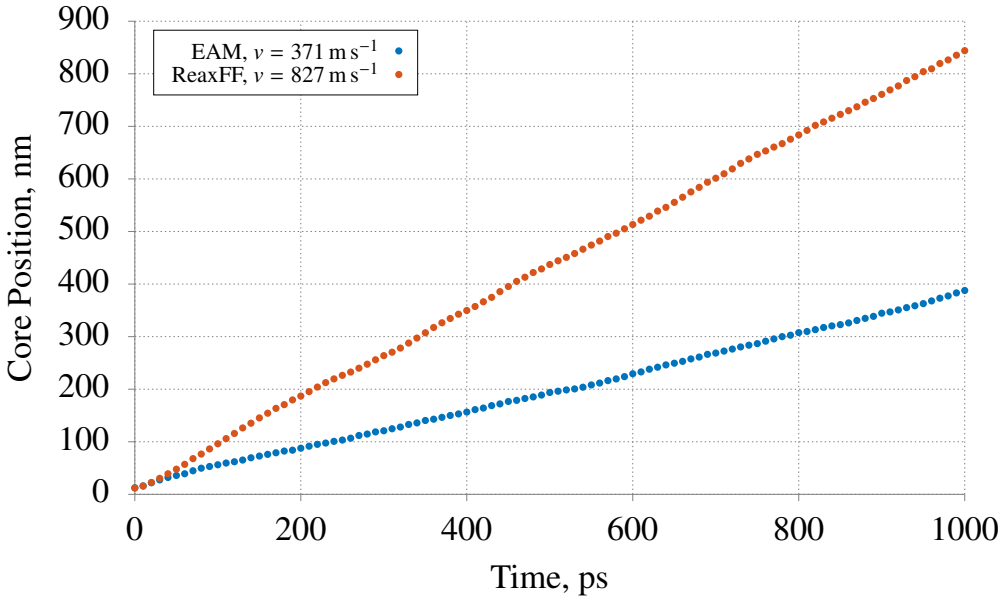

Figure 5.6. Core position versus time under 100 MPa applied shear stress at 500 K for both ReaxFF and EAM potentials.

Calculated glide velocities shown in figure 5.7 range from 99 to 1,719 m s^{-1} for EAM and range from 190 to 1,819 m s^{-1} for ReaxFF. A reduction in the applied stress results in a decrease in the calculated glide velocity. Even when applying stresses as low as 20 MPa, the dislocation core moves at a constant velocity. This fact suggests that the stress needed to initiate glide is very low, which can be attributed to the low Peierls stress and low lattice resistance of edge dislocations in BCC metals. The Peierls stress, the stress needed to initiate glide on a dislocation at 0 K, has been calculated using molecular statistics simulations as 25 MPa for an edge dislocation in Fe using an embedded-atom

method potential [75]. For the ReaxFF potential, this stress is approximately 10 MPa. The energy needed to overcome the Peierls barrier at 0 K comes exclusively in the form of mechanical work done by the applied load. However, the significant thermal assistance at 500 K allows the dislocation to overcome the Peierls barrier at stresses lower than the Peierls stress, explaining the constant glide at low stresses shown in figure 5.7.

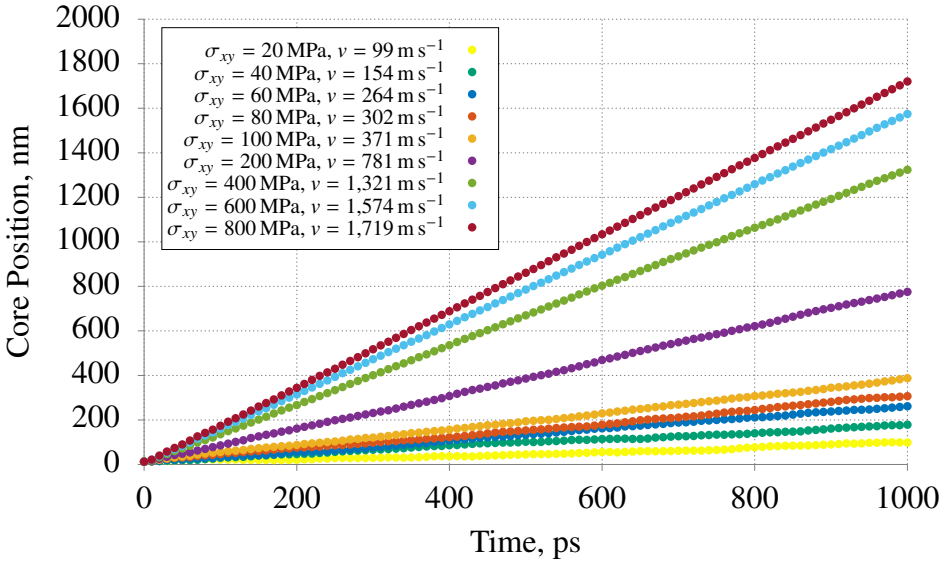

(a) EAM

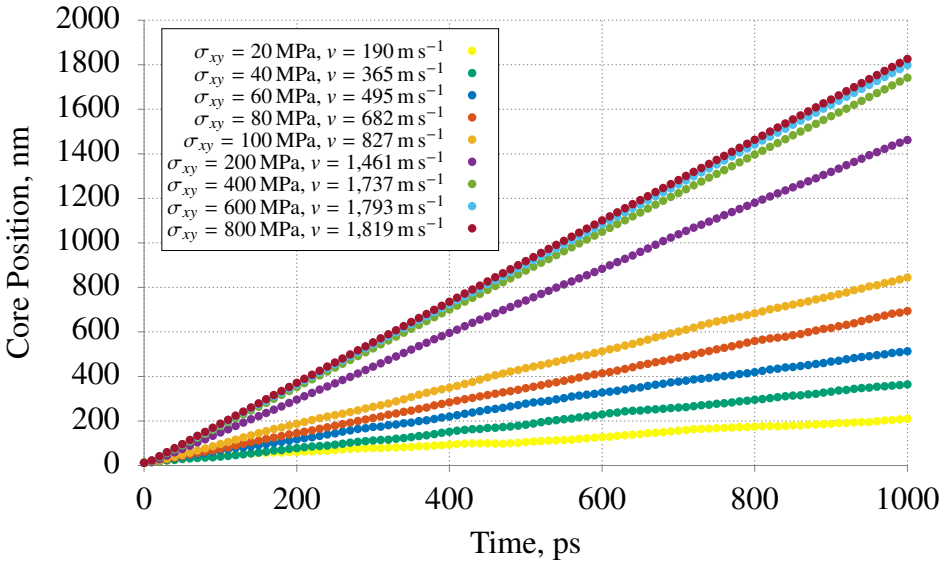

(b) ReaxFF

Figure 5.7. Core position versus time under different applied shear stress at 500 K for EAM and ReaxFF potentials.

Figure 5.7 shows that the glide velocity is proportional to the applied shear stress. The relationship between them is shown in figure 5.8. Two regimes can be distinguished: at low applied stress ($\sigma_{xy} < 400$ MPa for EAM and $\sigma_{xy} < 200$ MPa for ReaxFF), there is a linear relationship between the glide velocity and the applied stress. At high shear stresses ($\sigma_{xy} > 400$ MPa for EAM and $\sigma_{xy} > 200$ MPa for ReaxFF), the velocity begins to saturate

with increasing applied stress, converging at a value of approximately 2,000 m s^{-1}. In the lower stress regime, the movement of the dislocation follows 'viscous drag' dynamics, in which the motion is similar to that of a particle moving through a viscous medium [166]. In this regime, the velocity of the dislocation is a linear function of the applied shear stress and is described by the following equation [167]:

$$v = \frac{b}{B}\sigma_{xy} \tag{5.3}$$

where b is the magnitude of the Burgers vector and B is the drag coefficient. In the range of velocities in which equation (5.3) is valid, the drag coefficient is dominated by the interactions of the dislocation with lattice vibrations [167]. B can be obtained from the slope of the linear region of the velocity-stress plot (figure 5.8). At 500 K, the calculated drag coefficients are 6.34×10^{-5} Pa · s and 2.88×10^{-5} Pa · s for EAM and ReaxFF, respectively. Molecular dynamics simulations using EAM potentials in the literature have reported values of the viscous drag coefficient for an edge dislocation in Fe at the same temperature ranging between 3.1×10^{-5} and 3.3×10^{-5} Pa · s [168, 169]. This range is of the same order of magnitude as the drag coefficient calculated in this work.

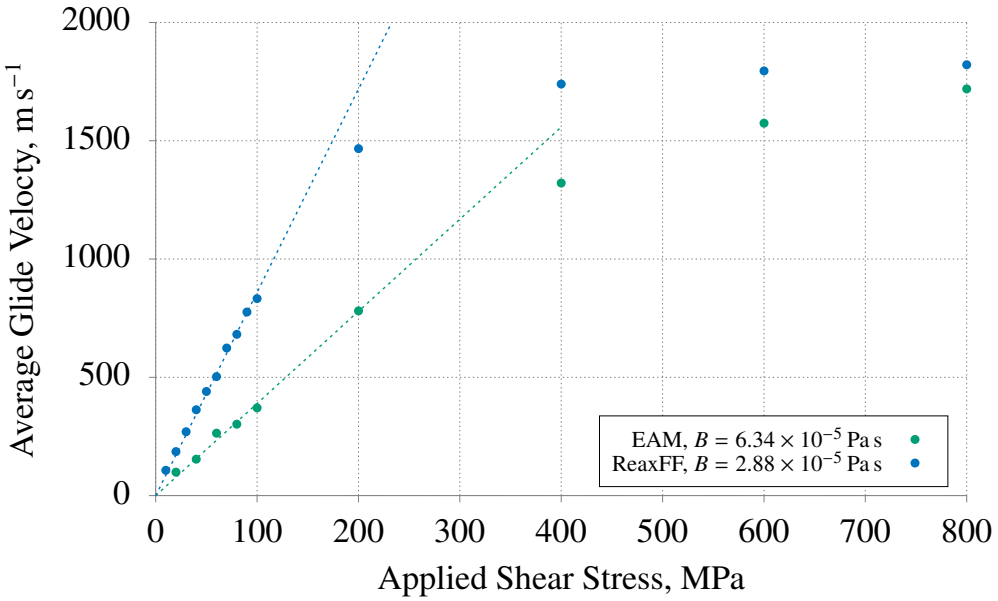

Figure 5.8. Average glide velocity as a function of the applied stress at 500 K, showing that the glide velocity increases linearly with the applied stress for stresses up to 200 100 MPa, respectively for EAM and ReaxFF.

For higher applied stresses, the average glide velocity converges to a value of approximately 1,900 m s^{-1} for the applied shear stresses tested here, as can be seen in figure 5.8. In theory, the limit for the dislocation velocity is the transverse speed of the sound in the material, around 3,200 m s^{-1} (although for these potentials it is approximately 3,800 m s^{-1}), because the energy needed to drive the dislocation becomes infinite at that speed [170]. However, it

has been reported that if created at strong stress concentrators, dislocations can nucleate in a transonic and supersonic state, since they do not have to pass through the sound barrier [171]. The behaviour of dislocations at these velocities is beyond the scope of this work.

The drag coefficient B is a function of the temperature. As mentioned earlier, the drag coefficient is dominated by interactions with lattice vibrations. These vibrations become more numerous at higher temperatures, which results in lower glide velocities as the temperature increases. This can be seen in figure 5.9, where dependence of the drag coefficient with temperature is shown. For the range of temperatures tested, the drag coefficient varies linearly with the temperature, and an equation for B as a function of the temperature can be obtained from linear regression:

$$B(T) = 6.48 \times 10^{-8} T + 3.24 \times 10^{-5} \tag{5.4}$$

for EAM, and

$$B(T) = 4.11 \times 10^{-8} T + 9.3 \times 10^{-6} \tag{5.5}$$

for ReaxFF. Where B is the drag coefficient in $\mathrm{Pa} \cdot \mathrm{s}$ and T is the temperature in K. The drag coefficients calculated in these simulations are an order of magnitude smaller than those calculated in experiments for edge dislocations in pure iron. For instance, using the pulse method, B was estimated as $3.4 \times 10^{-4}\,\mathrm{Pa} \cdot \mathrm{s}$ at 298 K [172]. This value is more than an order of magnitude larger than the one estimated from these simulations at the same temperature, $5.07 \times 10^{-5}\,\mathrm{Pa} \cdot \mathrm{s}$ and $1.92 \times 10^{-5}\,\mathrm{Pa} \cdot \mathrm{s}$, respectively for EAM and ReaxFF. However, values of the drag coefficient cannot be directly compared with experiments because, in the atomistic simulations presented here, the dislocation glides in a perfect crystal, having no impediment for its motion aside from viscous drag; consequently, drag coefficients are low. In the case of the pulse experiments, even though high purity specimens were used (total impurities: 40.6 ppm), some impurities and other defects are still present in the crystal, as the authors attributed the range of velocities observed to the 'ever present interstitial atoms' that interact strongly with dislocations in BCC metals [172]. Other obstacles such as vacancies, whose concentration is known to increase with temperature, can also lock dislocations and hinder their motion. The inability of edge dislocations to cross-slip suggests that dislocations have to rely on thermal assistance to overcome obstacles. A thermally activated motion would result in an inverse relationship between the drag coefficient and temperature as reported in those experiments. This results from the dislocation overcoming obstacles more easily at higher temperatures. This trend is opposite to what is observed in the simulations discussed in this section, suggesting that different mechanisms control the dislocation motion. In other words, the velocity measured experimentally is dominated by the contact time between

dislocation and obstacles, while that estimated from these simulations is the 'free-flight' velocity of the dislocation without obstacles.

A variety of microstructural defects can hinder dislocation motion in steels. A clear example are interstitials which bind to the dislocation core due to their elastic interaction, resulting in dislocation pinning. However, other defects such as vacancies, inclusions, other dislocations and dislocation loops can also impede dislocation motion. The effect of C interstitials, on the dislocation mobility is explored in the next section.

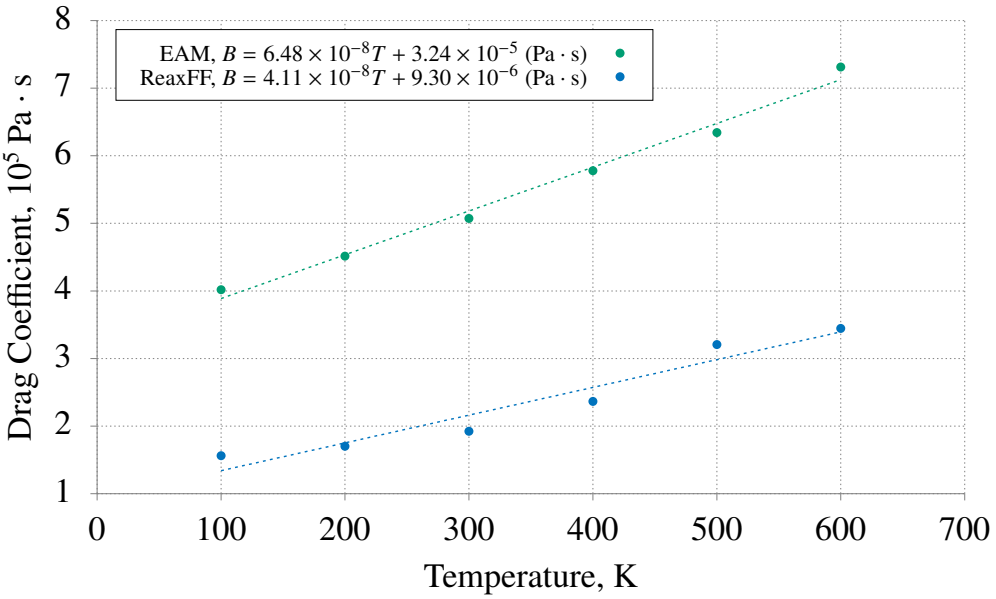

Figure 5.9. Dependence of the drag coefficient B with temperature for EAM and ReaxFF. B varies linearly with temperature in the tested temperature range, between 100 and 600 K

.

5.2.2 Glide in Fe–C

It is known that obstacles, such as interstitial atoms, hinder the movement of dislocations. Due to elastic interactions, carbon interstitials pose an energy barrier that the dislocation needs to overcome for glide to take place. This behaviour was reproduced in the simulations as the average glide velocity decreased significantly when a C interstitial was placed at the dislocation core. Figure 5.10 shows the core position over time for a dislocation with a C interstitial placed at the core. For EAM, the glide velocities were nearly 4 times lower under 200 MPa and 400 MPa of applied shear stress and 3 times higher under 600 MPa when compared with glide velocities in pure Fe supercells.

The presence of the C interstitial in the dislocation core locks the dislocation, preventing its movement. The result of applying shear stress depends on whether the forces driving dislocation motion are sufficient to overcome the energy barrier that the interstitial poses. If they are not, the dislocation will remain locked to the interstitial and glide will not take place. This is the case for the ReaxFF prediction under 200 MPa of applied shear

stress, depicted by the flat blue line in figure 5.10b. Due to the inability to cross-slip, edge dislocations cannot overcome obstacles effectively. Climb mechanisms are not operative in this temperature range, so that the thermal assistance is required for the dislocation to overcome the C interstitial.

For the simulations in which glide was observed, an established trend can be recognised. To illustrate, consider the dislocation under $\sigma_{xy} = 400\,\text{MPa}$ predicted by EAM, represented by the orange series in figure 5.10a and also presented in figure 5.10c. It can be seen that for the first 90 ps of the simulation, the dislocation remained pinned by the C interstitial, represented by the horizontal segment on the core position versus time plot. The applied stress and the thermal assistance provided enough driving force to overcome the obstacle, so that the dislocation breaks free and glides for 230 ps, passing the C interstitial several times until it becomes pinned again for approximately 60 ps. This process is repeated throughout the simulation with some fluctuations in the time the dislocation spent pinned and the time spent gliding. The resulting average glide velocity is calculated as $336\,\text{m}\,\text{s}^{-1}$, well below that calculated for the dislocation gliding in pure iron for the same potential, $1{,}321\,\text{m}\,\text{s}^{-1}$. While in pure Fe, the free-flight velocity of the dislocation is high, the average velocity of the dislocation in the presence of a C interstitial is significantly lower. This can be explained by the long contact times between the dislocation and the C atom, represented by the horizontal segments of the plots in figure 5.10. These segments vary in length due to the random nature of thermally assisted processes. Under 400 MPa of applied stress, the dislocation spends more than 60 % of the simulation pinned by the C interstitial. Furthermore, once the dislocation breaks free from the obstacle, the glide velocity calculated from the slopes of the lines fitted to the inclined segments of the plots in figure 5.10c, are $v_1 = 767\,\text{m}\,\text{s}^{-1}$ and $v_2 = 1{,}171\,\text{m}\,\text{s}^{-1}$. These velocities are lower than those calculated in pure Fe under the same loading conditions. This suggests that while the dislocation glides at seemingly constant velocity, it becomes pinned by the interstitial for short periods on every pass over the C interstitial. Some of these encounters are too short to be resolved on the graph using the chosen simulation parameters. These contact times must be shorter than 10 ps, the interval at which the core position was recorded. Figure 5.10c shows that the step controlling the dislocation motion is the contact between the dislocation and the C atom, as for the major part of the simulation the dislocation remained locked to the C interstitial.

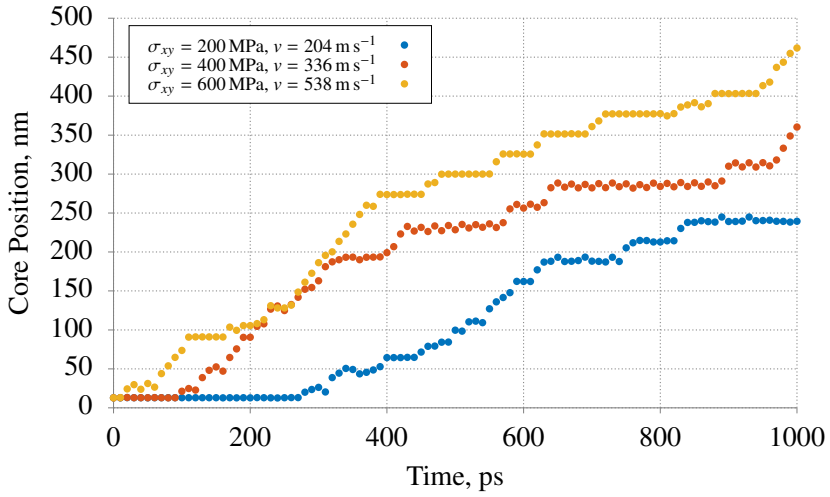

(a) EAM

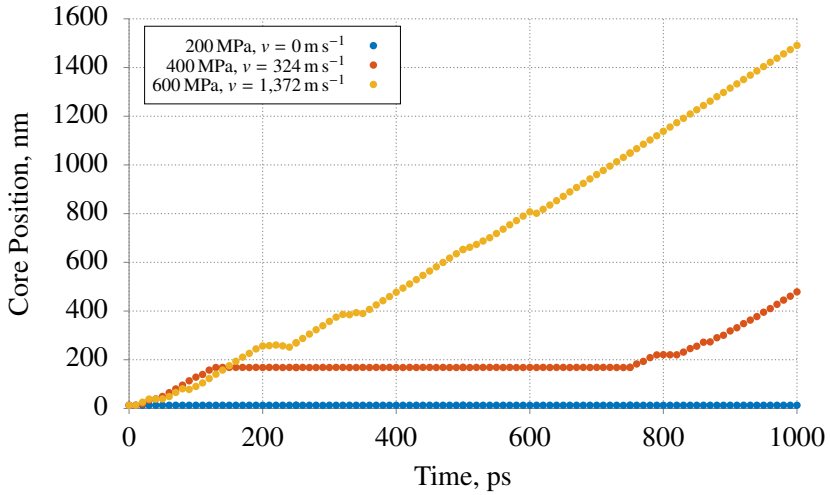

(b) ReaxFF

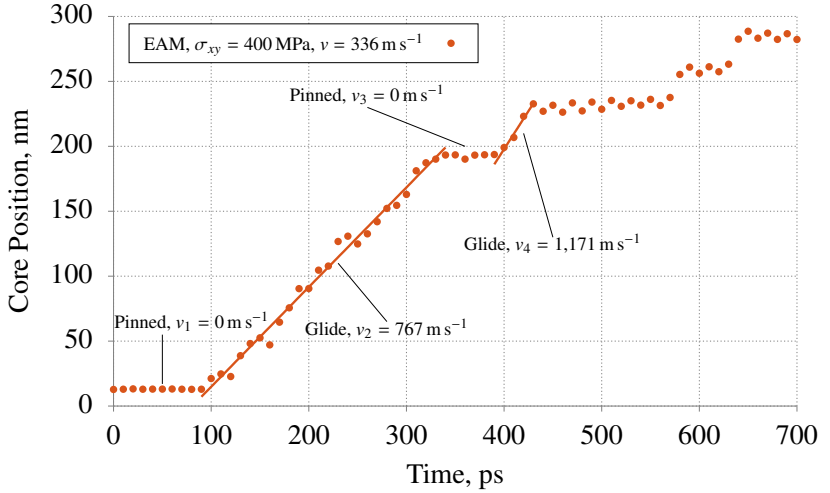

(c) EAM $\sigma_{xy} = 400\,\text{MPa}$

Figure 5.10. Core position versus time for an edge dislocation in Fe-C under different applied shear stress at 500 K using a) EAM and b) ReaxFF potentials. c) Core position versus time for $\sigma_{xy} = 400\,\text{MPa}$ using EAM potential showing that contact times between the dislocation and C interstitial limit the glide process.

Raising the applied stress to 600 MPa reduces considerably the contact times with the C interstitial, increasing the average glide velocity to 538 and 1,372 $\mathrm{m\,s^{-1}}$, for EAM and ReaxFF respectively. Dislocation-obstacle contact times are a function of the applied stress and temperature. Any obstacle poses an energy barrier that the dislocation needs to surmount in order to break free. At finite temperatures, the energy driving the dislocation comes in the form of the mechanical work resulting from the applied stress, and thermal assistance. At high applied stresses, the amount of energy provided by the former increases, reducing the thermal contribution needed to overcome the obstacle. From figures 5.10a and 5.10b, it can be seen that under 600 MPa of shear stress the dislocation spends significantly less time pinned by the C interstitial, depicted by shorter horizontal segments in the position-time plot, than under 400 MPa load.

At lower temperatures, thermal assistance is less significant and the average glide velocity is reduced because the dislocation's ability to overcome the C interstitial is affected. As a result, contact times are increased and average glide velocities reduced. This can be seen in figure 5.11a, which shows the core position versus time for different temperatures under 600 MPa of applied shear stress. It can be seen that the main effect of reducing the temperature is to increase the time the dislocation remains pinned by the C interstitial. This is depicted by increase in length of the horizontal segments in the plots. At 500 K, the dislocation spent on average 60 ps pinned by the C interstitial before gliding. This time was increased to approximately 120 ps by reducing the temperature to 300 K. Further reduction to 100 K resulted in the dislocation remaining pinned for almost the entirety of the simulation.

The effect of the temperature on the drag coefficient is presented in figure 5.11b. It can be seen that, unlike the case of dislocation motion in pure Fe, the drag coefficient decreases with temperature, suggesting that the mobility is enhanced by increasing the temperature. This behaviour is consistent with the pulse experiments reported in the literature on high purity Fe [172], discussed in the previous section. In fact, the drag coefficient at 300 K was calculated from the simulations as $B = 4.49 \times 10^{-4}\,\mathrm{Pa \cdot s}$ and $B = 3.21 \times 10^{-4}\,\mathrm{Pa \cdot s}$ for EAM and ReaxFF, respectively. These values are close to the experimental one of $3.4 \times 10^{-4}\,\mathrm{Pa \cdot s}$ [172]. This evidence supports the claim that the dislocation mobility reported in experiments are dominated by the contact times between the dislocation and any obstacle it encounters as it glides. The C content of the supercells used in this simulations, 13 ppm, was comparable to the impurity content reported in the pulse experiments, 43 ppm.

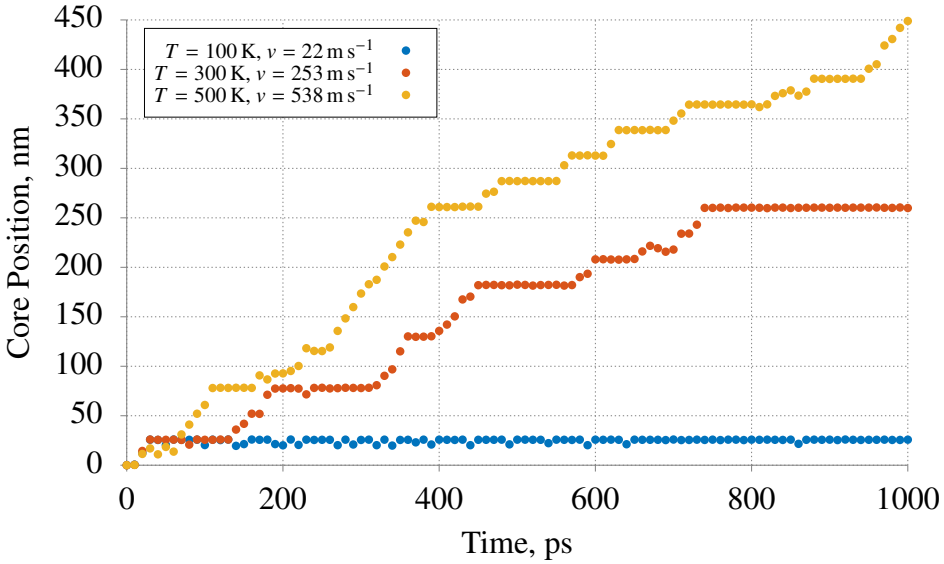

(a)

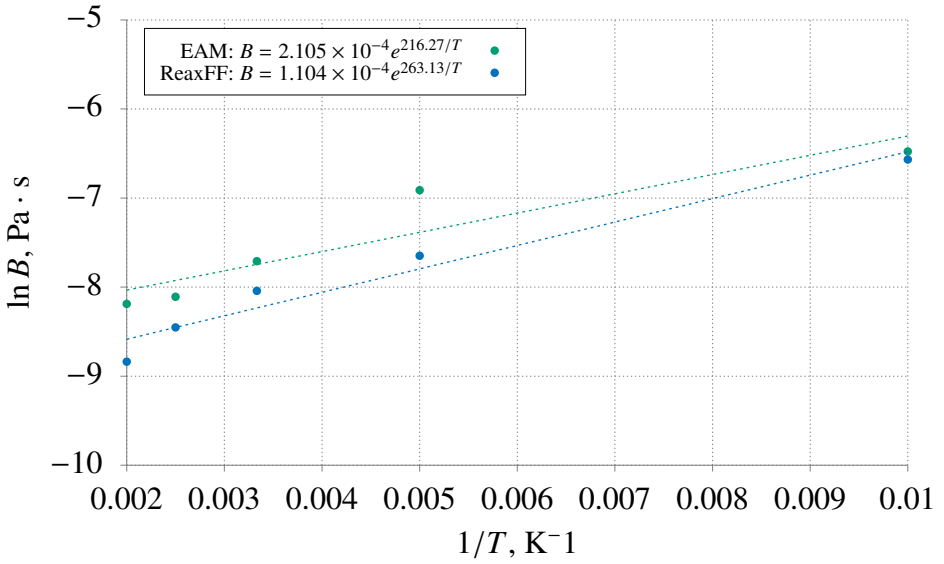

(b)

Figure 5.11. a) Core position versus time for an edge dislocation in Fe-C under $\sigma_{xy} = 600\,\text{MPa}$ for different temperatures using EAM potential. b) Effect of the temperature in the drag coefficient.

5.2.3 Glide in Fe–H

In order to evaluate the effect of H on mobility of dislocations, it is necessary to apply shear stress to an equilibrium configuration of the dislocation in the presence of H solutes. Equilibrium was achieved by introducing H atoms to the PAD supercell and performing a relaxation at the target temperature. The number of H atoms inserted in the simulations was 25, 50, 100 and 250, corresponding to far-field concentrations C_0 of 0.033, 0.066, 0.133 and 0.33 at.%, respectively. At the beginning of the simulations, H solutes were inserted randomly, and a minimisation of the potential energy places them at the most favourable sites in the lattice, e.g. tetrahedral interstitial sites. A relaxation at 500 K allows H atoms

to diffuse to the dislocation core, whose tensile stress field provides a strong driving force for H migration, forming Cottrell atmospheres [80].

At equilibrium, the number of atoms arriving at the core should balance that of those leaving it, and the total should remain constant or fluctuate around a constant value. Figure 5.12a shows the number of H atoms at the dislocation core per unit length of dislocation line, N_{H}/L_Z, predicted by the EAM potential. It can be seen that with a concentration $C_0 = 0.33\,\mathrm{at.\%}$, equilibrium is reached within 10 ns of relaxation as the number of H atoms present at the dislocation core fluctuates around 25 atoms/nm of dislocation length[2]. Longer relaxation times have no appreciable effect on the number of H atoms bound to the dislocation. When $C_0 = 0.133\,\mathrm{at.\%}$, the number of H atoms at the dislocation core converges after 5 ns of relaxation, at around 11 atoms/nm. Similarly, at lower concentrations, $C_0 = 0.066\,\mathrm{at.\%}$ and $C_0 = 0.033\,\mathrm{at.\%}$ equilibrium is reached within 3 ns with 6 and 4 atoms/nm, respectively. Figure 5.12a suggests that the relaxation time needed depends on the concentration C_0, with longer times needed for higher concentrations.

This trend is also observed using the ReaxFF potential. However, the time needed for equilibrium at the highest concentration was considerably larger than when using the EAM potential. As shown in figure 5.12b, at $C_0 = 0.33\,\mathrm{at.\%}$, it takes approximately 22 ns for the number of H atoms at the dislocation core to reach a stable value. The number of atoms at the dislocation core converges at approximately 70 atoms/nm, almost double that using EAM, which partially explains the longer relaxation time needed to reach equilibrium.

[2]The core of edge dislocations in BCC Fe shows moderate spreading in the glide plane and its radius has been reported as $3b$, where $b = 0.74\,\mathrm{nm}$ [75]; thus, H atoms within that distance are considered to be bound to the core.

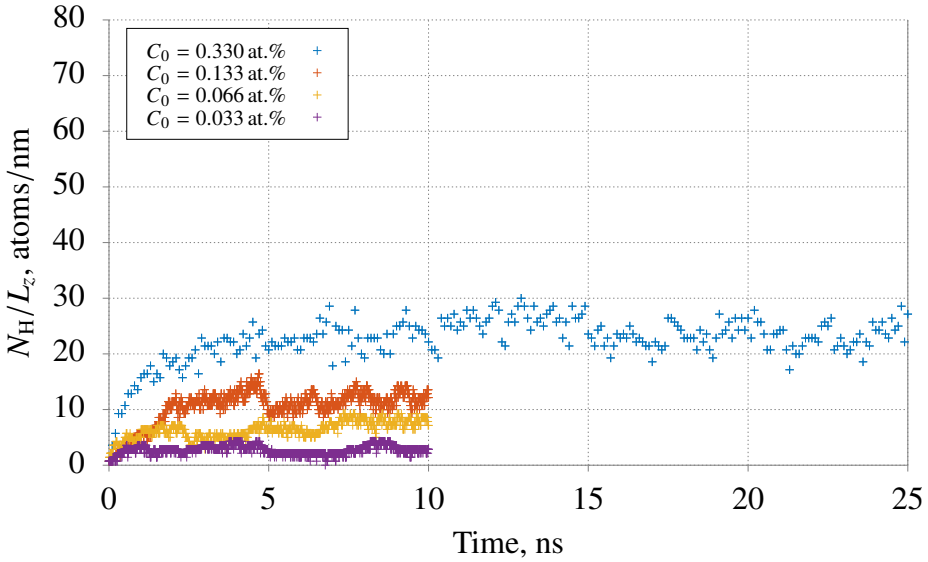

(a) EAM

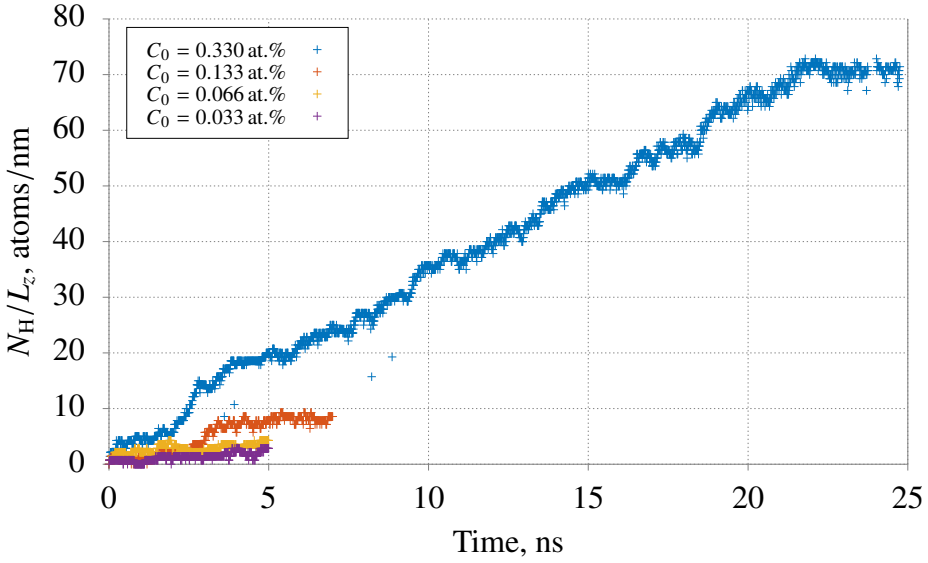

(b) ReaxFF

Figure 5.12. Number of H atoms at the dislocation core per unit length of dislocation line, N_H/Lz, for a) EAM and b) ReaxFF. N_H/Lz plateaus at equilibrium.

For supercells at the highest concentrations, Cottrell clouds form as a result of the H migration in the tensile stress field of the edge dislocation. This process can be observed in figure 5.13. Initially, hydrogen solutes are randomly distributed through the supercell, and the dislocation core is practically free of H solutes. As the relaxation continues, the high temperature facilitates the diffusion of H atoms to the dislocation core. Having a positive misfit volume, H atoms are attracted to the tensile side of the edge dislocation, in this case the inferior side. While both potentials show this, there is a noticeable difference in the distribution H atoms adopt around the dislocation core. For EAM, H atoms aggregate diagonally, forming approximately 45° angles with the slip plane, as seen in figure 5.13b. While this H aggregation occurs asymmetrically, with a pronounced aggregation at either left or right of the dislocation line, it is likely that this is the consequence of the constant

jumps of the dislocation line that results from the significant thermal assistance at 500 K. At times, an inverted V-shaped pattern is recognised, which is consistent with the 'double hump' pattern reported with some Fe-H EAM potentials [173]. For the ReaxFF potential (figures 5.13c and 5.13d), the aggregation to the dislocation core is compact and no 'double hump' pattern is observed. The predicted stress field around the dislocation is nearly identical for both potentials, differing only quantitatively. This suggests that the different H aggregation behaviour predicted by these two potentials arises from a difference in the description of the H-H interactions. A similar behaviour was observed in the supercells containing H solutes and a C interstitial at the dislocation core.

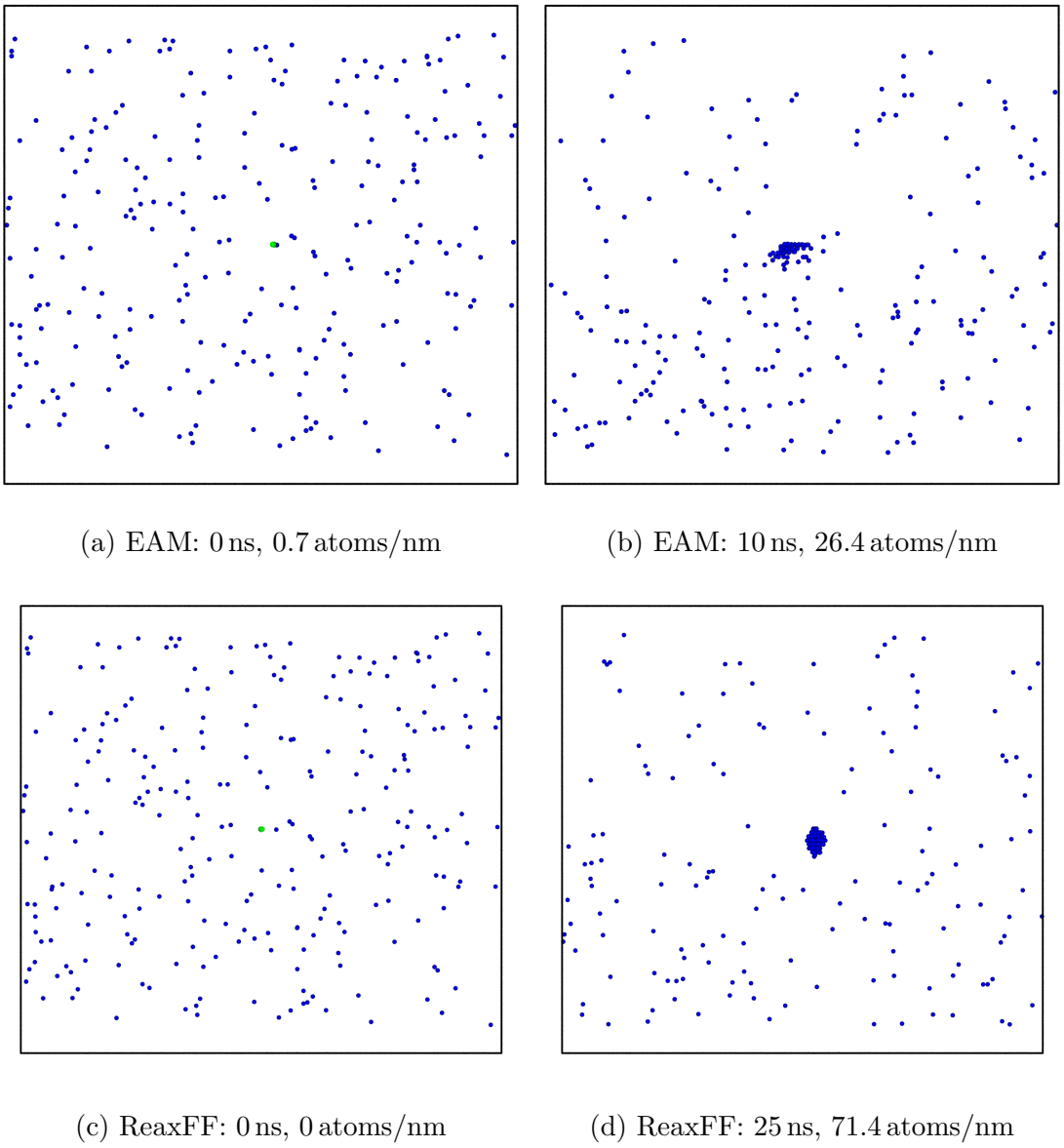

(a) EAM: 0 ns, 0.7 atoms/nm (b) EAM: 10 ns, 26.4 atoms/nm

(c) ReaxFF: 0 ns, 0 atoms/nm (d) ReaxFF: 25 ns, 71.4 atoms/nm

Figure 5.13. Hydrogen diffusion to dislocation core: a) and c) hydrogen solutes are initially distributed randomly through the supercell. b) and d) Hydrogen atoms aggregate to the dislocation core, forming highly concentrated Cottrell clouds.

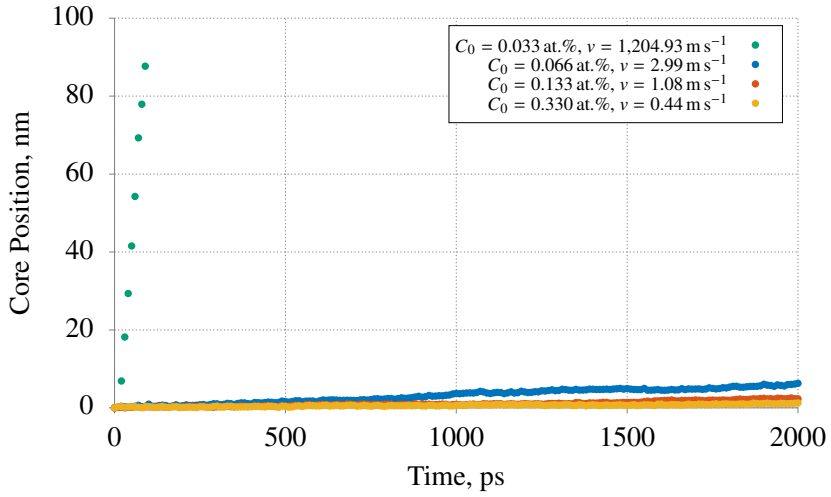

(a) EAM

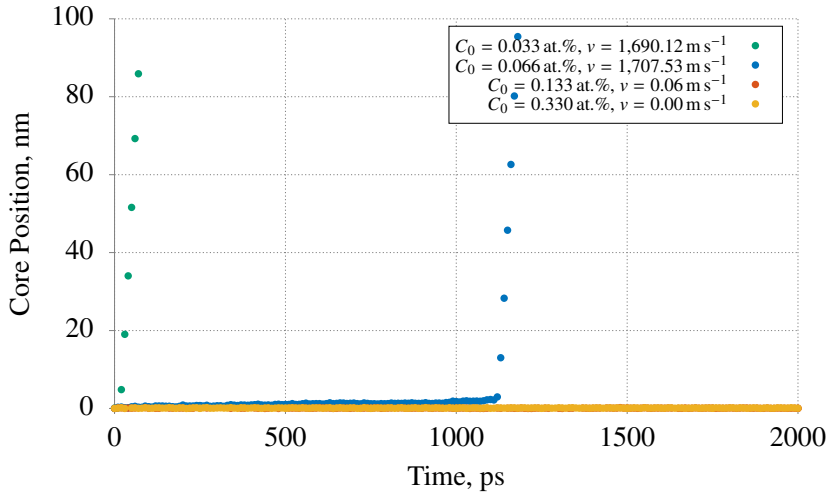

(b) ReaxFF

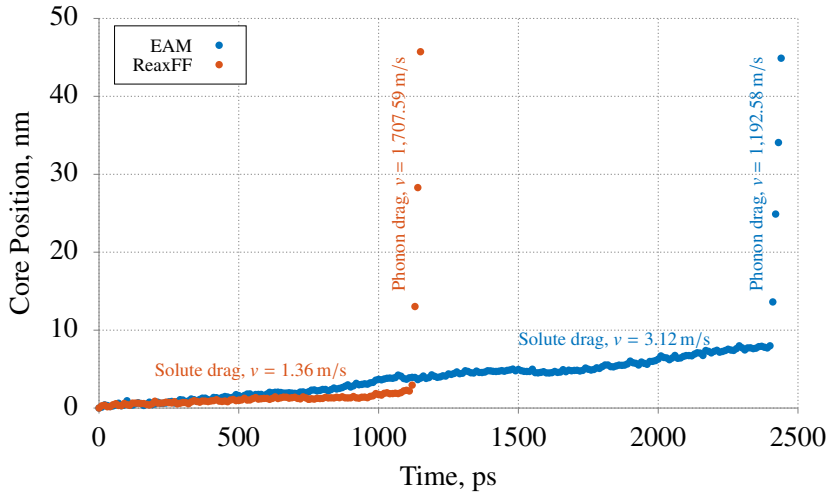

(c) $C_0 = 0.066$ at.%

Figure 5.14. (a) and b) Core position versus time for different H concentrations C_0, for $\sigma_{xy} = 350$ MPa. c) Core position versus time for $C_0 = 0.066$ at.% showing a slow and a fast glide regimes, with the transition between them occurring at $t \approx 2{,}400$ ps and $t \approx 1{,}100$ ps, for EAM and ReaxFF, respectively.

Applying shear stress to the Fe-H supercells resulted in dislocation glide. However, calculated glide velocities at a given applied shear stress are significantly lower than those in the absence of H solutes. Figure 5.14 shows the dislocation core position over time for different far-field H concentrations, C_0, under 350 MPa of applied shear stress predicted by EAM and ReaxFF. It can be seen that at the lowest concentration tested, $C_0 = 0.033$ at.%, the glide velocity is as high as that calculated for pure Fe, approximately 1,200 and 1,700 $\mathrm{m\,s^{-1}}$, respectively for EAM and ReaxFF. At the higher concentrations, $C_0 = 0.133$ at.% and $C_0 = 0.33$ at.%, the calculated glide velocities are 1.08 and 0.44 $\mathrm{m\,s^{-1}}$ for EAM and 0.06 and 0 $\mathrm{m\,s^{-1}}$ for ReaxFF. These velocities are three orders of magnitude lower than those seen at lower H concentrations and in pure Fe, which suggests that a different mechanism dominates the glide process.

Two different slopes can be seen in the core position versus time plot for $C_0 = 0.066$ at.% predicted by ReaxFF (blue series in figure 5.14b), and were also observed in the EAM prediction for that concentration. These two plots are shown in figure 5.14c. The two different slopes are indicative of a period of the simulation in which the dislocation glides at low speed, followed by another in which it glides more rapidly, under the same applied stress and far-field H concentration. From figure 5.14c, it can be seen that for the first 2,400 ps (for EAM) and 1,100 ps (for ReaxFF), the dislocation glides at a low velocity, 3.12 and 1.36 $\mathrm{m\,s^{-1}}$, for EAM and ReaxFF, respectively. Then the dislocation suddenly accelerates, gliding at 1192 and 1,707 $\mathrm{m\,s^{-1}}$, respectively for EAM and ReaxFF. It is evident that the high-velocity regime depicted by the steeper slopes correspond to free-flight velocities and that dislocation motion is dominated by phonon drag (section 5.2.1), as the calculated velocities are consistent with those observed in pure Fe. The low-speed regime, on the other hand, is not that obvious. From figures 5.14a and 5.14b, it can be seen that increasing the H concentration of the supercell shifts the dislocation motion from the fast phonon drag regime to a much slower motion, as the glide velocity was reduced several orders of magnitude by increasing C_0 from 0.033 to 0.133 at.%. Furthermore, in the low-speed regime, the glide velocity decreases as the H concentration is increased; increasing C_0 from 0.066 to 0.133 at.% led to a reduction of the calculated glide velocities from 3.12 to 1.08 $\mathrm{m\,s^{-1}}$ and from 1.36 to 0.06 $\mathrm{m\,s^{-1}}$, respectively for EAM and ReaxFF.

These traits are indicative of the solute drag mechanism, in which dislocation motion is controlled by the diffusion of the solutes. Solute atoms exert a drag force on the gliding dislocation because when the dislocation moves, the solute atmosphere is no longer in the lowest energy position. If the force driving dislocation motion is lower than this drag force (in the absence of thermal activation), the dislocation will not be able to break free from the solute atmosphere and motion can only occur by dragging the solute atoms, a process controlled by diffusion. For a dislocation gliding at low speed in the presence of (non-core) solute atoms, the relationship between the glide velocity and the shear stress needed to sustain the motion is given by [170]

$$\sigma_{xy} = \frac{vC_0\beta^2}{DbkT} \ln \frac{R}{r_0} \tag{5.6}$$

where σ_{xy} is the applied shear stress, v is the glide velocity, C_0 is the far-field solute concentration, β is a material parameter describing the interaction between the solute and the dislocation, D is the bulk diffusion coefficient, k is the Boltzmann constant, T is the temperature, R is the distance between dislocations and r_0 is a cut-off radius for the dislocation core. Since all the terms in equation (5.6) aside from σ_{xy} and v are constant, a linear relationship between v and σ_{xy} is predicted at low glide velocities. Furthermore, equation (5.6) also shows that the far-field concentration C_0 is inversely proportional to the glide velocity. These features are observed in the plots shown in figure 5.14 and can be more clearly seen by plotting the glide velocity in the solute drag regime as a function of the applied stress, as shown in figure 5.15. For both potentials the drag coefficient B is several orders of magnitude larger in Fe-H than it is in pure Fe (at 500 K, $B = 2.93 \times 10^{-5}$ Pa s for EAM and $B = 6.52 \times 10^{-5}$ Pa s for ReaxFF). This marked difference supports the idea that two different mechanisms control the glide process; in pure Fe, B is controlled by phonon drag while in Fe-H B is control by solute drag. Moreover, figure 5.15 shows a linear relationship between B and C_0, as increasing C_0 an order of magnitude resulted in a similar increment in B, in agreement with equation (5.6).

The dependence of the drag coefficient on the far-field hydrogen concentration is shown in figure 5.16. For the ReaxFF prediction at the highest concentration, $C_0 = 0.33$ at.%, glide did not take place even under applied shear stresses as high as 1,500 MPa, as illustrated by the horizontal yellow line in figure 5.15b. This was the result of a highly concentrated H cloud pinning the dislocation and impeding dislocation motion. For this reason, that data point was not included in figure 5.16. For the rest of the simulations, the drag coefficient varied linearly with the concentration and is described by equations

$$B = 0.477C_0 - 6.715 \times 10^{-5}, \quad 0.033 \leq C_0 \leq 0.33 \,(\text{at.}\%) \tag{5.7}$$

for EAM, and

$$B = 1.238C_0 - 3.509 \times 10^{-2}, \quad 0.033 \leq C_0 \leq 0.133 \,(\text{at.}\%) \tag{5.8}$$

for ReaxFF. Where B is the drag coefficient in Pa·s, and C_0 is the far-field H concentration in at.%. While the drag coefficients given by equations (5.7) and (5.8) are quantitatively different, they predict qualitatively the same outcome: reduced dislocation motion due to solute drag. Reduced dislocation motion can be interpreted as a form of hardening caused by H charging as has been in reported in the literature [54].

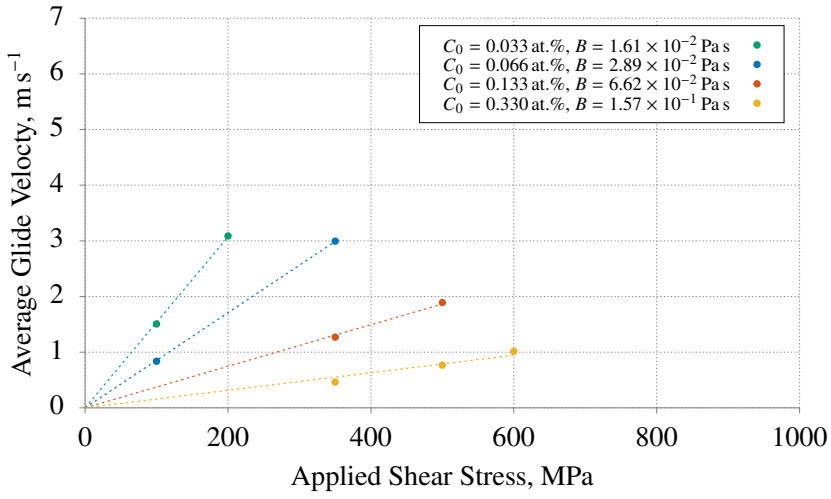

(a) EAM

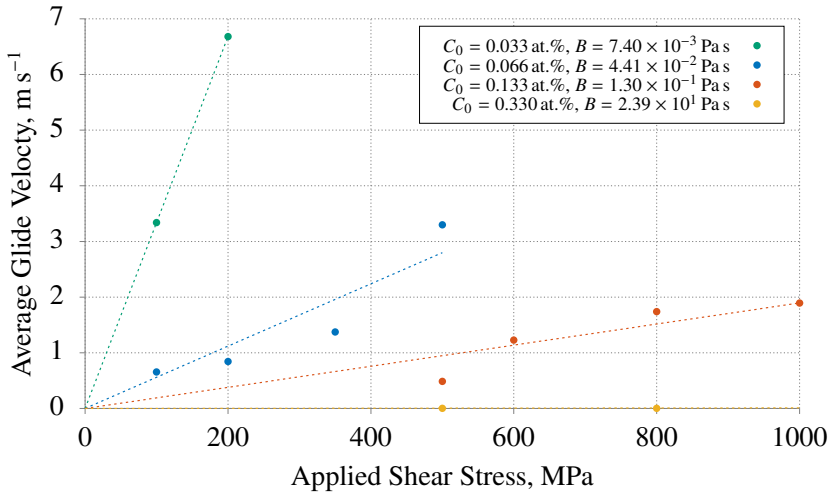

(b) ReaxFF

Figure 5.15. Dependance of the glide velocity with applied shear stress in the solute drag regime for EAM and ReaxFF.

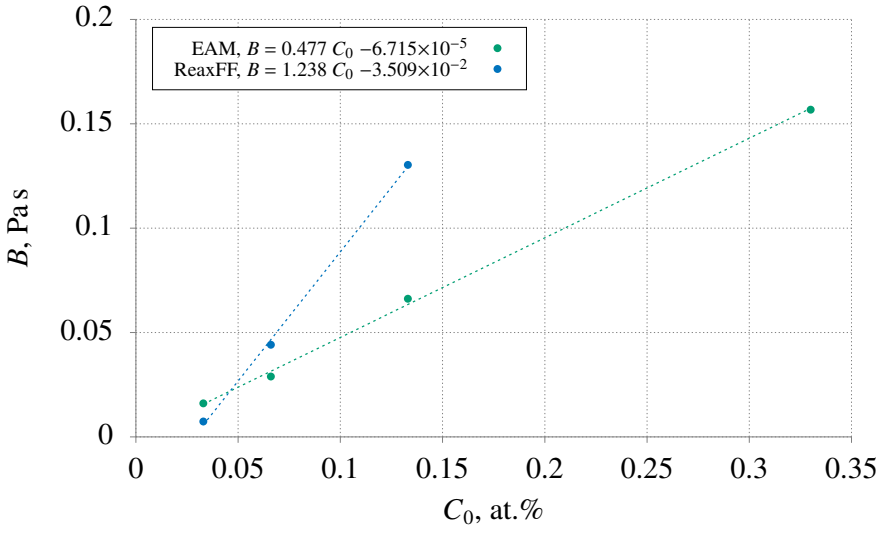

Figure 5.16. Variation of the drag coefficient B with the far-field H concentration C_0.

Snapshots of the glide process, presented in figure 5.17, confirm the presence of the two different glide mechanisms discussed earlier. The glide plane normal, the $[1\,1\,\overline{0}]$ direction, is shown perpendicular to the plane of the page and the glide direction, the $[1\,1\,1]$ direction, from left to right. The dislocation line and H atoms are displayed in green and blue, respectively, and Fe atoms have been removed from the visualisation. At the beginning of the simulation the dislocation line, whose initial position is $x = 14.59\,\text{nm}$, is surrounded by a number of H atoms forming Cottrell clouds, as shown in figure 5.17a. The concentrated solute atmosphere locks the dislocation due to the attractive nature of the solute-dislocation interactions, and opposes dislocation movement. As the simulation progresses, the applied shear stress drives the dislocation forward, and thermal fluctuations help a portion of the dislocation line to overcome the opposing force, as can be seen in figure 5.17b. This configuration is energetically unfavourable as the dislocation strain energy increases with longer dislocation lines, which results in the portion of the dislocation line left behind catching up the rest. This process is similar to the kink-pair nucleation mechanism [174] in which two kinks are formed to overcome the Peierls barrier. At 500 K, H diffusion is fast enough for H solutes to diffuse to the dislocation core and establish the lock again, resulting in the configuration presented in figure 5.17c. Further advance of the dislocation line takes places by repeating this process and corresponds to the slow-speed regime discussed before. Diffusion does not seem occur at a high enough rate to match the dislocation glide, so that after 1,060 ps the number of H atoms at the dislocation core is considerably lower that it was at the beginning of the simulation, as can be seen in figure 5.17d. The significant thermal assistance allows the dislocation to overcome the depleted H cloud and to break free (figure 5.17e). The dislocation then glides to the end of the supercell and is reinserted on the left-hand side due to the periodic boundary conditions for the simulation, as shown in figure 5.17f. Free from the H solute atmosphere, the dislocation glides at velocities comparable to those calculated in the pure iron simulations as there is little impediment to dislocation motion, suggesting that the viscous drag mechanism is operative. The snapshots presented in figure 5.17 show that the motion of edge dislocations in the presence of H solutes is dominated by solute drag (figures 5.17a to 5.17d) at high H concentrations and by viscous drag (figure 5.17f) at low H concentrations.

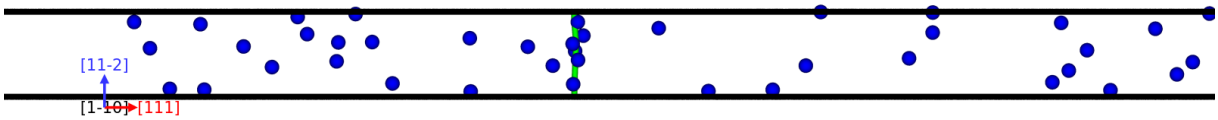

(a) $t = 0\,\text{ps}$, $x = 14.59\,\text{nm}$

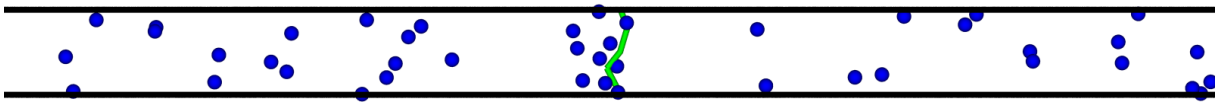

(b) $t = 200\,\text{ps}$, $x = 15.46\,\text{nm}$

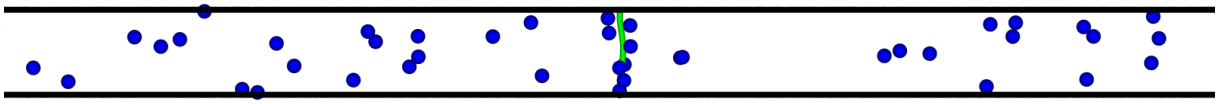

(c) $t = 400\,\text{ps}$, $x = 15.50\,\text{nm}$

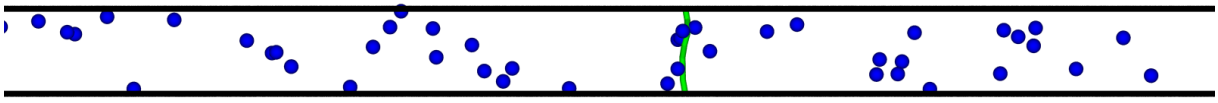

(d) $t = 1{,}060\,\text{ps}$, $x = 16.49\,\text{nm}$

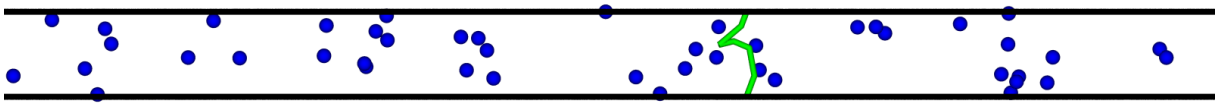

(e) $t = 1{,}120\,\text{ps}$, $x = 17.53\,\text{nm}$

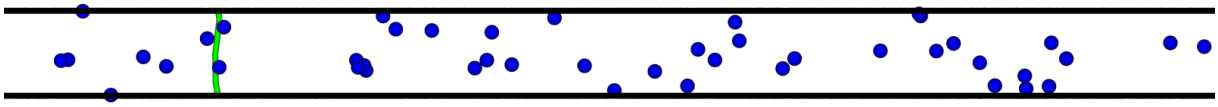

(f) $t = 1{,}150\,\text{ps}$, $x = 28.75\,\text{nm}$

Figure 5.17. Snapshots of the glide process for an edge dislocation in the presence of H solutes. Two regimes can be seen: solute drag (a-d) and free-flight glide (f). The dislocation line and H atoms are displayed in green and blue, respectively. Fe atoms have been removed from the visualisation.

5.2.4 Glide in Fe-C-H

Dislocation mobility was severely reduced by the presence of H atoms when the dislocation was initially pinned by a C interstitial. If compared with the glide in the Fe-C scenario (section 5.2.2), the average glide velocity was consistently lower when H atoms were present. In many cases, the dislocation did not glide and remained pinned to the C interstitial for the entirety of the simulation. For instance, when applying 600 MPa of shear stress to the supercell with the lowest H concentration tested (0.033 at.%), the dislocation was unable to overcome the C interstitial. Even when applying this level of stress for 5 ns, dislocation glide was not observed. On the other hand, the dislocation

glided readily in the H-free supercell with an average glide velocity of 1,520 m s^{-1} under the same applied load. This reduction in mobility resulting from the addition of H solutes is shown in figure 5.18a. Higher applied stresses were needed for dislocation glide when H was present. At this concentration, 700 MPa were sufficient to overcome the C interstitial, resulting in an average glide velocity of 905 m s^{-1}. Once the dislocation breaks free from the C interstitial, glide occurs in a similar manner to that of glide in absence of H: the dislocation becomes pinned by the C atom for a brief period every time it passes over the C interstitial and the average glide velocity is mostly dependent on the contact times of the dislocation with the C atom. The H atmosphere is dissolved once the dislocation glides fast enough for H solutes to keep up, which explains why, as it occurs in the absence of H solutes, the C-dislocation contact times dominate the glide process. Furthermore, because 700 MPa is sufficient to overcome the H cloud, increasing the applied stress has a similar effect to that of the H-free scenario, that is, the average glide velocity is increased due to the reduction the contact times of the dislocation and the C interstitial. This behaviour is shown in figure 5.18b.

The stress at which the dislocation becomes unpinned by the C interstitial increases with the H concentration. Figure 5.19 shows the core position versus time for the different concentrations tested and at the lowest stress under which glide was observed within 1 ns of simulation (except for $C_0 = 0$ at.%, which is shown at 600 MPa). As discussed previously, when hydrogen is not present in the supercell, the C interstitial poses little resistance to dislocation glide, so that under 600 MPa of applied shear stress the dislocation glides readily. When 0.033 at.% of H solutes were present in the supercell, the stress needed to initiate glide was 700 MPa. This value was increased to 1,200 MPa by increasing the H concentration to 0.066 at.%. Furthermore, with a H concentration of 0.133 at.%, 1,800 MPa was needed for the dislocation to break free from the C interstitial. Finally, at the highest concentration, 0.33 at.%, no glide was observed under applied shear stresses as high as 2,000 MPa. While glide is certainly possible under these conditions, it would require longer simulation times due to the random nature of thermally assisted processes. The time scale needed to capture this process seems to be beyond the current computational resource available.

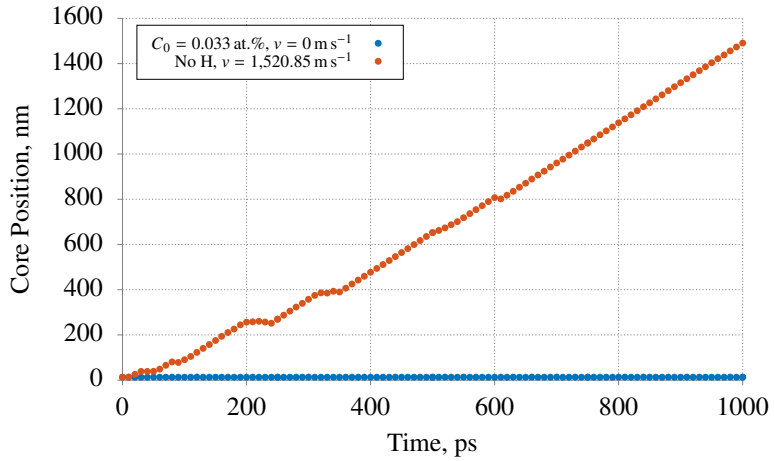

(a)

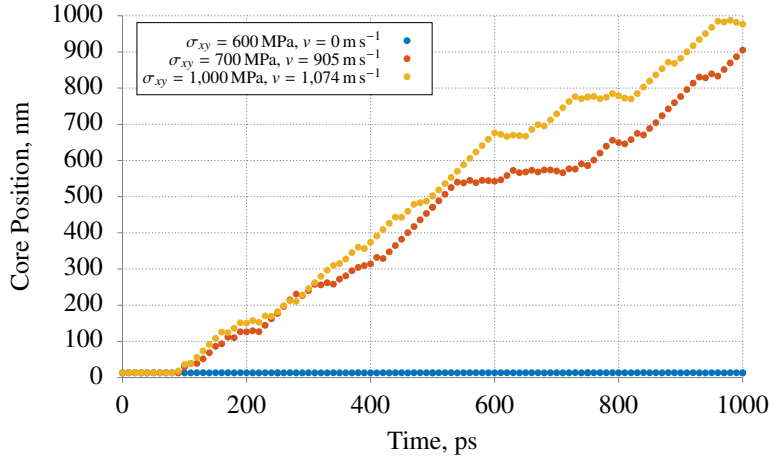

(b)

Figure 5.18. Effect of adding 0.033 at.% of H on the mobility of an edge dislocation pinned by a C interstitial. a) Dislocation glide is prevented by the presence of hydrogen solutes, when applying 600 MPa of shear stress. b) The average glide velocity increases with the applied shear stress.

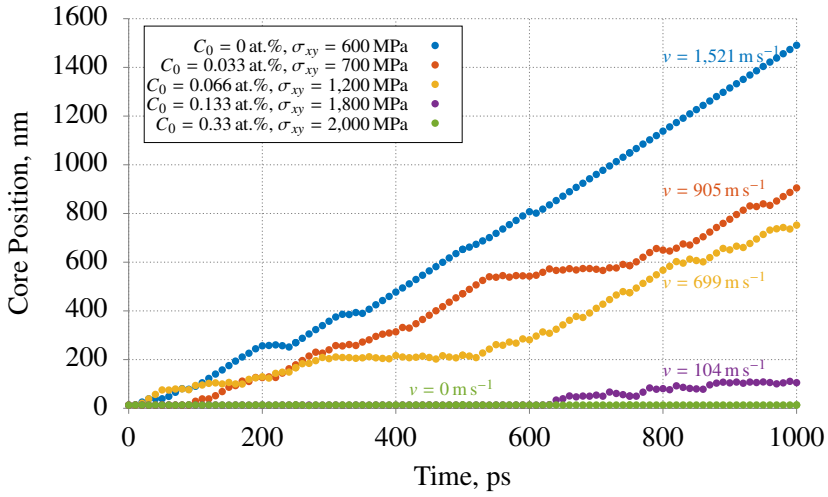

Figure 5.19. Effect of the H concentration on the glide stress and mobility when a C interstitial is present. Increasing the H concentration leads to higher required stresses to overcome the C interstitial and lower average glide velocities.

The observed reduction of the dislocation mobility is likely to be caused by the interaction between the H-cloud and the C interstitial. The presence of these obstacles alone, while detrimental to dislocation mobility, has a considerably smaller impact on mobility than when acting in synergy with H solutes. To illustrate, consider the motion of a dislocation under the same applied load in the presence of these three defects, namely, a C interstitial, a H cloud and both of them simultaneously, as shown in figure 5.20. It can be seen that under these simulation conditions, glide occurs when either of these defects are present but not when both of them are. When surrounded by the H cloud, the dislocation can glide at a constant velocity under solute drag conditions. However, when both H solutes and the C interstitial are present, glide is impeded. While solute drag can also be possible with C atoms, its diffusion in Fe is several orders of magnitude slower than that of H [175, 176]. This suggests that dislocation motion in the Fe-C-H scenario will be significantly slower and would require timescales in the order of microseconds to be captured by simulation. For this reason, a drag coefficient could not be calculated as it was done in sections 5.2.1, 5.2.2 and 5.2.3. Figures 5.18 to 5.20 suggest that hydrogen is unlikely to facilitate the movement of edge dislocations through a field of obstacles. Conversely, the presence of H solutes reduces the ability of the dislocation to overcome the C interstitial, as the stress needed for glide to be observed increases with the H concentration.

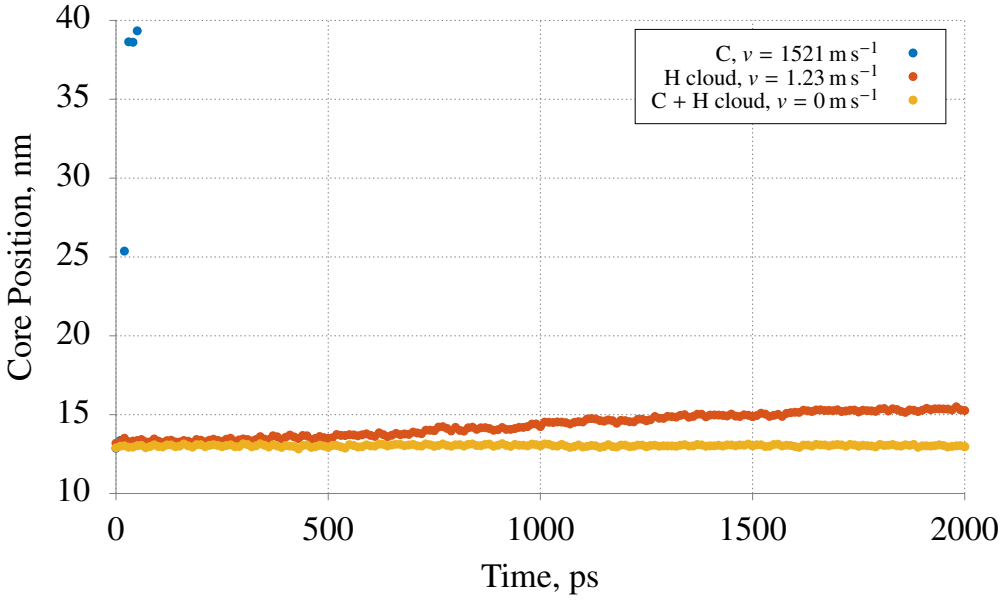

Figure 5.20. Core position versus time under 600 MPa of applied shear stress for a dislocation pinned by a C interstitial (C), a cloud of solute H atoms (H cloud) and both of them (C + H cloud).

The mechanism through which the dislocation overcomes the C interstitial in the presence of hydrogen is similar to that found in the absence of H. In both cases, the dislocation initially consists of a practically straight segment with the C interstitial sitting in the middle of the dislocation line. When H solutes are present, they sit along the entire length of the dislocation line, as shown in figures 5.21a and 5.22a. For the H-free scenario, the

dislocation commences its motion finding as its main opposition the drag force caused by the C interstitial, effectively pinning a portion of the dislocation line. Due to the applied stress, the dislocation line bows out, so that there is a line tension acting against the increase of curvature of the dislocation line. If the combination of applied stress and thermal assistance is large enough to overcome these forces, the dislocation is able to overcome the C interstitial and glide freely until it encounters the C atom again. Otherwise, the dislocation will remain pinned to the C interstitial for the rest of simulation. When H is present, the glide process is similar, however, the presence of H produces extra drag force due to solute drag. Furthermore, as can be seen in figure 5.22b, H solutes, initially distributed somewhat evenly at both sides of the C interstitial, seem to diffuse asymmetrically along the dislocation line when it bows out and prefer to sit at one side of the C interstitial. This leads to the formation of a H-rich portion of the dislocation line. This small H cluster could pose extra resistance to dislocation motion, contributing to the increase in glide stress and reduction of average glide velocity when both C and H solutes are present in the supercell. The formation of hydrogen clusters in a bowing dislocation have been predicted theoretically and through atomistic simulation [24, 177].

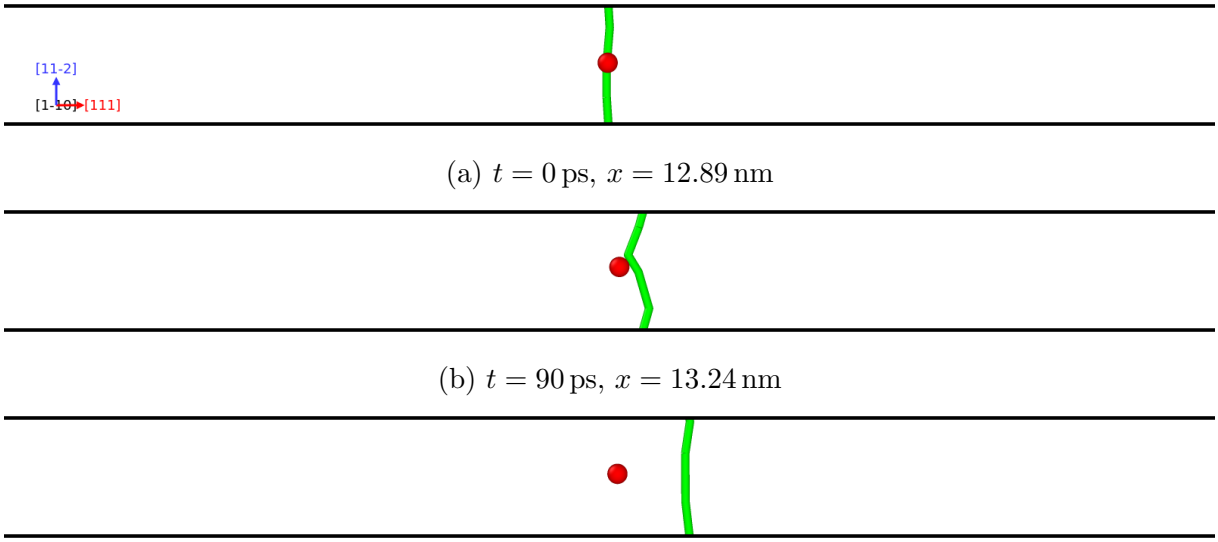

(a) $t = 0\,\text{ps}$, $x = 12.89\,\text{nm}$

(b) $t = 90\,\text{ps}$, $x = 13.24\,\text{nm}$

(c) $t = 100\,\text{ps}$, $x = 13.82\,\text{nm}$

Figure 5.21. Snapshots of the glide process for an edge dislocation initially pinned by a C interstitial under 400 MPa of applied shear stress. a) Initially, the C interstitial sits in the middle of the straight dislocation line. b) Under applied stress, the dislocation bows out as the C interstitial pins a segment of the dislocation. c) The applied stress and the thermal assistance are sufficient to overcome the drag posed by the C interstitial.

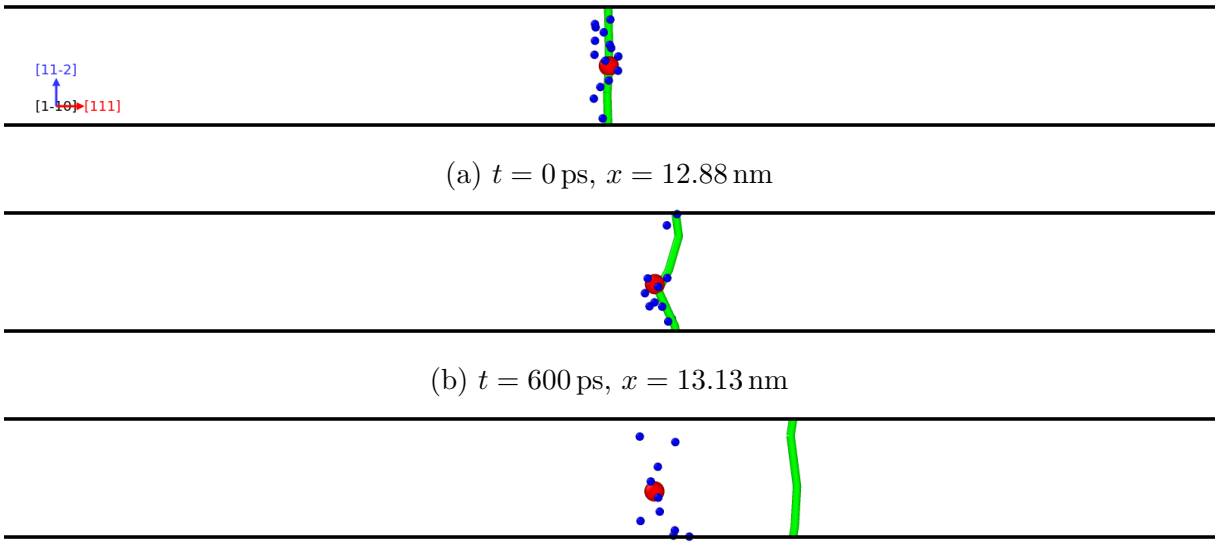

(a) $t = 0\,\text{ps}$, $x = 12.88\,\text{nm}$

(b) $t = 600\,\text{ps}$, $x = 13.13\,\text{nm}$

(c) $t = 630\,\text{ps}$, $x = 15.08\,\text{nm}$

Figure 5.22. Snapshots of the glide process for an edge dislocation initially pinned by a C interstitial in the presence of H solutes under 1,700 MPa of applied shear stress. a) Initially, H atoms are distributed along the straight dislocation line. b) Under stress, the dislocation bows out and H solutes accumulate at one side of the C interstitial. c) The applied stress and the thermal assistance are sufficient to overcome the drag posed by the C and H solutes.

5.3 Discussion

5.3.1 H aggregation to the dislocation core

H atoms, initially distributed randomly throughout the supercell, are attracted to the dislocation core due to the elastic interaction with the tensile stress field, resulting in the formation of a highly dense H cloud. While this was reproduced by both EAM and ReaxFF potentials, as shown in figure 5.13, there is a visible difference in the hydrogen distribution. As discussed in section 5.2.3, an inverted 'V- shaped' pattern can be distinguished at times, and this is consistent with the 'double hump' pattern reported in other EAM potentials [173]. The hydrogen cloud in the ReaxFF prediction is considerably more compact than that of EAM; it is formed by more H atoms and it is less spread out. A possible explanation for this could be that given by Cui et al. [173]. They studied the equilibrium H distribution around an edge dislocation using Grand Canonical Monte Carlo (GCMC) simulations and Density Functional Theory (DFT) calculations. In their work, they concluded that is the strong H-H interactions, particularly from the 3rd and 4th nearest neighbour on octahedral sites, which dominate the growth of the cluster, as opposed to the elastic interaction of the H atoms with the dislocation pressure field. This was supported by DFT as well as Molecular Statistics (MS) calculations of the binding energies for different H-H pairs, showing very strong attractive interactions between a H atom and its 3rd nearest neighbour in a octahedral site (3NNOS) and its 4th nearest

neighbour in a octahedral site (4NNOS)[3]. These interactions are also present in the EAM potential used in this work. As discussed by Cui et al. [173], if the growth of the cluster takes place by the incorporation of the 3NNOS, the cluster would grow tridimensionally on any of the 8 equivalent $\langle 1\,1\,1 \rangle$ directions, explaining the appearance of the 'double hump pattern'. Similar examination of the binding energies of H-H pairs using the ReaxFF potential reveals strong attraction not only with the 3rd and 4th nearest octahedral neighbours but also with the 2nd. The binding energies were found to be 0.19, 0.28 and 0.27 eV, for 2NNOS, 3NNOS and 4NNOS, respectively. For other octahedral pairs, the binding energies were found to be negative. If the H atoms are incorporated via the 2NNOS and 3NNOS, the H cluster will grow in $\langle 1\,1\,0 \rangle$ and $\langle 1\,1\,1 \rangle$ directions, suggesting that tridimensional growth is also possible. Furthermore, it also means that the possible lattice sites available for incorporating H atoms are doubled, as there are 8 each of 2NNOS and 3NNOS for a given octahedral site. This would explain the higher density of the H cloud in the ReaxFF prediction when compared to that of EAM. Examination of the interatomic distances of the H atoms in the H cloud that forms in the dislocation shown in figure 5.13d reveals that H atoms occupy 2nd and 3rd nearest neighbouring sites.

The number of H atoms taking part in the H cloud at the dislocation core differs between both potentials, with the ReaxFF potential having nearly double the number of atoms than EAM. This noticeable difference can be explained by looking into the H clustering process. As discussed by Hou et al. [180, 181], there is a critical H concentration under which spontaneous cluster growth (self-clustering) is possible and its value depends the nature of the H-H interactions of the cluster. For instance, for a cluster consisting of a $(1\,1\,0)$ monolayer constructed by repeatedly incorporating 3NNOS, the critical H concentration has been reported as 34 appm at 300 K [173]. This value is expected to increase with temperature, as the entropic effect favouring the dissociation of H atoms from the cluster becomes significant at higher temperatures. For the temperature used in our simulations, the critical H concentration for the same type of cluster corresponds to 2,079 appm. The H concentrations used in the simulations presented here ranged from 332 to 3,320 appm and self-clustering was only observed in the supercells with the highest concentration, which is just above the critical value. The cluster growth was mild in the case of the EAM prediction, which is expected as H concentration around the H cluster quickly falls below the critical value due to the H depletion of the supercell. For ReaxFF, the strong 2NNOS binding energy suggests that the H critical concentration predicted by this potential is lower than that of EAM. Self clustering is possible when the average binding energy of the H cluster with a hydrogen atom is large enough to overcome entropy effects favouring dissociation. Because the average binding energy increases with the size of the H cluster, there is a critical cluster size ('critical nucleus size' as referred to by Hou

[3]While it is known that in perfect body-centred cubic Fe, hydrogen dissolves into tetrahedral sites, the trapping preference can be changed to octahedral sites under shear strain [178, 179]. Shear stresses, as high as 5 GPa, can be found around the dislocation core, as shown in figure 5.5, supporting the idea that H aggregation takes place via the occupation of octahedral nearest neighbours.

et al. [180]) at which self clustering can take place. The strong attractive interactions of a H atom and its 2NNOS are likely to increase the rate at which the average binding energy increases with the cluster size so that the critical size (and critical H concentration) for self clustering is reduced. As a result, the H cluster in the ReaxFF prediction can continue to grow for longer and larger than that of EAM before it depletes of H atoms, as depicted in figure 5.12b. The strong attraction between a H atom and its 2NNOS is in disagreement with DFT calculations [173], which show that only the 3NNOS and 4NNOS are attractive pairs.

5.3.2 Effect of H solutes on dislocation-C interactions

The main effect of introducing H to the supercell containing a dislocation pinned by a C interstitial is the increase in the minimum glide stress and reduction of the average glide velocity, as shown by figure 5.19. This behaviour is an indication of hydrogen-induced hardening which conflicts the HELP theory. For softening to occur, H solutes should reduce the stress needed to unpin the dislocation from the C interstitial, which would require that the interaction energy of the dislocation with the C-H complex be lower than with the C interstitial. The interaction energy could be reduced if the misfit volume of the C-H complex is lower than that of the C interstitial alone, which depends on whether H atoms bind to the C interstitial at the dislocation core. Simulations presented in this work suggest that this is not the case. Furthermore, similar behaviour is found for C-H complexes in fcc Ni [151]. DFT calculations indicate that the interaction energy of C and H in Ni is repulsive and that their change in misfit volume is negligible, suggesting that H is unlikely to cause softening via the modification of the pinning behaviour in dislocations. Nevertheless, it is possible that in bcc Fe, C and H have an attractive interaction when both of them occupy octahedral sites. As discussed before, H solutes could sit in octahedral interstitial under shear stress, and this scenario has not been investigated. The increase of mobility via the reduction of the misfit volume could be viable for other point defects, such as vacancies, as they form stable complexes with H and the presence of H solutes can ease the formation of vacancies [182, 183].

Another possible factor preventing softening via the modification of dislocation-obstacle interactions is what happens when a dislocation bows out when pinned in the presence of H solutes. Theoretical formulations and atomistic simulations suggests that presence of H solutes on a bowing dislocation results in the formation of secondary pinning points consisting of H clusters [24, 177]. When pinned, a $\frac{1}{2}[1\,1\,1](1\,\bar{1}\,0)$ dislocation in bcc Fe bows out asymmetrically, consisting of a 70° and 45° segments that are connected via an intermediate edge segment. H diffusion along the dislocation line is not uniform, as H atoms can diffuse more easily along the 70° segment while diffusion along the 45° segment is difficult. This causes a local increase in the concentration of H atoms along the dislocation line which results in the formation of a cluster that acts as an additional pinning point. This mechanism is consistent with the increase in the stress needed for

dislocation glide shown in figure 5.19 and with the self-clustering discussed in the previous subsection.

5.4 Conclusions

The following conclusions can be drawn from the simulations of dislocation glide using the periodic array of dislocation (PAD) model.

In the absence of hydrogen:

- For pure Fe, dislocation glide obeyed viscous drag dynamics. In this regime, the velocity was proportional to the applied stress. The measured velocity corresponded to the free-flight of the dislocation as there was little resistance to dislocation motion, which came from lattice vibrations. Phonon drag increases with temperature as lattice vibrations are more numerous, which resulted in lower velocity. The variation of the drag coefficient with temperature could be described by $B(T) = 6.48\times10^{-8}T + 3.24\times10^{-5}$ and $B(T) = 4.11\times10^{-8}T + 9.3\times10^{-5}$, respectively for EAM and ReaxFF.
- In the presence of a C interstitial, average glide velocities were significantly lower than those in pure Fe. Dislocation motion was controlled by contact times between the dislocation and the C atom, a thermally assisted process. Unlike glide in pure Fe, increasing the temperature resulted in more thermal assistance for the dislocation to overcome the C interstitial, which led to reduced contact times and higher average velocities. The variation of the drag coefficient with temperature was given by $B(T) = -3.22 \times 10^{-6}T + 1.68 \times 10^{-9}$ and $B(T) = -2.78 \times 10^{-6} + 1.35 \times 10^{-3}$, respectively for EAM and ReaxFF.

In the presence of H solutes:

- The presence of hydrogen solutes had a significant impact on the glide velocity. At high enough H concentrations, Cottrell clouds at the dislocation core formed, hindering its mobility. In these conditions, dislocation glide was significantly slower than that in pure Fe and was controlled by solute drag, the drag force resulting from the recursive pinning and unpinning of H solutes as the dislocation moves. In the solute drag regime, dislocation glide is limited by the diffusion of the H solutes. Consequently, increasing the H concentration resulted in greater drag on the moving dislocation. The relationship between the drag coefficient and the H concentration is $B(C_0) = 0.48C_0 - 6.71 \times 10^{-5}$ and $B(C_0) = 1.24C_0 - 3.51 \times 10^{-2}$, respectively for EAM and ReaxFF.
- In the presence of a C interstitial and H solutes, dislocation mobility was prevented. The reduction in mobility was attributed to the combined pinning effects of the C and H solutes. Solute drag was not observed as C has limited diffusivity in Fe under the conditions tested, which locked the dislocation. Dislocation motion was

only possible when the dislocation became unpinned from the C interstitial, which required higher shear stresses when H solutes were present.

These simulations suggest that it is unlikely that hydrogen enhances dislocation glide. On the contrary, hydrogen greatly reduced glide velocity and increased dislocation–C interstitial contact times.

Chapter 6

Hydrogen Effects on Fracture

Since it was first identified by Johnson in the late 18th century [2], great effort has been devoted to a better understanding of the detrimental effect of hydrogen in metals and alloys. Yet, the mechanisms by which hydrogen embrittles most metallic materials remain unclear. Some of the models most often cited to rationalise experimental observations of hydrogen embrittlement of steel are Hydrogen Enhanced Decohesion (HEDE) [3, 4, 43], Hydrogen Enhanced Localised Plasticity (HELP) [5, 6, 53] and Adsorption Induced Dislocation Emission [8, 18, 62]. The HEDE model proposes that hydrogen reduces the cohesive strength of the lattice so that cleavage fracture can occur at lower stress than in absence of hydrogen. HEDE is usually quoted to explain hydrogen embrittlement failure with featureless fracture surfaces [25, 49, 50]. The HELP model attributes the weakening effect of hydrogen to increased localised plasticity occurring ahead of the crack tip which results in subcritical crack growth. HELP is used to explain ductile hydrogen related failure; dimpled fracture surfaces and extensive slip bands are usually considered an indication that the HELP mechanism is operative [26, 184].

For HEDE and HELP, diffusion of hydrogen to regions ahead of the crack tip is required. Hydrogen aggregation in sufficient quantities is needed to achieve a significant cohesive strength reduction for HEDE, and localised plasticity for HELP. While it is clear that hydrogen embrittlement occurs extensively when hydrogen can diffuse readily, hydrogen damage has also been observed in conditions where diffusion is limited. For instance, under conditions where the crack velocity is high compared with the diffusion coefficient of hydrogen, subcritical crack growth with ductile features has been reported [8, 62]. These observations suggest that a different mechanism might be operative.

The AIDE mechanism is less commonly referred to when explaining hydrogen embrittlement phenomena compared with HEDE and HELP. It proposes that the role of hydrogen is to facilitate the emission of dislocations from the crack tip in slip planes oriented favourably for crack growth [8, 18, 62]. Unlike the two mechanisms described above, AIDE proposes that hydrogen adsorbed on the crack surfaces, as opposed to hydrogen

absorbed into the bulk, is responsible for the enhanced crack growth.

These 3 mechanisms have supporting and contradictory evidence, and it is possible that they operate under different conditions with possible overlaps e.g. HEDE and HELP might be operative at higher diffusible hydrogen concentrations and AIDE when most hydrogen is found on the crack surfaces. Unfortunately, there are no techniques allowing direct observation of hydrogen and atomic scale crack tip events in bulk materials, so that identifying crack tip conditions in which each of these mechanisms may operate is difficult.

Molecular dynamics simulations offer the possibility to elucidate the deformation events occurring at the atomic scale that cannot be studied otherwise. The crack tip can be examined using identification algorithms that reveal microstructural defects in regions around the crack tip. Based on the evolution of the crack tip events, the viability of the mechanisms described above can be evaluated. In this chapter, fracture simulations of an atomically sharp crack have been performed to study the role of hydrogen in the fracture process of Fe.

6.1 K-Controlled Fracture

In K-controlled simulations, the goal is to study the fracture behaviour in the region near the crack tip, in which stresses and strains are only a function of the stress intensity factor K. The value of K at which crack extension takes place is a measure of the fracture toughness. To illustrate this simulation approach, consider an edge crack in an isotropic linear elastic solid with the origin centred at the crack tip, as shown in Fig. 6.1. General solutions for the stress field anywhere in the body can be found in the literature [185–188]. For a semi-infinite crack as the one shown in Fig. 6.1, the stresses are given by

$$\sigma_{ij} = \frac{K}{\sqrt{2\pi r}} f_{ij}\left(\theta\right) + \sum_{m=0}^{\infty} A_m r^{\frac{m}{2}} h_{ij}^{(m)}\left(\theta\right) \tag{6.1}$$

where K is the stress intensity factor and f_{ij} is a dimensionless function of the θ in the leading term. A_m is the amplitude for the mth term and h_{ij} is a dimensionless function of θ. The higher order terms depend on geometry and define the stresses far away from the crack tip, where $r \to \infty$. Close to the crack tip, as $r \to 0$, the leading term tends to infinity while the other terms remain finite or approach zero. Sufficiently close to the crack tip, the stresses are given by [189] (for mode I loading):

$$\sigma_{xx} = \frac{K_{\mathrm{I}}}{\sqrt{2\pi r}} \cos\left(\frac{\theta}{2}\right)\left[1 - \sin\left(\frac{\theta}{2}\right)\sin\left(\frac{3\theta}{2}\right)\right] \tag{6.2}$$

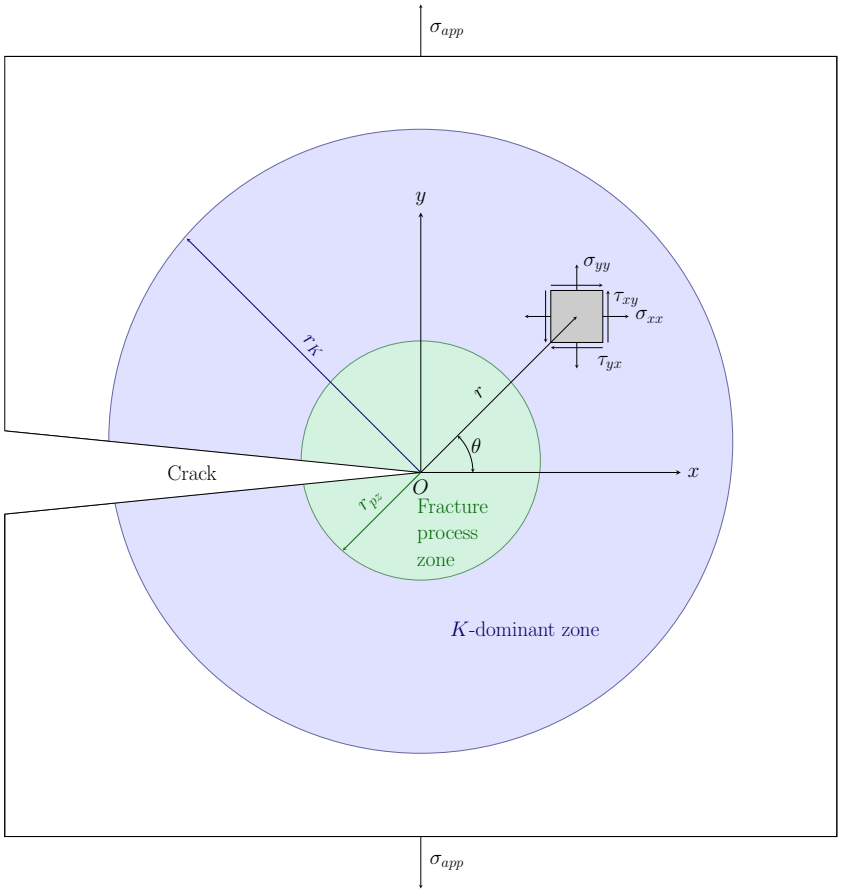

Figure 6.1. Semi infinite crack geometry used in K-controlled fracture simulations.

$$\sigma_{yy} = \frac{K_{\mathrm{I}}}{\sqrt{2\pi r}} \cos\left(\frac{\theta}{2}\right)\left[1 + \sin\left(\frac{\theta}{2}\right)\sin\left(\frac{3\theta}{2}\right)\right] \tag{6.3}$$

$$\tau_{xy} = \frac{K_{\mathrm{I}}}{\sqrt{2\pi r}} \cos\left(\frac{\theta}{2}\right)\sin\left(\frac{\theta}{2}\right)\cos\left(\frac{3\theta}{2}\right) \tag{6.4}$$

$$\sigma_{zz} = \nu\left(\sigma_{xx} + \sigma_{yy}\right) \text{(Plane strain)} \tag{6.5}$$

$$\tau_{xz} = \tau_{yz} = 0 \tag{6.6}$$

where θ and r are the polar coordinates defining the position, ν is the Poisson's ratio, and K_{I} is the stress intensity factor for mode I loading. It can be seen that the stresses are proportional to $1/\sqrt{r}$, so that a stress singularity is produced at $r = 0$. Equations (6.2) to (6.6) are only valid at near the crack tip, in the *K-dominant zone* or *singularity dominated zone*, where the leading term in equation (6.1) dominates. This region is shown in blue in Fig. 6.1. In this region, the stresses and displacements depend only on the stress intensity factor, so that K is the only variable defining the crack tip conditions. The

stresses and strains in the K-dominant region of two bodies with different crack configurations and under different loads (of the same mode), but otherwise identical, will be the same if their stress intensity factors are equal.

The $1/\sqrt{r}$ singularity results in infinite stresses being predicted at $r = 0$; however, real materials cannot withstand infinite stresses. The stresses at the crack tip are finite because the crack tip radius is finite (even for atomically sharp cracks), and because inelastic behaviour (plasticity in metals) help to relax crack tip stresses. For ductile materials, when the stresses exceed the strength of the material, yielding occurs, which leads to non-linear behaviour. For this reason, equations (6.2) to (6.9) do not describe the crack tip conditions in the *plastic zone*, the region around the crack tip where plastic deformation takes place. This region is shown in green in Fig. 6.1. However, as long as the plastic zone is contained within the K-dominant zone, K still uniquely characterises the conditions at the crack tip. This scenario, referred to as *small-scale yielding*, is illustrated in Fig. 6.1. An initial estimation of the size of the plastic zone r_{pz} can be obtained by equating σ_{yy} to the yield strength of the material σ_{yield} in equation (6.3) with $\theta = 0$

$$r_{pz} = \frac{1}{2\pi}\left(\frac{K_{\text{I}}}{\sigma_{\text{yield}}}\right)^2 \tag{6.7}$$

Since equation (6.7) is based on the elastic crack tip solution, the size of the plastic zone is underestimated. This is because stresses in an elastic-plastic material cannot exceed the yield strength, so a larger plastic zone is needed to accommodate the same level of stress. A more accurate second-order estimate takes this into account, resulting in a plastic zone twice as large than that predicted by equation (6.7).

It is possible to control K_{I} by applying a displacement field corresponding to the desired value of K_{I} (if a closed form for the geometry used is available). For the semi-infinite crack shown in Fig. 6.1, the displacements are given by equations (6.8) and (6.9) [189]:

$$u_x = \frac{K_{\text{I}}}{2G}\sqrt{\frac{r}{2\pi}}\cos\left(\frac{\theta}{2}\right)\left[\kappa - 1 + 2\sin^2\left(\frac{\theta}{2}\right)\right] \tag{6.8}$$

$$u_y = \frac{K_{\text{I}}}{2G}\sqrt{\frac{r}{2\pi}}\sin\left(\frac{\theta}{2}\right)\left[\kappa + 1 - 2\cos^2\left(\frac{\theta}{2}\right)\right] \tag{6.9}$$

where G is the shear modulus and $\kappa = 3 - 4\nu$. Equations (6.8) and (6.9) assume isotropic elasticity. However, iron single crystals and other materials often used in atomistic simulations are elastically anisotropic. Therefore, anisotropic treatment is necessary to correctly apply the displacement field for accurate control of K. The anisotropic solution of elasticity equations makes use of the Stroh formalism [190]. The displacement field in the

K-dominant zone is given by equation (6.10) [119, 191]

$$\mathbf{u} = K_{\mathrm{I}}\sqrt{\frac{2r}{\pi}}\,\mathrm{Re}\left\{\mathbf{A}\left\langle\cos\theta + v_\alpha \sin\theta\right\rangle\mathbf{B}^{-1}\right\} \tag{6.10}$$

where Re{} stands for "the real part of". Equation (6.10) shows that in order to compute the displacement vector of an atom $\mathbf{u}$, three quantities, namely, v_α, $\mathbf{A}$ and $\mathbf{B}$ are needed. A discussion on how these quantities can be computed is provided in appendix B.

6.2 Simulation Methodology

Molecular dynamics simulations using the K-controlled fracture approach, described in the previous section, were conducted. The crack was created as follows: A Fe single crystal with four different groups of atoms was created, as showed in Fig. 6.2. Atoms in the outermost region of the simulation supercell are boundary atoms (blue) and they are used to control the applied K. The equations of motion of these atoms will not be integrated, as their position is solely prescribed by equation (6.10). The rest of the atoms (red, grey and yellow), contained within a radius r_{mobile}, are mobile atoms and their positions will be integrated using molecular dynamics. The size of the supercell can be characterised by the radius of the region containing the mobile atoms, r_{mobile}, measured from the crack tip. The EAM potential developed by Ramasubramaniam et al. [13, 14] was used to describe the Fe–H interactions.

In order to prevent spontaneous closure of the crack caused by the attractive interaction of the atoms on opposite crack surfaces, the 'screening' technique [119] has been used. This technique consists on deleting the interatomic interactions of atoms on the crack surfaces (grey and yellow) with atoms on opposite crack surfaces. The side effects of using screening technique are minor compared with those of alternative ways to create the crack (e.g removing atoms to create a crack) [119].

Three crack orientations, namely the $(1\,1\,1)[1\,1\,\overline{2}]$, $(1\,1\,1)[1\,\overline{1}\,0]$ and $(1\,0\,0)[0\,1\,0]$ were studied. They relate to figure 6.2 as shown in table 6.1. Simulations were carried out at 500 K to increase the mobility of H solutes and reduce the time needed for the simulations. The displacement corresponding to $K_{\mathrm{I}} = 0.8\,\mathrm{MPa}\sqrt{\mathrm{m}}$ was initially applied to all atoms to create the crack. This value of K_{I} was chosen in order to avoid crack growth or any plastic deformation. H atoms were introduced at a rate of 1 atom/ps at the surfaces of the crack to simulate the hydrogen environment. After 50 hydrogen atoms were introduced in the supercell, the system was allowed to relaxed for 500 ps using the NVT ensemble with a timestep of 0.4 fs. Simulations were performed with H concentrations C_0 ranging from 0.14 to 1.45 at.%, not including boundary atoms. For the pure Fe simulations, the system was equilibrated for 50 ps. In order to apply the load, atoms in the boundary

region are displaced according to the anisotropic displacement solution and the value of K_{I} is increased by $0.01\,\mathrm{MPa}\sqrt{\mathrm{m}}$ every 1 ns. The elevated temperature and the rapid diffusion of hydrogen in Fe provide sufficient time for the relaxation of H atoms between K increments. As K_{I} increases, deformation takes place in the supercell, which can be in the form of cleavage, dislocation emission or twinning.

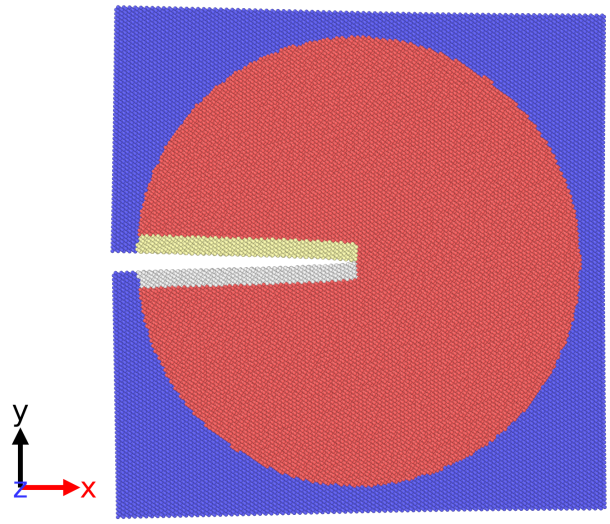

Figure 6.2. Typical supercell used for fracture simulations. Boundary atoms (blue) are used to apply the displacement corresponding to desired K_{I} value. Mobile atoms (red, grey and yellow) follow Newtonian mechanics. Interactions between opposite crack surface atoms (yellow and grey) have been deleted to prevent spontaneous closure of the crack tip (screening technique).

Crack orientation	**Crack plane** x	**Crack growth direction** y	**Crack front** z
$(1\,1\,1)[1\,1\,\bar{2}]$	$(1\,1\,1)$	$[1\,1\,\bar{2}]$	$[1\,\bar{1}\,0]$
$(1\,1\,1)[1\,\bar{1}\,0]$	$(1\,1\,1)$	$[1\,\bar{1}\,0]$	$[1\,1\,\bar{2}]$
$(1\,0\,0)[0\,1\,0]$	$(1\,0\,0)$	$[0\,1\,0]$	$[0\,0\,1]$

Table 6.1. Crack orientations used for K-controlled simulations.

6.2.1 Size optimization

As mentioned in section 6.1, small-scale yielding conditions (plastic zone contained within the K-dominant zone) are needed to obtain meaningful fracture behaviour from K-controlled simulations. To achieve this, it is necessary that all plastic behaviour occurring at the crack tip takes place within the simulation domain. As discussed in section 6.1, the size of the plastic zone depends on the applied K and the yield strength of the material. Using the second-order approximation (twice r_{pz} computed in equation (6.7)), for $K_{\mathrm{I}} = 3\,\mathrm{MPa}\sqrt{\mathrm{m}}$ and $\sigma_{\mathrm{yield}} = 20\,\mathrm{GPa}$[1], the radius of the plastic zone is $r_{pz} = 7.2\,\mathrm{nm}$. This

[1]It was shown in section 4.2.1 that σ_{yield} for an Fe single crystal when loaded on the [1 1 1] direction fluctuates by approximately 20 GPa for strain rates below $1 \times 10^{9}\,\mathrm{s}^{-1}$.

value is an estimate of the minimum size of the supercell.

Simulations on pure Fe supercells with different sizes were carried out in order to test the dependence of the crack tip behaviour with the simulation box size. Orientations chosen for these set of simulations were the $(1\,0\,0)[0\,1\,0]$ and $(1\,1\,1)[1\,\bar{1}\,0]$. In these orientations, crack growth takes place due to cleavage and dislocation emission, respectively, allowing us to examine the size effects for two of the main crack growth mechanisms in Fe. Details of the supercells used in these simulations are shown in tables 6.2 and 6.3. The sizes of these supercells range from $L_x = 10\,\text{nm}$ to $L_x = 50\,\text{nm}$, where L_x is the nominal size of the supercell in the x (crack growth) direction. These supercell sizes are large enough to contain the plastic zone predicted by equation (6.7). The radius of the mobile region, defined in the previous section, of the smallest supercell $r_{\text{mobile}} = 4.5\,\text{nm}$ is larger than the predicted size of the plastic zone even for the smallest of the supercells.

No.	$L_x \times L_y \times L_z, \text{nm}^3$	$r_{\text{mobile}}, \text{nm}$	atoms	$K_{\text{I}}, \text{MPa}\sqrt{\text{m}}$ at event
1	$10 \times 10 \times 1.5$	4.5	23,500	1.29
2	$20 \times 20 \times 1.5$	9	48,000	1.31
3	$30 \times 30 \times 1.5$	13.5	108,336	1.36
4	$40 \times 40 \times 1.5$	18	196,000	1.37
5	$50 \times 50 \times 1.5$	22.5	306,250	1.37

Table 6.2. Effect of system size on crack growth behaviour for a crack oriented on the $(1\,1\,1)[1\,\bar{1}\,0]$. Fracture occurs via dislocation emission.

No.	$L_x \times L_y \times L_z, \text{nm}^3$	$r_{\text{mobile}}, \text{nm}$	atoms	$K_{\text{I}}, \text{MPa}\sqrt{\text{m}}$ at event
1	$10 \times 10 \times 1.5$	4.5	23,500	1.07
2	$20 \times 20 \times 1.5$	9	49,000	1.12
3	$30 \times 30 \times 1.5$	13.5	110,250	1.17
4	$40 \times 40 \times 1.5$	18	196,000	1.17
5	$50 \times 50 \times 1.5$	22.5	196,000	1.37

Table 6.3. Effect of system size on crack growth behaviour for a crack oriented on the $(1\,0\,0)[0\,1\,0]$. Fracture occurs via cleavage.

The effect of the nominal size of the supercell L_x on the value of the stress intensity factor at which either dislocation emission or cleavage begins, K_{I} at event, is shown in Fig. 6.3. It can be seen that the smallest supercells underpredict the value of K_{I} at event, which could be the result of the elastic interaction of dislocations and crack tip fields with the edge of the supercell. For $L_x > 30\,\text{nm}$, the predicted value of K_{I} converges at around 1.36 and $1.17\,\text{MPa}\sqrt{\text{m}}$, for dislocation emission and cleavage, respectively. Further increase of the size of the supercell has no significant impact of value of K_{I} at which crack tip phenomena occur. Figure 6.3 suggests that the optimal size for the crack simulations is $L_x = 30\,\text{nm}$, that is, supercells No. 3 in tables 6.2 and 6.3. For supercells of this size, the mobile region has radius $r_{\text{mobile}} = 13.5\,\text{nm}$, almost twice the size of the plastic zone predicted by the second-order approximation. This simulation size will be used for the rest of the simulations.

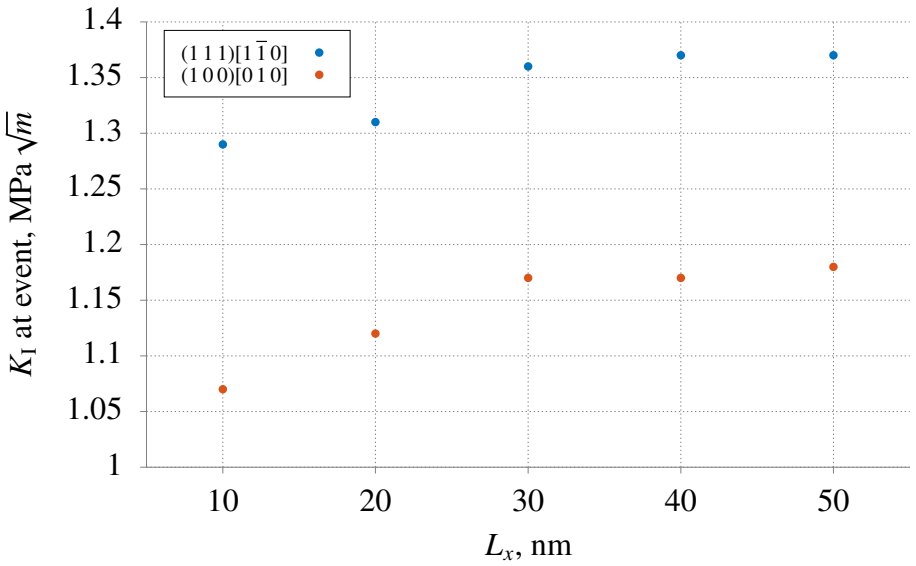

Figure 6.3. Effect of the simulation size L_x on the stress intensity factor at which dislocation emission or cleavage occur, K_I at event. The variation of K_I at event with simulation size is negligible for $L_x \geq 30\,\mathrm{nm}$.

6.3 Results

6.3.1 Fracture on pure Fe

Fracture in pure iron, for the orientations and conditions described in section 6.2, occurred in two different manners: ductile and brittle. Cracks in the $(1\,1\,1)[1\,1\,\bar{2}]$ and $(1\,1\,1)[1\,\bar{1}\,0]$ orientations, fracture in a ductile manner, showing the emission of dislocations from the crack tip at a critical value of the stress intensity factor. This process blunts the initially sharp crack and prevents crack growth. On the other hand, cracks oriented on the $(1\,0\,0)[0\,1\,0]$ fracture in a brittle manner, with little plasticity around the crack tip and extensive crack growth. These two distinctive fracture mechanisms are discussed in the following paragraphs.

Ductile failure

The fracture process on the cracks with $(1\,1\,1)[1\,1\,\bar{2}]$ and $(1\,1\,1)[1\,\bar{1}\,0]$ orientations takes place in a ductile manner. The fracture behaviour is controlled by the emission (nucleation and subsequent glide) of dislocations from the crack tip. The emission of dislocations is possible due to the high stresses found at the crack tip and favourably oriented slip systems. Crack growth is limited due to dislocation emission, which blunts the crack tip. This process is illustrated in Fig. 6.4. At the beginning of the simulation (Fig. 6.4a), $K_\mathrm{I} = 0.8\,\mathrm{MPa}\sqrt{\mathrm{m}}$, which is not enough to produce crack growth Δa. It can be seen that the crack is sharp and that the supercell contains atoms in BCC positions (blue atoms) and defect atoms (grey atoms), which in this case, are all part of the crack surface. As K_I is increased to $1.18\,\mathrm{MPa}\sqrt{\mathrm{m}}$, little crack growth is produced, $\Delta a = 0.04\,\mathrm{nm}$, before

a $\frac{1}{2}\langle 1\,1\,1\rangle$ dislocation (highlighted in red circles) nucleates at and glides away from the crack tip. Dislocation emission takes place in glide planes that are perpendicular to the crack plane, which blunts the crack tip and arrests crack growth. Increasing K_{I} to $1.59\,\mathrm{MPa}\sqrt{\mathrm{m}}$ produces limited crack growth $\Delta a = 0.651\,\mathrm{nm}$ and a second dislocation on the opposite side of the crack plane (Fig. 6.4c). The crack growth process continues by alternating events of crack advance, followed by dislocation emission and crack arrest (Fig. 6.4d). Higher values of K_{I} are needed to produce more crack growth, which is typical of ductile materials. Emitted dislocations produce a back-stress on the crack tip, making it harder for subsequent dislocations to nucleate, thus increasing the value of K_{I} required for dislocation emission.

The fracture behaviour of the $(1\,1\,1)[1\,\bar{1}\,0]$ crack orientation is qualitatively identical to that of the $(1\,1\,1)(1\,1\,\bar{2})$ orientation shown in Fig. 6.4. The main difference between them is the value K_{I} at which dislocation emission takes place. For the $(1\,1\,1)[1\,\bar{1}\,0]$ orientation, the first dislocation nucleated at $K_{\mathrm{I}} = 1.36\,\mathrm{MPa}\sqrt{\mathrm{m}}$, showing a higher toughness compared with that of the $(1\,1\,1)(1\,1\,\bar{2})$ orientation. Another difference is the slip plane on which emitted dislocations glide. For the $(1\,1\,1)(1\,1\,\bar{2})$ orientation dislocations glide on $(1\,1\,\bar{2})$ slip planes whereas for the $(1\,1\,1)[1\,\bar{1}\,0]$ crack orientation is the $(1\,\bar{1}\,0)$. In both cases, active slip planes are perpendicular to the crack plane.

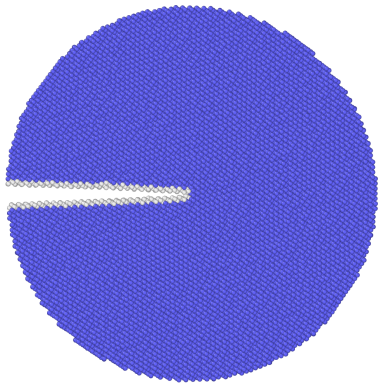

(a) $K_{\mathrm{I}} = 0.8\,\mathrm{MPa}\sqrt{\mathrm{m}}$, $\Delta a = 0\,\mathrm{nm}$

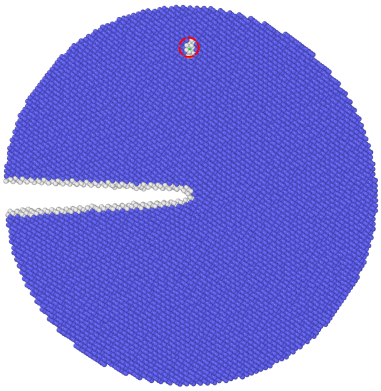

(b) $K_{\mathrm{I}} = 1.18\,\mathrm{MPa}\sqrt{\mathrm{m}}$, $\Delta a = 0.04\,\mathrm{nm}$

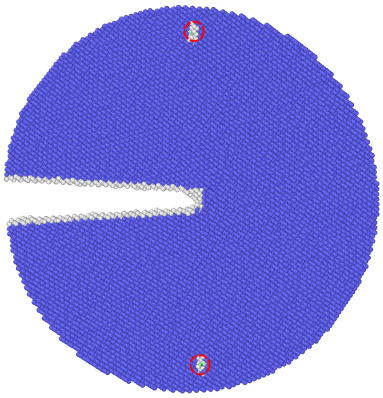

(c) $K_{\mathrm{I}} = 1.59\,\mathrm{MPa}\sqrt{\mathrm{m}}$, $\Delta a = 0.651\,\mathrm{nm}$

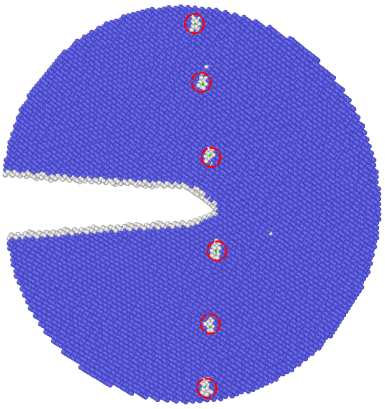

(d) $K_{\mathrm{I}} = 2.2\,\mathrm{MPa}\sqrt{\mathrm{m}}$, $\Delta a = 1.6\,\mathrm{nm}$

Figure 6.4. Deformation of the $(1\,1\,1)[1\,1\,\bar{2}]$ crack. In blue, atoms in BCC positions, and in grey defect atoms. Dislocations highlighted in red circles. a) The applied K_{I} is not high enough to drive crack growth, $\Delta a = 0$. b) Under $K_{\mathrm{I}} = 1.18\,\mathrm{MPa}\sqrt{\mathrm{m}}$, a $\frac{1}{2}[1\,1\,1]$ dislocation is emitted from the crack-tip which blunts the crack-tip and arrests crack growth. c) Increasing K_{I} produces another dislocation and limited crack growth. d) The fracture process consists on alternating crack growth, dislocation emission and blunting events as K_{I} is increased.

Brittle fracture

When the crack is oriented on the $(1\,0\,0)[0\,1\,0]$ orientation, fracture occurs via cleavage, that is, the permanent separation of atomic planes when a critical crack-tip opening displacement (CTOD) is achieved. This process is shown in Fig. 6.5. Atoms in blue and grey are atoms in BCC coordination and defect atoms, respectively. At the beginning of the simulation (Fig. 6.5a), $K_{\mathrm{I}} = 0.8\,\mathrm{MPa}\sqrt{\mathrm{m}}$, which it is not high enough for crack growth onset. Crack growth begins when K_{I} is increased to $1.15\,\mathrm{MPa}\sqrt{\mathrm{m}}$, resulting in a crack extension of $\Delta a = 0.93\,\mathrm{nm}$, as can be seen in Fig. 6.5b. At the crack-tip, two sets of non-surface atoms on planes forming approximately 45° with the crack growth direction are shown in grey, suggesting that they form part of a deformed region of the crystal. This localised strain could be the result of a complex shearing process of atoms at the

crack-tip necessary to achieve the critical CTOD similar to that suggested by Knott [192]. Cleavage occurs via the cooperative movement of atoms ('shuffles'), in this case on {1 1 0} planes, immediately close to the crack-tip (within 1 nm), as can be seen in Fig. 6.5d. As opposed to the ductile fracture mechanism seen in Fig. 6.4 where limited crack growth was observed, a small increase in the applied stress intensity factor results in considerable crack extension. As shown in Fig. 6.5c, increasing K_{I} to $1.3\,\mathrm{MPa}\sqrt{\mathrm{m}}$ results in crack extension of 4.8 nm. This behaviour captures the brittle nature of the (1 0 0)[0 1 0] crack orientation.

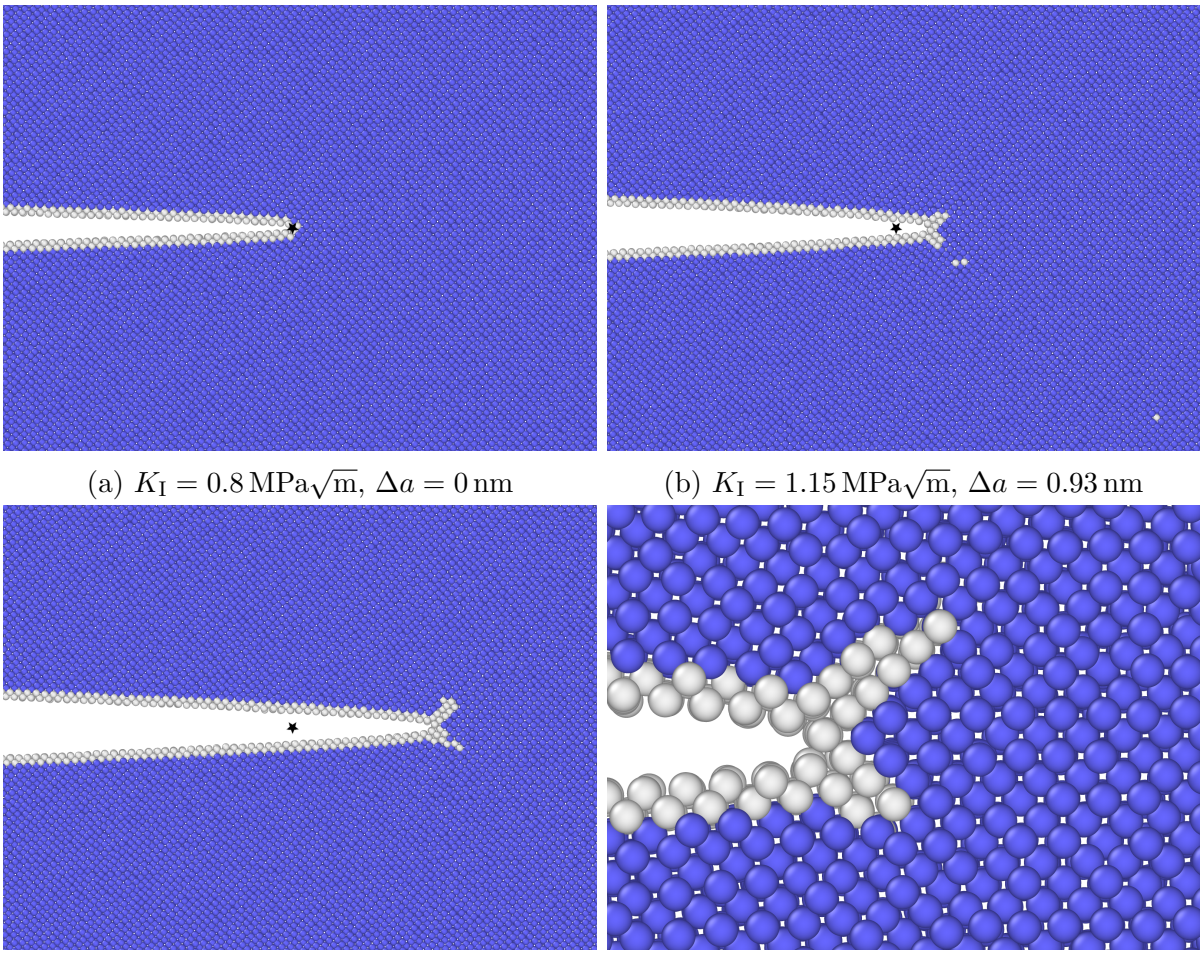

(a) $K_{\mathrm{I}} = 0.8\,\mathrm{MPa}\sqrt{\mathrm{m}}$, $\Delta a = 0\,\mathrm{nm}$

(b) $K_{\mathrm{I}} = 1.15\,\mathrm{MPa}\sqrt{\mathrm{m}}$, $\Delta a = 0.93\,\mathrm{nm}$

(c) $K_{\mathrm{I}} = 1.3\,\mathrm{MPa}\sqrt{\mathrm{m}}$, $\Delta a = 4.8\,\mathrm{nm}$

(d) Atomic shearing

Figure 6.5. Deformation of the (1 0 0)[0 1 0] crack. In blue, atoms in BCC positions, and in grey, defect atoms. The star indicates the initial crack-tip position. a) The applied K_{I} is not high enough to drive crack growth. b) Under $K_{\mathrm{I}} = 1.15\,\mathrm{MPa}\sqrt{\mathrm{m}}$, crack growth begins, resulting in a crack extension of $\Delta a = 0.93\,\mathrm{nm}$ c) Small increases of K_{I} produces considerable crack growth. d) At the crack-tip a complex atomic shearing process occurs.

6.3.2 Fracture on Fe-H

Equilibrium H distribution

The distribution of hydrogen around the crack-tip after its introduction is shown in Fig. 6.6. For H concentrations below $C_0 = 0.29\,\text{at.}\%$, hydrogen atoms are only present on the crack surfaces as can be seen in Fig. 6.6a. Due to their strong binding, the adsorption of hydrogen atoms on the crack surfaces is thermodynamically favourable. At higher concentrations (e.g. $C_0 > 0.43\,\text{at.}\%$), hydrogen is present in sufficient quantities to saturate the crack surfaces, which results in the absorption of hydrogen into the bulk, as shown in Fig. 6.6b. Solute hydrogen can easily diffuse to the crack-tip due to the elastic interaction between the hydrogen misfit volume and the highly tensile pressure field found at the vicinity of the crack-tip. With further increase of the concentration (e.g. to $C_0 = 1.45\,\text{at.}\%$) there is plenty of H solutes available to aggregate at the crack-tip. The aggregation of hydrogen occurs asymmetrically, at approximately 90° from the crack plane normal, as can be seen in Fig. 6.6c. The high local H concentration at the crack-tip results in a BCC to FCC phase transformation, as shown in Fig. 6.6d. This phase transformation was suggested to occur via a reverse Bain mechanism [14, 193]. A BCC unit cell can be seen as a faced-centred tetragonal (FCT) unit cell in which the (1 1 0) planes of the BCC unit cell are the (1 1 1) of the FCT unit cell. Straining uniaxially the FCT unit cell would result in the transformation to FCC.

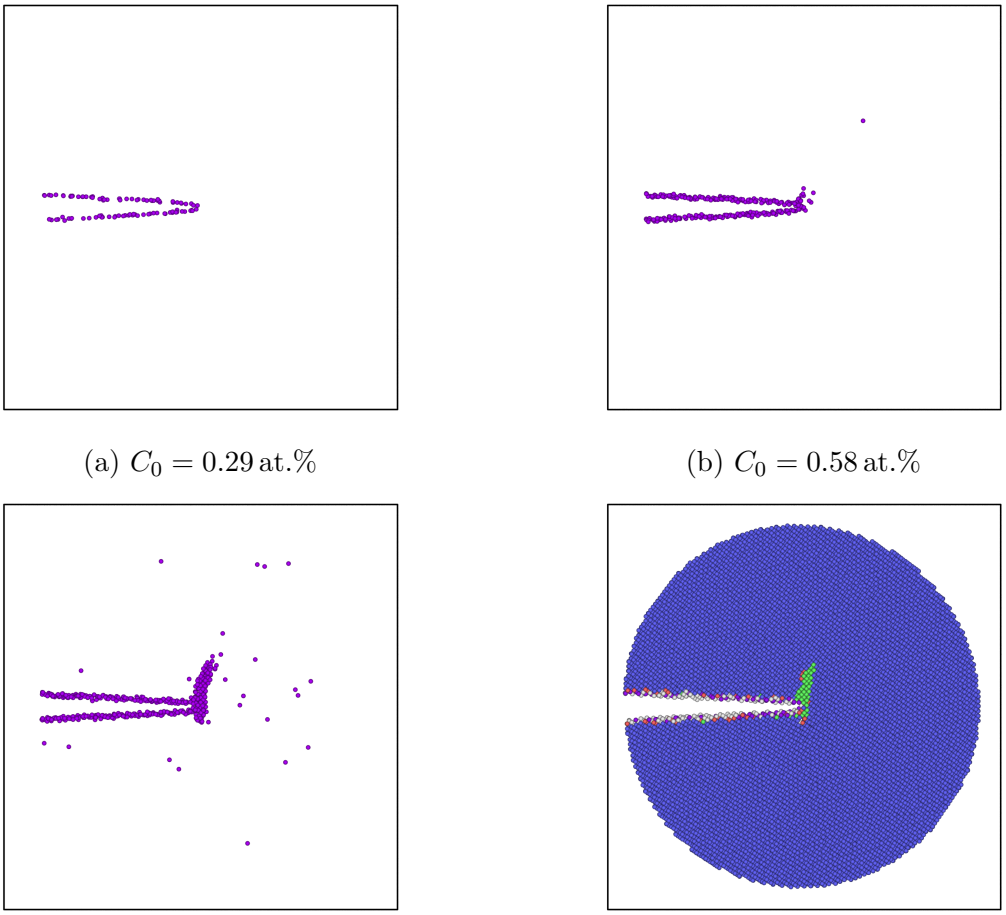

(a) $C_0 = 0.29\,\text{at.}\%$ (b) $C_0 = 0.58\,\text{at.}\%$

(c) $C_0 = 1.45\,\text{at.}\%$ (d) $C_0 = 1.45\,\text{at.}\%$

Figure 6.6. Equilibrium hydrogen distribution around the crack-tip for different H concentrations. a) At low concentrations all hydrogen is located on the crack surfaces. b)-c) Higher concentrations saturate the crack surfaces and hydrogen is absorbed into the bulk, where can readily diffuse to the crack-tip. d) For $C_0 > 1.16\,\text{at.}\%$, a BCC (blue) to FCC (green) phase transition at the crack-tip occurs due to the aggregation of H solutes of the crack-tip.

Ductile failure

For the ductile orientations, hydrogen had noticeable effect on the fracture events (e.g. crack blunting and crack extension) and the values of the stress intensity factor needed to produce such events. The dependence of the fracture behaviour for the $(1\,1\,1)[1\,1\,\bar{2}]$ orientation with the hydrogen concentration goes as follows. At low concentrations, e.g. $C_0 = 0.14\,\text{at.}\%$, the crack surface is unsaturated and no bulk hydrogen atoms are present. The fracture behaviour at this concentration was identical to the H-free scenario, in which dislocation emission blunts the crack-tip preventing crack advance.

At a concentration of $C_0 = 0.29\,\text{at.}\%$ crack surfaces are nearly saturated, and the fracture behaviour deviates from that of the pure Fe. To illustrate, snapshots of the fracture behaviour at this concentration are shown in Fig. 6.7. H atoms (in purple) are located on the crack surface. Similarly to the fracture in pure Fe, initially $K_\text{I} = 0.8\,\text{MPa}\sqrt{\text{m}}$, which is

not enough to produce crack extension (Fig. 6.7a). The first dislocation nucleates at $K_{\mathrm{I}} = 1.23\,\mathrm{MPa}\sqrt{\mathrm{m}}$ (Fig. 6.7b), slightly higher than in pure Fe. However, the crack advance produced before the dislocation nucleated, $\Delta a = 0.79\,\mathrm{nm}$, was considerably higher in the presence of H than that of pure Fe ($\Delta a = 0.04\,\mathrm{nm}$). This crack extension was produced in a cleavage-like manner, with little plasticity seen during the crack growth process. As shown in Fig. 6.7c, the second dislocation nucleated at a lower value of stress intensity factor and a higher crack extension, respectively $K_{\mathrm{I}} = 1.37\,\mathrm{MPa}\sqrt{\mathrm{m}}$ and $\Delta a = 0.94\,\mathrm{nm}$, compared with that of pure Fe ($K_{\mathrm{I}} = 1.59\,\mathrm{MPa}\sqrt{\mathrm{m}}$, $\Delta a = 0.04\,\mathrm{nm}$). Since there is no H solute in the bulk, due to the low H concentration, the increased crack extension per increment of stress intensity factor can be attributed to the effect of hydrogen adsorbed on the crack surfaces. Increasing K_{I} further produces considerable plastic deformation. The emission of dislocations gliding on $\{1\,1\,0\}$ slip planes at approximately 35° from the crack plane can be seen at $K_{\mathrm{I}} = 2.22\,\mathrm{MPa}\sqrt{\mathrm{m}}$ (Fig. 6.7d). This type of dislocation was not seen in the pure Fe simulations, suggesting that the surface hydrogen atoms can favour the activation of secondary slip planes. Unlike the previous dislocations whose slip planes are perpendicular to the crack plane, the emission of dislocations on planes oblique to the crack plane seems to contribute to crack-tip re-sharpening, as opposed to blunting, as can be seen in Fig. 6.7d. The estimated radius of curvature of the crack-tip was approximately 3.3 and 1.6 Å, before and after the emission of oblique dislocations, respectively, as shown in figure 6.8. Furthermore, the emission of oblique dislocations was also observed when reducing the relaxation time[2] between K_{I} increments to 10 ps, as can be seen in Fig. 6.9a. Under these conditions, crack advance can occur at rates above $1\,\mathrm{m\,s^{-1}}$ along distances of a couple of nanometres, which is too high for diffusion to play a role and suggests that adsorption is responsible. This fracture behaviour is reminiscent of the Adsorption Induced Dislocation Emission mechanism proposed by Lynch [8, 18, 62], in which dislocations are emitted on slip planes bisecting the crack plane normal at an angle that re-sharpens the crack-tip and promotes crack growth.

[2]The relaxation time between K_{I} increments for the rest of the simulations was 1 ns.

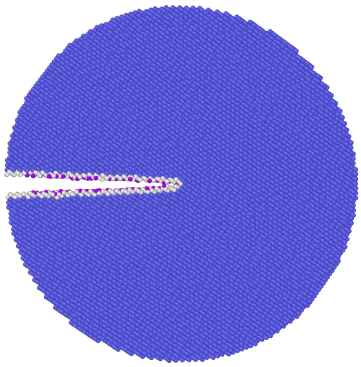

(a) $K_{\mathrm{I}} = 0.8\,\mathrm{MPa}$, $\Delta a = 0\,\mathrm{nm}$

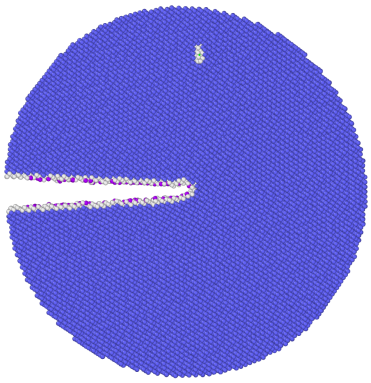

(b) $K_{\mathrm{I}} = 1.23\,\mathrm{MPa}$, $\Delta a = 0.79\,\mathrm{nm}$

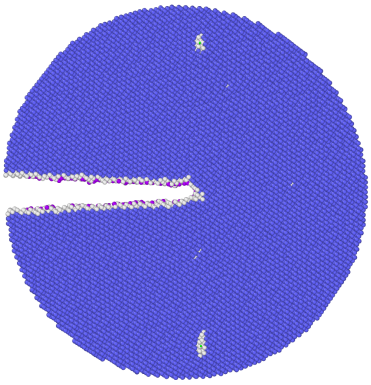

(c) $K_{\mathrm{I}} = 1.37\,\mathrm{MPa}$, $\Delta a = 0.94\,\mathrm{nm}$

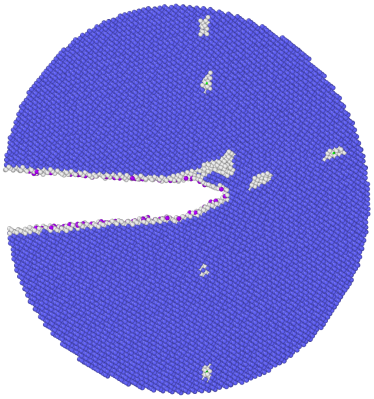

(d) $K_{\mathrm{I}} = 2.22\,\mathrm{MPa}$, $\Delta a = 2.2\,\mathrm{nm}$

Figure 6.7. Deformation of the $(1\,1\,1)[1\,1\,\overline{2}]$ crack with $C_0 = 0.29\,\mathrm{at.\%}$. H atoms in purple, Fe atoms in BCC positions in blue and defect Fe atoms in grey. a) The applied K_{I} is not high enough to drive crack growth, Δa. b) The first dislocation nucleates under slightly higher K_{I} than that of pure Fe; however, the crack extension produced, $\Delta a = 0.79\,\mathrm{nm}$, is considerably higher than in the absence of H. c) Lower K_{I} is needed for the nucleation of the second dislocation, which occurs at a crack extension of $\Delta a = 0.94\,\mathrm{nm}$. d) Extensive plastic deformation is produced with increasing K_{I}. The nucleation of dislocations gliding on slip planes oblique to the crack plane promote crack growth and re-sharpen the crack-tip.

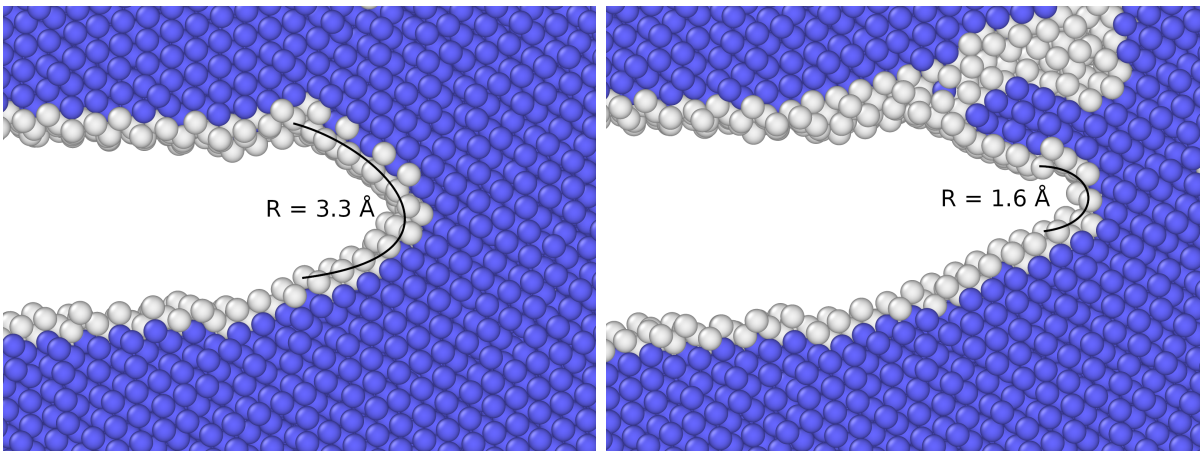

(a) Before emission (b) After emission

Figure 6.8. $(1\,1\,1)[1\,1\,\bar{2}]$ crack-tip before and after the emission of a $\frac{1}{2}$ $(1\,1\,1)$ dislocation on a slip plane oblique to the crack plane. The emission of the dislocation seems to re-sharpen the crack-tip.

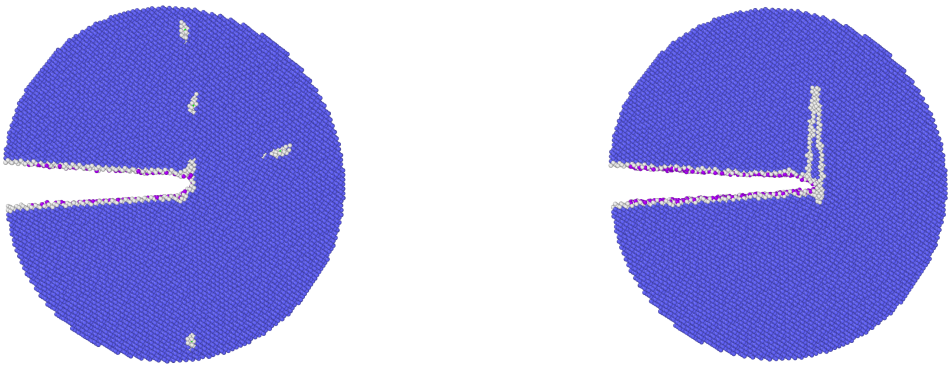

(a) $C_0 = 0.29\,\text{at.}\%$ (b) $C_0 = 0.87\,\text{at.}\%$

Figure 6.9. Deformation of the $(1\,1\,1)[1\,1\,\bar{2}]$ crack with 10 ps between K_I increments. a) Dislocation emission. b) Twinning.

The fracture behavour at higher concentrations is shown in Fig. 6.10. With a concentration of $C_0 = 0.87\,\text{at.}\%$, hydrogen is present in sufficient quantities to aggregate at the crack-tip. The accumulation of hydrogen prevents dislocations being emitted from the crack-tip and crack growth occurs in a cleavage-like manner when K_I is high enough, in this case $1.11\,\text{MPa}\sqrt{\text{m}}$ (Fig. 6.10a). Crack growth stops with the nucleation of a pair of dislocations with slip planes parallel to the crack plane. The nucleation of these dislocations seems to be a consequence of hydrogen atoms not being able to keep up with the crack growth rate.Once crack growth stops, hydrogen atoms can reach the crack-tip and crack growth restarts due to increasing local H concentration and the increasing K_I (Fig. 6.10b). This process of slow crack growth involving hydrogen diffusion to the crack-tip, crack growth via cleavage and crack arrest due to dislocation emission is similar to the one reported by Song and Curtin [14]. This fracture behaviour is clearly time depen-

dent as it requires H diffusion to the crack-tip. Therefore, this failure mechanism is not observed when reducing the time between K_{I} increments, as shown in Fig. 6.9b.

The relaxation time between K_{I} increments of 1 nm might seem short for hydrogen to diffuse to the crack-tip. However, given the small length scale of these simulations, relaxation times are long enough. The diffusion coefficient of H in BCC Fe at 500 K has been calculated using Molecular Dynamics and the interatomic potential used in this work as $1.3 \times 10^{-8}\,\mathrm{m}^2/\mathrm{s}$ [38]. This value is in agreement with experimental measurements in high purity Fe for the same temperature $2 \times 10^{-8}\,\mathrm{m}^2/\mathrm{s}$ [42]. Using the value obtained from simulation, the hydrogen diffusion distance $\sim \sqrt{Dt}$ in 1 ns is approximately 3.6 nm (or linear velocities of $3.6\,\mathrm{m\,s}^{-1}$). Therefore, hydrogen diffusion to the crack tip is possible provided that crack velocities are below this value. In this scenario, dislocation nucleation is prevented and crack occurs in a cleavage-like fashion. Crack growth might also occur at higher rates during short intervals and H solutes might not be able to keep up with the crack tip. In this case, dislocation emission from the crack-tip will take place and the crack will arrest. Reducing the relaxation time between K_{I} increments results in higher crack rates, preventing hydrogen diffusion to the crack-tip. In this case, crack growth occurs via other stress relieving mechanism e.g. twinning, as shown in figure 6.9b. Twinning has been reported in fractured Fe single crystals loaded at strain rates of $10^3\,\mathrm{s}^{-1}$ [138].

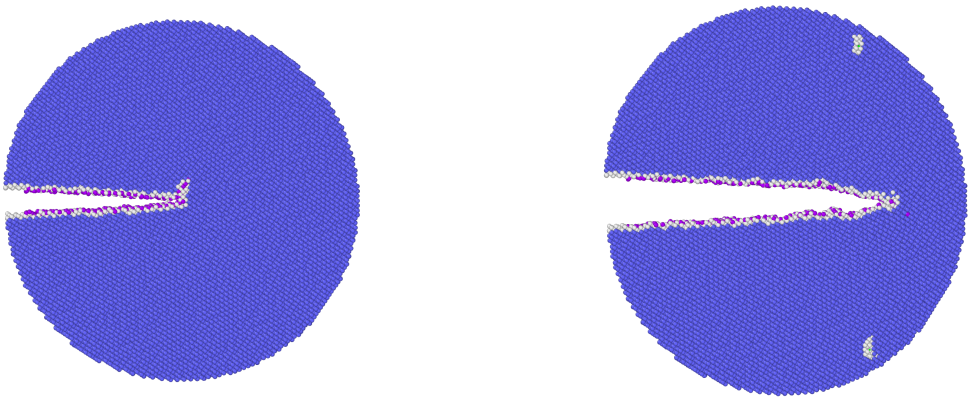

(a) $K_{\mathrm{I}} = 1.11\,\mathrm{MPa}$, $\Delta a = 0.11\,\mathrm{nm}$ (b) $K_{\mathrm{I}} = 1.75\,\mathrm{MPa}$, $\Delta a = 6.3\,\mathrm{nm}$

Figure 6.10. Deformation of the $(1\,1\,1)[1\,1\,\bar{2}]$ crack orientation with $C_0 = 0.87$ at.%. H atoms in purple, atoms with BCC coordination in blue and defect atoms in grey.a) Hydrogen atoms saturate the crack surface and accumulate at the crack-tip. Crack growth begins at $K_{\mathrm{I}} = 1.11\,\mathrm{MPa}\sqrt{\mathrm{m}}$. b) The bulk hydrogen accumulated at the crack-tip prevents dislocation emission and crack extension occurs via cleavage until it arrests due to the nucleation of a pair of dislocations. As K_{I} is increase and as H atoms diffuse to the crack-tip and crack growth onsets again.

The deformation process of the $(1\,1\,1)[1\,\bar{1}\,0]$ crack orientation, shown in Fig. 6.11, was qualitatively similar to that of the $(1\,1\,1)[1\,1\,\bar{2}]$ orientation. At low H concentrations, in

which all hydrogen is located on the crack surfaces, the fracture process was identical to that of pure Fe (Fig. 6.4). At higher H concentrations, when H is also present in the bulk, the deformation is analogous to that shown in Fig. 6.10, in which hydrogen prevented the nucleation of dislocations and pronounced crack growth took place. Further increase of the concentration, e.g. to $C_0 = 1.16\,\text{at.}\%$, leads to intense localised plasticity ahead of the crack-tip. Extensive dislocation nucleation and the formation of a nanovoid can be seen in Fig. 6.11c and 6.11d. These features resemble those described by the HELP model. Unlike the fracture on the $(1\,1\,1)[1\,1\,\bar{2}]$ crack orientation, the emission of oblique dislocations, as those seen in Fig. 6.7, was not observed on the $(1\,1\,1)[1\,\bar{1}\,0]$ orientation. This suggests that for this crack orientation, surface hydrogen has little effect on the fracture behaviour, which is controlled by the amount of hydrogen aggregated at the crack-tip. A possible reason for absence of oblique dislocations on the $(1\,1\,1)[1\,\bar{1}\,0]$ crack orientation is discussed in section 6.4.

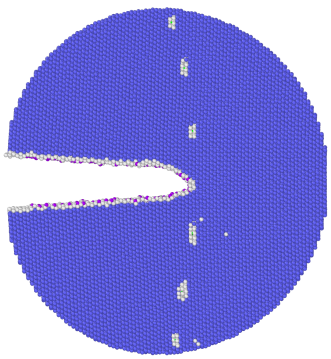

(a) $C_0 = 0.29\,\text{at.}\%$, $K_\text{I} = 2.2\,\text{MPa}$

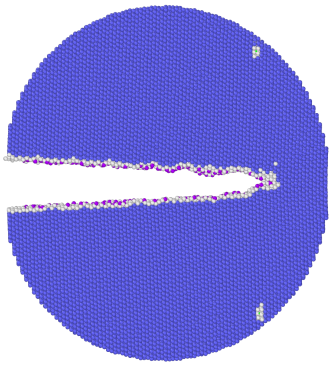

(b) $C_0 = 0.58\,\text{at.}\%$, $K_\text{I} = 1.7\,\text{MPa}$

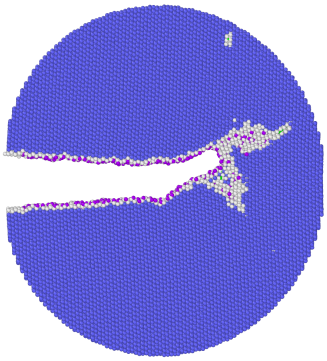

(c) $C_0 = 1.16\,\text{at.}\%$, $K_\text{I} = 2.4\,\text{MPa}$

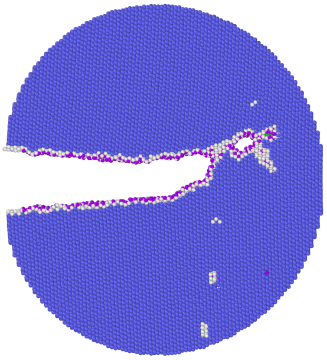

(d) $C_0 = 1.45\,\text{at.}\%$, $K_\text{I} = 2.4\,\text{MPa}$

Figure 6.11. Deformation of the $(1\,1\,1)[1\,\bar{1}\,0]$ crack as a function of the H concentration C_0. H atoms in purple, Fe atoms in BCC positions in blue and Fe atoms with no crystalline structure in grey.

Brittle fracture

On the $(1\,0\,0)[0\,1\,0]$ orientation, the effect of adding hydrogen on the fracture behaviour was to reduce the stress intensity needed to produce crack growth. Figures 6.12 and 6.13 show the fracture process at different hydrogen concentrations. Hydrogen concentrations as low as 0.29 at.% resulted in noticeable reductions to the applied K_{I} that produced crack extension. At this concentration hydrogen is mainly present adsorbed on the crack surfaces, with very limited aggregation in the region ahead of the crack-tip. As can be seen in figures 6.5c and 6.12, with a concentration of 0.58 at.% crack growth begins when $K_{\mathrm{I}} = 0.97\,\mathrm{MPa}\sqrt{\mathrm{m}}$, a considerably lower value compared with that seen in pure Fe ($1.17\,\mathrm{MPa}\sqrt{\mathrm{m}}$). Fracture occurs via cleavage of $(1\,0\,0)$ planes, leaving a completely planar fracture surface. Although similar quasi-cleavage features were seen in the $(1\,1\,1)[1\,1\,\bar{2}]$ crack orientation at concentrations above 0.87 at.% (Fig. 6.7), that fracture processes is different from that of the $(1\,0\,0)[0\,1\,0]$ crack orientation. In the $(1\,1\,1)[1\,1\,\bar{2}]$ crack orientation the role of hydrogen was to prevent dislocation emission from the crack-tip. Instead, hydrogen seems to reduce the work of fracture, so that lower stresses are needed to break atomic bonds at the crack-tip. This reduction of the cohesive strength of the lattice might be associated with the 'shuffles' of atoms at the crack-tip by which cleavage is produced, as discussed in section 6.3.1. If atoms at the crack-tip can be more easily re-arranged, the separation of the crack-tip will happen at lower stresses, and greater crack extension will be produced for a given stress intensity when compared with pure Fe. As shown in Fig. 6.12b, the crack extension produced when applying $K_{\mathrm{I}} = 1.3\,\mathrm{MPa}\sqrt{\mathrm{m}}$ was 4.8 and 7.1 nm for pure Fe and with a concentration of 0.58 at.%, respectively.

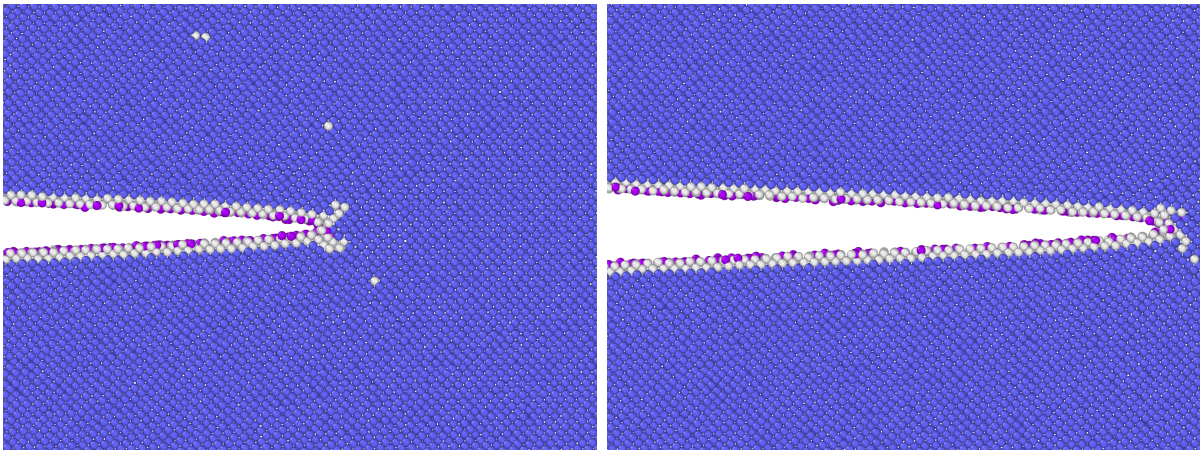

(a) $K_{\mathrm{I}} = 0.97\,\mathrm{MPa}$, $\Delta a = 0.71\,\mathrm{nm}$ (b) $K_{\mathrm{I}} = 1.3\,\mathrm{MPa}$, $\Delta a = 7.1\,\mathrm{nm}$

Figure 6.12. Deformation of the $(1\,0\,0)[0\,1\,0]$ crack with $C_0 = 0.58$ at.%. H atoms in purple, Fe atoms in BCC positions in blue and defect atoms in grey.

At higher hydrogen concentrations, hydrogen builds up at the crack-tip, inducing a phase transformation to FCC similar to that shown in Fig. 6.6d. However, the aggregation in this orientation seems to occur directly in front of the crack-tip as opposed to asymmetrically as it was the case of the $(1\,1\,1)[1\,1\,\bar{2}]$ crack orientation. Furthermore, H aggregation seems

to induce the formation of a stacking fault a $\{1\,1\,0\}$ plane in the FCC transformed phase, which is represented by the red atoms in Fig. 6.13a. Crack growth occurs extensively after onset at $K_{\mathrm{I}} = 1.43\,\mathrm{MPa}\sqrt{\mathrm{m}}$. Cleavage seems to occur along stacking fault, resulting in fracture along the $(1\,1\,0)$ plane at 45° from the original crack plane. This deviation from the original $(1\,0\,0)$ cleavage plane is a consequence of the hydrogen aggregation at the crack-tip. However, considerably higher values of K_{I} were needed to drive the crack compared with that in the absence of hydrogen ($K_{\mathrm{I}} = 1.17\,\mathrm{MPa}\sqrt{\mathrm{m}}$), suggesting that hydrogen damage is limited under these conditions.

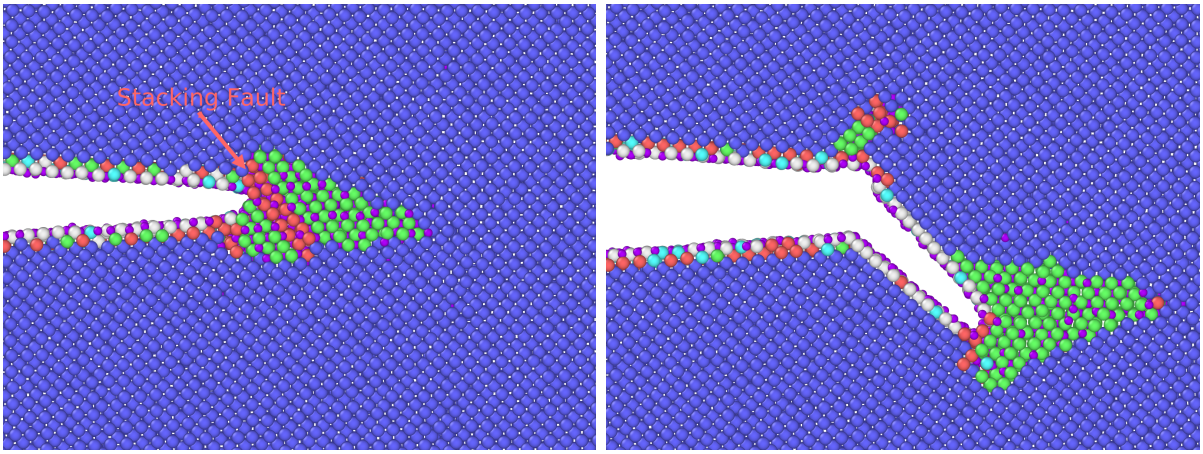

(a) $K_{\mathrm{I}} = 0.9\,\mathrm{MPa}$, $\Delta a = 0.09\,\mathrm{nm}$ (b) $K_{\mathrm{I}} = 1.7\,\mathrm{MPa}$, $\Delta a = 2.5\,\mathrm{nm}$

Figure 6.13. Deformation of the $(1\,0\,0)[0\,1\,0]$ crack with $C_0 = 1.45\,\mathrm{at.\%}$. H atoms in purple, Fe atoms in BCC, FCC and HPC structure in blue, green and red, respectively. Defect atoms in grey and cyan.

6.3.3 Effect of H on fracture toughness

The effect of hydrogen on the fracture toughness can be seen by plotting the applied stress intensity factor K_{I} versus the resulting crack extension Δa. Such a plot is shown in Fig. 6.14 for the $(1\,1\,1)[1\,1\,\bar{2}]$ and $(1\,1\,1)[1\,\bar{1}\,0]$ crack orientations and concentrations up to $C_0 = 1.16\,\mathrm{at.\%}$. For pure Fe, crack growth is steady and results from the iterative process of crack growth followed by dislocation emission and blunting, illustrated by the progressively raising blue series in figures 6.14a and 6.14b.

For the $(1\,1\,1)[1\,1\,\bar{2}]$ crack orientation with a concentration of $0.29\,\mathrm{at.\%}$ (red), hydrogen is only present at the crack surfaces which resulted in moderate increase of the crack extension compared with that of pure Fe. As discussed in section 6.3.2, when dislocations are emitted on slip planes oblique to the crack plane normal, crack growth is promoted and the crack-tip is re-sharpened. Such a process resulted in increased crack extension depicted by the sudden increase of the slope of the orange series when $K_{\mathrm{I}} = 2.2\,\mathrm{MPa}\sqrt{\mathrm{m}}$ in Fig. 6.14a.

At higher H concentrations (e.g. $C_0 = 0.58\,\mathrm{at.\%}$), in which there is plenty of hydrogen to aggregate at the crack-tip, fracture occurs via the slow crack growth process shown

in figures 6.10 and 6.11b. This process corresponds to the purple and yellow series in figures 6.14a and 6.14b, respectively. When hydrogen is present at the crack-tip, dislocation emission is prevented and growth occurs readily in a cleavage-like manner with little plastic deformation, corresponding to steep slopes of the aforementioned series. Crack growth is fast and the tip becomes H depleted, so that dislocation emission is possible and the crack blunts. This is shown by the horizontal segments. Once sufficient hydrogen solutes aggregate at the crack-tip, cleavage-like growth can continue.

For the $(1\,1\,1)[1\,\bar{1}\,0]$ crack orientation from concentrations of $C_0 = 1.16\,\text{at.}\%$, extensive dislocation nucleation leads to the formation of a highly localised plastic zone ahead of the crack-tip, as shown in figures 6.11c and 6.11d. This fracture mechanism corresponds to the green series in Fig. 6.14b. While crack extension is below that seen at lower concentrations (e.g. $0.58\,\text{at.}\%$), it is larger than that seen in pure Fe. The development of the plastic zone initially leads to blunting. However, at higher values of applied K_I, the formation of nanovoids, seen in Fig. 6.11d, are likely to result in abrupt crack growth via nanovoid coalescence.

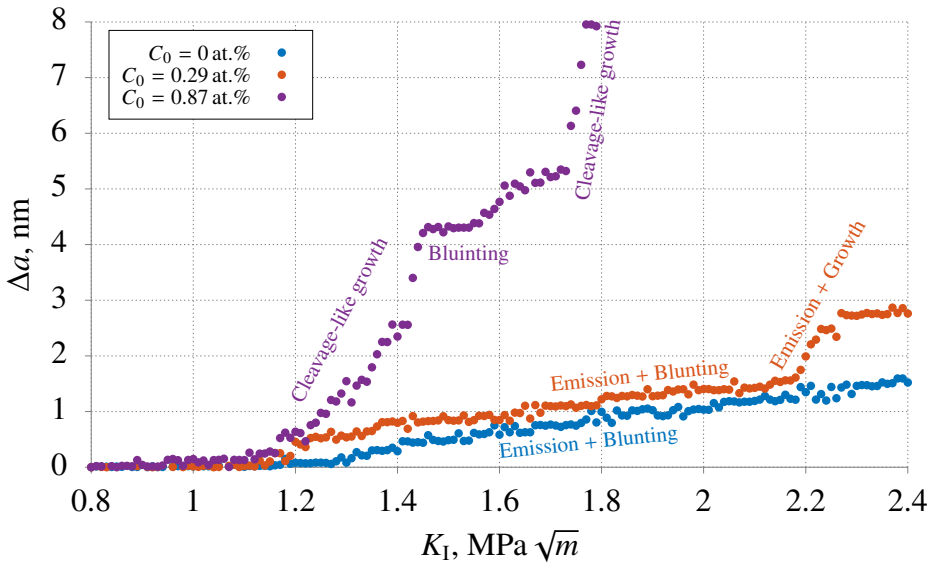

(a) $(1\,1\,1)[1\,1\,\bar{2}]$

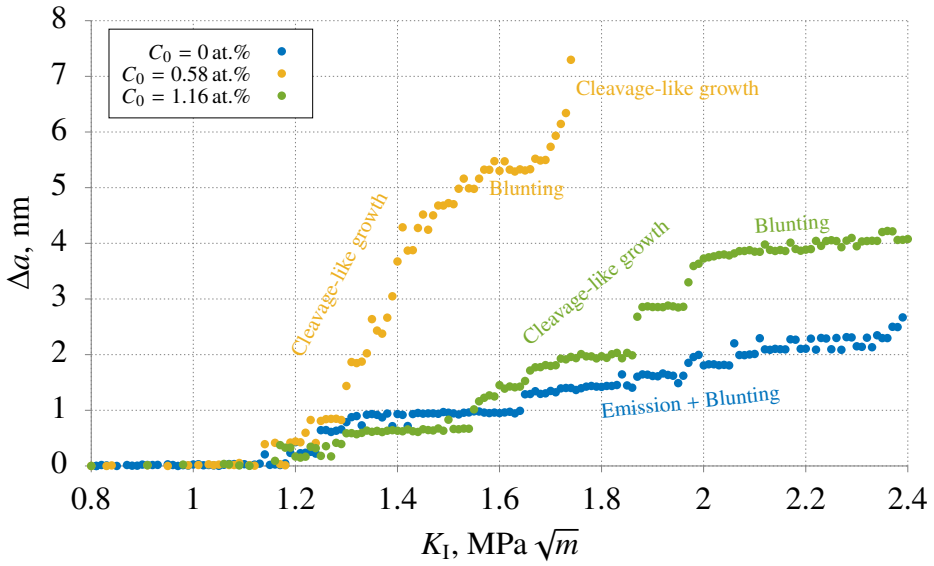

(b) $(1\,1\,1)[1\,\bar{1}\,0]$

Figure 6.14. Applied stress intensity factor K_I versus crack extension Δa for $(1\,1\,1)[1\,1\,\bar{2}]$ and $(1\,1\,1)[1\,\bar{1}\,0]$ crack orientations.

The effect of hydrogen on the fracture toughness on the $(1\,0\,0)[0\,1\,0]$ crack orientation can be seen in Fig. 6.15. It can be seen that increasing the hydrogen concentration to $C_0 = 0.29$ at.% reduces the stress intensity needed to start crack growth by nearly $0.2\,\text{MPa}\sqrt{\text{m}}$. This reduction is maintained for concentrations below 1.45 at.%. Increasing the H concentration above that value delays the onset of crack growth to nearly $1.4\,\text{MPa}\sqrt{\text{m}}$ due to the formation of an FCC phase at the crack-tip, as shown in Fig. 6.13. Figure 6.15 suggests that for the $(1\,0\,0)[0\,1\,0]$ crack orientation hydrogen damage is severe within a concentration window. Concentrations above this range, approximately between 0.29 and 1.16 at.%, will not result in greater crack extensions than in the absence of H.

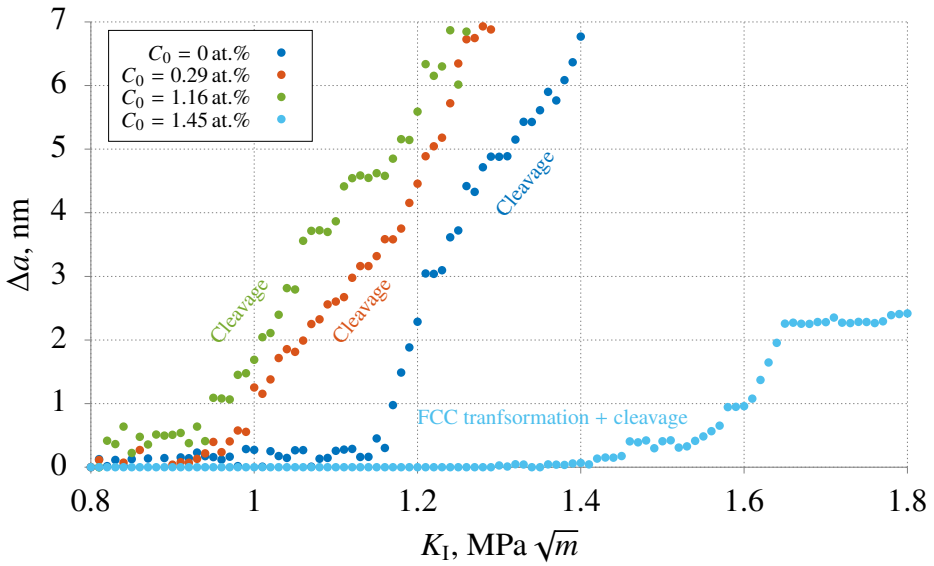

Figure 6.15. Applied stress intensity factor K_I versus crack extension Δa for (1 0 0)[0 1 0] crack orientation.

6.4 Discussion

6.4.1 Connection with experimental fracture mechanics results

The applied values of K_I that produced crack growth in these simulations are more than an order of magnitude below fracture toughness values reported for steels. For instance, K_{Ic} for an ANSI 1144 steel was reported as 66 MPa$\sqrt{\text{m}}$ [194], whereas in this work, crack advance was observed at values of K_I lower than 3 MPa$\sqrt{\text{m}}$. This discrepancy can be attributed to the fact that in these simulations the region around the crack-tip consists of perfect material as microstuctural defects that play a significant role in the deformation process (e.g. grain boundaries, inclusions, other dislocations, etc.) have not been included. The fracture process in a real material is affected by the presence of these defects, in many cases increasing the stress needed to sustain crack growth; for instance, when the crack-tip encounters a grain boundary. Another important factor is the significant length scale difference between experimental tests and MD simulations. The fracture toughness values obtained from these simulations correspond to crack extensions in the nanometre length scale, which are too small to be detected in experimental K-controlled fracture tests. For K-controlled fracture MD simulations, as the resistance to crack extension increases (e.g. due to the blunting of the crack-tip by dislocation emission), higher values of stress intensity factor are needed to produce crack growth. When K_I is high enough, other stress relieving mechanisms (e.g. microvoid coalescence) are possible. Unstable crack growth can then take place at values of K_I similar to those reported in K-controlled fracture experiments. While in theory is possible to capture this behaviour using MD simulations, the computational effort needed to maintain small scale yielding conditions as the plastic zone increases with the applied K_I makes such simulations impractical.

6.4.2 Effect of H on crack-tip dislocation emission

The fracture process on the $(1\,1\,1)[1\,1\,\overline{2}]$ crack orientation showed the emission of dislocations from the crack-tip. In the absence of hydrogen or at very low concentrations (e.g. 0.14 at.%), dislocations were emitted on $\{1\,1\,2\}$ planes perpendicular to the crack plane normal. However, at concentrations close to 0.29 at.% the emission of $\frac{1}{2}\langle 1\,1\,1\rangle$ dislocations on $\{1\,1\,0\}$ slip planes at approximately 35° from the crack plane normal was also observed (Fig. 6.7). The emission of these dislocations re-sharpened the crack which resulted in greater crack extension per increment of stress intensity factor.

These observations can be rationalised as follows. The nucleation of a dislocation from the crack-tip requires the simultaneous formation of a dislocation core and a surface step, a process that occurs via the shearing of the atomic planes near the surface. Surface hydrogen atoms could modify the energy barrier required for shearing, so that certain atomic planes can be sheared more easily than others (e.g. the $\{1\,1\,0\}$ planes compared with $\{1\,1\,2\}$ planes). The conditions at the crack-tip at which dislocation emission will occur can be estimated using the Rice emission criterion [195]. The stress needed to nucleate a dislocation is closely related to the unstable stacking fault energy γ_{us}. This quantity is a measure of the resistance to dislocation emission of the material, and depends on the slip plane and sliding direction. In an isotropic material, the energy release rate for dislocation emission under mode I loading is given by equation (6.11) [195, 196]

$$G_{\text{Ie}} = \gamma_{\text{us}} \frac{1 + (1-\nu)\tan^2\phi}{f_{\text{I}}^2(\theta)} \tag{6.11}$$

where θ is the angle between the slip plane and the crack plane, ϕ is the angle between the dislocation burgers vector in the slip plane under consideration and the vector perpendicular to the crack front on the slip plane, and $f_{\text{I}}(\theta)$ the θ-dependent portion of the shear stress resolved on the slip plane. G_{Ie} gives an indication of the driving force needed for dislocation emission. If hydrogen favoured the nucleation of dislocations on $\{1\,1\,0\}$ plane, that could happen via the modification of γ_{us}. Accurate determination of γ_{us} is difficult as it requires the dependence of the generalised stacking fault energy on the hydrogen concentration, the effects of hydrogen on the surface step created by the nucleation of the dislocation and the modification of stress fields due to hydrogen. Estimations using molecular statistics on FCC and BCC materials suggest that γ_{us} can be modified due to the presence of hydrogen [44, 197]. If hydrogen produced an increase of γ_{us} on the $\{1\,1\,2\}$ planes greater than that of the $\{1\,1\,0\}$, that could tilt the balance in favour of the activation of $\{1\,1\,0\}$ planes. The simulations in pure iron performed in this work suggest that the preferred slip planes are those perpendicular to the crack plane, namely, the $(1\,1\,\overline{2})$ on the $(1\,1\,1)[1\,1\,\overline{2}]$ crack orientation and the $(1\,\overline{1}\,0)$ on the and $(1\,1\,1)[1\,\overline{1}\,0]$ crack orientation. In the case of the latter crack orientation, if hydrogen favoured slip on $\{1\,1\,0\}$

planes, this would reinforce the preference of the $(1\,\bar{1}\,0)$ plane and dislocation emission would only occur perpendicularly to the crack plane, as observed in the simulations done in this work (Fig. 6.11a). In the case of the $(1\,1\,1)[1\,1\,\bar{2}]$ crack orientation, if slip on the $\{1\,1\,0\}$ was favoured, that would make $\{1\,1\,0\}$ slip planes oblique to the crack plane also possible, resulting in two slip planes available for dislocation emission: the $(1\,1\,\bar{2})$ plane, perpendicular with the crack plane, and the $(1\,1\,0)$ plane, oblique to the crack plane. The $(1\,1\,\bar{2})$ is still the main slip plane, however, at higher values of K_{I} the activation of secondary slip planes, e.g. the $(1\,1\,0)$ plane, can also occur.

6.4.3 Connection to AIDE mechanism

The AIDE mechanism proposes that, since hydrogen damage can also occur at low D/v ratios ($D/v < 10^{-8}\,\mathrm{cm}^{-1}$), where v is the crack velocity and D is the diffusivity of H, adsorption is responsible. Under these circumstances, enhanced plasticity has been reported despite diffusion of hydrogen ahead of the crack-tip being unlikely [8, 62]. Lynch suggested that the enhanced plasticity at the crack-tip was caused by hydrogen adsorbed on the surfaces of the crack-tip as opposed to diffusible hydrogen. The simulations performed in this work allowed sufficiently long relaxations between K_{I} increments. However, dislocations nucleating on oblique slip planes were also observed when allowing shorter simulation times. As shown in Fig. 6.9, these type of dislocations were emitted when using relaxation times as short as 10 ps, which can result in crack velocities producing D/v ratios close to $10^{-8}\,\mathrm{cm}^{-1}$. The same was not true for concentrations where hydrogen was present in the bulk, where the fracture behaviour changed considerably by reducing the relaxation time between K_{I} increments. The slow crack growth process shown in Fig. 6.10 was no longer observed, due to the insufficient time for H atoms to diffuse to the crack-tip. This suggests that the effect hydrogen on the plasticity around the crack-tip seen in Fig. 6.7 is not time-dependant and supports the idea that it is caused by adsorbed hydrogen, as proposed by the AIDE mechanism.

Furthermore, the crack-tip observations on which AIDE was based, show considerable amount of localised plasticity, suggesting that the Hydrogen Enhance Decohesion (HEDE) mechanism does not predominate [8, 62]. In this work, Fig. 6.7 shows increased crack extension and noticeable plastic deformation around the crack-tip, confirming that the HEDE mechanism is not operative at that H concentration. Dislocations emitted from the crack-tip on $\{1\,1\,2\}$ and $\{1\,1\,0\}$ planes, perpendicular and oblique to the crack plane, are responsible for the localised plasticity seen in Fig. 6.7. The main role of hydrogen seems to be to facilitate the emission of dislocations on $\{1\,1\,0\}$ slip planes. Dislocations on secondary slip systems could contribute to the development of other types of defects around the crack-tip. The presence of dislocations emitted on oblique planes will likely interact with the nucleation of new dislocations, which can lead to formation of other defects not seen in the absence of hydrogen. For instance, in Fig. 6.7d the formation of a twin, resulting from the interaction of $\frac{1}{2}\langle 1\,1\,1\rangle$ dislocations gliding on $\{1\,1\,2\}$ planes, can

be seen. Twinning was not observed in the fracture of pure Fe as dislocations tend to form pile-ups.

6.4.4 Viability of HE mechanisms

The manifestations of hydrogen embrittlement seen in section 6.3 can be related to some of the HE mechanisms proposed in the literature. Aside from the similarities with the AIDE mechanism discussed in the previous paragraph, other mechanisms such as HELP and HEDE may operate. In the case of HELP, increased plasticity localised at the crack-tip is needed. Plasticity comes in the form of high dislocation activity, leading to the formation of nanovoids and crack growth. These features have been observed on the $(1\,1\,1)[1\,\bar{1}\,0]$ crack orientation from H concentrations of 1.16 at.%, as shown in figures 6.11c and 6.11d. As the HELP model proposes, transport of hydrogen solutes in sufficient quantities to the regions ahead of the crack-tip is necessary. As shown in Fig. 6.11, the fracture behaviour is changed considerably by reducing the H concentration. For concentrations below 1.16 at.%, the dislocation activity was limited.

The relatively planar fracture surfaces seen in the $(1\,1\,1)[1\,1\,\bar{2}]$ crack orientation at H concentrations of 0.87 at.% (figure 6.10) and the $(1\,1\,1)[1\,\bar{1}\,0]$ crack orientation at 0.58 at.% (Fig. 6.11b) could be considered a manifestation of the HEDE mechanism. For instance, a similar slow crack growth process observed in K-test experiments using Fe–3 % Si single crystals under H gas environment were rationalised using the HEDE model [198]. HEDE proposes that cleavage is achieved by the weakening of the interatomic bonds at the crack-tip and that dislocation activity plays a secondary role in the fracture process [199]. However, in the simulations in this work, it can be seen that such planar fracture surfaces are the result of the prevention of dislocation emission from the crack-tip as opposed to a decrease in lattice cohesion. Furthermore, while these features would appear flat at the hundreds of nanometre length scale, they are not atomically flat as crack growth does not seem to follow any particular cleavage plane. This suggests that rather than weakening interatomic bonds, hydrogen hinders dislocation emission and cleavage occurs as an alternative stress relieving mechanism. The cleavage fracture seen on the $(1\,0\,0)[0\,1\,0]$ orientation seems more inline with the HEDE mechanism, as the reduction in stress intensity needed for crack growth can be related to reduction of cohesion at the crack-tip. However, this reduction in cohesion was not only seen at high H concentrations in which H aggregation at the crack-tip occurs, but also at low concentrations in which limited H was present in the bulk. This conflicts with the HEDE mechanism as H diffusion to regions ahead of the crack-tip is an important part of the embrittlement process, as hydrogen needs to be present in sufficient quantities to induce decohesion. The cohesion reduction when HEDE was active was noticeable, as demonstrated by the lower stress intensity needed to produce crack growth (approximately $0.2\,\mathrm{MPa}\sqrt{\mathrm{m}}$). This effect could be greater if factoring in microstructural defects such as inclusions and grain boundaries. These defects function as cleavage sources that become more potent with H segregation.

6.4.5 Spectrum of HE mechanisms

A number of distinct HE failure modes were observed in the simulations carried out in this work:

1. Crack-tip re-sharpening due to emission of dislocations oblique to the crack plane: e.g on the $(1\,1\,1)[1\,1\,\overline{2}]$ orientation at $C_0 = 0.29$ at.% (figure 6.7).
2. Slow crack growth resulting from alternation of cleavage and dislocation emission from the crack-tip: e.g. on the $(1\,1\,1)[1\,1\,\overline{2}]$ orientation at $C_0 = 0.87$ at.% and $(1\,1\,1)[1\,\overline{1}\,0]$ orientation at $C_0 = 0.58$ at.% (figures 6.10 and 6.11b, respectively).
3. Increased plasticity and nano-void formation at the crack-tip: e.g. on the $(1\,1\,1)[1\,\overline{1}\,0]$ orientation at $C_0 = 1.45$ at.% (figure 6.11d).
4. Cleavage at reduced stress intensity: e.g. on the $(1\,0\,0)[0\,1\,0]$ orientation at $C_0 = 0.58$ at.% (figure 6.12).
5. Hydrogen induced FCC transformation and cleavage: e.g. $(1\,0\,0)[0\,1\,0]$ orientation at $C_0 = 1.45$ at.% (figure 6.13).

For a simplified scenario, with only a few tens of nanometres around the crack-tip in an initially perfect crystal, like the one considered in these simulations, the number of observed failure modes that resulted from the variation in hydrogen concentration and crystal orientation was high. It is reasonable to assume that the possible number of failure mechanisms that can be operative in a real crack in a material containing microstructural defects that affect the fracture process would be even higher. Therefore, we might have a spectrum of HE mechanisms as opposed to a single mechanism that operates for a given material or that is responsible for a certain fracture morphology. The models proposed in the literature might be only a small part of such spectrum.

6.5 Conclusions

The effect of hydrogen on the fracture behaviour of three crack orientations, in BCC Fe was investigated using molecular dynamics. Results indicate that hydrogen can reduce the material's load bearing capacity in a number of ways depending on the hydrogen concentration and crack orientation, leading to failure in either ductile or brittle mode.

Increasing the hydrogen concentration resulted in reduced fracture toughness, as the crack growth started at lower stress intensity factor values and resulted in larger crack extensions when compared with pure Fe. For crack orientations that fail in a ductile manner in the absence of hydrogen, crack growth was more severe at medium H concentrations (0.58 – 0.87 at.%), when the emission of dislocations from the crack-tip was prevented and fracture occurred in a cleavage-like fashion. Other failure mechanisms resembling the HELP and AIDE mechanisms were also observed in certain conditions. HELP was observed on the

$(1\,1\,1)[1\,\bar{1}\,0]$ orientation with H concentrations above 1.16 at.%, and AIDE was observed on the $(1\,1\,1)[1\,1\,\bar{2}]$ orientation with a H concentration of 0.29 at.%. Crack growths produced by these mechanisms were higher than those in pure Fe, suggesting a detrimental effect on the material's fracture toughness.

In the orientation failing in a brittle manner in the absence of hydrogen, the $(1\,0\,0)[0\,1\,0]$, the most severe hydrogen damage occurred with H concentrations between 0.29 and 1.16 at.%. At these concentrations, crack growth started at lower stress intensity factor values than those in pure Fe. This behaviour is consistent with the HEDE mechanism, as the lower stress intensity needed for crack growth is an indication of the reduction of the lattice cohesion. At higher concentrations, H accumulation at the crack-tip resulted in a FCC transformation, and cleavage was produced along a stacking fault that formed as the stress intensity was increased. This deformation mechanism require higher stress intensity than the deformation in pure Fe. Nevertheless, it illustrates how hydrogen can affect the fracture process of Fe.

Chapter 7

Conclusions and Further Work

The aim of this work was to investigate the mechanisms of hydrogen embrittlement that operate in steels using molecular dynamics simulation. Consequently, three different molecular dynamics studies were carried out. The main findings of these studies are presented in the following paragraphs.

7.1 Atomistic simulations of tensile test

Chapter 4 investigated the impact of C on the mechanical properties of ferrite with the aim of determining whether neglecting C atoms from the solid solution was detrimental to the accuracy of the simulation. The tensile strength of α-Fe and ferrite single crystals was calculated from tensile test simulations. The tests were performed in two configurations (periodic and non-periodic boundary conditions) along four different orientations ([1 1 1], [1 $\overline{1}$ 0], [1 1 $\overline{2}$] and [1 0 0]), and using strain rates ranging from 10^7 to $10^{10}\,\mathrm{s}^{-1}$.

Results showed that the strength of the supercell can be increased by up to 20 % by including C atoms in the simulation. These differences were noticeable in orientations that failed due to dislocation slip, namely the [1 1 1] and the [1 $\overline{1}$ 0] orientations, indicating that the increased strength is a consequence of dislocations locking up to C interstitials. The strengthening effect of carbon was not seen in nanowhiskers, most likely due to the high surface-to-volume ratio that controls the mechanical response. As shown in tables 4.1 and 4.2, the strongest orientations were those failing due to dislocation slip, the [1 1 1] and [1 $\overline{1}$ 0] orientations, followed by those failing due to twinning, the [1 1 $\overline{2}$] and the [1 0 0] orientations. This trend was seen in both ferrite and α-Fe. The higher strength of the [1 1 1] and [1 $\overline{1}$ 0] orientations was attributed to the higher energy required for the nucleation of a full $\frac{1}{2}$ [1 1 1] dislocation, which in these two orientations is favourably oriented.

Two regimes were observed when describing the dependence of $\sigma_{\max}$ on the strain rate $\dot{\varepsilon}$, as shown in figure 4.6: 1) at low strain rates, $\dot{\varepsilon}$ seem to have no influence on $\sigma_{\max}$ as the

latter fluctuates around a constant value, and 2) at high strain rates, σ_{max} is a function of $\dot{\varepsilon}$. This behaviour was attributed to the transition between thermally assisted and athermal yielding that results from the encounters of dislocations with obstacles in the crystal such as C interstitials and other dislocations. High strain rates limit the amount thermal assistance so that more mechanical energy is required for dislocation motion, resulting in higher recorded stresses.

7.2 Hydrogen effects on dislocation mobility

The effects of hydrogen on the mobility of an edge dislocation was investigated in chapter 5 in order to test one of the main concepts of the HELP theory: hydrogen enhanced dislocation mobility. The simulations used the periodic array of dislocations (PAD) model, in which an edge dislocation is introduced in the supercell and, due to the periodicity in the glide direction, is allowed to glide indefinitely through the application of shear stress. The dislocation mobility was tested under 4 different scenarios: 1) in pure Fe, 2) in the presence of a C interstitial, 3) in the presence of H solutes, and 4) in the presence of a C interstitial and H solutes.

In pure Fe, the dislocation was able to glide readily and dislocation motion followed viscous drag dynamics, as shown in figures 5.8 and 5.9. In this regime, the calculated glide velocity was proportional to the applied stress and corresponded to the free-flight velocity of the dislocation as there was little resistance to dislocation motion, which came mainly from lattice vibrations. These vibrations are more numerous at higher temperatures, which resulted in higher drag coefficients and lower glide velocities as the temperature was increased.

In the presence of a C interstitial, the mobility of the dislocation was controlled by the time taken to overcome the C interstitial that initially pinned the dislocation, as shown in figure 5.10. Consequently, glide velocities were significantly lower when compared to the pure Fe scenario. The glide velocity was approximately 5 times lower in the presence of a C interstitial than in pure Fe, as seen in figures 5.7 and 5.10. Because the dislocation motion was dominated by the contact times with the C interstitial, increasing the temperature, which also increased the amount of thermal assistance for unpinning the dislocation, resulted in higher glide velocities and lower drag coefficients, as seen in figure 5.11. This behaviour is consistent with experimental measurements of glide velocities in Fe.

Adding H solutes to the supercell resulted in the formation of Cottrell clouds in the tensile stress field of the dislocation core. The formation of this clouds was detrimental for dislocation motion as solute drag controlled the glide process. As shown in figure 5.14, glide velocities in the solute drag regime were up to three orders of magnitude lower than in the viscous drag regime (pure Fe), suggesting that the effect of hydrogen in the core of edge dislocations alone is unlikely to result in enhanced dislocation motion.

In the presence of a C interstitial and H solutes, dislocation mobility was restricted even further as glide was only observed when the dislocation became unpinned from the C interstitial and the H cloud dissolved, as seen in figure 5.20. Since the stress needed to unpin the dislocation from the C interstitial increased with the H concentration, the limited dislocation mobility was attributed to the synergy between C and H solutes. Hydrogen solutes do not seem to reduce the interaction energy of the C interstitial with the dislocation, resulting in higher stresses needed to unpin the dislocation. Furthermore, solute drag, another viable mechanism for dislocation glide, was not observed due to the low diffusivity of C in Fe. As discussed in section 5.3.2, additional pinning points consisting of H clusters that form due to the asymmetrical bow out of the dislocation when locked to the C interstitial might further hinder dislocation mobility.

These results indicate that hydrogen decreases the mobility of edge dislocations when gliding unobstructed or when gliding through a field of obstacles such a C interstitials. Enhanced dislocation motion was not observed in these simulations.

7.3 Hydrogen effects on fracture

The effects of hydrogen on the fracture process of BCC Fe was studied in chapter 6. Three crack orientations were studied, namely, the $(1\,1\,1)[1\,1\,\overline{2}]$, the $(1\,1\,1)[1\,\overline{1}\,0]$ and the $(1\,0\,0)[0\,1\,0]$ orientations and the fracture behaviour with H concentrations ranging from 0.14 to 1.45 at.% was investigated.

Results show how increasing the H concentration changed the fracture process, which in several cases resulted in an overall decrease of the material's fracture toughness. As shown in figures 6.7 to 6.11, orientations in which failure is ductile in the absence of hydrogen (the $(1\,1\,1)[1\,1\,\overline{2}]$ and $(1\,1\,1)[1\,\overline{1}\,0]$ orientations), toughness was high and increasing the stress intensity factor resulted only in limited crack extension. However, in the presence of hydrogen, toughness decreased and failure occurred via mechanisms that resulted in greater crack extensions for a given stress intensity. These mechanisms resemble well-known HE mechanisms such as AIDE, HEDE and HELP.

In the $(1\,0\,0)[0\,1\,0]$ orientation, fracture was brittle in the absence of hydrogen, as seen in figure 6.5. When hydrogen was present in concentrations below 1.16 at.%, the effect of hydrogen was to reduce the stress intensity needed for the crack growth onset, as shown in figure 6.12. This is an indication of a reduction in lattice cohesion, which together with the completely planar fracture surface, is consistent with the HEDE model. At higher concentrations, hydrogen accumulated at the crack-tip and induced an FCC transformation, as seen in figure 6.13. Cleavage occurred along planes oblique to the original crack plane. While this failure mechanism required higher values of stress intensity, it illustrates how hydrogen can influence the fracture process.

These simulations showed that HE mechanisms proposed in the literature can be operative

in pure Fe (e.g. HEDE, HELP and AIDE), depending on the crack tip conditions. It was also suggested that a full spectrum of HE mechanism might be possible. The preference of one HE mechanism over others seems to be affected by a number of factors, such as the local hydrogen concentration, the active cleavage and slip planes and the crack velocity; this explains the great number of findings reported in the literature.

7.4 Further Work

The role of different microstructural defects on the fracture process of Fe and the effect that hydrogen has in their presence should be investigated further. Grain boundaries were not studied in this work, and there is debate on the HE mechanisms that are responsible for intergranular failure. The author also believes that the role of cementite in hydrogen embrittlement deserves greater attention. It has been suggested that this phase can function as an irreversible hydrogen trap when located at grain boundaries and lath interfaces [200]. Furthermore, there is great interest in repurposing natural gas pipelines to hydrogen service. Pipeline materials with ferritic-pearlitic microstructure can be widely found in the UK gas transmission network. Therefore, in order to achieve safe and cost-effective operation of repurposed hydrogen pipelines, the effect of hydrogen on cementite, as well as on cementite-ferrite interfaces, must be understood. This knowledge could contribute to the general understanding of hydrogen embrittlement mechanisms and help to design of steels with reduced susceptibility to this hydrogen damage.

Finally, there are other HE mechanisms proposed in the literature that can be investigated using atomistic simulations. For instance, the Hydrogen-Enhanced Strain-Induced Vacancies mechanism [201], in which hydrogen assisted vacancy cluster formation leads to the creation of nano-voids, causing premature failure when located near stress concentrators. Hydrogen is known to stabilise vacancies and reduce its energy of formation, which could enable the formation of nano-voids. Direct observations of vacancies and hydrogen is difficult with current characterisation techniques, making atomistic simulations a viable alternative for the study of this mechanism.

References

[1] BP, *Global and national perspectives. & BP statistical review of world energy*, https://www.bp.com/en/global/corporate/energy-economics/statistical-review-of-world-energy.html, Accessed: 2020-10-07, 2020. [Online]. Available: https://www.bp.com/content/dam/bp/business-sites/en/global/corporate/pdfs/energy-economics/statistical-review/bp-stats-review-2020-full-report.pdf.

[2] W. H. Johnson and W. Thomson, "II. On some remarkable changes produced in iron and steel by the action of hydrogen and acids," *Proceedings of the Royal Society of London*, vol. 23, no. 156-163, pp. 168–179, Jan. 1875. DOI: 10.1098/rspl.1874.0024. [Online]. Available: https://royalsocietypublishing.org/doi/abs/10.1098/rspl.1874.0024 (visited on 12/16/2021).

[3] A. R. Troiano, "The Role of Hydrogen and Other Interstitials in the Mechanical Behavior of Metals," en, *Metallography, Microstructure, and Analysis*, vol. 5, no. 6, pp. 557–569, Dec. 2016, ISSN: 2192-9270. DOI: 10.1007/s13632-016-0319-4. [Online]. Available: https://doi.org/10.1007/s13632-016-0319-4 (visited on 03/20/2021).

[4] R. A. Oriani, "A mechanistic theory of hydrogen embrittlement of steels," en, *Berichte der Bunsengesellschaft für physikalische Chemie*, vol. 76, no. 8, pp. 848–857, 1972, ISSN: 0005-9021. DOI: https://doi.org/10.1002/bbpc.19720760864. [Online]. Available: https://onlinelibrary.wiley.com/doi/abs/10.1002/bbpc.19720760864 (visited on 03/20/2021).

[5] C. D. Beachem, "A new model for hydrogen-assisted cracking (hydrogen "embrittlement")," en, *Metallurgical and Materials Transactions B*, vol. 3, no. 2, pp. 441–455, Feb. 1972, ISSN: 1543-1916. DOI: 10.1007/BF02642048. [Online]. Available: https://doi.org/10.1007/BF02642048 (visited on 03/20/2021).

[6] H. K. Birnbaum and P. Sofronis, "Hydrogen-enhanced localized plasticity—a mechanism for hydrogen-related fracture," en, *Materials Science and Engineering: A*, vol. 176, no. 1, pp. 191–202, Mar. 1994, ISSN: 0921-5093. DOI: 10.1016/0921-5093(94)90975-X. [Online]. Available: https://www.sciencedirect.com/science/article/pii/092150939490975X (visited on 03/20/2021).

[7] I. M. Robertson, "The effect of hydrogen on dislocation dynamics," en, *Engineering Fracture Mechanics*, vol. 68, no. 6, pp. 671–692, Apr. 2001, ISSN: 0013-7944.

DOI: 10.1016/S0013-7944(01)00011-X. [Online]. Available: https://www.sciencedirect.com/science/article/pii/S001379440100011X (visited on 03/20/2021).

[8] S. P. Lynch, "Environmentally assisted cracking: Overview of evidence for an adsorption-induced localised-slip process," en, *Acta Metallurgica*, vol. 36, no. 10, pp. 2639–2661, Oct. 1988, ISSN: 0001-6160. DOI: 10.1016/0001-6160(88)90113-7. [Online]. Available: https://www.sciencedirect.com/science/article/pii/0001616088901137 (visited on 03/20/2021).

[9] S. Lynch, "Hydrogen embrittlement phenomena and mechanisms," en, *Corrosion Reviews*, vol. 30, no. 3-4, pp. 105–123, Jun. 2012, ISSN: 2191-0316. DOI: 10.1515/corrrev-2012-0502. [Online]. Available: https://www.degruyter.com/document/doi/10.1515/corrrev-2012-0502/html (visited on 03/20/2021).

[10] M. S. Daw and M. I. Baskes, "Embedded-atom method: Derivation and application to impurities, surfaces, and other defects in metals," *Physical Review B*, vol. 29, no. 12, pp. 6443–6453, Jun. 1984. DOI: 10.1103/PhysRevB.29.6443. [Online]. Available: https://link.aps.org/doi/10.1103/PhysRevB.29.6443 (visited on 11/09/2021).

[11] S. Cheung, W.-Q. Deng, A. C. T. van Duin, and W. A. Goddard, "ReaxFF MgH Reactive Force Field for Magnesium Hydride Systems," *The Journal of Physical Chemistry A*, vol. 109, no. 5, pp. 851–859, Feb. 2005, ISSN: 1089-5639. DOI: 10.1021/jp0460184. [Online]. Available: https://doi.org/10.1021/jp0460184 (visited on 11/09/2021).

[12] M. M. Islam, C. Zou, A. C. T. v. Duin, and S. Raman, "Interactions of hydrogen with the iron and iron carbide interfaces: A ReaxFF molecular dynamics study," en, *Physical Chemistry Chemical Physics*, vol. 18, no. 2, pp. 761–771, Dec. 2015, ISSN: 1463-9084. DOI: 10.1039/C5CP06108C. [Online]. Available: https://pubs.rsc.org/en/content/articlelanding/2016/cp/c5cp06108c (visited on 03/20/2021).

[13] A. Ramasubramaniam, M. Itakura, and E. A. Carter, "Interatomic potentials for hydrogen in α–iron based on density functional theory," *Physical Review B*, vol. 79, no. 17, p. 174 101, May 2009. DOI: 10.1103/PhysRevB.79.174101. [Online]. Available: https://link.aps.org/doi/10.1103/PhysRevB.79.174101 (visited on 03/20/2021).

[14] J. Song and W. A. Curtin, "Atomic mechanism and prediction of hydrogen embrittlement in iron," en, *Nature Materials*, vol. 12, no. 2, pp. 145–151, Feb. 2013, ISSN: 1476-4660. DOI: 10.1038/nmat3479. [Online]. Available: https://www.nature.com/articles/nmat3479 (visited on 03/20/2021).

[15] D. H. Herring, "Hydrogen embrittlement," *Wire Forming Technology International*, vol. 13, no. 4, pp. 24–27, 2010.

[16] D. G. Westlake, "The habit planes of zirconium hydride in zirconium and zircaloy," en, *Journal of Nuclear Materials*, vol. 26, no. 2, pp. 208–216, May 1968, ISSN: 0022-3115. DOI: 10.1016/0022-3115(68)90072-X. [Online]. Available: https://www.sciencedirect.com/science/article/pii/002231156890072X (visited on 12/16/2021).

[17] H. K. Birnbaum, "Mechanical properties of metal hydrides," en, *Journal of the Less Common Metals*, vol. 104, no. 1, pp. 31–41, Dec. 1984, ISSN: 0022-5088. DOI: 10.1016/0022-5088(84)90433-8. [Online]. Available: https://www.sciencedirect.com/science/article/pii/0022508884904338 (visited on 12/16/2021).

[18] S. P. Lynch, "2 - Hydrogen embrittlement (HE) phenomena and mechanisms," en, in ser. Woodhead Publishing Series in Metals and Surface Engineering, V. S. Raja and T. Shoji, Eds., Woodhead Publishing, Jan. 2011, pp. 90–130, ISBN: 9781845696733. DOI: 10.1533/9780857093769.1.90. [Online]. Available: https://www.sciencedirect.com/science/article/pii/B978184569673350002X (visited on 11/17/2021).

[19] S. Simonetti, L. Moro, G. Brizuela, and A. Juan, "The interaction of carbon and hydrogen in a α-Fe divacancy," en, *International Journal of Hydrogen Energy*, vol. 31, no. 10, pp. 1318–1325, Aug. 2006, ISSN: 0360-3199. DOI: 10.1016/j.ijhydene.2005.11.019. [Online]. Available: https://www.sciencedirect.com/science/article/pii/S0360319905003526 (visited on 12/18/2021).

[20] Y. Tang and J. A. El-Awady, "Atomistic simulations of the interactions of hydrogen with dislocations in fcc metals," *Physical Review B*, vol. 86, no. 17, p. 174 102, Nov. 2012. DOI: 10.1103/PhysRevB.86.174102. [Online]. Available: https://link.aps.org/doi/10.1103/PhysRevB.86.174102 (visited on 12/18/2021).

[21] A. M. Tahir, R. Janisch, and A. Hartmaier, "Hydrogen embrittlement of a carbon segregated Σ5(310)[001] symmetrical tilt grain boundary in α-Fe," en, *Materials Science and Engineering: A*, vol. 612, pp. 462–467, Aug. 2014, ISSN: 0921-5093. DOI: 10.1016/j.msea.2014.06.071. [Online]. Available: https://www.sciencedirect.com/science/article/pii/S0921509314007886 (visited on 12/18/2021).

[22] W. T. Geng, A. J. Freeman, and G. B. Olson, "Influence of alloying additions on the impurity induced grain boundary embrittlement," en, *Solid State Communications*, vol. 119, no. 10, pp. 585–590, Aug. 2001, ISSN: 0038-1098. DOI: 10.1016/S0038-1098(01)00298-8. [Online]. Available: https://www.sciencedirect.com/science/article/pii/S0038109801002988 (visited on 12/18/2021).

[23] L. Zhong, R. Wu, A. J. Freeman, and G. B. Olson, "Charge transfer mechanism of hydrogen-induced intergranular embrittlement of iron," *Physical Review B*, vol. 62, no. 21, pp. 13 938–13 941, Dec. 2000. DOI: 10.1103/PhysRevB.62.13938. [Online].

Available: https://link.aps.org/doi/10.1103/PhysRevB.62.13938 (visited on 12/18/2021).

[24] A. Tehranchi and W. A. Curtin, "The role of atomistic simulations in probing hydrogen effects on plasticity and embrittlement in metals," en, *Engineering Fracture Mechanics*, vol. 216, p. 106 502, Jul. 2019, ISSN: 0013-7944. DOI: 10.1016/j.engfracmech.2019.106502. [Online]. Available: https://www.sciencedirect.com/science/article/pii/S001379441930308X (visited on 03/20/2021).

[25] R. Gangloff, "Hydrogen assisted cracking of high strength alloys," in *Comprehensive Structural Integrity*, I. Milne, R. Ritchie, and B. Karihaloo, Eds., Oxford: Pergamon, 2003, pp. 31–101, ISBN: 978-0-08-043749-1. DOI: https://doi.org/10.1016/B0-08-043749-4/06134-6. [Online]. Available: https://www.sciencedirect.com/science/article/pii/B0080437494061346.

[26] I. M. Robertson *et al.*, "Hydrogen Embrittlement Understood," en, *Metallurgical and Materials Transactions B*, vol. 46, no. 3, pp. 1085–1103, Jun. 2015, ISSN: 1543-1916. DOI: 10.1007/s11663-015-0325-y. [Online]. Available: https://doi.org/10.1007/s11663-015-0325-y (visited on 12/08/2021).

[27] Q. Liu, Q. Zhou, J. Venezuela, M. Zhang, and A. Atrens, "Hydrogen influence on some advanced high-strength steels," en, *Corrosion Science*, vol. 125, pp. 114–138, Aug. 2017, ISSN: 0010-938X. DOI: 10.1016/j.corsci.2017.06.012. [Online]. Available: https://www.sciencedirect.com/science/article/pii/S0010938X17304493 (visited on 12/18/2021).

[28] M. Koyama, E. Akiyama, Y.-K. Lee, D. Raabe, and K. Tsuzaki, "Overview of hydrogen embrittlement in high-Mn steels," en, *International Journal of Hydrogen Energy*, vol. 42, no. 17, pp. 12 706–12 723, Apr. 2017, ISSN: 0360-3199. DOI: 10.1016/j.ijhydene.2017.02.214. [Online]. Available: https://www.sciencedirect.com/science/article/pii/S0360319917308418 (visited on 12/18/2021).

[29] A. V. Bochkaryova, Y. V. Li, S. A. Barannikova, and L. B. Zuev, "The effect of hydrogen embrittlement on the mechanical properties of aluminum alloy," en, *IOP Conference Series: Materials Science and Engineering*, vol. 71, p. 012 057, Jan. 2015, ISSN: 1757-899X. DOI: 10.1088/1757-899X/71/1/012057. [Online]. Available: https://doi.org/10.1088/1757-899x/71/1/012057 (visited on 12/18/2021).

[30] Y. Yao, X. Pang, and K. Gao, "Investigation on hydrogen induced cracking behaviors of Ni-base alloy," en, *International Journal of Hydrogen Energy*, vol. 36, no. 9, pp. 5729–5738, May 2011, ISSN: 0360-3199. DOI: 10.1016/j.ijhydene.2011.01.123. [Online]. Available: https://www.sciencedirect.com/science/article/pii/S0360319911002138 (visited on 12/18/2021).

[31] G. A. Young, E. Richey, and D. S. Morton, "5 - Hydrogen embrittlement in nuclear power systems," en, in ser. Woodhead Publishing Series in Metals and Surface En-

gineering, R. P. Gangloff and B. P. Somerday, Eds., vol. 2, Woodhead Publishing, Jan. 2012, pp. 149–176, ISBN: 9781845696771. DOI: 10.1533/9780857093899.1.149. [Online]. Available: https://www.sciencedirect.com/science/article/pii/B9781845696771500053 (visited on 12/17/2021).

[32] T. Michler, M. Lindner, U. Eberle, and J. Meusinger, "3 - Assessing hydrogen embrittlement in automotive hydrogen tanks," en, in ser. Woodhead Publishing Series in Metals and Surface Engineering, R. P. Gangloff and B. P. Somerday, Eds., vol. 2, Woodhead Publishing, Jan. 2012, pp. 94–125, ISBN: 9781845696771. DOI: 10.1533/9780857093899.1.94. [Online]. Available: https://www.sciencedirect.com/science/article/pii/B978184569677150003X (visited on 12/18/2021).

[33] M. Nagumo and H. Matsuda, "Function of hydrogen in intergranular fracture of martensitic steels," *Philosophical Magazine A*, vol. 82, no. 17-18, pp. 3415–3425, Nov. 2002, ISSN: 0141-8610. DOI: 10.1080/01418610208240452. [Online]. Available: https://doi.org/10.1080/01418610208240452 (visited on 12/10/2021).

[34] D. Hardie, E. A. Charles, and A. H. Lopez, "Hydrogen embrittlement of high strength pipeline steels," en, *Corrosion Science*, vol. 48, no. 12, pp. 4378–4385, Dec. 2006, ISSN: 0010-938X. DOI: 10.1016/j.corsci.2006.02.011. [Online]. Available: https://www.sciencedirect.com/science/article/pii/S0010938X06000710 (visited on 03/22/2021).

[35] S. V. Brahimi, S. Yue, and K. R. Sriraman, "Alloy and composition dependence of hydrogen embrittlement susceptibility in high-strength steel fasteners," *Philosophical Transactions of the Royal Society A: Mathematical, Physical and Engineering Sciences*, vol. 375, no. 2098, p. 20 160 407, Jul. 2017. DOI: 10.1098/rsta.2016.0407. [Online]. Available: https://royalsocietypublishing.org/doi/10.1098/rsta.2016.0407 (visited on 04/07/2022).

[36] J. Venezuela *et al.*, "Determination of the equivalent hydrogen fugacity during electrochemical charging of 3.5NiCrMoV steel," en, *Corrosion Science*, vol. 132, pp. 90–106, Mar. 2018, ISSN: 0010-938X. DOI: 10.1016/j.corsci.2017.12.018. [Online]. Available: https://www.sciencedirect.com/science/article/pii/S0010938X17319595 (visited on 12/09/2021).

[37] H. Hagi, "Diffusion Coefficient of Hydrogen in Iron without Trapping by Dislocations and Impurities," *Materials Transactions, JIM*, vol. 35, no. 2, pp. 112–117, 1994. DOI: 10.2320/matertrans1989.35.112.

[38] T. Lu *et al.*, "Molecular dynamics study of the diffusion properties of H in Fe with point defects," en, *Fusion Engineering and Design*, vol. 113, pp. 340–345, Dec. 2016, ISSN: 0920-3796. DOI: 10.1016/j.fusengdes.2016.06.044. [Online]. Available: https://www.sciencedirect.com/science/article/pii/S0920379616304446 (visited on 08/10/2021).

[39] T. Michler, F. Schweizer, and K. Wackermann, "Review on the Influence of Temperature upon Hydrogen Effects in Structural Alloys," en, *Metals*, vol. 11, no. 3,

p. 423, Mar. 2021, ISSN: 2075-4701. DOI: 10.3390/met11030423. [Online]. Available: https://www.mdpi.com/2075-4701/11/3/423 (visited on 05/06/2022).

[40] C. Borchers, T. Michler, and A. Pundt, "Effect of Hydrogen on the Mechanical Properties of Stainless Steels," en, *Advanced Engineering Materials*, vol. 10, no. 1-2, pp. 11–23, 2008, ISSN: 1527-2648. DOI: 10.1002/adem.200700252. [Online]. Available: https://onlinelibrary.wiley.com/doi/abs/10.1002/adem.200700252 (visited on 05/06/2022).

[41] Y. Momotani, A. Shibata, D. Terada, and N. Tsuji, "Effect of strain rate on hydrogen embrittlement in low-carbon martensitic steel," en, *International Journal of Hydrogen Energy*, vol. 42, no. 5, pp. 3371–3379, Feb. 2017, ISSN: 0360-3199. DOI: 10.1016/j.ijhydene.2016.09.188. [Online]. Available: https://www.sciencedirect.com/science/article/pii/S0360319916329512 (visited on 12/10/2021).

[42] M. Nagumo, "Fundamentals of hydrogen embri," en, in M. Nagumo, Ed. Singapore: Springer, 2016, ch. Diffusion and Transport of Hydrogen, pp. 65–77, ISBN: 9789811001611. DOI: 10.1007/978-981-10-0161-1_4. [Online]. Available: https://doi.org/10.1007/978-981-10-0161-1_4 (visited on 12/18/2021).

[43] L. B. Pfeil and H. C. H. Carpenter, "The effect of occluded hydrogen on the tensile strength of iron," *Proceedings of the Royal Society of London. Series A, Containing Papers of a Mathematical and Physical Character*, vol. 112, no. 760, pp. 182–195, Aug. 1926. DOI: 10.1098/rspa.1926.0103. [Online]. Available: https://royalsocietypublishing.org/doi/10.1098/rspa.1926.0103 (visited on 12/08/2021).

[44] M. S. Daw and M. I. Baskes, "Application of the embedded atom method to hydrogen embrittlement," in *Chemistry and Physics of Fracture*, R. M. Latanision and R. H. Jones, Eds. Dordrecht: Springer Netherlands, 1987, pp. 196–218, ISBN: 978-94-009-3665-2. DOI: 10.1007/978-94-009-3665-2_12. [Online]. Available: https://doi.org/10.1007/978-94-009-3665-2_12.

[45] R. G. Hoagland and H. L. Heinisch, "An atomic simulation of the influence of hydrogen on the fracture behavior of nickel," en, *Journal of Materials Research*, vol. 7, no. 8, pp. 2080–2088, Aug. 1992, ISSN: 2044-5326, 0884-2914. DOI: 10.1557/JMR.1992.2080. [Online]. Available: https://www.cambridge.org/core/journals/journal-of-materials-research/article/abs/an-atomic-simulation-of-the-influence-of-hydrogen-on-the-fracture-behavior-of-nickel/F542EA74C50E0B368A8792810A459EA0 (visited on 12/08/2021).

[46] W.-T. Geng, A. J. Freeman, G. B. Olson, Y. Tateyama, and T. Ohno, "Hydrogen-promoted grain boundary embrittlement and vacancy activity in metals: Insights from *Ab Initio* total energy calculatons," *Materials Transactions*, vol. 46, no. 4, pp. 756–760, 2005. DOI: 10.2320/matertrans.46.756.

[47] T. C. Lee, I. M. Robertson, and H. K. Birnbaum, "An HVEM In situ deformation study of nickel doped with sulfur," en, *Acta Metallurgica*, vol. 37, no. 2, pp. 407–415, Feb. 1989, ISSN: 0001-6160. DOI: 10.1016/0001-6160(89)90225-3. [Online]. Available: https://www.sciencedirect.com/science/article/pii/0001616089902253 (visited on 12/08/2021).

[48] W. W. Gerberich, R. A. Oriani, M.-J. Lji, X. Chen, and T. Foecke, "The necessity of both plasticity and brittleness in the fracture thresholds of iron," *Philosophical Magazine A*, vol. 63, no. 2, pp. 363–376, Feb. 1991, ISSN: 0141-8610. DOI: 10.1080/01418619108204854. [Online]. Available: https://doi.org/10.1080/01418619108204854 (visited on 12/08/2021).

[49] B. Sun, W. Krieger, M. Rohwerder, D. Ponge, and D. Raabe, "Dependence of hydrogen embrittlement mechanisms on microstructure-driven hydrogen distribution in medium Mn steels," en, *Acta Materialia*, vol. 183, pp. 313–328, Jan. 2020, ISSN: 1359-6454. DOI: 10.1016/j.actamat.2019.11.029. [Online]. Available: https://www.sciencedirect.com/science/article/pii/S1359645419307608 (visited on 12/08/2021).

[50] J. Han, J.-H. Nam, and Y.-K. Lee, "The mechanism of hydrogen embrittlement in intercritically annealed medium Mn TRIP steel," en, *Acta Materialia*, vol. 113, pp. 1–10, Jul. 2016, ISSN: 1359-6454. DOI: 10.1016/j.actamat.2016.04.038. [Online]. Available: https://www.sciencedirect.com/science/article/pii/S1359645416303068 (visited on 12/08/2021).

[51] C. J. McMahon, "Hydrogen-induced intergranular fracture of steels," en, *Engineering Fracture Mechanics*, vol. 68, no. 6, pp. 773–788, Apr. 2001, ISSN: 0013-7944. DOI: 10.1016/S0013-7944(00)00124-7. [Online]. Available: https://www.sciencedirect.com/science/article/pii/S0013794400001247 (visited on 12/08/2021).

[52] M. Yamaguchi, J. Kameda, K.-I. Ebihara, M. Itakura, and H. Kaburaki, "Mobile effect of hydrogen on intergranular decohesion of iron: First-principles calculations," *Philosophical Magazine*, vol. 92, no. 11, pp. 1349–1368, Apr. 2012, ISSN: 1478-6435. DOI: 10.1080/14786435.2011.645077. [Online]. Available: https://doi.org/10.1080/14786435.2011.645077 (visited on 12/08/2021).

[53] H. K. Birnbaum, I. M. Robertson, and P. Sofronis, "Hydrogen Effects on Plasticity," en, in ser. NATO Science Series, J. Lépinoux, D. Mazière, V. Pontikis, and G. Saada, Eds., Dordrecht: Springer Netherlands, 2000, pp. 367–381, ISBN: 9789401140485. DOI: 10.1007/978-94-011-4048-5_29. [Online]. Available: https://doi.org/10.1007/978-94-011-4048-5_29 (visited on 12/08/2021).

[54] H. Matsui, H. Kimura, and S. Moriya, "The effect of hydrogen on the mechanical properties of high purity iron I. Softening and hardening of high purity iron by hydrogen charging during tensile deformation," en, *Materials Science and Engineering*, vol. 40, no. 2, pp. 207–216, Oct. 1979, ISSN: 0025-5416. DOI: 10.1016/0025-

5416(79)90191-5. [Online]. Available: https://www.sciencedirect.com/science/article/pii/0025541679901915 (visited on 03/22/2021).

[55] E. Lunarska, V. Novak, N. Zarubova, and S. Kadeckova, "Effect of electrolytic hydrogen charging on flow stress and slip line pattern in iron single crystals," en, *Scripta Metallurgica*, vol. 17, no. 6, pp. 705–710, Jun. 1983, ISSN: 0036-9748. DOI: 10.1016/0036-9748(83)90478-7. [Online]. Available: https://www.sciencedirect.com/science/article/pii/0036974883904787 (visited on 12/08/2021).

[56] G. Lu, Q. Zhang, N. Kioussis, and E. Kaxiras, "Hydrogen-Enhanced Local Plasticity in Aluminum: An *Ab Initio* Study," *Physical Review Letters*, vol. 87, no. 9, p. 095 501, Aug. 2001. DOI: 10.1103/PhysRevLett.87.095501. [Online]. Available: https://link.aps.org/doi/10.1103/PhysRevLett.87.095501 (visited on 12/08/2021).

[57] A. Barnoush and H. Vehoff, "Electrochemical nanoindentation: A new approach to probe hydrogen/deformation interaction," en, *Scripta Materialia*, vol. 55, no. 2, pp. 195–198, Jul. 2006, ISSN: 1359-6462. DOI: 10.1016/j.scriptamat.2006.03.041. [Online]. Available: https://www.sciencedirect.com/science/article/pii/S1359646206002417 (visited on 12/08/2021).

[58] A. Barnoush and H. Vehoff, "In situ electrochemical nanoindentation: A technique for local examination of hydrogen embrittlement," en, *Corrosion Science*, vol. 50, no. 1, pp. 259–267, Jan. 2008, ISSN: 0010-938X. DOI: 10.1016/j.corsci.2007.05.026. [Online]. Available: https://www.sciencedirect.com/science/article/pii/S0010938X07001655 (visited on 03/22/2021).

[59] I. M. Robertson, H. K. Birnbaum, and P. Sofronis, "Chapter 91 Hydrogen Effects on Plasticity," en, in J. P. Hirth and L. Kubin, Eds. Elsevier, Jan. 2009, vol. 15, ch. 91, pp. 249–293. DOI: 10.1016/S1572-4859(09)01504-6. [Online]. Available: https://www.sciencedirect.com/science/article/pii/S1572485909015046 (visited on 12/08/2021).

[60] J. Song and W. A. Curtin, "Mechanisms of hydrogen-enhanced localized plasticity: An atomistic study using α-Fe as a model system," en, *Acta Materialia*, vol. 68, pp. 61–69, Apr. 2014, ISSN: 1359-6454. DOI: 10.1016/j.actamat.2014.01.008. [Online]. Available: https://www.sciencedirect.com/science/article/pii/S1359645414000172 (visited on 03/20/2021).

[61] D. Xie *et al.*, "Hydrogenated vacancies lock dislocations in aluminium," en, *Nature Communications*, vol. 7, no. 1, p. 13 341, Nov. 2016, ISSN: 2041-1723. DOI: 10.1038/ncomms13341. [Online]. Available: https://www.nature.com/articles/ncomms13341 (visited on 12/08/2021).

[62] S. P. Lynch, "Metallographic contributions to understanding mechanisms of environmentally assisted cracking," en, *Metallography*, vol. 23, no. 2, pp. 147–171, Sep. 1989, ISSN: 0026-0800. DOI: 10.1016/0026-0800(89)90016-5. [Online]. Available:

https://www.sciencedirect.com/science/article/pii/0026080089900165 (visited on 12/08/2021).

[63] S. P. Lynch, "A fractographic study of gaseous hydrogen embrittlement and liquid-metal embrittlement in a tempered-martensitic steel," en, *Acta Metallurgica*, vol. 32, no. 1, pp. 79–90, Jan. 1984, ISSN: 0001-6160. DOI: 10.1016/0001-6160(84)90204-9. [Online]. Available: https://www.sciencedirect.com/science/article/pii/0001616084902049 (visited on 12/09/2021).

[64] S. P. Lynch, "A fractographic study of hydrogen-assisted cracking and liquid-metal embrittlement in nickel," en, *Journal of Materials Science*, vol. 21, no. 2, pp. 692–704, Feb. 1986, ISSN: 1573-4803. DOI: 10.1007/BF01145543. [Online]. Available: https://doi.org/10.1007/BF01145543 (visited on 12/09/2021).

[65] J. A. Clum, "The role of hydrogen in dislocation generation in iron alloys," en, *Scripta Metallurgica*, vol. 9, no. 1, pp. 51–58, Jan. 1975, ISSN: 0036-9748. DOI: 10.1016/0036-9748(75)90145-3. [Online]. Available: https://www.sciencedirect.com/science/article/pii/0036974875901453 (visited on 12/08/2021).

[66] A. Pundt and R. Kirchheim, "Hydrogen in metals: Microstructural aspects," *Annual Review of Materials Research*, vol. 36, no. 1, pp. 555–608, 2006. DOI: 10.1146/annurev.matsci.36.090804.094451. [Online]. Available: https://doi.org/10.1146/annurev.matsci.36.090804.094451 (visited on 12/08/2021).

[67] K. Christmann, "Some general aspects of hydrogen chemisorption on metal surfaces," en, *Progress in Surface Science*, Proceedings of the Seventeenth International Seminar on Surface Physics, vol. 48, no. 1, pp. 15–26, Jan. 1995, ISSN: 0079-6816. DOI: 10.1016/0079-6816(95)93412-Z. [Online]. Available: https://www.sciencedirect.com/science/article/pii/007968169593412Z (visited on 12/08/2021).

[68] K. M. Entwistle, *Basic principles of the finite element method*. London, United Kingdom: CRC Press LLC, 2001, ISBN: 9781907625237. [Online]. Available: http://ebookcentral.proquest.com/lib/ncl/detail.action?docID=677905 (visited on 05/24/2022).

[69] R. LeSar, *Introduction to Computational Materials Science: Fundamentals to Applications*, en. Cambridge University Press, Mar. 2013, ISBN: 9781139033398. DOI: 10.1017/CBO9781139033398. [Online]. Available: https://www.cambridge.org/highereducation/books/introduction-to-computational-materials-science/327CCEC340E5C466CE08D6A6FD8520E1 (visited on 11/09/2021).

[70] M. J. Buehler, A. Hartmaier, H. Gao, M. Duchaineau, and F. F. Abraham, "Atomic plasticity: Description and analysis of a one-billion atom simulation of ductile materials failure," en, *Computer Methods in Applied Mechanics and Engineering*, Advances in Computational Plasticity, vol. 193, no. 48, pp. 5257–5282, Dec. 2004, ISSN: 0045-7825. DOI: 10.1016/j.cma.2003.12.066. [Online]. Available: https:

//www.sciencedirect.com/science/article/pii/S0045782504002749 (visited on 11/05/2021).

[71] N. Allsopp, G. Ruocco, and A. Fratalocchi, "Molecular dynamics beyonds the limits: Massive scaling on 72 racks of a BlueGene/P and supercooled glass dynamics of a 1 billion particles system," en, *Journal of Computational Physics*, vol. 231, no. 8, pp. 3432–3445, Apr. 2012, ISSN: 0021-9991. DOI: 10.1016/j.jcp.2012.01.019. [Online]. Available: https://www.sciencedirect.com/science/article/pii/S002199911200040X (visited on 11/05/2021).

[72] J. G. Lee, *Computational Materials Science: An Introduction, Second Edition*, 2nd ed. Boca Raton: CRC Press, Nov. 2016, ISBN: 9781315368429. DOI: 10.1201/9781315368429.

[73] A. Tehranchi, X. Zhang, G. Lu, and W. A. Curtin, "Hydrogen–vacancy–dislocation interactions in $\alpha-$Fe," en, vol. 25, no. 2, p. 025 001, Dec. 2016, ISSN: 0965-0393. DOI: 10.1088/1361-651X/aa52cb. [Online]. Available: https://doi.org/10.1088/1361-651x/aa52cb (visited on 11/05/2021).

[74] S. Schmauder and C. Kohler, "Atomistic simulations of solid solution strengthening of α-iron," en, *Computational Materials Science*, Proceedings of the 19th International Workshop on Computational Mechanics of Materials, vol. 50, no. 4, pp. 1238–1243, Feb. 2011, ISSN: 0927-0256. DOI: 10.1016/j.commatsci.2010.04.041. [Online]. Available: https://www.sciencedirect.com/science/article/pii/S0927025610002545 (visited on 05/14/2021).

[75] Y. N. Osetsky and D. J. Bacon, "An atomic-level model for studying the dynamics of edge dislocations in metals," en, *Modelling and Simulation in Materials Science and Engineering*, vol. 11, no. 4, pp. 427–446, May 2003, ISSN: 0965-0393. DOI: 10.1088/0965-0393/11/4/302. [Online]. Available: https://doi.org/10.1088/0965-0393/11/4/302 (visited on 03/20/2021).

[76] A. Tehranchi and W. A. Curtin, "Atomistic study of hydrogen embrittlement of grain boundaries in nickel: I. Fracture," en, *Journal of the Mechanics and Physics of Solids*, vol. 101, pp. 150–165, Jan. 2017, ISSN: 0022-5096. DOI: 10.1016/j.jmps.2017.01.020. [Online]. Available: https://www.sciencedirect.com/science/article/pii/S0022509616308274 (visited on 11/05/2021).

[77] H. Sun and L. K. Béland, "A molecular dynamics study of path-dependent grain boundary properties in nanocrystals prepared using different methods," en, *Scripta Materialia*, vol. 205, p. 114 183, Dec. 2021, ISSN: 1359-6462. DOI: 10.1016/j.scriptamat.2021.114183. [Online]. Available: https://www.sciencedirect.com/science/article/pii/S1359646221004632 (visited on 11/05/2021).

[78] M. Guziewski, S. P. Coleman, and C. R. Weinberger, "Atomistic investigation into the mechanical properties of the ferrite-cementite interface: The Bagaryatskii orientation," en, *Acta Materialia*, vol. 144, pp. 656–665, Feb. 2018, ISSN: 1359-6454. DOI: 10.1016/j.actamat.2017.10.070. [Online]. Available: https://

www.sciencedirect.com/science/article/pii/S1359645417309370 (visited on 08/03/2021).

[79] C. Wang, Z. Qin, Y. Zhang, Q. Sun, and Y. Jia, "A molecular dynamics simulation of self-diffusion on Fe surfaces," en, *Applied Surface Science*, vol. 258, no. 10, pp. 4294–4300, Mar. 2012, ISSN: 0169-4332. DOI: 10.1016/j.apsusc.2011.12.084. [Online]. Available: https://www.sciencedirect.com/science/article/pii/S0169433211019891 (visited on 11/05/2021).

[80] A. H. Cottrell, "Dislocations and Plastic Flow in Crystals," *American Journal of Physics*, vol. 22, no. 4, pp. 242–243, Apr. 1954, ISSN: 0002-9505. DOI: 10.1119/1.1933704. [Online]. Available: https://aapt.scitation.org/doi/abs/10.1119/1.1933704 (visited on 11/05/2021).

[81] M. J. Buehler, *Atomistic Modeling of Materials Failure*. Springer, 2008, ISBN: 978-0-387-76426-9. DOI: 10.1007/978-0-387-76426-9.

[82] L. Verlet, "Computer "Experiments" on Classical Fluids. I. Thermodynamical Properties of Lennard-Jones Molecules," *Physical Review*, vol. 159, no. 1, pp. 98–103, Jul. 1967. DOI: 10.1103/PhysRev.159.98. [Online]. Available: https://link.aps.org/doi/10.1103/PhysRev.159.98 (visited on 11/09/2021).

[83] W. C. Swope, H. C. Andersen, P. H. Berens, and K. R. Wilson, "A computer simulation method for the calculation of equilibrium constants for the formation of physical clusters of molecules: Application to small water clusters," *Journal of Chemical Physics*, vol. 76, no. 1, pp. 637–649, Jan. 1982. DOI: 10.1063/1.442716. eprint: https://doi.org/10.1063/1.442716. [Online]. Available: https://doi.org/10.1063/1.442716.

[84] A. Rahman, "Correlations in the Motion of Atoms in Liquid Argon," *Physical Review*, vol. 136, no. 2A, A405–A411, Oct. 1964. DOI: 10.1103/PhysRev.136.A405. [Online]. Available: https://link.aps.org/doi/10.1103/PhysRev.136.A405 (visited on 11/09/2021).

[85] A. F. Voter, F. Montalenti, and T. C. Germann, "Extending the time scale in atomistic simulation of materials," *Annual Review of Materials Research*, vol. 32, no. 1, pp. 321–346, 2002. DOI: 10.1146/annurev.matsci.32.112601.141541. eprint: https://doi.org/10.1146/annurev.matsci.32.112601.141541. [Online]. Available: https://doi.org/10.1146/annurev.matsci.32.112601.141541.

[86] W. K. Liu, E. G. Karpov, S. Zhang, and H. S. Park, "An introduction to computational nanomechanics and materials," en, *Computer Methods in Applied Mechanics and Engineering*, Multiple Scale Methods for Nanoscale Mechanics and Materials, vol. 193, no. 17, pp. 1529–1578, May 2004, ISSN: 0045-7825. DOI: 10.1016/j.cma.2003.12.008. [Online]. Available: https://www.sciencedirect.com/science/article/pii/S004578250400009X (visited on 11/09/2021).

[87] L. Maragliano and E. Vanden-Eijnden, "A temperature accelerated method for sampling free energy and determining reaction pathways in rare events simulations," en, *Chemical Physics Letters*, vol. 426, no. 1, pp. 168–175, Jul. 2006, ISSN: 0009-2614. DOI: 10.1016/j.cplett.2006.05.062. [Online]. Available: https://www.sciencedirect.com/science/article/pii/S0009261406007408 (visited on 11/09/2021).

[88] S. Nosé, "A unified formulation of the constant temperature molecular dynamics methods," *The Journal of Chemical Physics*, vol. 81, no. 1, pp. 511–519, Jul. 1984, ISSN: 0021-9606. DOI: 10.1063/1.447334. [Online]. Available: https://aip.scitation.org/doi/10.1063/1.447334 (visited on 11/09/2021).

[89] W. G. Hoover, "Canonical dynamics: Equilibrium phase-space distributions," *Physical Review A*, vol. 31, no. 3, pp. 1695–1697, Mar. 1985. DOI: 10.1103/PhysRevA.31.1695. [Online]. Available: https://link.aps.org/doi/10.1103/PhysRevA.31.1695 (visited on 11/09/2021).

[90] H. J. C. Berendsen, J. P. M. Postma, W. F. van Gunsteren, A. DiNola, and J. R. Haak, "Molecular dynamics with coupling to an external bath," *The Journal of Chemical Physics*, vol. 81, no. 8, pp. 3684–3690, Oct. 1984, ISSN: 0021-9606. DOI: 10.1063/1.448118. [Online]. Available: https://aip-scitation-org.libproxy.ncl.ac.uk/doi/abs/10.1063/1.448118 (visited on 11/09/2021).

[91] M. Parrinello and A. Rahman, "Polymorphic transitions in single crystals: A new molecular dynamics method," *Journal of Applied Physics*, vol. 52, no. 12, pp. 7182–7190, Dec. 1981, ISSN: 0021-8979. DOI: 10.1063/1.328693. [Online]. Available: https://aip-scitation-org.libproxy.ncl.ac.uk/doi/abs/10.1063/1.328693 (visited on 11/09/2021).

[92] J. E. Lennard-Jones, "Cohesion," en, *Proceedings of the Physical Society*, vol. 43, no. 5, pp. 461–482, Sep. 1931, ISSN: 0959-5309. DOI: 10.1088/0959-5309/43/5/301. [Online]. Available: https://doi.org/10.1088/0959-5309/43/5/301 (visited on 11/09/2021).

[93] P. M. Morse, "Diatomic molecules according to the wave mechanics. ii. vibrational levels," *Phys. Rev.*, vol. 34, pp. 57–64, 1 Jul. 1929. DOI: 10.1103/PhysRev.34.57. [Online]. Available: https://link.aps.org/doi/10.1103/PhysRev.34.57.

[94] M. Born and J. E. Mayer, "Zur Gittertheorie der Ionenkristalle," de, *Zeitschrift für Physik*, vol. 75, no. 1, pp. 1–18, Jan. 1932, ISSN: 0044-3328. DOI: 10.1007/BF01340511. [Online]. Available: https://doi.org/10.1007/BF01340511 (visited on 11/09/2021).

[95] N. Bernardes, "Theory of Solid Ne, A, Kr, and Xe at 0 K," *Physical Review*, vol. 112, no. 5, pp. 1534–1539, Dec. 1958. DOI: 10.1103/PhysRev.112.1534. [Online]. Available: https://link.aps.org/doi/10.1103/PhysRev.112.1534 (visited on 11/10/2021).

[96] M. S. Daw, S. M. Foiles, and M. I. Baskes, "The embedded-atom method: A review of theory and applications," en, *Materials Science Reports*, vol. 9, no. 7, pp. 251–310, Mar. 1993, ISSN: 0920-2307. DOI: 10.1016/0920-2307(93)90001-U. [Online]. Available: https://www.sciencedirect.com/science/article/pii/092023079390001U (visited on 11/09/2021).

[97] M. W. Finnis and J. E. Sinclair, "A simple empirical N-body potential for transition metals," *Philosophical Magazine A*, vol. 50, no. 1, pp. 45–55, Jul. 1984, ISSN: 0141-8610. DOI: 10.1080/01418618408244210. [Online]. Available: https://www.tandfonline.com/doi/10.1080/01418618408244210 (visited on 11/09/2021).

[98] M. I. Baskes, "Modified embedded-atom potentials for cubic materials and impurities," *Physical Review B*, vol. 46, no. 5, pp. 2727–2742, Aug. 1992. DOI: 10.1103/PhysRevB.46.2727. [Online]. Available: https://link.aps.org/doi/10.1103/PhysRevB.46.2727 (visited on 11/09/2021).

[99] D. J. Hepburn and G. J. Ackland, "Metallic-covalent interatomic potential for carbon in iron," *Physical Review B*, vol. 78, no. 16, p. 165 115, Oct. 2008. DOI: 10.1103/PhysRevB.78.165115. [Online]. Available: https://link.aps.org/doi/10.1103/PhysRevB.78.165115 (visited on 06/08/2021).

[100] S. M. Eich, D. Beinke, and G. Schmitz, "Embedded-atom potential for an accurate thermodynamic description of the iron–chromium system," en, *Computational Materials Science*, vol. 104, pp. 185–192, Jun. 2015, ISSN: 0927-0256. DOI: 10.1016/j.commatsci.2015.03.047. [Online]. Available: https://www.sciencedirect.com/science/article/pii/S0927025615002207 (visited on 11/09/2021).

[101] D. G. Pettifor and I. I. Oleynik, "Interatomic bond-order potentials and structural prediction," en, *Progress in Materials Science*, A Festschrift in Honor of T. B. Massalski, vol. 49, no. 3, pp. 285–312, Jan. 2004, ISSN: 0079-6425. DOI: 10.1016/S0079-6425(03)00024-0. [Online]. Available: https://www.sciencedirect.com/science/article/pii/S0079642503000240 (visited on 11/09/2021).

[102] G. C. Abell, "Empirical chemical pseudopotential theory of molecular and metallic bonding," *Physical Review B*, vol. 31, no. 10, pp. 6184–6196, May 1985. DOI: 10.1103/PhysRevB.31.6184. [Online]. Available: https://link.aps.org/doi/10.1103/PhysRevB.31.6184 (visited on 10/29/2021).

[103] J. Tersoff, "Modeling solid-state chemistry: Interatomic potentials for multicomponent systems," *Physical Review B*, vol. 39, no. 8, pp. 5566–5568, Mar. 1989. DOI: 10.1103/PhysRevB.39.5566. [Online]. Available: https://link.aps.org/doi/10.1103/PhysRevB.39.5566 (visited on 11/09/2021).

[104] K. O. E. Henriksson and K. Nordlund, "Simulations of cementite: An analytical potential for the Fe-C system," *Phys. Rev. B*, vol. 79, p. 144 107, 14 Apr. 2009. DOI: 10.1103/PhysRevB.79.144107. [Online]. Available: https://link.aps.org/doi/10.1103/PhysRevB.79.144107.

[105] K. O. E. Henriksson, C. Björkas, and K. Nordlund, "Atomistic simulations of stainless steels: A many-body potential for the Fe–Cr–C system," en, vol. 25, no. 44, p. 445 401, Oct. 2013, ISSN: 0953-8984. DOI: 10.1088/0953-8984/25/44/445401. [Online]. Available: https://doi.org/10.1088/0953-8984/25/44/445401 (visited on 11/09/2021).

[106] K. Chenoweth, A. C. T. van Duin, and W. A. Goddard, "ReaxFF Reactive Force Field for Molecular Dynamics Simulations of Hydrocarbon Oxidation," *The Journal of Physical Chemistry A*, vol. 112, no. 5, pp. 1040–1053, Feb. 2008, ISSN: 1089-5639. DOI: 10.1021/jp709896w. [Online]. Available: https://doi.org/10.1021/jp709896w (visited on 04/15/2021).

[107] M. F. Russo and A. C. T. van Duin, "Atomistic-scale simulations of chemical reactions: Bridging from quantum chemistry to engineering," en, *Nuclear Instruments and Methods in Physics Research Section B: Beam Interactions with Materials and Atoms*, Computer Simulations of Radiation Effects in Solids, vol. 269, no. 14, pp. 1549–1554, Jul. 2011, ISSN: 0168-583X. DOI: 10.1016/j.nimb.2010.12.053. [Online]. Available: https://www.sciencedirect.com/science/article/pii/S0168583X10009869 (visited on 05/10/2021).

[108] A. K. Rappe and W. A. Goddard, "Charge equilibration for molecular dynamics simulations," *The Journal of Physical Chemistry*, vol. 95, no. 8, pp. 3358–3363, 1991. DOI: 10.1021/j100161a070. eprint: https://doi.org/10.1021/j100161a070. [Online]. Available: https://doi.org/10.1021/j100161a070.

[109] M. R. LaBrosse, J. K. Johnson, and A. C. T. van Duin, "Development of a Transferable Reactive Force Field for Cobalt," *The Journal of Physical Chemistry A*, vol. 114, no. 18, pp. 5855–5861, May 2010, ISSN: 1089-5639. DOI: 10.1021/jp911867r. [Online]. Available: https://doi.org/10.1021/jp911867r (visited on 11/09/2021).

[110] C. Zou, A. C. T. van Duin, and D. C. Sorescu, "Theoretical Investigation of Hydrogen Adsorption and Dissociation on Iron and Iron Carbide Surfaces Using the ReaxFF Reactive Force Field Method," en, *Topics in Catalysis*, vol. 55, no. 5, pp. 391–401, Jun. 2012, ISSN: 1572-9028. DOI: 10.1007/s11244-012-9796-0. [Online]. Available: https://doi.org/10.1007/s11244-012-9796-0 (visited on 05/10/2021).

[111] D. E. Spearot, R. Dingreville, and C. J. O'Brien, "Atomistic Simulation Techniques to Model Hydrogen Segregation and Hydrogen Embrittlement in Metallic Materials," en, in S. Schmauder, C.-S. Chen, K. K. Chawla, N. Chawla, W. Chen, and Y. Kagawa, Eds., Singapore: Springer, 2019, pp. 357–390, ISBN: 9789811068843. DOI: 10.1007/978-981-10-6884-3_14. [Online]. Available: https://doi.org/10.1007/978-981-10-6884-3_14 (visited on 12/19/2021).

[112] P. Yu, Y. Cui, G.-z. Zhu, Y. Shen, and M. Wen, "The key role played by dislocation core radius and energy in hydrogen interaction with dislocations," en, *Acta*

Materialia, vol. 185, pp. 518–527, Feb. 2020, ISSN: 1359-6454. DOI: 10.1016/j.actamat.2019.12.033. [Online]. Available: https://www.sciencedirect.com/science/article/pii/S1359645419308729 (visited on 11/18/2021).

[113] H. Song, C. Li, S. Geng, M. An, M. Xiao, and L. Wang, "Atomistic simulations of effect of hydrogen atoms on mechanical behaviour of an α-Fe with symmetric tilt grain boundaries," *Phys. Lett. A*, vol. 382, no. 35, pp. 2464–2469, Sep. 2018, ISSN: 0375-9601. DOI: 10.1016/j.physleta.2018.06.005.

[114] S. Yin, G. Cheng, T.-H. Chang, G. Richter, Y. Zhu, and H. Gao, "Hydrogen embrittlement in metallic nanowires," en, *Nature Communications*, vol. 10, no. 1, p. 2004, May 2019, ISSN: 2041-1723. DOI: 10.1038/s41467-019-10035-0. [Online]. Available: https://www.nature.com/articles/s41467-019-10035-0 (visited on 12/19/2021).

[115] T. H. Xu, Z. Q. Zhu, S. F. Geng, and H. Y. Song, "Molecular dynamics study of effect of hydrogen atoms on mechanical properties of α-Fe nanowires," en, *Physics Letters A*, vol. 381, no. 37, pp. 3222–3227, Oct. 2017, ISSN: 0375-9601. DOI: 10.1016/j.physleta.2017.08.012. [Online]. Available: https://www.sciencedirect.com/science/article/pii/S0375960117307375 (visited on 12/19/2021).

[116] S. Li *et al.*, "The interaction of dislocations and hydrogen-vacancy complexes and its importance for deformation-induced proto nano-voids formation in α-Fe," en, *International Journal of Plasticity*, vol. 74, pp. 175–191, Nov. 2015, ISSN: 0749-6419. DOI: 10.1016/j.ijplas.2015.05.017. [Online]. Available: https://www.sciencedirect.com/science/article/pii/S0749641915000960 (visited on 12/19/2021).

[117] Y. Mishin, "Machine-learning interatomic potentials for materials science," en, *Acta Materialia*, vol. 214, p. 116 980, Aug. 2021, ISSN: 1359-6454. DOI: 10.1016/j.actamat.2021.116980. [Online]. Available: https://www.sciencedirect.com/science/article/pii/S1359645421003608 (visited on 12/18/2021).

[118] C. J. Healy and G. J. Ackland, "Molecular dynamics simulations of compression–tension asymmetry in plasticity of Fe nanopillars," *Acta Mater.*, vol. 70, pp. 105–112, 2014, ISSN: 1359-6454. [Online]. Available: http://www.sciencedirect.com/science/article/pii/S1359645414001049.

[119] P. Andric and W. A. Curtin, "Atomistic modeling of fracture," en, *Modelling and Simulation in Materials Science and Engineering*, vol. 27, no. 1, p. 013 001, Nov. 2018, ISSN: 0965-0393. DOI: 10.1088/1361-651X/aae40c. [Online]. Available: https://doi.org/10.1088/1361-651x/aae40c (visited on 04/01/2021).

[120] H. Ghaffarian, A. K. Taheri, S. Ryu, and K. Kang, "Nanoindentation study of cementite size and temperature effects in nanocomposite pearlite: A molecular dynamics simulation," *Curr. Appl Phys.*, vol. 16, no. 9, pp. 1015–1025, 2016, ISSN: 1567-1739. DOI: 10.1016/j.cap.2016.05.024.

[121] J. Kim, K. Kang, and S. Ryu, "Characterization of the misfit dislocations at the ferrite/cementite interface in pearlitic steel: An atomistic simulation study," *Int. J. Plast.*, vol. 83, pp. 302–312, 2016, ISSN: 0749-6419. DOI: 10.1016/j.ijplas.2016.04.016.

[122] S. S. Brenner, "Tensile Strength of Whiskers," *J. Appl. Phys.*, vol. 27, no. 12, pp. 1484–1491, 1956. DOI: 10.1063/1.1722294. eprint: 10.1063/1.1722294.

[123] G. Sainath, B. Choudhary, and T. Jayakumar, "Molecular dynamics simulation studies on the size dependent tensile deformation and fracture behaviour of body centred cubic iron nanowires," *Comp. Mater. Sci.*, vol. 104, pp. 76–83, 2015, ISSN: 0927-0256. DOI: 10.1016/j.commatsci.2015.03.053.

[124] G. Sainath and B. Choudhary, "Orientation dependent deformation behaviour of BCC iron nanowires," *Comp. Mater. Sci.*, vol. 111, pp. 406–415, 2016, ISSN: 0927-0256. DOI: 10.1016/j.commatsci.2015.09.055.

[125] D. Terentyev, P. Grammatikopoulos, D. Bacon, and Y. N. Osetsky, "Simulation of the interaction between an edge dislocation and a <100> interstitial dislocation loop in α–iron," *Acta Mater.*, vol. 56, no. 18, pp. 5034–5046, 2008, ISSN: 1359-6454. DOI: https://doi.org/10.1016/j.actamat.2008.06.032. [Online]. Available: http://www.sciencedirect.com/science/article/pii/S1359645408004527.

[126] C. Brandl, P. M. Derlet, and H. V. Swygenhoven, "Strain rates in molecular dynamics simulations of nanocrystalline metals," *Philos. Mag.*, vol. 89, no. 34–36, pp. 3465–3475, 2009. DOI: 10.1080/14786430903313690.

[127] L. Chang, C.-Y. Zhou, H.-X. Liu, J. Li, and X.-H. He, "Orientation and strain rate dependent tensile behavior of single crystal titanium nanowires by molecular dynamics simulations," *J. Mater. Sci. Technol.*, vol. 34, no. 5, pp. 864–877, 2018, ISSN: 1005-0302. DOI: 10.1016/j.jmst.2017.03.011.

[128] M. Tang and J. Marian, "Temperature and high strain rate dependence of tensile deformation behavior in single-crystal iron from dislocation dynamics simulations," *Acta Mater.*, vol. 70, pp. 123–129, 2014, ISSN: 1359-6454. DOI: 10.1016/j.actamat.2014.02.013.

[129] T. Massalski, H. Okamoto, and A. International, *Binary Alloy Phase Diagrams*. ASM International, 1990, vol. 1, ISBN: 9780871704047.

[130] S. Plimpton, "Fast Parallel Algorithms for Short-Range Molecular Dynamics," *J. Comput. Phys.*, vol. 117, pp. 1–19, 1995. DOI: 10.1006/jcph.1995.1039.

[131] D. Terentyev, A. Bakaev, and E. E. Zhurkin, "Effect of carbon decoration on the absorption of <111> dislocation loops by dislocations in iron," *J. Phys.: Condens. Matter*, vol. 26, no. 16, p. 165 402, 2014. DOI: 10.1088/0953-8984/26/16/165402.

[132] N. Gunkelmann, H. Ledbetter, and H. M. Urbassek, "Experimental and atomistic study of the elastic properties of α Fe–C martensite," *Acta Mater.*, vol. 60, no. 12, pp. 4901–4907, 2012, ISSN: 1359-6454. DOI: 10.1016/j.actamat.2012.05.038.

[133] M. Hestenes and E. Stiefel, "Methods of conjugate gradients for solving linear systems," *Journal of Research of the National Bureau of Standards*, vol. 49, no. 6, p. 409, Dec. 1952. DOI: 10.6028/jres.049.044.

[134] A. Stukowski, V. V. Bulatov, and A. Arsenlis, "Automated identification and indexing of dislocations in crystal interfaces," *Modelling Simul. Mater. Sci. Eng.*, vol. 20, no. 8, p. 085 007, 2012, ISSN: 1361-651X. DOI: 10.1088/0965-0393/20/8/085007.

[135] P. M. Larsen, S. Schmidt, and J. Schiøtz, "Robust structural identification via polyhedral template matching," *Modelling and Simulation in Materials Science and Engineering*, vol. 24, no. 5, p. 055 007, May 2016. DOI: 10.1088/0965-0393/24/5/055007. arXiv: 1603.05143 [cond-mat.mtrl-sci]. [Online]. Available: https://dx.doi.org/10.1088/0965-0393/24/5/055007.

[136] A. Stukowski, "Visualization and analysis of atomistic simulation data with OVITO-the Open Visualization Tool," *Modelling and Simulation in Materials Science and Engineering*, vol. 18, no. 1, Jan. 2010, ISSN: 0965-0393. DOI: {10.1088/0965-0393/18/1/015012}.

[137] W. Hosford, *Solid Mechanics*. Cambridge: Cambridge University Press, 2010, ISBN: 9780521192293.

[138] J. Harding and N. P. Allen, "The yield and fracture behaviour of high-purity iron single crystals at high rates of strain," *P. Roy. Soc. Lond. A. Mat.*, vol. 299, no. 1459, pp. 464–490, Jul. 1967. DOI: 10.1098/rspa.1967.0150. [Online]. Available: https://doi.org/10.1098/rspa.1967.0150.

[139] G. Sainath and B. K. Choudhary, "Atomistic simulations on ductile-brittle transition in <111> BCC Fe nanowires," *J. Appl. Phys.*, vol. 122, no. 9, p. 095 101, 2017. DOI: 10.1063/1.4999090. eprint: https://doi.org/10.1063/1.4999090.

[140] S. Li *et al.*, "Superelasticity in bcc nanowires by a reversible twinning mechanism," *Phys. Rev. B*, vol. 82, p. 205 435, 20 Nov. 2010. DOI: 10.1103/PhysRevB.82.205435. [Online]. Available: https://link.aps.org/doi/10.1103/PhysRevB.82.205435.

[141] H. S. Park, K. Gall, and J. A. Zimmerman, "Deformation of fcc nanowires by twinning and slip," *Journal of the Mechanics and Physics of Solids*, vol. 54, no. 9, pp. 1862–1881, 2006, ISSN: 0022-5096. DOI: https://doi.org/10.1016/j.jmps.2006.03.006. [Online]. Available: http://www.sciencedirect.com/science/article/pii/S0022509606000561.

[142] Y. M. Wang *et al.*, "Deforming nanocrystalline nickel at ultrahigh strain rates," *Appl. Phys. Lett.*, vol. 88, no. 6, pp. 061 917–, Feb. 2006, ISSN: 0003-6951. DOI: 10.1063/1.2173257. [Online]. Available: https://doi.org/10.1063/1.2173257.

[143] J. Roesler, H. Harder, and M. Baker, *Mechanical Behaviour of Engineering Materials – Metals, ceramics, polymers, and composites*. Berlin New York: Springer, 2007, ISBN: 978-3-540-73446-8.

[144] Y. Murakami, "The effect of hydrogen on fatigue properties of metals used for fuel cell system," en, in *Advances in Fracture Research*, A. Carpinteri, Y.-W. Mai, and R. O. Ritchie, Eds., Dordrecht: Springer Netherlands, Jan. 30, 2007, pp. 167–195, ISBN: 9781402054235. DOI: 10.1007/978-1-4020-5423-5_10. [Online]. Available: https://www.ebook.de/de/product/8896291/advances_in_fracture_research.html.

[145] H. Matsui, H. Kimura, and A. Kimura, "The effect of hydrogen on the mechanical properties of high purity iron III. The dependence of softening in specimen size and charging current density," en, *Materials Science and Engineering*, vol. 40, no. 2, pp. 227–234, Oct. 1979, ISSN: 0025-5416. DOI: 10.1016/0025-5416(79)90193-9. [Online]. Available: https://www.sciencedirect.com/science/article/pii/0025541679901939 (visited on 05/10/2021).

[146] N. M. Vlasov and V. A. Zaznoba, "The effect of hydrogen atoms on the mobility of edge dislocations," en, *Physics of the Solid State*, vol. 41, no. 3, pp. 404–406, Mar. 1999, ISSN: 1090-6460. DOI: 10.1134/1.1130791. [Online]. Available: https://doi.org/10.1134/1.1130791 (visited on 05/10/2021).

[147] J. P. Chateau, D. Delafosse, and T. Magnin, "Numerical simulations of hydrogen–dislocation interactions in fcc stainless steels.: Part I: Hydrogen–dislocation interactions in bulk crystals," en, *Acta Materialia*, vol. 50, no. 6, pp. 1507–1522, Apr. 2002, ISSN: 1359-6454. DOI: 10.1016/S1359-6454(02)00008-3. [Online]. Available: https://www.sciencedirect.com/science/article/pii/S1359645402000083 (visited on 05/10/2021).

[148] J. P. Chateau, D. Delafosse, and T. Magnin, "Numerical simulations of hydrogen–dislocation interactions in fcc stainless steels.: Part II: Hydrogen effects on crack tip plasticity at a stress corrosion crack," en, *Acta Materialia*, vol. 50, no. 6, pp. 1523–1538, Apr. 2002, ISSN: 1359-6454. DOI: 10.1016/S1359-6454(02)00009-5. [Online]. Available: https://www.sciencedirect.com/science/article/pii/S1359645402000095 (visited on 03/22/2021).

[149] P. J. Ferreira, I. M. Robertson, and H. K. Birnbaum, "Hydrogen effects on the interaction between dislocations," en, *Acta Materialia*, vol. 46, no. 5, pp. 1749–1757, Mar. 1998, ISSN: 1359-6454. DOI: 10.1016/S1359-6454(97)00349-2. [Online]. Available: https://www.sciencedirect.com/science/article/pii/S1359645497003492 (visited on 03/20/2021).

[150] P. Sofronis and H. K. Birnbaum, "Mechanics of the hydrogen–dislocation–impurity interactions–I. Increasing shear modulus," en, *Journal of the Mechanics and Physics of Solids*, vol. 43, no. 1, pp. 49–90, Jan. 1995, ISSN: 0022-5096. DOI: 10.1016/0022-5096(94)00056-B. [Online]. Available: https://www.sciencedirect.com/science/article/pii/002250969400056B (visited on 03/22/2021).

[151] A. Tehranchi, B. Yin, and W. A. Curtin, "Softening and hardening of yield stress by hydrogen–solute interactions," *Philosophical Magazine*, vol. 97, no. 6, pp. 400–418,

Feb. 2017, ISSN: 1478-6435. DOI: 10.1080/14786435.2016.1263402. [Online]. Available: https://doi.org/10.1080/14786435.2016.1263402 (visited on 03/20/2021).

[152] T. P. Senftle *et al.*, "The ReaxFF reactive force-field: Development, applications and future directions," en, *npj Computational Materials*, vol. 2, no. 1, pp. 1–14, Mar. 2016, ISSN: 2057-3960. DOI: 10.1038/npjcompumats.2015.11. [Online]. Available: https://www.nature.com/articles/npjcompumats201511 (visited on 05/10/2021).

[153] R. Chang and L. J. Graham, "Edge dislocation core structure and the peierls barrier in body-centered cubic iron," en, *physica status solidi (b)*, vol. 18, no. 1, pp. 99–103, 1966, ISSN: 1521-3951. DOI: https://doi.org/10.1002/pssb.19660180110. [Online]. Available: https://onlinelibrary.wiley.com/doi/abs/10.1002/pssb.19660180110 (visited on 04/15/2021).

[154] J. Schiffgens and K. Garrison, "Computer simulation studies of the a/2 ¡111¿ edge dislocation in α-iron," *Journal of Applied Physics*, vol. 43, no. 8, pp. 3240–3254, Aug. 1972, ISSN: 0021-8979. DOI: 10.1063/1.1661701. [Online]. Available: https://aip.scitation.org/doi/10.1063/1.1661701 (visited on 04/15/2021).

[155] S. Rao, C. Hernandez, J. P. Simmons, T. A. Parthasarathy, and C. Woodward, "Green's function boundary conditions in two-dimensional and three-dimensional atomistic simulations of dislocations," *Philosophical Magazine A*, vol. 77, no. 1, pp. 231–256, Jan. 1998, ISSN: 0141-8610. DOI: 10.1080/01418619808214240. [Online]. Available: https://doi.org/10.1080/01418619808214240 (visited on 04/15/2021).

[156] S. I. Golubov, X. Liu, H. Huang, and C. H. Woo, "GFCUBHEX: Program to calculate elastic Green's functions and displacement fields for applications in atomistic simulations of defects in cubic and HCP crystals," en, *Computer Physics Communications*, vol. 137, no. 2, pp. 312–324, Jun. 2001, ISSN: 0010-4655. DOI: 10.1016/S0010-4655(01)00157-6. [Online]. Available: https://www.sciencedirect.com/science/article/pii/S0010465501001576 (visited on 04/15/2021).

[157] D. J. Bacon and Y. N. Osetsky, "Hardening due to copper precipitates in α-iron studied by atomic-scale modelling," en, *Journal of Nuclear Materials*, Proceedings of the 11th International Conference on Fusion Reactor Materials (ICFRM-11), vol. 329-333, pp. 1233–1237, Aug. 2004, ISSN: 0022-3115. DOI: 10.1016/j.jnucmat.2004.04.256. [Online]. Available: https://www.sciencedirect.com/science/article/pii/S0022311504004179 (visited on 03/20/2021).

[158] D. J. Bacon and Y. N. Osetsky, "The atomic-scale modeling of dislocation-obstacle interactions in irradiated metals," en, *JOM*, vol. 59, no. 4, pp. 40–45, Apr. 2007, ISSN: 1543-1851. DOI: 10.1007/s11837-007-0053-0. [Online]. Available: https://doi.org/10.1007/s11837-007-0053-0 (visited on 03/20/2021).

[159] K. Tapasa, Y. N. Osetsky, and D. J. Bacon, "Computer simulation of interaction of an edge dislocation with a carbon interstitial in α-iron and effects on glide," en, *Acta Materialia*, vol. 55, no. 1, pp. 93–104, Jan. 2007, ISSN: 1359-6454. DOI: 10.1016/j.actamat.2006.08.015. [Online]. Available: https://www.sciencedirect.com/science/article/pii/S1359645406005581 (visited on 03/22/2021).

[160] D. L. Olmsted, L. G. HectorJr, W. A. Curtin, and R. J. Clifton, "Atomistic simulations of dislocation mobility in Al, Ni and Al/Mg alloys," en, *Modelling and Simulation in Materials Science and Engineering*, vol. 13, no. 3, pp. 371–388, Mar. 2005, ISSN: 0965-0393. DOI: 10.1088/0965-0393/13/3/007. [Online]. Available: https://doi.org/10.1088/0965-0393/13/3/007 (visited on 03/20/2021).

[161] C. Kohler, P. Kizler, and S. Schmauder, "Atomistic simulation of the pinning of edge dislocations in Ni by Ni_3Al precipitates," en, *Materials Science and Engineering: A*, Dislocations 2004, vol. 400-401, pp. 481–484, Jul. 2005, ISSN: 0921-5093. DOI: 10.1016/j.msea.2005.01.072. [Online]. Available: https://www.sciencedirect.com/science/article/pii/S0921509305003722 (visited on 03/20/2021).

[162] D. L. Olmsted, L. G. Hector, and W. A. Curtin, "Molecular dynamics study of solute strengthening in Al/Mg alloys," en, *Journal of the Mechanics and Physics of Solids*, vol. 54, no. 8, pp. 1763–1788, Aug. 2006, ISSN: 0022-5096. DOI: 10.1016/j.jmps.2005.12.008. [Online]. Available: https://www.sciencedirect.com/science/article/pii/S0022509606000354 (visited on 03/20/2021).

[163] I. A. Bryukhanov, "Dynamics of edge dislocation in Cu–Ni solid solution alloys at atomic scale," en, *International Journal of Plasticity*, vol. 135, p. 102 834, Dec. 2020, ISSN: 0749-6419. DOI: 10.1016/j.ijplas.2020.102834. [Online]. Available: https://www.sciencedirect.com/science/article/pii/S0749641920302254 (visited on 03/20/2021).

[164] B. A. Szajewski and W. A. Curtin, "Analysis of spurious image forces in atomistic simulations of dislocations," en, *Modelling and Simulation in Materials Science and Engineering*, vol. 23, no. 2, p. 025 008, Jan. 2015, ISSN: 0965-0393. DOI: 10.1088/0965-0393/23/2/025008. [Online]. Available: https://doi.org/10.1088/0965-0393/23/2/025008 (visited on 03/20/2021).

[165] D. Hull and D. J. Bacon, "Elastic Properties of Dislocations," en, in D. Hull and D. J. Bacon, Eds. Oxford: Butterworth-Heinemann, Jan. 2011, ch. 4, pp. 63–83, ISBN: 9780080966724. DOI: 10.1016/B978-0-08-096672-4.00004-9. [Online]. Available: https://www.sciencedirect.com/science/article/pii/B9780080966724000049 (visited on 03/24/2021).

[166] V. Bulatov and W. Cai, *Computer Simulations of Dislocations* (OSMM), eng. Oxford: Oxford University Press, 2006, ISBN: 9780198526148. DOI: 10.1093/oso/9780198526148.001.0001. [Online]. Available: https://oxford.universitypressscholarship.

com/10.1093/oso/9780198526148.001.0001/isbn-9780198526148 (visited on 07/20/2022).

[167] D. Hull and D. J. Bacon, "Movement of Dislocations," en, in *Introduction to Dislocations*, D. Hull and D. J. Bacon, Eds. Oxford: Butterworth-Heinemann, Jan. 2011, ch. 3, pp. 43–62, ISBN: 9780080966724. DOI: 10.1016/B978-0-08-096672-4.00003-7. [Online]. Available: https://www.sciencedirect.com/science/article/pii/B9780080966724000037 (visited on 03/20/2021).

[168] Z. Rong, Y. N. Osetsky, and D. J. Bacon, "A model for the dynamics of loop drag by a gliding dislocation," *Philosophical Magazine*, vol. 85, no. 14, pp. 1473–1493, May 2005, ISSN: 1478-6435. DOI: 10.1080/14786430500036371. [Online]. Available: https://doi.org/10.1080/14786430500036371 (visited on 03/20/2021).

[169] S. Queyreau, J. Marian, M. R. Gilbert, and B. D. Wirth, "Edge dislocation mobilities in bcc Fe obtained by molecular dynamics," *Physical Review B*, vol. 84, no. 6, p. 064 106, Aug. 2011. DOI: 10.1103/PhysRevB.84.064106. [Online]. Available: https://link.aps.org/doi/10.1103/PhysRevB.84.064106 (visited on 05/11/2021).

[170] J. P. Hirth, J. Lothe, and T. Mura, "Theory of dislocations," *Journal of Applied Mechanics*, vol. 50, no. 2, p. 476, 1983.

[171] P. Gumbsch and H. Gao, "Dislocations Faster than the Speed of Sound," en, *Science*, vol. 283, no. 5404, pp. 965–968, Feb. 1999, ISSN: 0036-8075, 1095-9203. DOI: 10.1126/science.283.5404.965. [Online]. Available: https://science.sciencemag.org/content/283/5404/965 (visited on 05/07/2021).

[172] N. Urabe and J. Weertman, "Dislocation mobility in potassium and iron single crystals," en, *Materials Science and Engineering*, vol. 18, no. 1, pp. 41–49, Mar. 1975, ISSN: 0025-5416. DOI: 10.1016/0025-5416(75)90071-3. [Online]. Available: https://www.sciencedirect.com/science/article/pii/0025541675900713 (visited on 03/20/2021).

[173] Y. Cui *et al.*, "Enhanced H-H binding and consequent H-aggregation around dislocation in α-Fe lattice," en, *Materials Research Express*, vol. 7, no. 6, p. 066 518, Jun. 2020, ISSN: 2053-1591. DOI: 10.1088/2053-1591/ab9a81. [Online]. Available: https://doi.org/10.1088/2053-1591/ab9a81 (visited on 03/20/2021).

[174] D. Hull and D. J. Bacon, "Strength of Crystalline Solids," en, in D. Hull and D. J. Bacon, Eds. Oxford: Butterworth-Heinemann, Jan. 2011, ch. 10, pp. 205–249, ISBN: 9780080966724. DOI: 10.1016/B978-0-08-096672-4.00010-4. [Online]. Available: https://www.sciencedirect.com/science/article/pii/B9780080966724000104 (visited on 07/30/2021).

[175] C. A. Wert, "Diffusion Coefficient of C in $\alpha-$Iron," *Physical Review*, vol. 79, no. 4, pp. 601–605, Aug. 1950. DOI: 10.1103/PhysRev.79.601. [Online]. Available: https://link.aps.org/doi/10.1103/PhysRev.79.601 (visited on 10/01/2021).

[176] J. Y. Choi, "Diffusion of hydrogen in iron," en, *Metallurgical Transactions*, vol. 1, no. 4, pp. 911–919, Apr. 1970, ISSN: 1543-1916. DOI: 10.1007/BF02811773. [Online]. Available: https://doi.org/10.1007/BF02811773 (visited on 09/22/2021).

[177] A. Tehranchi, "Atomistic mechanisms of hydrogen embrittlement," eng, Ph.D. dissertation, EPFL, Lausanne, 2017. DOI: 10.5075/epfl-thesis-8227.

[178] R. Matsumoto, Y. Inoue, S. Taketomi, and N. Miyazaki, "Influence of shear strain on the hydrogen trapped in bcc-Fe: A first-principles-based study," en, *Scripta Materialia*, vol. 60, no. 7, pp. 555–558, Apr. 2009, ISSN: 1359-6462. DOI: 10.1016/j.scriptamat.2008.12.009. [Online]. Available: https://www.sciencedirect.com/science/article/pii/S1359646208008531 (visited on 08/09/2021).

[179] H.-B. Zhou, S. Jin, Y. Zhang, G.-H. Lu, and F. Liu, "Anisotropic Strain Enhanced Hydrogen Solubility in bcc Metals: The Independence on the Sign of Strain," *Physical Review Letters*, vol. 109, no. 13, p. 135 502, Sep. 2012. DOI: 10.1103/PhysRevLett.109.135502. [Online]. Available: https://link.aps.org/doi/10.1103/PhysRevLett.109.135502 (visited on 08/09/2021).

[180] J. Hou *et al.*, "Hydrogen bubble nucleation by self-clustering: Density functional theory and statistical model studies using tungsten as a model system," en, *Nuclear Fusion*, vol. 58, no. 9, p. 096 021, Jul. 2018, ISSN: 0029-5515. DOI: 10.1088/1741-4326/aacdb6. [Online]. Available: https://doi.org/10.1088/1741-4326/aacdb6 (visited on 08/23/2021).

[181] J. Hou, X.-S. Kong, C. S. Liu, and J. Song, "Hydrogen clustering in bcc metals: Atomic origin and strong stress anisotropy," en, *Acta Materialia*, vol. 201, pp. 23–35, Dec. 2020, ISSN: 1359-6454. DOI: 10.1016/j.actamat.2020.09.048. [Online]. Available: https://www.sciencedirect.com/science/article/pii/S1359645420307424 (visited on 08/23/2021).

[182] Y. Fukai, "Superabundant Vacancies Formed in Metal–Hydrogen Alloys," en, *Physica Scripta*, vol. 2003, no. T103, p. 11, Jan. 2003, ISSN: 1402-4896. DOI: 10.1238/Physica.Topical.103a00011. [Online]. Available: https://iopscience.iop.org/article/10.1238/Physica.Topical.103a00011/meta (visited on 10/01/2021).

[183] E. Hayward and C.-C. Fu, "Interplay between hydrogen and vacancies in α-Fe," *Physical Review B*, vol. 87, no. 17, p. 174 103, May 2013. DOI: 10.1103/PhysRevB.87.174103. [Online]. Available: https://link.aps.org/doi/10.1103/PhysRevB.87.174103 (visited on 10/01/2021).

[184] H. E. Hänninen, T. C. Lee, I. M. Robertson, and H. K. Birnbaum, "In situ observations on effects of hydrogen on deformation and fracture of A533B pressure vessel steel," en, *Journal of Materials Engineering and Performance*, vol. 2, no. 6, pp. 807–817, Dec. 1993, ISSN: 1544-1024. DOI: 10.1007/BF02645681. [Online]. Available: https://doi.org/10.1007/BF02645681 (visited on 03/18/2022).

[185] H. M. Westergaard, "Bearing Pressures and Cracks: Bearing Pressures Through a Slightly Waved Surface or Through a Nearly Flat Part of a Cylinder, and Related Problems of Cracks," *Journal of Applied Mechanics*, vol. 6, no. 2, A49–A53, Mar. 1939, ISSN: 0021-8936. DOI: 10.1115/1.4008919. [Online]. Available: https://doi.org/10.1115/1.4008919 (visited on 03/18/2022).

[186] G. R. Irwin, "Analysis of Stresses and Strains Near the End of a Crack Traversing a Plate," *Journal of Applied Mechanics*, vol. 24, no. 3, pp. 361–364, Jun. 1957, ISSN: 0021-8936. DOI: 10.1115/1.4011547. [Online]. Available: https://doi.org/10.1115/1.4011547 (visited on 03/18/2022).

[187] I. N. Sneddon and N. F. Mott, "The distribution of stress in the neighbourhood of a crack in an elastic solid," *Proceedings of the Royal Society of London. Series A. Mathematical and Physical Sciences*, vol. 187, no. 1009, pp. 229–260, 1946. DOI: 10.1098/rspa.1946.0077. eprint: https://royalsocietypublishing.org/doi/pdf/10.1098/rspa.1946.0077. [Online]. Available: https://royalsocietypublishing.org/doi/abs/10.1098/rspa.1946.0077.

[188] M. L. Williams, "On the Stress Distribution at the Base of a Stationary Crack," en, *Journal of Applied Mechanics*, vol. 24, no. 1, pp. 109–114, Mar. 1956, ISSN: 0021-8936. [Online]. Available: https://resolver.caltech.edu/CaltechAUTHORS:20140729-122058948 (visited on 03/18/2022).

[189] T. L. Anderson, *Fracture Mechanics: Fundamentals and Applications*, 3rd ed. Boca Raton: CRC Press, Mar. 2017, ISBN: 9781315370293. DOI: 10.1201/9781315370293.

[190] A. N. Stroh, "Dislocations and Cracks in Anisotropic Elasticity," *The Philosophical Magazine: A Journal of Theoretical Experimental and Applied Physics*, vol. 3, no. 30, pp. 625–646, Jun. 1958, ISSN: 0031-8086. DOI: 10.1080/14786435808565804. [Online]. Available: https://doi.org/10.1080/14786435808565804 (visited on 03/21/2022).

[191] T. C.-t. Ting and T. C.-t. Ting, *Anisotropic elasticity: theory and applications*. Oxford University Press on Demand, 1996.

[192] J. F. Knott, "Fracture Toughness and Hydrogen-Assisted Crack Growth in Engineering Alloys," en, in *Hydrogen Effects in Materials*, John Wiley & Sons, Ltd, 1996, pp. 385–408, ISBN: 9781118803363. DOI: 10.1002/9781118803363.ch36. [Online]. Available: https://onlinelibrary.wiley.com/doi/abs/10.1002/9781118803363.ch36 (visited on 02/09/2022).

[193] L. M. Hale, X. W. Zhou, J. A. Zimmerman, N. R. Moody, R. Ballarini, and W. W. Gerberich, "Molecular dynamics simulation of delamination of a stiff, body-centered-cubic crystalline film from a compliant Si substrate," *Journal of Applied Physics*, vol. 106, no. 8, p. 083 503, Oct. 2009, ISSN: 0021-8979. DOI: 10.1063/1.3238521. [Online]. Available: https://aip.scitation.org/doi/full/10.1063/1.3238521 (visited on 02/15/2022).

[194] N. Dowling, K. Prasad, and R. Narayanasamy, *Mechanical Behavior of Materials: Engineering Methods for Deformation, Fracture, and Fatigue* (Always learning). Pearson, 2013, ISBN: 9780273764557. [Online]. Available: https://books.google.co.uk/books?id=OrlxMAEACAAJ.

[195] J. R. Rice, "Dislocation nucleation from a crack tip: An analysis based on the Peierls concept," en, *Journal of the Mechanics and Physics of Solids*, vol. 40, no. 2, pp. 239–271, Jan. 1992, ISSN: 0022-5096. DOI: 10.1016/S0022-5096(05)80012-2. [Online]. Available: https://www.sciencedirect.com/science/article/pii/S0022509605800122 (visited on 02/22/2022).

[196] P. A. Gordon, T. Neeraj, M. J. Luton, and D. Farkas, "Crack-Tip Deformation Mechanisms in α-Fe and Binary Fe Alloys: An Atomistic Study on Single Crystals," en, *Metallurgical and Materials Transactions A*, vol. 38, no. 13, pp. 2191–2202, Sep. 2007, ISSN: 1543-1940. DOI: 10.1007/s11661-007-9176-8. [Online]. Available: https://doi.org/10.1007/s11661-007-9176-8 (visited on 01/25/2022).

[197] J. Song, M. Soare, and W. A. Curtin, "Testing continuum concepts for hydrogen embrittlement in metals using atomistics," en, *Modelling and Simulation in Materials Science and Engineering*, vol. 18, no. 4, p. 045 003, Mar. 2010, ISSN: 0965-0393. DOI: 10.1088/0965-0393/18/4/045003. [Online]. Available: https://doi.org/10.1088/0965-0393/18/4/045003 (visited on 02/21/2022).

[198] X. Chen and W. W. Gerberich, "The kinetics and micromechanics of hydrogen assisted cracking in Fe-3 pct Si single crystals," en, *Metallurgical Transactions A*, vol. 22, no. 1, pp. 59–70, Jan. 1991, ISSN: 1543-1940. DOI: 10.1007/BF03350949. [Online]. Available: https://doi.org/10.1007/BF03350949 (visited on 04/04/2022).

[199] M. Nagumo, "Mechanistic Aspects of Fracture $\sim$ Brittle Fracture Models," en, in M. Nagumo, Ed. Singapore: Springer, 2016, ch. 9, pp. 197–215, ISBN: 9789811001611. DOI: 10.1007/978-981-10-0161-1_9. [Online]. Available: https://doi.org/10.1007/978-981-10-0161-1_9 (visited on 04/07/2022).

[200] Y. Song *et al.*, "Effect of Cementite on the Hydrogen Diffusion/Trap Characteristics of 2.25Cr-1Mo-0.25V Steel with and without Annealing," *Materials*, vol. 11, no. 5, p. 788, May 2018, ISSN: 1996-1944. DOI: 10.3390/ma11050788. [Online]. Available: https://www.ncbi.nlm.nih.gov/pmc/articles/PMC5978165/ (visited on 06/27/2022).

[201] M. Nagumo, M. Nakamura, and K. Takai, "Hydrogen thermal desorption relevant to delayed-fracture susceptibility of high-strength steels," en, *Metallurgical and Materials Transactions A*, vol. 32, no. 2, pp. 339–347, Feb. 2001, ISSN: 1543-1940. DOI: 10.1007/s11661-001-0265-9. [Online]. Available: https://doi.org/10.1007/s11661-001-0265-9 (visited on 06/24/2022).

[202] X. Xing *et al.*, "Molecular Dynamics Studies of Hydrogen Effect on Intergranular Fracture in α-Iron," en, *Materials*, vol. 13, no. 21, p. 4949, Jan. 2020, ISSN: 1996-

1944. DOI: 10.3390/ma13214949. [Online]. Available: https://www.mdpi.com/1996-1944/13/21/4949 (visited on 04/13/2022).

[203] Y. Tateyama and T. Ohno, "Stability and clusterization of hydrogen-vacancy complexes in α-Fe: An ab initio study," *Physical Review B*, vol. 67, no. 17, p. 174 105, May 2003. DOI: 10.1103/PhysRevB.67.174105. [Online]. Available: https://link.aps.org/doi/10.1103/PhysRevB.67.174105 (visited on 04/13/2022).

[204] H. J. Grabke and R. E., "Absorption and diffusion of hydrogen in steels," *Materiali in tehnologije*, vol. 34, no. 6, p. 331, 2000.

[205] P. A. Korzhavyi, I. A. Abrikosov, B. Johansson, A. V. Ruban, and H. L. Skriver, "First-principles calculations of the vacancy formation energy in transition and noble metals," *Physical Review B*, vol. 59, no. 18, pp. 11 693–11 703, May 1999. DOI: 10.1103/PhysRevB.59.11693. [Online]. Available: https://link.aps.org/doi/10.1103/PhysRevB.59.11693 (visited on 04/13/2022).

[206] Y. K. Shin, H. Kwak, C. Zou, A. V. Vasenkov, and A. C. T. van Duin, "Development and Validation of a ReaxFF Reactive Force Field for Fe/Al/Ni Alloys: Molecular Dynamics Study of Elastic Constants, Diffusion, and Segregation," *The Journal of Physical Chemistry A*, vol. 116, no. 49, pp. 12 163–12 174, Dec. 2012, ISSN: 1089-5639. DOI: 10.1021/jp308507x. [Online]. Available: https://doi.org/10.1021/jp308507x (visited on 04/13/2022).

Appendix A

Validation of Interatomic Potentials

In classical Molecular Dynamics, the validity of the simulations largely depends on the accuracy of the interatomic potential used. In order to evaluate the accuracy of the interatomic potentials used in this work, several physical properties predicted by these potentials were compared to DFT and experimental data and are shown in tables A.1 to A.3. The EAM interatomic potential developed by Ramasubramaniam et al. [13, 14] has been widely used to study hydrogen related phenomena in bulk and defective Fe [14, 38, 60, 73, 202]. On the other hand, the ReaxFF potential developed by Islam et al. [12] has been considerably less used. Its accuracy seems to be comparable with that of the EAM potential.

Table A.1. Various physical properties predicted by the EAM [13, 14] and ReaxFF [12] for Fe–H interatomic potentials used in this work.

	Ref	**EAM**	**ReaxFF**
a	2.855	2.855	2.855
E_{coh}	4.103	4.103	4.103
E_{H}	0.34 [203]	0.297	0.4
E_{H}^{m}	0.042 [204]	0.040	0.032
E_{Vac}^{f}	2.25 [205]	1.72	2.51
$E_{\text{Vac-H}}^{b}$	0.63 [203]	0.609	0.501

All energies in eV. a: Fe lattice parameter (Å), E_{coh}: Fe cohesive energy, E_{H}: dissolution energy, E_{H}^{m}: H diffusion barrier, E_{Vac}^{f}: vacancy formation energy, $E_{\text{Vac-H}}^{b}$: H-vacancy binding energy.

Table A.2. Formation and binding energies (eV) for other defects predicted by EAM [13, 14] and ReaxFF [12] potentials.

	Ref	**EAM**	**ReaxFF**
$\gamma_s^{(1\,0\,0)}$	2.30 [206]	1.75	2.29
$\gamma_s^{(1\,1\,0)}$	2.29 [206]	1.75	2.29
$E_b^{(1\,0\,0)}$	0.768 [13]	0.749	1.59
$E_b^{(1\,1\,0)}$	1.003 [13]	0.734	1.098
$E^b_{\text{dislo-H}}$	0.47[73]	0.42	0.33

$\gamma_s^{(h\,k\,l)}$: formation energy of $(h\,k\,l)$ surface, $E_b^{(h\,k\,l)}$: H binding energy on $(h\,k\,l)$ surface, $E^b_{\text{dislo-H}}$: H binding energy with an edge dislocation.

Table A.3. Elastic constants (GPa) for Fe predicted by EAM [13, 14] and ReaxFF [12] potentials.

	Ref [170]	**EAM**	**ReaxFF**
C_{11}	242	243	240
C_{12}	146	145	115
C_{44}	112	116	115

Appendix B

Stroh Formalism and Anisotropic Displacement Field

As discussed in section 6.1, a closed form solution for the displacement field for a semi infinite crack in anisotropic media can be obtained using the Stroh formalism [190]. Such solution is given by [119, 191]

$$\mathbf{u} = K_{\mathrm{I}}\sqrt{\frac{2r}{\pi}}\,\mathrm{Re}\left\{\mathbf{A}\left\langle\cos\theta + v_\alpha \sin\theta\right\rangle\mathbf{B}^{-1}\right\} \tag{B.1}$$

$\mathrm{Re}\{\}$ stands for "the real part of". Equation (B.1) shows that in order to compute the displacement vector $\mathbf{u}$ of an atom, v_α, $\mathbf{A}$ and $\mathbf{B}$ are needed. They can be obtained from

$$\mathbf{N}\begin{bmatrix}\mathbf{A}\\ \mathbf{B}\end{bmatrix} = \boldsymbol{v}\begin{bmatrix}\mathbf{A}\\ \mathbf{B}\end{bmatrix} \tag{B.2}$$

where $\mathbf{N}$ is the *fundamental elasticity matrix*, which is a 6x6 matrix that depends only on the stiffness tensor. Equation (B.2) is an eigenequation which has the form ($\mathbf{Ax} = \lambda\mathbf{x}$) [1]. Since $\mathbf{N}$ is a 6x6 matrix, there are 6 eigenvalues, with their respective 6x1 eigenvectors. As explained by Ting [191], for real problems, the 6 eigenvalues will always consist of 3 pairs of complex conjugates, v_α ($\alpha = 1, 2, 3$) for the positive conjugates and v_β ($\beta = \alpha + 3$) for the negative conjugates. Furthermore, if we refer to each eigenvector as ξ, the first three components of ξ as the vector $\mathbf{a}$ and the last three components as the vector $\mathbf{b}$, the eigenequation (B.2) can also be written as

$$\mathbf{N}\xi = v_\alpha\xi \tag{B.3}$$

with

[1] Where $\mathbf{A}$, λ and $\mathbf{x}$ are a square matrix, an eigenvalue and an eigenvector, respectively.

$$\xi = \begin{bmatrix} \mathbf{a}_\alpha \\ \mathbf{b}_\alpha \end{bmatrix}, \ \alpha = 1, 2, 3 \tag{B.4}$$

A and **B** are then, 3x3 complex matrices consisting of three 3x1 eigenvectors that satisfy equation (B.3), that is, $\mathbf{A} = \begin{bmatrix} \mathbf{a}_1 & \mathbf{a}_2 & \mathbf{a}_3 \end{bmatrix}$ and $\mathbf{B} = \begin{bmatrix} \mathbf{b}_1 & \mathbf{b}_2 & \mathbf{b}_3 \end{bmatrix}$. In equation (B.2), $\boldsymbol{v} = \langle v_\alpha \rangle = \text{diag}\,[v_\alpha]$ is a diagonal matrix composed by the Stroh eigenvalues v_α.

N in equation (B.2) depends on the material's stiffness. **N** is defined as

$$\mathbf{N} = \begin{bmatrix} \mathbf{N}_1 & \mathbf{N}_2 \\ \mathbf{N}_3 & \mathbf{N}_1^T \end{bmatrix} \tag{B.5}$$

with

$$\mathbf{N}_1 = -\mathbf{T}^{-1}\mathbf{R}^T, \qquad \mathbf{N}_2 = \mathbf{T}^{-1}, \qquad \mathbf{N}_3 = \mathbf{R}\mathbf{T}^{-1}\mathbf{R}^T - \mathbf{Q} \tag{B.6}$$

and

$$\mathbf{Q} = \begin{bmatrix} C_{11} & C_{16} & C_{15} \\ C_{16} & C_{66} & C_{56} \\ C_{15} & C_{56} & C_{55} \end{bmatrix}, \quad \mathbf{R} = \begin{bmatrix} C_{16} & C_{12} & C_{14} \\ C_{66} & C_{26} & C_{46} \\ C_{56} & C_{25} & C_{45} \end{bmatrix}, \quad \mathbf{T} = \begin{bmatrix} C_{66} & C_{26} & C_{46} \\ C_{26} & C_{22} & C_{24} \\ C_{46} & C_{24} & C_{44} \end{bmatrix} \tag{B.7}$$

where C_{ij} are the components of the material stiffness tensor in contracted Voigt notation.